Ruthenium Complexes as Water Oxidation Catalysts and Photosensitizers

Dissertation zur Erlangung des
naturwissenschaftlichen Doktorgrades
der Julius-Maximilians-Universität Würzburg

vorgelegt von
Marcus Schulze
aus Reichenbach im Vogtland

Würzburg 2016

Eingereicht bei der Fakultät für Chemie und Pharmazie am:
08.09.2016

Gutachter der schriftlichen Arbeit:

1. Gutachter: Prof. Dr. Frank Würthner
2. Gutachter: Prof. Dr. Udo Radius

Prüfer des öffentlichen Promotionskolloquiums:

1. Prüfer: Prof. Dr. Frank Würthner
2. Prüfer: Prof. Dr. Udo Radius
3. Prüfer: Prof. Dr. Christoph Lambert
4. Prüfer: Prof. Dr. Maik Finze
5. Prüfer: Dr. Florian Beuerle

Datum des öffentlichen Promotionskolloquiums:
22.12.2016

Doktorurkunde ausgehändigt am:

_____

für Birgit

und

meine Eltern

ABBREVIATIONS

ab	azabenz-annulated/azabenz-annulation
anth	anthracene
abs	absorption
bpb	1,4-bis(pyrid-3′-yl) benzene
bda	2,2′-bipyridine-6,6′-dicarboxylic acid
bpy	2,2′-bipyridine
CAN	cerium(IV) ammonium nitrate
CNC	Center for Nanosystems Chemistry
COSY	correlation spectroscopy
Cp^*	pentamethylcyclopentadiene
CV	cyclic voltammetry
dape	1,12-diazaperylene
dbneil	dibenzoeilatine
(TD-)DFT	(time-dependent) density functional theory
DP	differential pulse voltammetry
dmbpy	4,4'-dimethyl-2,2'-bipyridine
dpb	2,3-bis(2-pyridyl)benzoquinoxaline)
dppn	4,5,9,16-tetraazadibenzo[*a,c*]naphthacene
dppz	dipyrido[3,2-*a*:2′,3′-c]phenazine
eil	eilatine
EnT	energy transfer
ESI	electrospray ionization
ET	electron transfer
$Fc^{+/0}$	ferrocenium/ferrocene redox couple
fl	fluorescence

GS	ground state
HMBC	heteronuclear multiple-bond correlation spectroscopy
HOMO	highest occupied molecular orbital
HR	high-resolution
HSB	heterosuperbenzene
I2M	interaction of two high-valent metal oxo units (mechanism)
ic	internal conversion
ieil	isoeilatine
ILCT	intraligand charge transfer
irr	irreversible
ISC	intersystem crossing
L	ligand
LC	ligand-centered
LMCT	ligand-to-metal charge transfer
LUMO	lowest unoccupied molecular orbital
M	metal
MALDI	matrix-assisted laser desorption/ionization
MC	metal-centered
MLCT	metal-to-ligand charge transfer
MO	molecular orbital
MS	mass spectrometry
N∩N	bidentate ligand with two N-donor atoms
naph	naphthalene
NDI	naphthalene diimide
NMR	nuclear magnetic resonance
NOESY	nuclear overhauser effect spectroscopy
nr	non-radiative
OD	optical density

OEC	oxygen-evolving catalyst/complex
OEG	oligoethyleneglycol
ox	oxidation/oxidative
PAH	polycyclic aromatic hydrocarbon
PBI	perylene bisimide
PBS	phosphate buffer solution
PCET	proton-coupled electron transfer
PDT	photodynamic therapy
Ph	phenyl
ph	phosphorescence
phen	1,10-phenanthroline
phz	phenazine
pic	4-picoline
PiSp	Pictet-Spengler
PMIDE	perylene monoimide diester
PMIMA	perylene monoimide monoanhydride
PS	photosensitizer
PSII	photosystem II
PTE	perylene tetraester
PTZ	phenothiazine
pydppn	3-(pyrid-2′-yl)-4,5,9,16-tetraaza-dibenzo-[a,c]naphthacene
pydppz	3-(pyrid-2′-yl)dipyrido[3,2-a:2′,3′-c]phenazine
pyHdbn	3-pyrid-2′-yl-4,9,16-triazadibenzo [a,c]naphthacene
pyr	pyrene
Q	quencher
r	radiative
RDS	rate-determining step
red	reduction/reductive

rEnT	reversible energy transfer
RNO	*p*-nitrosodimethyl aniline
S	singlet
SEA	sacrificial electron acceptor
SED	sacrificial electron donor
SolTech	Solar Technologies Go Hybrid (research network)
SOMO	singly occupied molecular orbital
T	triplet
tape	1,6,7,12-tetraazaperylene
TFE	2,2,2-trifluoroethanol
THF	tetrahydrofuran
TON	turnover number
TOF	turnover frequency
tpy	2,2';6',2"-terpyridine
UV	ultraviolet
VE	valence electron
Vis	visible
WNA	water nucleophilic attack (mechanism)
WO	water oxidation
WOC	water oxidation catalyst

TABLE OF CONTENT

CHAPTER 1 AIM OF THE THESIS

The global energy consumption of human society has rapidly increased since the beginning of the industrial revolution and will continue to increase in the future.[1, 2] In the 19th and 20th centuries, this demand was mainly satisfied by burning coal or hydrocarbons like oil and gas. Unfortunately, fossil fuels are limited and thus their prices are determined by market mechanisms of supply and demand. Besides those cost effects, it has generally been recognized that the prevalent combustion of natural products and the so formed carbon dioxide will considerably influence the global climate.[3, 4] Accordingly, on a long-term time scale, an alternative sustainable energy source should be exploited which could provide the basis for our future wealth.

Nuclear energy is one possible carbon-neutral energy source. However, the omnipresent radioactive risk of the fissile material, the nuclear waste as well as the unsolved issue of long-term storage turns it primarily into a bridging technology. Especially since the nuclear disaster in Fukushima (Japan) in 2011, atomic power has become socially unacceptable in Germany. Subsequently, the use of alternative forms of energy – such as wind, water and sun energy – is considered to be the leading strategy for the transformation from a fossil fuel-based to a climate-friendly and sustainable energy generation like it is envisaged with the German "Energiewende". Although all options of renewable energy have their own benefits and drawbacks, they provide a low-carbon, environmentally sound and continuous power source.

In contrast to wind and water, solar energy has the advantage that it cannot only be utilized to produce electricity but due to the high energy of photons also to directly generate energy carriers like hydrogen, methanol or methane. Within the so-called solar fuels, the energy of sun light is fixed into chemical bonds of molecules providing access to a storable energy source. In this regard, the most important light-driven chemical transformations are the reduction of protons and CO_2 as well as the oxidation of water. Interestingly, all fossil fuels are solar fuels, too, because they were created in organisms by natural photosynthesis millions of years ago. There are many advantages of solar fuels which proof their superiority over other renewable energy sources: (i) Fuels have higher energy densities than electricity storage in batteries. (ii) Once generated they can be used all day even

without sunshine or windy weather. (iii) The already existing infrastructure and internal combustion technology for fossil fuels can be used which implies for instance transportation with trucks, the filling station network or liquid and gas based automotive engines. (iv) No extended power grids are required as for electricity produced in solar cells. (v) Sun energy is better distributed than wind and water energy, which represent stronger localized energy sources at coasts, rivers or lakes. Accordingly, energy production becomes decentralized and independent of large producer companies, which makes it also attractive for developing countries. Especially the energy transportation and storage issue has been highly underestimated by the German Government during their Energiewende. The production of renewable electricity was heavily subsidized without supporting the expansion of the existing power grid, which has become a current and important bottleneck of the Energiewende.

In 2012, the Bavarian State Government decided to support the innovative concept of converting solar energy into electricity and non-fossil fuels with 50 million Euros. As a result, the interdisciplinary network ”Solar Technologies Go Hybrid” (SolTech) was founded and at different Bavarian universities five Key Laboratories (KeyLabs) were founded, which focus on specific projects depending on their already existing research expertise. At the University of Würzburg, the KeyLab on Supramolecular Photosystems was established at the “Center for Nanosystems Chemistry” (CNC) which explores the supramolecular organization of small molecules into large functional architectures. On the one hand, the novel materials are used to accomplish light-harvesting in organic solar cells to improve electricity generation (photovoltaics). On the other hand, the connection of light-harvesting systems with photocatalytic units for solar fuel production (artificial photosynthesis, photocatalytic water splitting) became a major goal of research for this KeyLab.

The research on the self-assembly of single components into large structures is strongly correlated to the natural photosynthesis, in which many self-assembled biomacromolecules play an integral role. Plants have quite perfectly accomplished to organize the different parts of photosynthesis – the light-harvesting dye assembly, the photosensitizer (primary charge separation unit for the generation of free electrons and holes), the oxidative and the reductive catalyst – into one fully operating system, which can even be partly repaired while running (**Figure 1**). The research at CNC takes inspiration of this highly sophisticated system, namely the Photosystem II (PSII), that is primarily responsible for

the absorption of light *via* a chromophore antenna system and the oxidation of water into molecular oxygen. Nature uses the process of self-assembly in the PSII to construct a light-harvesting system with an integrated catalytic active center for water oxidation. In the light-harvesting system, different chlorophyll and β-carotene chromophores are utilized to absorb light very efficiently; in the oxygen-evolving catalyst complex, single manganese metal centers are gathered in a Mn_4CaO_5 cluster to perform the sophisticated four-electron transfer to oxidize water.

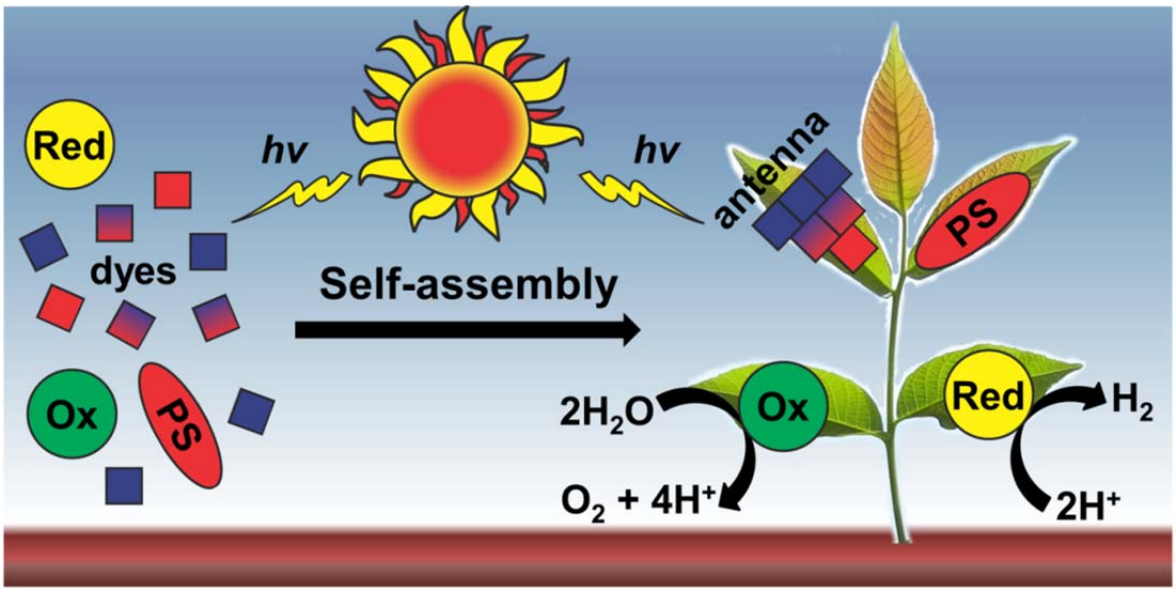

Figure 1 Schematic illustration of the self-assembly processes in natural systems, which combine all integral parts required for the successful light-driven water splitting (Ox = oxidation catalyst, Red = reduction catalyst, PS = photosensitizer). Reproduced from Ref. [5] with permission from The Royal Society of Chemistry.

One aim of this thesis was to realize a metallosupramolecular catalyst assembly based on ruthenium water oxidation catalysts (WOCs). In this regard, a stable self-assembled system was to be constructed bringing multiple catalytic active centers into close proximity to each other, as it is done in nature´s Mn_4CaO_5 cluster. Subsequently, the influence of the catalytic centers on the neighboring WOCs was to be studied. The second aim of this work was to evaluate whether the popular dye class of perylene bisimides (PBI) can be used as photosensitizer for light-driven chemical transformations. PBI chromophores are appreciated because they have a strong absorptivity of around 500 nm and thus, have better absorption profiles than many existing photosensitizers based on ruthenium(II) polypyridyl complexes. Furthermore, perylene bisimides are strong electron acceptor molecules and thus strong photooxidants. After light excitation they should in principle be able to extract electrons from a catalyst unit and thus drive oxidative conversions.

In **Chapter 2** a brief overview about the water oxidation reaction and the development of molecular ruthenium complexes as catalysts is given. In this regard, the two established mechanisms, WNA (water nucleophilic attack) and I2M (interaction of two high-valent metal oxo units), are described based on typical catalyst representatives known from literature. After these mechanistic details, the photocatalytic oxidation of water and the integral role of the photosensitizer are outlined. The second part of the literature survey summarizes the most widespread photosensitizer class of ruthenium(II) polypyridyl complexes and its fundamental photophysics and photochemistry. Subsequently, the bichromophoric concept is introduced in which the light absorption of a second chromophore is used to improve the overall photosensitizer properties. Special attention is devoted to PBI-based dyads.

Chapter 3 is concerned with the experimental results and their interpretations, and is divided into three parts (**Scheme 1**).

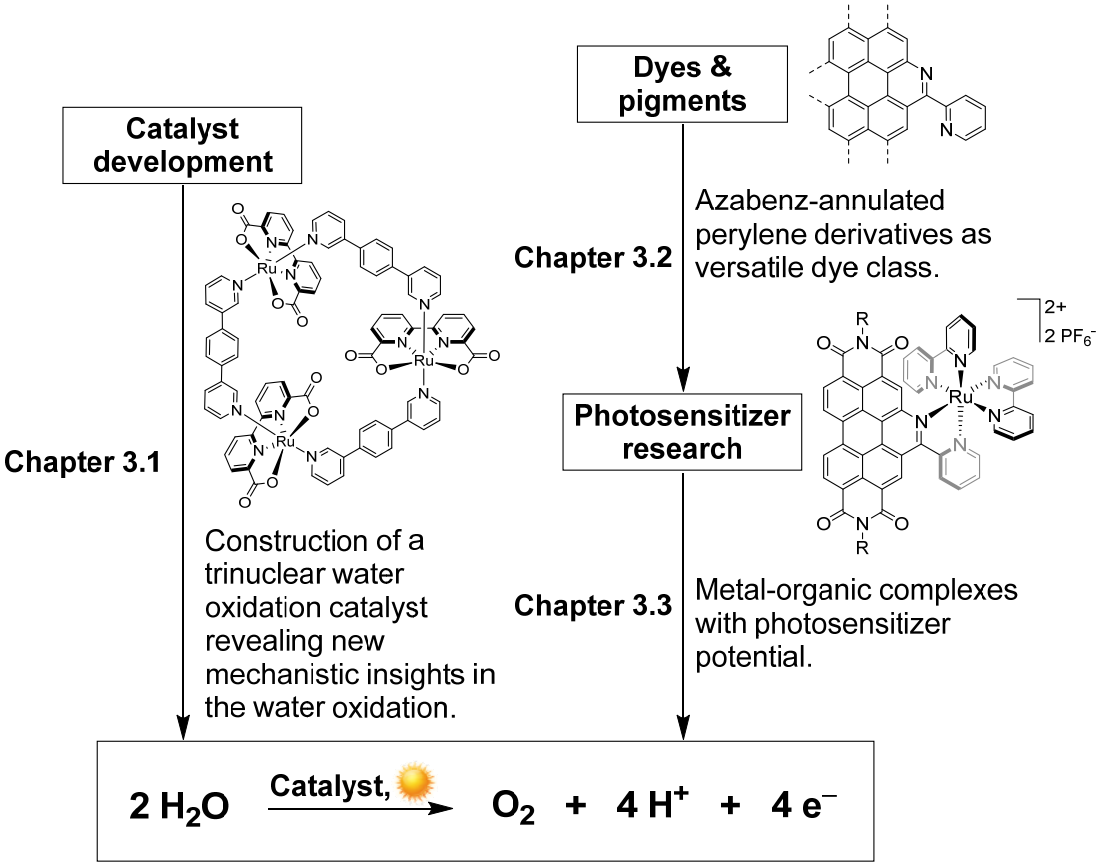

Scheme 1 Overview of important aspects to realize photocatalytic water oxidation on a homogeneous molecular level with regard to the achieved results within this thesis.

Subchapter **3.1** summarizes the synthesis and characterization of metallosupramolecular catalyst systems based on ruthenium water oxidation catalysts. In this regard, the preparation of a trinuclear Ru-based macrocycle, its structural characterization, the in-depth study of the electrochemical, chemical and photochemical water oxidation capability and its mechanistic investigations are presented. In subchapter **3.2**, the dye class of azabenz-annulated (ab-) perylene derivatives is then introduced focusing on structural modifications by diverse synthetic approaches. The prepared ab-PBI chromophores allow the preparation of novel ruthenium(II) polypyridyl complexes with a closely linked PBI ligand. At the beginning of subchapter **3.3**, the synthesis and the optical and electronic characterization of these PBI-metal substances are discussed. Subsequently, the potential of this new photosensitizer class is evaluated in organic and aqueous solvents.

Chapter 4 summarizes the results obtained in this thesis in English and German.

C**hapter 5** contains the experimental section, in which the used materials and methods are documented. Furthermore, the synthetic procedures and the characterization of the newly synthesized substances are outlined.

CHAPTER 2 LITERATURE SURVEY

The devotion to renewable energy sources raised especially the light-driven water oxidation process to an integral step towards the realization of efficient and carbon-neutral cyclic water splitting.[6, 7] Light-driven water oxidation demands the development of water oxidation catalysts (WOCs) as well as adjustable photosensitizer (PS) molecules that are required to capture the sun light and to provide oxidation potential for the catalyst to drive the chemical reaction. The first part of the literature survey will review important milestones of homogenous ruthenium catalyst development. In the following, the more specialized catalysis topics as mechanistic considerations and light-driven water oxidation are reviewed, which are required for the interpretations in the *Results and Discussion* subchapter **3.1**. Afterwards, the very popular PS class of ruthenium(II) polypyridyl complexes is introduced. Finally, the improvement of this PS class by attaching additional chromophores, then called bichromophoric systems, is discussed with a variety of example structures.

2.1 Water Oxidation

2.1.1 A Brief History of Water Oxidation Catalysts and General Considerations

In the water oxidation (WO) process, the anodic half-reaction of the complete water splitting (equation (1)), four electrons and four protons are removed from two water molecules to form molecular oxygen:

$$H_2O \rightarrow O_2 + 4H^+ + 4e^- \qquad (1)$$

This simple-looking reaction is one of the key steps in natural photosynthesis and plays an integral part of the photosystem II (PSII), which allows the prospering life around us.[8] Nature utilizes a small metallo-oxo cluster consisting of four manganese centers, Mn_4CaO_5, to perform the sophisticated four-electron conversion (**Figure 2a**).

Mimicking the ingenuity of nature was always a strong driving force for scientists. After the understanding of the natural photosynthesis has increased over time, the desire to split water into its individual components hydrogen and oxygen grew and finally ended up in

the research field of artificial photosynthesis.[9, 10, 11] This research area became extremely divers because it covers not only homogeneous WOCs of all elements[12, 13, 14] but also heterogeneous materials.[6, 15, 16, 17] The here presented survey will only consider homogeneous ruthenium WOCs.

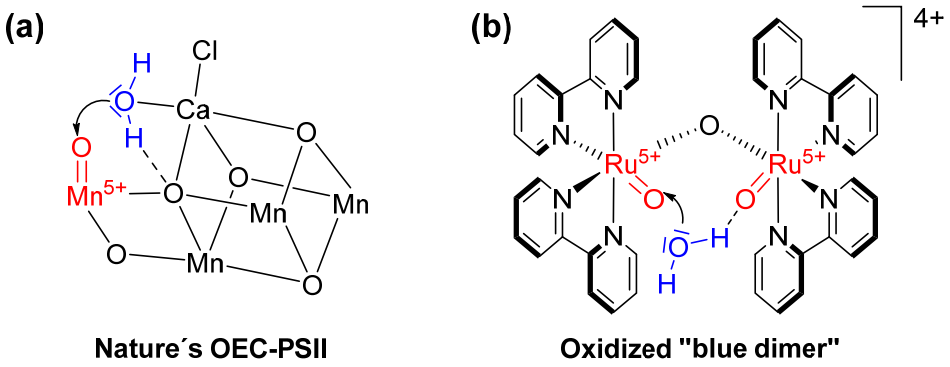

Figure 2 Comparison of the O-O bond forming step in the water oxidation process between the natural Mn_4CaO_5 oxygen evolving complex of PSII (a) and the artificial blue dimer *cis,cis*-$[[Ru(bpy)_2(H_2O)]_2(\mu\text{-}O)]^{4+}$ **1** (b).

Although not named artificial WOC by that time, in 1982 the first example of well-defined molecular and artificial water oxidation catalyst was published by Meyer and coworkers – an oxo-bridged dinuclear ruthenium complex (*cis,cis*-$[[Ru(bpy)_2(H_2O)]_2(\mu\text{-}O)]^{4+}$ **1**, bpy = 2,2′-bipyridine), better known as the "blue dimer" (**Figure 2b**).[18] The water oxidation in the natural and this artificial system have close similarities: First, the metal centers are oxidized to highly reactive metal-oxo species, in which the oxygen atom becomes Lewis-acidic. In the next step a surrounding water molecule can nucleophilically attack the metal-oxide to form the O–O bond (**Figure 2**).[19, 20, 21] Subsequently, the oxygen is released by a sequence of follow-up reaction steps and the starting species of the catalyst is regenerated (for detailed discussion see section **2.1.2** and **2.1.3**). There are numerous debates about the true mechanistic picture of the water oxidation in the oxygen evolving catalyst of PSII (OEC-PSII) but the cooperation of the metal centers is accepted to be crucial.[22, 23, 24] In case of the blue dimer the catalytic cycle can be passed 13 times before the catalyst decomposes.[25] This criterion is called turnover number (TON) and represents one of two key benchmark numbers in catalytic processes. The second, the turnover frequency (TOF), describes the turnover per time unit ([TOF] = s^{-1} or min^{-1}) and is 0.004 s^{-1} for the blue dimer.[26] The TON is indicative for the stability of a system, whereas the TOF represents the catalytic activity. For comparison, the TON and TOF of OEC-PSII are with $1.8 \cdot 10^5$ and 100–400 s^{-1}, respectively, many orders of magnitude higher than in the first artificial

system (**Figure 3**).[27, 28] Depending on the light intensity, the OEC-PSII has a half-life period between 30 min and 8 h and has to be completely rebuilt afterwards.[29] Therefore, the association between stability and TON values should always be done carefully.

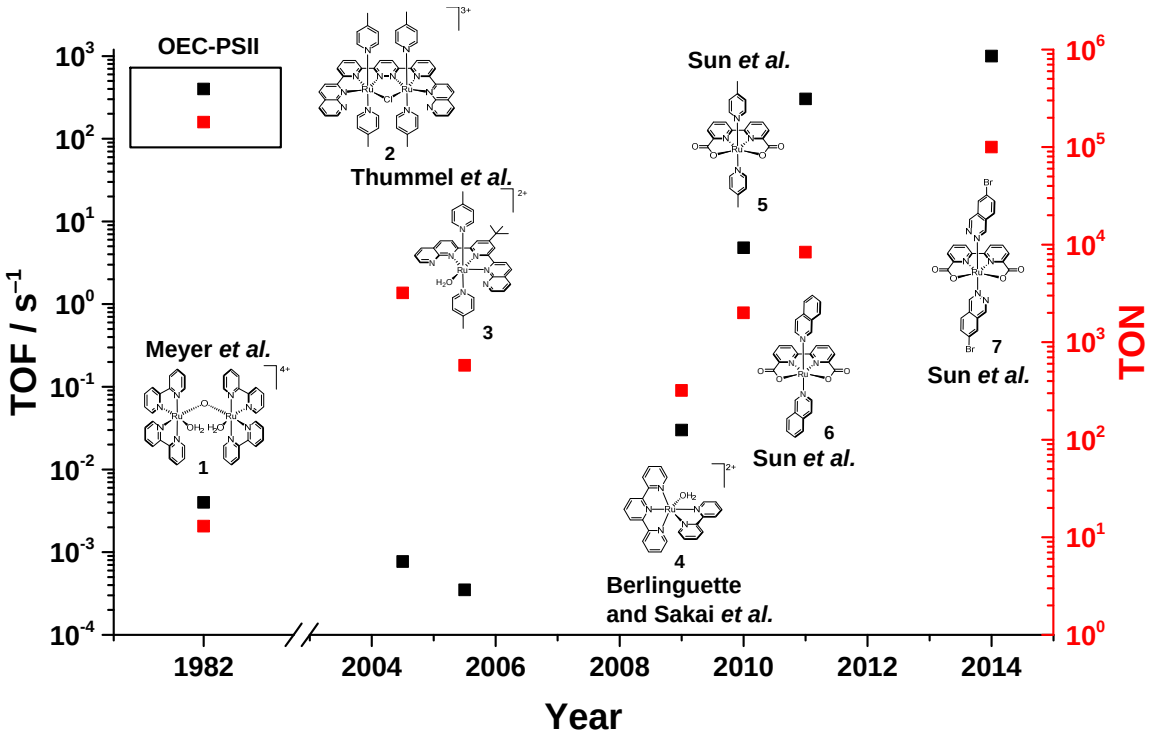

Figure 3 Chronological listing of representative homogenous ruthenium-based WOCs reported over the past 34 years and the corresponding development of catalytic benchmark numbers TOF and TON. The natural system OEC-PSII is given as reference.

At the beginning of the water oxidation catalyst research, which was mainly focused on nature-related multinuclear manganese complexes,[30, 31, 32] a scientific consensus emerged that only multinuclear metal complexes can manage the four electron release process because single metal centers cannot deal with this wide range of different redox states. It took until 2005 that Thummel and coworkers presented the mononuclear ruthenium water oxidation catalyst **3** which disproved the dogma for the element ruthenium.[33] Notably, the mononuclear ruthenium complex **3** was initially only prepared as a reference substance to an analogue dinuclear complex **2** (for structures see **Figure 3**). This finding was somehow the real starting point for the research field of artificial photosynthesis. Since then a surprising performance rally has taken place (**Figure 3**). In 2009/2010, Sakai and Berlinguette and their coworkers revealed that also the quite simple complex $[Ru(OH_2)(tpy)(bpy)]^{2+}$ **4** (tpy = 2,2';6',2''-terpyridine) is feasible of water oxidation with improved catalytic stability and activity values of a TON of 320 and a TOF of 0.03 s^{-1}.[34, 35]

Subsequently, Sun and coworkers established the catalyst class of [Ru(bda)L_2] (bda = 2,2′-bipyridine-6,6′-dicarboxylic acid, L = aromatic N-heterocycles, complexes **5-7**) and a significant efficiency increase was achieved to TONs of up to $1 \cdot 10^5$ and TOFs of up to 1000 s^{-1}.[36]

The [Ru(bda)L_2] catalyst family had deepened the mechanistic understanding of the water oxidation because these catalysts operate *via* a different mechanism than the other depicted complexes in **Figure 3**. It was shown that the rate-determining step (RDS) of the WO with [Ru(bda)L_2] complexes is based on the interaction of two high-valent metal oxo units (I2M, **Figure 4**).[37] Prior to the [Ru(bda)L_2] complexes, the most widespread mechanism showed the nucleophilic attack of water (WNA) as the RDS, as demonstrated for instance for the blue dimer **1** or $[Ru(OH_2)(tpy)(bpy)]^{2+}$ **4**.[19, 38] Nowadays, WNA and I2M are both accepted WO pathways and are mostly distinguished by (i) the molecularity of the reaction in regard to the catalyst concentration, (ii) the proton involvement in the RDS and (iii) the origin of the oxygen atoms in the produced molecular oxygen.[39] In the following two subchapters, these two mechanisms are discussed in more detail with the aid of selected examples.

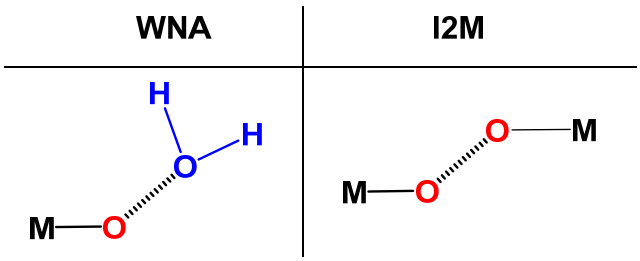

Figure 4 O-O bond formation pathways during the water oxidation process with high-valent transition metal oxides. Left: Water nucleophilic attack (WNA). Right: Interaction of two high-valent metal oxo species (I2M).

2.1.2 $[Ru(OH_2)(tpy)(bpy)]^{2+}$ – Mononuclear Catalyst with WNA Mechanism

Ruthenium metal complexes can realize 11 different oxidation states and thus, have one of the most diverse redox chemistries of the whole elements in the periodic table.[40] Consequently, they have conquered a dominant position as versatile redox catalysts. Most of these catalysts are ruthenium(II) polypyridyl complexes and have neutral and/or moderate σ- donating and π-accepting ligands like H_2O and N-donors (*e.g.* amines, pyridine and corresponding derivatives like bpy and tpy) favoring the oxidation states +II and +III. Water oxidation requires oxidation states up to +V so that such complexes are not

capable of oxidizing water. Furthermore, a catalyst for water oxidation needs obviously a vacant coordination site to which water is accessible and can be bound.

Water is not an innocent neutral σ-donor in the coordination sphere and is very adaptable to the coordination situation by the release of protons. The stepwise H^+ losses of the H_2O ligand can lead to the monoanionic hydroxido (HO^-) or even to the dianionic oxido (O^{2-}) ligand. The process of the concerted abstraction (or addition) of an electron and a proton is called proton-coupled electron transfer (PCET).[41] Because of the PCET processes, water can more efficiently stabilize higher oxidation states of the ruthenium center in its stronger σ-donating anionic forms. T. J. Meyer and coworkers investigated ruthenium complexes with PCET phenomena for metalorganic catalysis applications already in the early 1980s.[42] In this course, also the above mentioned blue dimer *cis,cis*-$[[Ru(bpy)_2(H_2O)]_2(\mu\text{-}O)]^{4+}$ **1** was synthesized and fully characterized.[18] However, to recap fundamental aspects of water oxidation catalysis the focus in this survey is put on the more simple mononuclear complex $[Ru(OH_2)(tpy)(bpy)]^{2+}$ **4**, which was also characterized by Meyer and shares many important catalytic features with the blue dimer.[19, 43]

A necessary routine in the classic evaluation of water oxidation catalysts is the electrochemical characterization in aqueous solutions because it gives information about the different oxidation states of the metal center and the possibly involved PCET processes. Electrochemical measurements of $[Ru(OH_2)(tpy)(bpy)]^{2+}$ **4** in aqueous pH 7 solutions (**Figure 5** top) revealed that the first $Ru^{2+/3+}$ redox couple is at +0.74 V *vs* NHE (normal hydrogen electrode; most widespread standard reference electrode for aqueous investigations).[43] Hence, $[Ru(OH_2)(tpy)(bpy)]^{2+}$ is by 0.52 V easier to oxidize than $[Ru(bpy)_3]^{2+}$ (1.26 V *vs* NHE, red line **Figure 5**).[44] This large difference can be explained by the simultaneous proton release during the oxidation process forming the hydroxido ligand in $[Ru^{3+}(OH)(tpy)(bpy)]^{2+}$. The subsequent oxidation from Ru^{3+} to Ru^{4+} takes place at +0.87 V in the resulting hydroxide-complex, which is very close to the first redox event and still under the +1.26 V of $[Ru(bpy)_3]^{2+}$. These low oxidation potentials are only feasible because the PCET processes allow the ruthenium complex to keep its overall charge at 2+. At pH 7 the oxidation of the $[Ru^{4+}{=}O(tpy)(bpy)]^{2+}$ species is equal to the standard potential of the anodic water oxidation half reaction, $E^0 = +1.23\ V - (0.059\ V \cdot pH)$ (blue dashed line in **Figure 5**).

Consequently, without any electrochemical overpotential, which is a kinetic effect inhibiting the thermodynamic possible reaction, the water oxidation could already take place. But unfortunately, there is nearly always a certain overpotential because the kinetics of this four electron and four proton release process are quite complex. Catalyst development devoted much attention to reduce such effects.

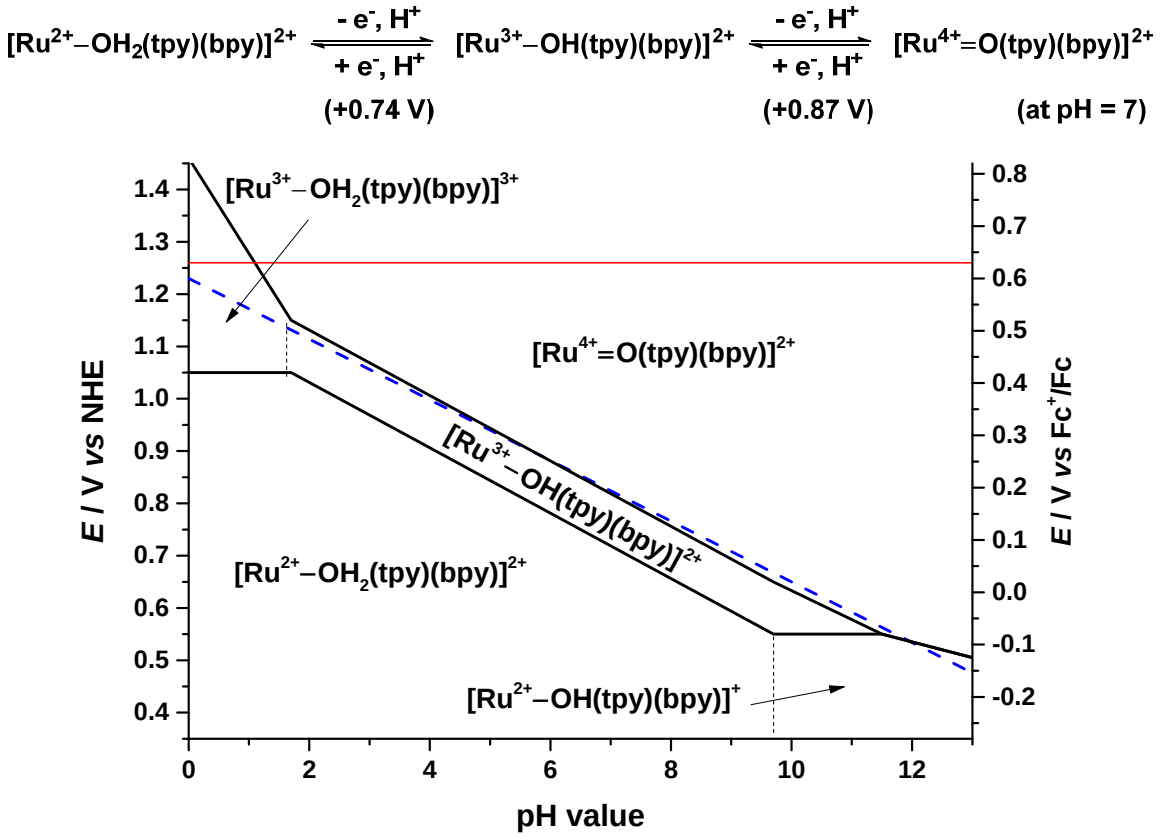

Figure 5 Proton-coupled electron transfer (PCET) processes of $[Ru(OH_2)(tpy)(bpy)]^{2+}$ **4** at pH 7 (top). Bottom: Potential-pH diagram (Pourbaix diagram) of $[Ru(OH_2)(tpy)(bpy)]^{2+}$ in aqueous solution derived from electrochemical measurements at certain pH values. Adapted from Meyer and coworkers.[43] The red line marks the $Ru^{2+/3+}$ proton-uncoupled redox couple of $[Ru(bpy)_3]^{2+}$. The blue dashed line marks the standard potential of the water oxidation anodic half reaction $H_2O \rightarrow O_2 + 4H^+ + 4e^-$ ($E^0 = +1.23$ V – (0.059 V · pH) without any overpotential. The conversion factor between the NHE and the Fc^+/Fc electrode is 0.63 V.[45]

PCET processes are strongly pH-dependent because the proton release depends on the proton uptake capability of the environment, which correlates to the pH value of the bulk solution (see equations (2) and (3)). The pH-dependence is generally recorded in a potential-pH diagram (also called Pourbaix diagram)[46], which is obtained by different electrochemical measurements (cyclic voltammograms or differential-pulse polarograms) at defined pH-values (**Figure 5**). Therefore, the Pourbaix diagram can be read like a phase diagram in which the stability of a certain species (phase) under specific conditions (here pH value and electrochemical potential) is depicted. For instance, the starting species

$[Ru(OH_2)(tpy)(bpy)]^{2+}$ is only existing until the pH value of 9.7, which is in consequence also the pK_a value of the compound.[43] The subsequently formed complex $[Ru^{2+}(OH)(tpy)(bpy)]^{+}$ is stable until very basic pH conditions. At a pH higher than 11.5 the oxidation of $[Ru^{2+}–OH]^{+}$ leads directly to the $[Ru^{4+}=O(tpy)(bpy)]^{2+}$ species. Consequently, at pH >11.5 only one redox event would be observed, in which two electrons and one proton are released at the same time. This means that the ruthenium oxidation state +III is in that particular pH range not stable and two Ru^{3+} molecules would spontaneously disproportionate into one Ru^{2+} and one Ru^{4+} complex. In this manner, the whole Pourbaix diagram can be interpreted and gives comprehensive information about the pH-dependent electrochemistry and the stability of certain redox states of a compound. Furthermore, the slope of a line between two stability regions provides information about the number of involved electrons and protons. The oxidation from Ru^{2+}-OH_2 to Ru^{3+}-OH is a one proton (m) and a one electron (z) process for instance. According to equation (3), the expected pH dependency of this process would be 59 mV/pH, which is indeed found in experimental data (**Figure 5**).

$$a\ Ru^{2+}–OH_2 \rightarrow a\ Ru^{3+}–OH + m\ H^{+} + z\ e^{-}$$

$$E = E^{0} + \frac{RT}{zF} \ln \frac{\left[Ru^{2+}–OH_2\right]^{a}}{\left[Ru^{3+}–OH\right]^{a}\left[H^{+}\right]^{m}} \qquad (2)$$

$$E = E^{0} + \frac{0.0591}{z} \log \frac{\left[Ru^{2+}–OH_2\right]^{a}}{\left[Ru^{3+}–OH\right]^{a}} - \frac{m}{z} 0.0591\ pH \qquad (3)$$

Surprisingly, it endured until 2009 before Sakai and Masaoka confirmed finally that the highly oxidized $[Ru^{4+}=O(tpy)(bpy)]^{2+}$ species is feasible to catalyze the oxidation of water.[34] The catalytic cycle at pH 1 with cerium(IV) ammonium nitrate (CAN) as sacrificial electron acceptor (**Scheme 2**) passes at the beginning the same redox states as in the electrochemical experiment (see potentials in the Pourbaix diagram at pH 1). Firstly, $[Ru(OH_2)(tpy)(bpy)]^{2+}$ **4** is oxidized stepwise to the $[Ru^{4+}=O]^{2+}$ by the release of two protons and two electrons. In $[Ru^{4+}=O]^{2+}$ the electrophilicity of the oxido ligand is high enough that the water nucleophilic attack can take place and the peroxo compound $[Ru^{3+}–OOH]^{2+}$ can be formed (plus additional release of one electron and one proton). There are still discussions in the scientific community, if the rate-determining step in the WNA mechanism is a consecutive two-step pathway *via* an extremely high oxidized $[Ru^{5+}=O]^{3+}$ species or a concerted one-step procedure without a concrete

intermediate.[35, 38, 47] $[Ru^{3+}–OOH]^{2+}$ can be further oxidized to produce the side-on bounded dioxo species $[Ru^{4+}–OO]^{2+}$, in which the dioxygen is rapidly replaced by a water molecule from the bulk solution.[48] In this way the catalytic starting point $[Ru(OH_2)(tpy)(bpy)]^{2+}$ is retained and the catalysis can start from the beginning. The catalytic activity of the complex vanishes after 320 WNA catalytic cycles (≡ TON) because of catalyst decomposition.[35]

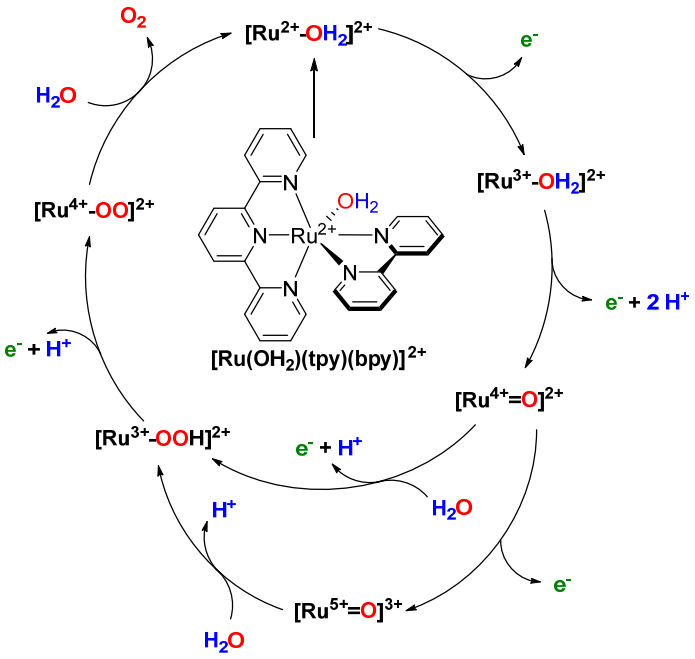

Scheme 2 Proposed WNA mechanism of the catalytic water oxidation with $[Ru(OH_2)(tpy)(bpy)]^{2+}$ **4** as catalyst (conditions: pH 1 and cerium(IV) ammonium nitrate as sacrificial electron acceptor).

2.1.3 Ru(bda) Catalyst Family – Mononuclear Catalysts with I2M Mechanism

The $[Ru(bda)L_2]$ complexes represent a special catalyst class and obtained a significant amount of attention after Sun and coworkers had shown its water oxidation potential.[49] The bda unit represents a dianionic and tetradentate ligand so that overall neutral complexes are obtained (**Figure 6**). As a consequence of the carboxylate coordination pattern, the oxidation of the ruthenium center ($Ru^{2+/3+}$) is already reached at a potential of –0.06 V (for L = 4-picoline (pic), $[Ru(bda)(pic)_2]$ **5**).[49] This indicates a cathodic shift of outstanding 0.9 V in comparison to $[Ru(OH_2)(tpy)(bpy)]^{2+}$ **4** (E ($Ru^{2+/3+}$) = +0.8 V *vs* $Fc^{+/0}$ (ferrocenium/ ferrocene redox couple)). In organic aprotic solvents, no further oxidation events are observed.

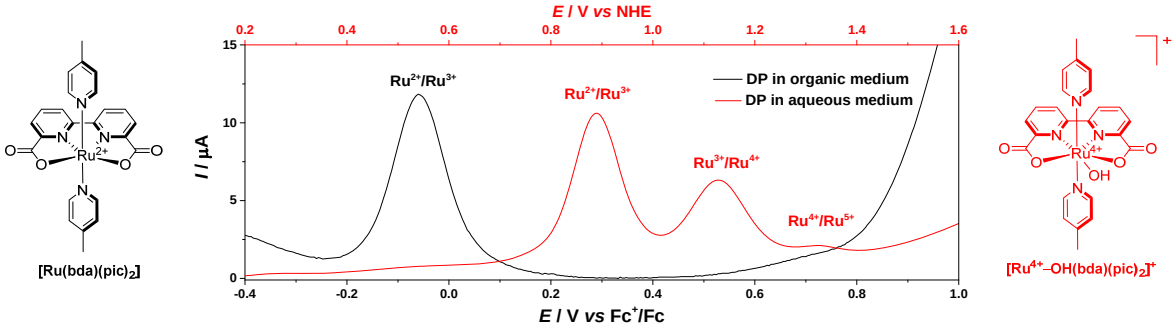

Figure 6 Schematic representation of [Ru(bda)(pic)$_2$] **5** and its electrochemistry in organic medium (CH_2Cl_2, black). In red: Electrochemistry in aqueous pH 1 solution (50% CH_3CN and 50% aq. CF_3SO_3H) and the corresponding structure of the intermediate $[Ru^{4+}–OH(bda)(pic)_2]^+$.

At the beginning, it was a surprise that [Ru(bda)(pic)$_2$] **5** showed a more complex electrochemistry in aqueous solvent mixtures (co-solvent mostly acetonitrile or 2,2,2-trifluoroethanol (TFE)) than in an organic medium (**Figure 6**).[37, 50] Instead of one oxidation, now three redox events appeared at +0.89, +1.13 and +1.32 V *vs* NHE in 1:1 mixture of acetonitrile and pH 1 aq. CF_3SO_3H. Profound investigations revealed that these three redox couples can be assigned to the oxidation events $Ru^{2+}\rightarrow Ru^{3+}$, $Ru^{3+}\rightarrow Ru^{4+}$ and $Ru^{4+}\rightarrow Ru^{5+}$.[37] The appearance of these three redox couples at very low potential is only possible because [Ru(bda)(pic)$_2$] can incorporate a seventh ligand, namely water, in its coordination sphere. Sun and coworkers provided a crystal structure of the Ru^{4+} species, in which an additional hydroxido ligand is coordinated to the ruthenium center stabilizing the high oxidation state (**Figure 6**, red structure).[49] The seventh coordination site in [Ru(bda)(pic)$_2$] for hydroxide is feasible because the bda ligand creates a large O–Ru–O bite angle of 120°. Therefore, the Ru^{4+} species forms a stable pentagonal bipyramidal 18-valence electron (VE) coordination configuration.

The pH-dependency of the oxidation events have supported the water coordination (Pourbaix diagram in **Figure 7**).[37] At the oxidation state +II the water is most likely only weakly bound to the complex.[51] Every additional ruthenium oxidation strengthens gradually the Ru–O bond to water and finally, at the ruthenium oxidation stage +IV a real seven-bonded ruthenium metal center with an additional hydroxido ligand exists. Interestingly, even the last proton-coupled oxidation to Ru^{5+}=O creates only a complex with an overall charge of +1 which is an important feature of this catalyst class.

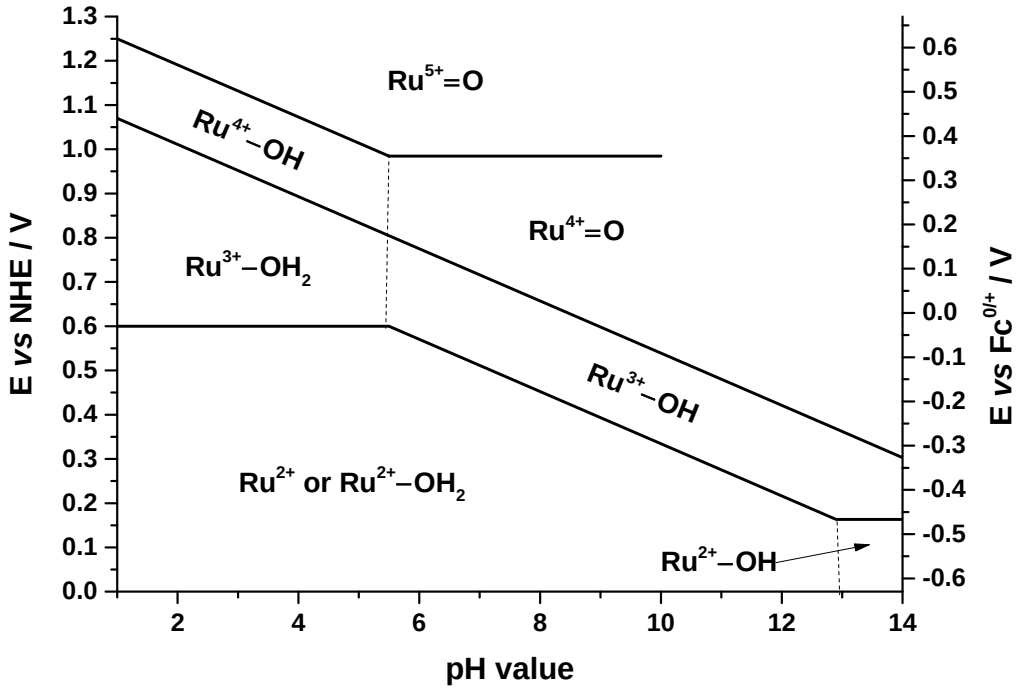

Figure 7 Potential-pH diagram (Pourbaix diagram) of [Ru(bda)(pic)$_2$] **5** in aqueous solution (1:2 mixture of TFE and pH 1.0 water) derived from electrochemical measurements at certain pH values. Adapted from Sun and coworkers.[37] The conversion factor between the NHE and the $Fc^{0/+}$ electrode is 0.63 V.[45]

[Ru(bda)(pic)$_2$] **5** with its TON_{max} and TOF_{max} of 2,000 and 14.7 s^{-1}, respectively, became one of the most promising lead structures for water oxidation catalysts in the scientific community.[36] Surprisingly, the high catalytic activity was achieved by a completely different mechanism in comparison to $[Ru(OH_2)(tpy)(bpy)]^{2+}$ **4**.[39] As described in section **2.1.2**, $[Ru(OH_2)(tpy)(bpy)]^{2+}$ performs the WO *via* the WNA mechanistic pathway, in which water attacks nucleophilically a highly oxidized $[Ru^{4+}=O]^{2+}$ or $[Ru^{5+}=O]^{3+}$ species, respectively. In contrast, in [Ru(bda)(pic)$_2$] the O–O bond forming step involves two highly oxidized $[Ru^{5+}=O(bda)(pic)_2]^{+}$ metal complexes, which make an intermolecular radical coupling (I2M mechanism, **Scheme 3**). It is still part of the scientific discussion, if the $[Ru^{5+}=O(bda)(pic)_2]^{+}$ species is not better be described as $[Ru^{4+}=O^{+}(bda)(pic)_2]^{+}$ which has a significant oxyl radical character.[52] Such an electronic structure would still satisfy an 18-valence electron configuration and is quite reasonable with the proposed radical coupling mechanism.

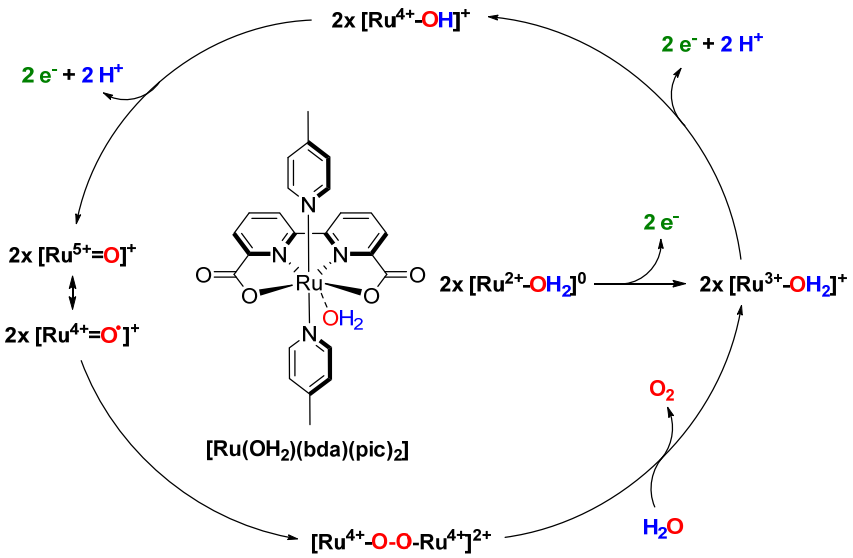

Scheme 3 Proposed I2M catalytic mechanism of the catalytic water oxidation with $[Ru(OH_2)(bda)(pic)_2]$ **5** as catalyst (conditions: pH = 1 and cerium(IV) ammonium nitrate as sacrificial electron acceptor).

2.1.4 Photocatalytic Water Oxidation

Electrochemically or chemically driven water oxidation reactions contradict the aim of carbon-neutral cyclic water splitting process. Very often electricity is to a large degree obtained by fossil fuels and also the chemical potential of a sacrificial oxidant is accompanied by an energy and resource-intense production process; for instance, the very strong oxidant CAN is obtained by refluxing Ce_2O_3 in hot concentrated HNO_3. In contrast, WO powered by the nearly inexhaustible energy reservoir of the sun keeps the promise to create a true carbon-neutral sustainable energy source.

The photosensitizers of choice on the homogeneous molecular water oxidation level are the ruthenium(II) *tris*-bipyridine complex ($[Ru(bpy)_3]^{2+}$ **8**) and its derivatives because they combine a myriad of ideal PS properties (for details see subchapter **2.2.1**). The most widespread setup to obtain a light-driven water oxidation is a three-component system based on a $[Ru(bpy)_3]^{2+}$ salt, sodium peroxodisulfate and a WOC (**Figure 8**).[53] In this combination, the PS $[Ru(bpy)_3]^{2+}$ **8** and the sacrificial electron acceptor (SEA) $Na_2S_2O_8$ in cooperation with light are responsible to create continuously the chemical oxidant $[Ru(bpy)_3]^{3+}$, which then oxidizes the WOC. In more detail, firstly the PS absorbs a photon and goes into an excited state. The generated excited PS reacts with the peroxodisulfate ion and becomes in the course oxidized, whereas $S_2O_8^{2-}$ is transformed into SO_4^{2-} and $SO_4^{\bullet-}$. Subsequently, the oxidized photosensitizer $[Ru(bpy)_3]^{3+}$ has a oxidation potential of +1.26 V (*vs* NHE) and thus, can oxidize for instance the WOC $[Ru(bda)(pic)_2]$ **5**.

The water oxidation onset with this Ru(bda) catalyst is ~1.0 V at pH = 7 (see **Figure 7**). Consequently, the combination of the photosensitizer $[Ru(bpy)_3]^{2+}$ **8** and the WOC $[Ru(bda)(pic)_2]$ **5** is feasible to power the water oxidation by light.

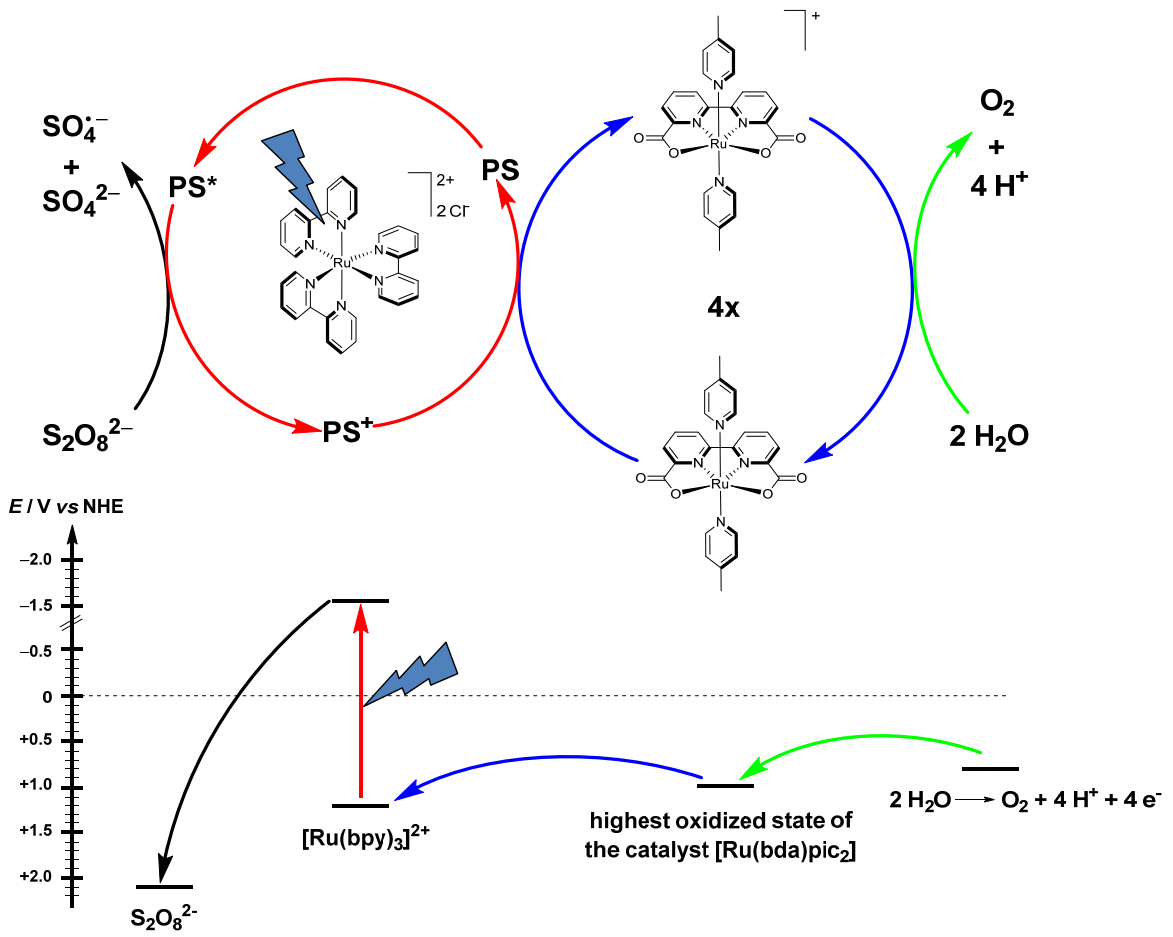

Figure 8 Top: Scheme of the photocatalytic water oxidation with $[Ru(bda)(pic)_2]$ **5** as water oxidation catalyst, $[Ru(bpy)_3][Cl]_2$ **8** as photosensitizer (PS), and $Na_2S_2O_8$ as SEA after a 450 nm light pulse has excited the photosensitizer. To preserve the simplicity of the schematic representation, the oxidation cycle of $[Ru(bda)(pic)_2]$ **5** contains only the two redox states $[Ru^{2+}(bda)(pic)_2]$ and $[Ru^{3+}(bda)(pic)_2]^+$. A more appropriate scheme has to include the proton-coupled electron transfer processes of the higher oxidation states of ruthenium (Ru^{3+}, Ru^{4+} and Ru^{5+}) in which water is coordinated to the ruthenium center as well. Bottom: Energy scheme diagram with energy levels of the individual water oxidation components and the electron flow after a 450 nm light pulse has excited the photosensitizer $[Ru(bpy)_3]^{2+}$.

Interestingly, sodium peroxodisulfate has an oxidation potential of +2.1 V *vs* NHE (sulfate radical anion $SO_4^{\bullet-}$ of +2.4 V), which is even higher than the oxidation power of CAN at pH 1 (+1.7 V).[44, 54] Although the thermodynamics of peroxodisulfate would be in favor to accomplish the water oxidation (E^0 = +1.23 V – (0.059 V · pH) by its own, it is kinetically very stable in aqueous solution. The light used in this photocatalytic WO experiment is only utilized to overcome this kinetic activation barrier of $Na_2S_2O_8$. Because the light

energy has not created a net energy gain at the end of the reaction, this three-component setup should more precisely be called light-triggered than light-driven.

The combination of the photosensitizer $[Ru(bpy)_3]^{2+}$ and the SEA $Na_2S_2O_8$ became so successful that also a large number of covalently connected photosensitizer-WOC assemblies like the dyads **9**-**12** had been synthesized (**Chart 1**).[55, 56, 57, 58] The advantages of a linked system are the improved electron transfer processes between both units. In the disconnected case of independently solvated photosensitizer and catalyst, there has to be an effective collision between the two reaction partners to execute the electron transfer. This improved electron transfer characteristics can be reflected for example in the TON value of PS-WOC assembly. For instance, the dyad **10** prepared by Thummel and coworkers could perform 134 catalytic cycles in the photocatalytic WO, whereas the analogous combination of the single components provides only a TON of 6. Similar results were also obtained for the assemblies **11** and **12** containing $[Ru(bda)L_2]$ complexes as catalysts.

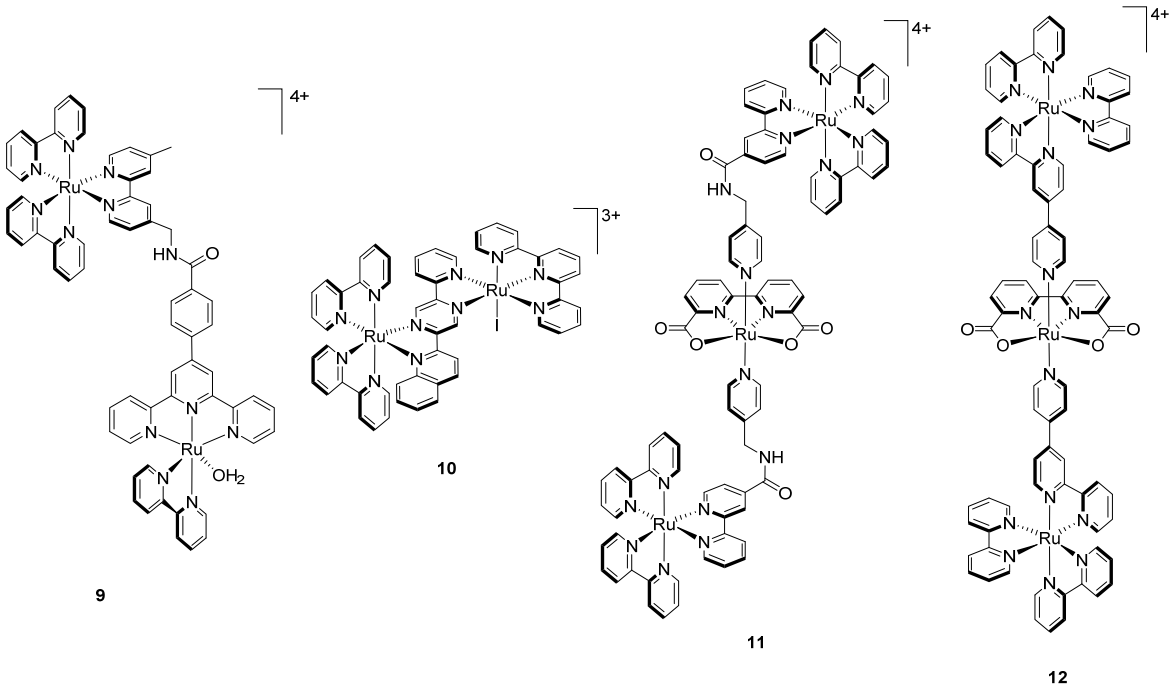

Chart 1 Schematic representation of photosensitizer-catalyst assemblies consisting of either a $[Ru(X)(tpy)(bpy)]^{2+}$- (**9** (X = H_2O) and **10** (X = I^-)) or of a $[Ru(bda)(pic)_2]$-type complex (**11** and **12**) as the catalyst and a $[Ru(bpy)_3]^{2+}$-derivative as a photosensitizer.

2.2 Ru(II) Polypyridyl Photosensitizers

Sun light provides large amounts of energy, which are however difficult to collect and afterwards it is challenging to manipulate this energy properly for desired chemical applications. Photosensitizing molecules are one possibility to make the energy of photons available (*i.e.* long-lived triplet state) and thus create a useful chemical energy source. The so generated energy source can be utilized in many research fields like dye-sensitized photovoltaic,[59] organocatalysis[60], biological imaging,[61] photodynamic therapy[62] or light-driven chemical conversions[11] for instance the water splitting which was addressed in section **2.1.4**. Because Ruthenium(II) polypyridyl complexes combine the properties stability, reactivity and synthetic access in a most advantageous way, they represent the most widespread photosensitizer class. The available extensive literature about this compound class makes it impossible to present an entire literature overview. The first comprehensive review was given by Balzani *et al*. nearly 30 years ago.[63] Since then further comprehensive publications concerning basic photophysical and photochemical properties,[64, 65, 66, 67, 68] photonic and optoelectronic materials,[69, 70, 71, 72], molecular machines,[73, 74] polynuclear complexes,[75] dendrimers,[76, 77] anion recognition,[78] supra-molecular photochemistry[79, 80] and organocatalysis[81] were released. The following chapter contains a summary of the most fundamental photophysical and photochemical properties of this compound class, which are relevant for the experimental results presented in this thesis.

2.2.1 Ground State Properties

Ruthenium(II) polypyridyl complexes gained a major interest with respect to their photophysical and photochemical properties in the last decades and hundreds of different derivatives had been synthetized up to now.[63, 79] The most prominent representatives of this substance class are ruthenium(II) *tris*-bipyridine ($[Ru(bpy)_3]^{2+}$ **8**) and ruthenium(II) *bis*-terpyridine ($[Ru(tpy)_2]^{2+}$ **13**, **Chart 2**). All Ru(II) polypyridyl complexes unite important photochemical parameters like (photo)chemical stability, reversible redox properties in the ground and excited state, broad visible light absorption, excited state lifetime, emission and excited state reactivity. But especially $[Ru(bpy)_3]^{2+}$ **8** combines all these features in one molecule in a way which is hardly found a second time and thus, makes it such a successful and often applied photosensitizer.

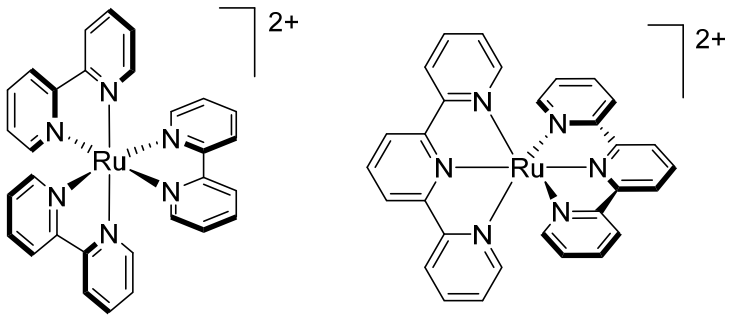

8 **13**

Chart 2 Schematic representation of the two most prominent Ru(II) polypyridyl complexes $[Ru(bpy)_3]^{2+}$ **8** and $[Ru(tpy)_2]^{2+}$ **13**.

The fundament of these favorable photophysical and photochemical characteristics is laid by the unique molecular orbital (MO) diagram of ruthenium(II) polypyridyl complexes. A typical energy level diagram of a ruthenium metal ion, which is octahedrally surrounded by six organic *N*-ligands (mainly σ-donating with a weak π-accepting nature) is depicted in **Figure 9a**.

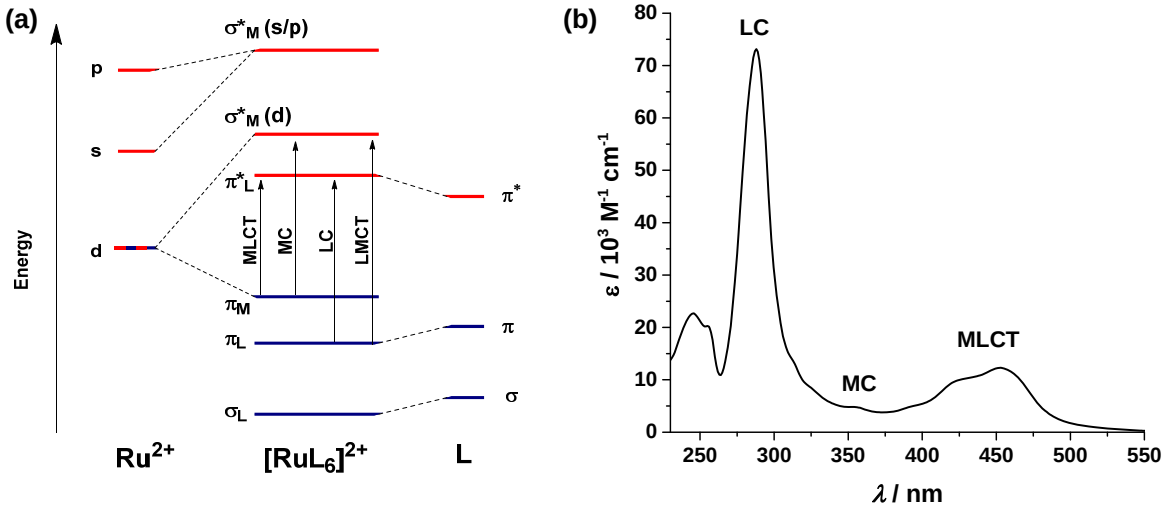

Figure 9 (a) Simplified MO diagram of an octahedral ruthenium metal complex in d^6 electronic configuration with six σ-donating N-ligands with a weak π-accepting nature ($[RuL_6]^{2+}$). Blue: occupied molecular orbitals; red: unoccupied molecular orbitals. The arrows indicate the possible optical transitions in the UV/Vis region of light for such a complex. (b) Absorption spectrum of $[Ru(bpy)_3]^{2+}$ **8** in dichloromethane with a concentration of $1 \cdot 10^{-5}$ M and the assignment of the optical transitions.

Due to the coulombic interactions of such an electrostatic ligand field, the s- and p-orbitals of the metal are energetically lifted (σ^*_M (s/p)), while the five d-orbitals are split into two sets of atom orbitals (σ^*_M (d) and π_M). Hereby, the annotations σ and π stand for the orbital symmetry, * for anti-bonding and M for the main orbital character, in this case metal. The σ^*_M (d) orbitals (more precisely d_{z^2} and $d_{x^2-y^2}$) pointing directly to the ligands are raised in

energy, whereas the π_M orbitals (d_{xz}, d_{xy} and d_{yz}) exposing between the ligands are lowered. The other way around, the filled ligand orbitals σ_L and π_L, which interact mainly with the empty s, p and d-orbitals (d_{z^2} and $d_{x^2-y^2}$), are energetically lowered. In contrast, the empty π^* orbitals of the ligands are affected by the filled d-orbitals (d_{xz}, d_{xy} and d_{yz}), due to their appropriate symmetry to each other, and get lifted in energy as a consequence. Although the so obtained final MO scheme contains many simplifications such as an ideal octahedral coordination geometry, it is quite appropriate to many different closed-shell Ru(II) polypyridyl complexes. Notably, the MO also explains the often-found high stability of these complexes – the fulfillment of the 18-valence electron rule (the inorganic analog to the noble gas rule) with 12 ligand electrons and 6 metal electrons and without any anti-bonding orbital contribution.

By interaction with light, electrons can be lifted from a filled orbital (blue marked) into a vacant one (red marked) leading to different absorption types. Based on the d^6 electronic configuration (completely filled π_M) there are different transitions possible: metal-centered (MC) absorption ($\pi_M \rightarrow \sigma^*_M$) promoting an electron from one metal d-orbital to another empty metal orbital; ligand-centered (LC) absorption ($\pi_L \rightarrow \pi^*_L$) exciting a ligand π-electron to its anti-bonding π^*; ligand-to-metal charge transfer (LMCT) absorption ($\pi_L \rightarrow \sigma^*_M$) lifting a ligand electron to a metal-centered d-orbital; and metal-to-ligand charge transfer (MLCT) absorption ($\pi_M \rightarrow \pi^*_L$) promoting an electron from the metal to the ligand. The last-mentioned transition is the energetic lowest transition in Ru(II) polypyridyl complexes between the highest occupied molecular orbital (HOMO) and the lowest unoccupied molecular orbital (LUMO).

These theoretical considerations derived from the MO scheme are also supported by experimental findings. In a typical absorption spectrum of Ru(II) polypyridyl complexes (*e.g.* $[Ru(bpy)_3]^{2+}$ **8** in **Figure 9b**), the HOMO-LUMO MLCT absorption lies around 460 nm and explains the orange/reddish color of that compound class. The most intense peak around 270 nm belongs to the LC excitation from π_L to π^*_L of the bipyridine ligand. The shoulder of this band at 350 nm is assigned to the MC transition which is symmetry-forbidden (Laporte selection rule) and thus, has a low extinction coefficient.[82]

2.2.2 Excited State Photophysics – Monomolecular Deactivation Pathways

Light excitation leads to the promotion of an electron from a bonding orbital into an anti-bonding one; put another way, from the ground state into the excited state. In the ground state of Ru(II) polypyridyl complexes all electrons are paired and thus, it is described as closed-shell singlet ground state (^{1}GS). The excited state consists naturally of two unpaired electrons. Depending on the electron spin orientation among each other, there is a singlet (anti-parallel arrangement) and triplet excited state (parallel arrangement). Because absorption is a very fast process ($k_{abs} = 10^{-15}$ s^{-1}), the spin of the ground state is preserved in the excited state and hence, only transitions of the same multiplicity are allowed. In case of Ru(II) polypyridyl complexes, the lowest energetic singlet states are the ^{1}MLCT and ^{1}MC state – the states have the same name as the underlying transitions. These states can be summarized in a Jablonski term scheme, which is a useful illustration to follow the photophysical pathways in such a system (**Figure 10**).

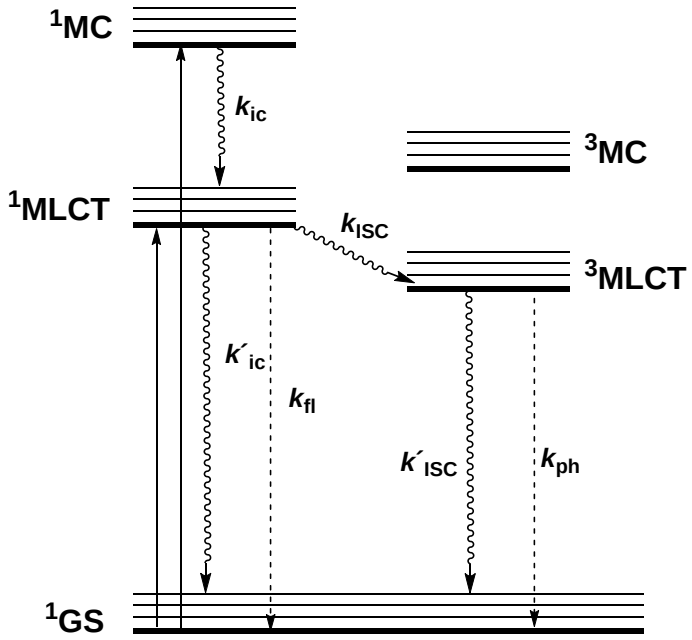

Figure 10 Energy level scheme (Jablonski diagram) of the two lowest energy transitions, MLCT and MC, of ruthenium(II) polypyridyl complexes and the photophysical deactivation pathways. Arrows: solid = absorption, wavy = non-radiative relaxation and dashed = radiative emission.

The excited state is a metastable and reactive intermediate, which seeks to release its excessive energy. In general, higher electronic states like ^{1}MC deactivate rapidly by internal conversion ($k_{ic} = 10^{10}$–10^{14} s^{-1}) into the lowest exciting state following Kasha´s rule.[83, 84] In the absence of heavy atoms or charge transfer states the depopulation of this

state to the ground state can be accomplished either by an emissive process called fluorescence ($k_{fl} = 10^7–10^9$ s^{-1}) or by another non-radiative internal conversion pathway ($k'_{ic} = 10^6–10^7$ s^{-1}).[85] However, $[Ru(bpy)_3]^{2+}$ **8** shows no fluorescence behavior. In the presence of heavy atoms like here ruthenium, the strict spin-conversion rule is overruled by the spin-orbit coupling of the metal center and allows transitions between states of different multiplicity, the so-called intersystem crossing here between the ^{1}MLCT and the ^{3}MLCT (organic molecules: $k_{ISC} = 10^5–10^8$ s^{-1}, **8**: $k_{ISC} = \sim 2.5 \cdot 10^{13}$ s^{-1}). According to the fast rate, the lowest excited ^{3}MLCT of Ru(II) polypyridyl complexes is formed with unity efficiency.[86, 87] The so populated ^{3}MLCT can relax to the ground state either by a second radiationless intersystem crossing (k'_{ISC}) or by a long-lived emission better known as phosphorescence (organic molecules: $k_{ph} = 10^3–10^{-2}$ s^{-1}, **8**: $k_{ph} = 10^6$ s^{-1}).

The emission of $[Ru(bpy)_3]^{2+}$ **8** is centered around 611 nm with a quantum yield (Φ_{ph}) of 6% and a lifetime (τ) of ~1 μs in degassed acetonitrile clearly indicating phosphorescence emission out of a triplet state.[88] The quantum yield is defined by $\Phi = k_r / (k_r + k_{nr})$ in which k_r is the radiative rate constant and k_{nr} summarizes the non-radiative processes. In the case under consideration, k_{nr} is composed of the two ISC rates k'_{ISC} from the ^{3}MLCT to the ^{1}GS and k''_{ISC} from the ^{3}MC state to the ^{1}GS (**Figure 11a**). The former becomes significant, if the energy gap between the HOMO and LUMO is too small ("energy-gap law"),[89] but is assumed to be the less important depopulation pathway. In contrast, k''_{ISC} is depending on the energy difference between ^{3}MLCT and ^{3}MC (ΔE). A ΔE value of less than <2500 cm^{-1} (~0.3 eV) as given for $[Ru(tpy)_2]^{2+}$ **13** is considered to lead to a situation in which the ^{3}MC can be significantly thermally populated (k_{da}) out of the ^{3}MLCT at room temperature.[84, 90] The potential well of the ^{3}MC is characterized by a large reorganization energy in respect to the ground state (see reaction path axis in **Figure 11b**) because in this state anti-bonding metal orbitals are populated leading to significant bond elongation. Therefore, it is not surprising that the potential surface has good overlap with the ^{1}GS potential. The ^{3}MC/^{1}GS potential crossing deactivates very efficiently the excited state (**Figure 11b** and **Figure 11c**).[91] In the worst case these effects result into the loss of any emission properties and also excited state reactivity of Ru(II) polypyridyl complexes.

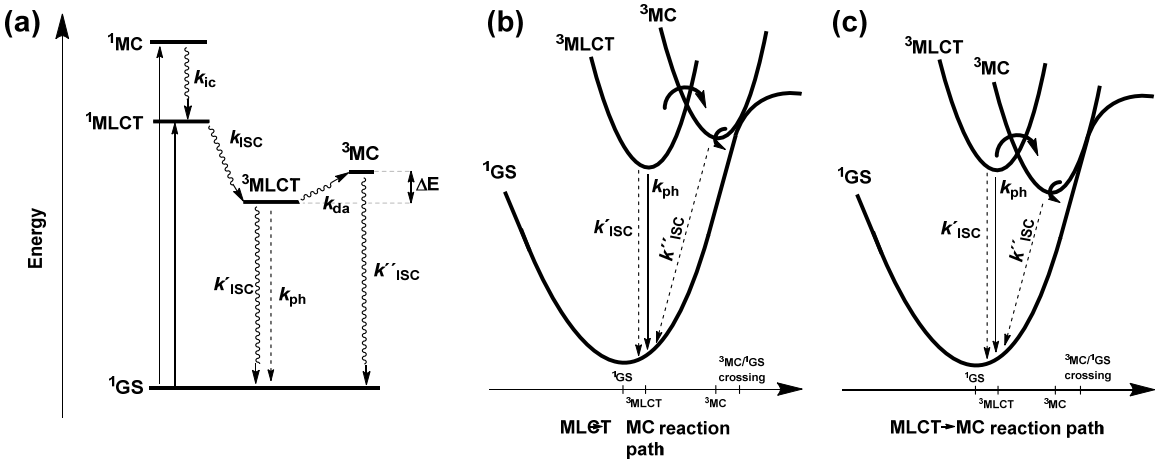

Figure 11 (a) Simplified Jablonski scheme of ruthenium(II) polypyridyl complexes. (b) Potential well diagram for ^{3}MC higher than ^{3}MLCT as given for $[Ru(bpy)_3]^{2+}$ **8**. c) Potential well diagram for ^{3}MLCT higher than ^{3}MC. Arrows: solid = absorption, wavy = non-radiative relaxation and dashed = radiative emission. Adapted from Balzani *et al*.[79]

The unique interplay of these outlined factors is the reason why Ru(II) polypyridyl complexes have gained so much interest in the last decades. Numerous manipulations of this system have been explored to overcome shortages and to improve the already remarkable properties of $[Ru(bpy)_3]^{2+}$.

2.2.3 Bimolecular Deactivation Processes – Energy and Electron Transfer

In general, an excited state aspires to reduce its excessive energy by different deactivation processes. The intramolecular monomolecular pathways like radiative fluorescence and phosphorescence and non-radiative internal conversion and intersystem crossing were discussed in section **2.2.2**.

A sufficiently long-lived excited state (τ of several hundred ns or few µs) can undergo also intermolecular deactivation processes because it can encounter another solute molecule by diffusion in this period. In the following, there can be on the one hand "non-productive" non-radiative deactivating collisions, which lead to the quenching of the excited state energy by simple energy dissipation into heat. Of greater interest are interactions, which lead to energy or electron transfer phenomena from the excited molecule to the collision partner. The former process is often termed quenching because it focuses on the oppression of the excited state energy and the outflow of the excitation energy is irrelevant. Whereas the latter is called (photo)sensitization because it concentrates on the tracking and final state of the photochemical transformation. The Gold Book of IUPAC defines photosensitization as followed: "*The process by which a photochemical or photophysical*

alteration occurs in one molecular entity as a result of initial absorption of radiation by another molecular entity called a photosensitizer.".[92] The light mediator is named photosensitizer (PS) and the altered molecule is labeled as quencher (Q). Depending whether the transfer involves energy or an electron, there are three important types of this second-order kinetic photosensitization interactions (4)−(6):

$$^{*}PS + Q \longrightarrow PS^{+} + Q^{-} \quad \text{oxidative electron transfer } (ET_{ox}) \quad (4)$$

$$^{*}PS + Q \longrightarrow PS^{-} + Q^{+} \quad \text{reductive electron transfer } (ET_{red}) \quad (5)$$

$$^{*}PS + Q \longrightarrow PS + {}^{*}Q \quad \text{energy transfer (EnT)} \quad (6)$$

The luminescent properties of the photosensitizer (emission or phosphorescence) are limited by these quenching processes and can get completely lost under certain conditions. In contrast, (4)−(6) lead to light-driven chemical changes in the quencher molecule, which are otherwise inaccessible because Q absorbs no visible light in a specific range. In such a case, the PS plays the part of an energy mediator.

The general quantum mechanical description of energy and electron transfer processes is quite complex and can be found in excellent monographies and thus, is not discussed here (see key words: trivial emission-absorption energy transfer, Dexter energy transfer by electron-exchange interactions, Förster energy transfer by dipole-dipole interactions and electron transfer by frontier orbital interaction).[93, 94] Both transfer processes can exist separately or at the same time depending on the distance, the orbital overlap, the transition dipole moments and the energetic situation between photosensitizer and quencher.

In particular, the last parameter, the energetic situation, is a more concrete parameter for a practical operating chemist because it can be extracted from electrochemical, absorption and emission properties of the molecules. In this regard, there are some general requirements and important differences between energy and electron transfer (**Figure 12**). Energy transfer can only take place when the energy of the excited photosensitizer ΔE_{PS} is larger than the excited state energy difference of the quencher ΔE_{Q} (**Figure 12a**, SOMO = singly occupied molecular orbital). In contrast for electron transfer, the energy difference of the photosensitizer and the quencher plays no crucial role. The requirement for oxidative electron transfer is that the LUMO of the quencher lies beneath the highest SOMO (2) level of $^{*}PS$ (**Figure 12b**). Whereas reductive quenching is only possible if the SOMO 1 is below the HOMO of the quencher. Interestingly, because of its MLCT character the excited state of $[Ru(bpy)_3]^{2+}$ is often considered as $[Ru^{3+}(bpy)_2(bpy)^{-}]^{2+}$, which visualizes

well the oxidative quenching potential by Ru^{3+} and the reductive quenching potential by bpy^{-} of this photosensitizer.

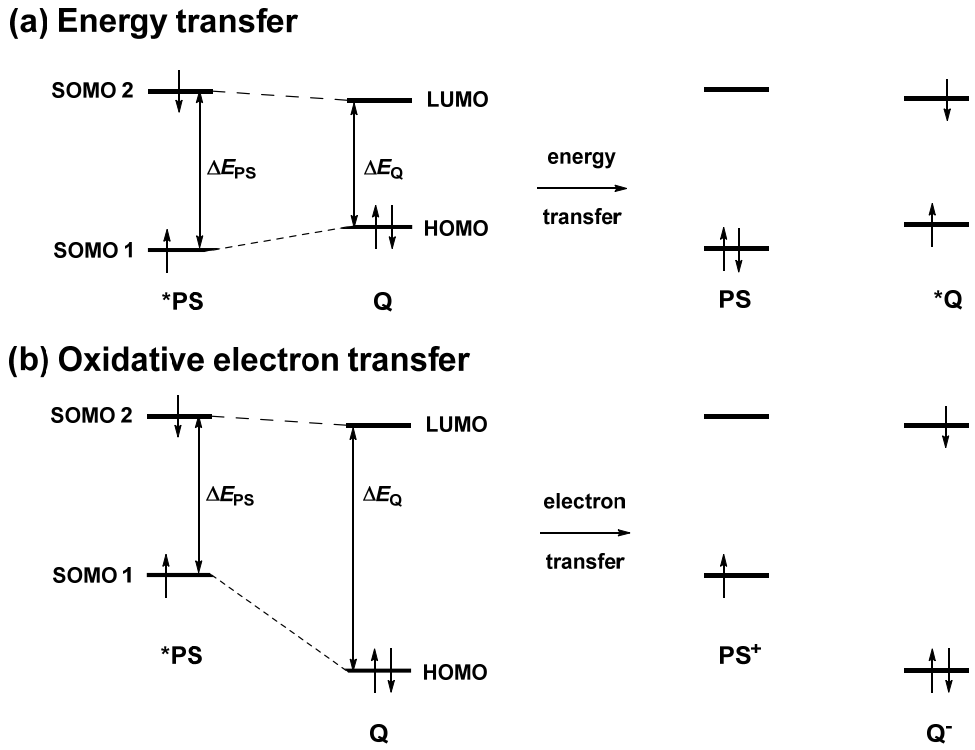

Figure 12 Energetic conditions in case of energy transfer (a) and oxidative electron transfer (b) between an singlet excited photosensitizer *PS and a ground state quencher molecule Q.

The perfect energy level alignment of photosensitizers and quenchers is difficult to adjust, but can be well observed in natural photosystems. Natural photosynthesis makes immense use of energy and electron transfer processes to harvest sun light into chemical bond energy of carbohydrates. By total control over energy and electron transfer processes, it is believed that human society can funnel and direct the sun light and thus huge amounts of energy into any desired solar application (solar cells, photoelectrochemical cells, *etc*).[95, 96, 97]

Normally, the usage of one dye molecule is not sufficient to gather the complete spectral sun light and to guide successfully the energy or the electrons. Therefore, bi- and multichromophoric systems combining different dyes were established to achieve this goal. It is impossible to manage all possible energy or electron transfer processes in multicomponent systems based on a simple mixture of separately dissolved chromophores, because the statistical collision dictated by diffusion would be random und thus disordered. Consequently, scientists started to construct covalently or supramolecularly arranged dye assemblies inspired by the photosystem II in nature.[98] The combination of two chromo-

phores into one system is called dyad, of three chromophores triad and so on. In this regard, it is often spoken of supramolecular photochemistry but this terminology has to be treated with caution and hints to some problems in the classification of such systems. The notation supramolecular is hereby not based on the connection of subunits without covalent bonds, but on the degree of intercomponent electronic interaction. Therefore, a system covalently connected but with a relative small ground state interaction between the units is called supramolecular species too.[67] In contrast, a bichromophoric compound, in which the two chromophores are merged into each other so that they show completely new electronic and optical properties, is regarded as “large molecule”. There are examples of bichromophoric systems of Ru(II) polypyridyl complexes and aromatic dye molecules which can be considered as pure supramolecular species or as a fusion into a new large molecule. The former types are discussed in section **2.3.1** and **2.3.2** whereas the later in **2.3.3**. This strict separation is problematic because the transition proceeds smoothly. There are also compounds, which show a modest electronic interaction and thus, display still the single signatures of the subunits.

2.3 Bichromophoric Systems

Ruthenium(II) polypyridyl complexes have a fairly week absorption in the visible light ($\varepsilon_{450\,nm}^{MLCT}$ ([Ru(bpy)$_3$]$^{2+}$) = 12,300 M^{-1} cm^{-1}) compared to other dye molecules like for instance perylene bisimide ($\varepsilon_{527\,nm}$ (PBI) = 94,700 M^{-1} cm^{-1}). Accordingly, hundreds of bichromophoric systems containing Ru(II) polypyridyl complexes and a covalently linked second chromophore have been synthesized and investigated to improve the light absorption of these systems. There are many options for the additional dye like metal complexes, pyrene, anthracene, naphthalene diimide, bodipy, coumarine derivatives and so on.[99] In the following section the attention lies only on organic flat π-aromatic dye molecules due to the reduction of the sheer amount of examples and the structural similarity of these chromophores to the perylene co-dyes described in the later *Results and Discussion* chapter **3.2** of this thesis.

2.3.1 Supramolecular Bichromophoric Assemblies

The reason why Ru(II) polypyridyl complexes are so frequently used in bichromophoric systems to trigger electron or energy transfer processes is determined by their favorable energy content, long excited state lifetime and advantageous electron distribution in the excited state;[63] more precisely: (i) high excited state energy of 2.12 eV, (ii) 100% quantum yield for the lowest excited state and thus no loss of the excitation during the population process (also proven by photochemical conversion),[100] (iii) μs-lifetime of the ^{3}MLCT and (iv) charge-separated character of the excited state, [Ru^{3+}(bpy)$_2$(bpy)$^-$]$^{2+}$, is a strong reductant and oxidant at the same time.

The demands on the co-dye in bichromophoric systems are high (photo)stability, easy functionalization of the molecule and suitable energy levels. Especially flat aromatic dye molecules are often used because they fulfill these requirements and in addition their HOMO and LUMO energy are in the range of [Ru(bpy)$_3$]$^{2+}$. Furthermore, they can be easily modified by extension of the π-system or the introduction of heteroatoms and/or functional groups. This fact is well shown by the compound series [Ru(bpy)$_2$(bpy-PAH)]$^{2+}$ **14** of Wilson and coworkers in which [Ru(bpy)$_3$]$^{2+}$ was functionalized with different polycyclic aromatic hydrocarbons (PAH, **Figure 13**).[101, 102] Naphthalene´s triplet state ^{3}(π–π*) is too high-lying and thus, does not influence the photophysical processes at all and [Ru(bpy)$_2$(bpy-naph)]$^{2+}$ **14a** shows unchanged phosphorescent properties like in the

parent complex. In contrast, triplet state ^{3}Pyr is nearly isoenergetic and thus, the close-lying energetic levels in **14b** exist. Therefore, reversible energy transfer (rEnT) between both units is possible and the pyrene′s triplet state acts as a "reservoir", which repopulates the emissive ^{3}MLCT state and leads to an increased emission lifetime. Consequently, the emission lifetime out of the ^{3}MLCT of **14b** increases from 0.72 μs in the parent complex to 5.23 μs in **14b**. However, in $[Ru(bpy)_2(bpy\text{-}anth)]^{2+}$ **14c** with anthracene as a co-dye, the ^{3}anth energy lies 0.32 eV below the ^{3}MLCT and thus, irreversible energy transfer takes place. Therefore, the excited triplet state of anthracene is formed in unit quantum yield, which is impossible by light irradiation of pure anthracene in solution. As a second consequence, the emissive properties of the $[Ru(bpy)_3]^{2+}$-part are fully quenched. Notably, the π–π^* excitation of the organic chromophore naphthalene, pyrene or anthracene in these three bichromophoric systems leads to the singlet state formation $^1(\pi$–$\pi^*)$, which subsequently undergoes fast energy transfer into the lower energetic ^{1}MLCT.

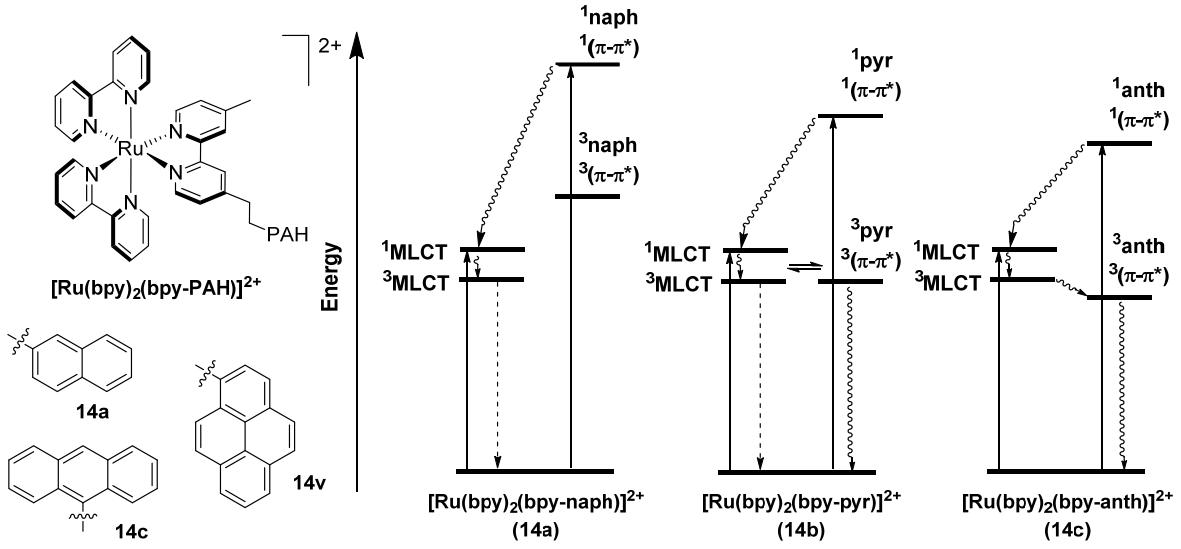

Figure 13 Compound series of $[Ru(bpy)_2(bpy\text{-}PAH)]^{2+}$ **14** containing naphthalene, pyrene or anthracene as organic co-dyes and their graphically summarized photophysical processes.

Polycyclic aromatic hydrocarbons are not the only compound class which can trigger energy transfer processes in bichromophoric ruthenium(II) polypyridyl systems. There are also the bichromophore examples **15-18** containing other organic dyes like coumarine, bithiophene, naphthalene monoimide or bodipy showing promising directed energy transfer (**Chart 3**).[103, 104, 105, 106] However, the basic concepts for the energy transfer differ only slightly from the PAH discussed cases and consequently, also the reversible energy transfer is an important aspect in these assemblies.

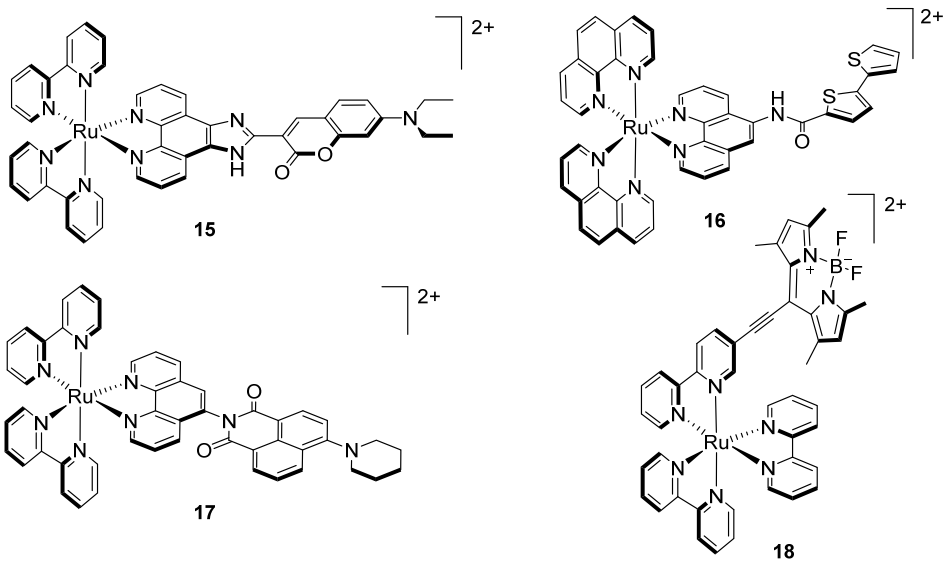

Chart 3 Bichromophoric systems **15-18** composed of ruthenium(II) polypyridyl complexes and the organic dye molecules coumarine, bithiophene, naphthalene monoimide and bodipy.

To trigger electron transfer in $[Ru(bpy)_3]^{2+}$ bichromophores the HOMO and the LUMO levels of the co-dye have to fit well to the frontier orbitals of the metal complex. To access for example oxidative electron transfer, the co-dye requires a lower LUMO energy in comparison to the LUMO of the metal complex, which can be obtained by the introduction of strong electron withdrawing substituents for instance. Åkermark and coworkers realized such an approach and published an interesting dyad composed of $[Ru(bpy)_3]^{2+}$ and naphthalene diimide as a good electron acceptor (**Figure 14a**).[107] Dyad $[Ru(bpy)_2(bpy\text{-}NDI)]^{2+}$ **19** also nicely illustrates the simultaneous appearance of energy and electron transfer processes in the same system. After MLCT excitation with 456 nm light, there is a fast formation of the ^{3}MLCT. Out of this state either energy transfer from the complex to the ^{3}NDI or the oxidative electron transfer quenching to Ru^{3+}-NDI^- can take place. The electron transfer with the rate k_{ET} of 10^8 s^{-1} outcompetes the slower energy transfer rate k_{EnT} of 10^7 s^{-1} and thus, leads mainly to the charge-separated state Ru^{3+}-NDI^-, which recombines non-emissively to the ground state. Because these processes are faster by a factor 100 in comparison to the classical phosphorescence, emission out of the ^{3}MLCT drops from 6% under 0.06%.

An often used organic electron donor to trigger reductive electron transfer in metal complexes is phenothiazine (PTZ) because it has a very high-lying HOMO energy level (+0.32 V *vs* $Fc^{0/+}$).[108] In the dyad $[Ru(dmbpy)_2(bpy\text{-}PTZ)]^{2+}$ **20** (dmbpy = 4,4'-dimethyl-2,2'-bipyridine, **Figure 14b**), the MLCT state after 460 nm light excitation is quenched by electron donation from the PTZ unit leading to the charge-separated state Ru^+-PTZ^+.[109]

The electron transfer in **20** with $k_{ET} = 5.4 \cdot 10^6\ s^{-1}$ is slower compared to the phosphorescence rate k_{ph} of $6.6 \cdot 10^6\ s^{-1}$ so that the complex still shows moderate phosphorescence emission.

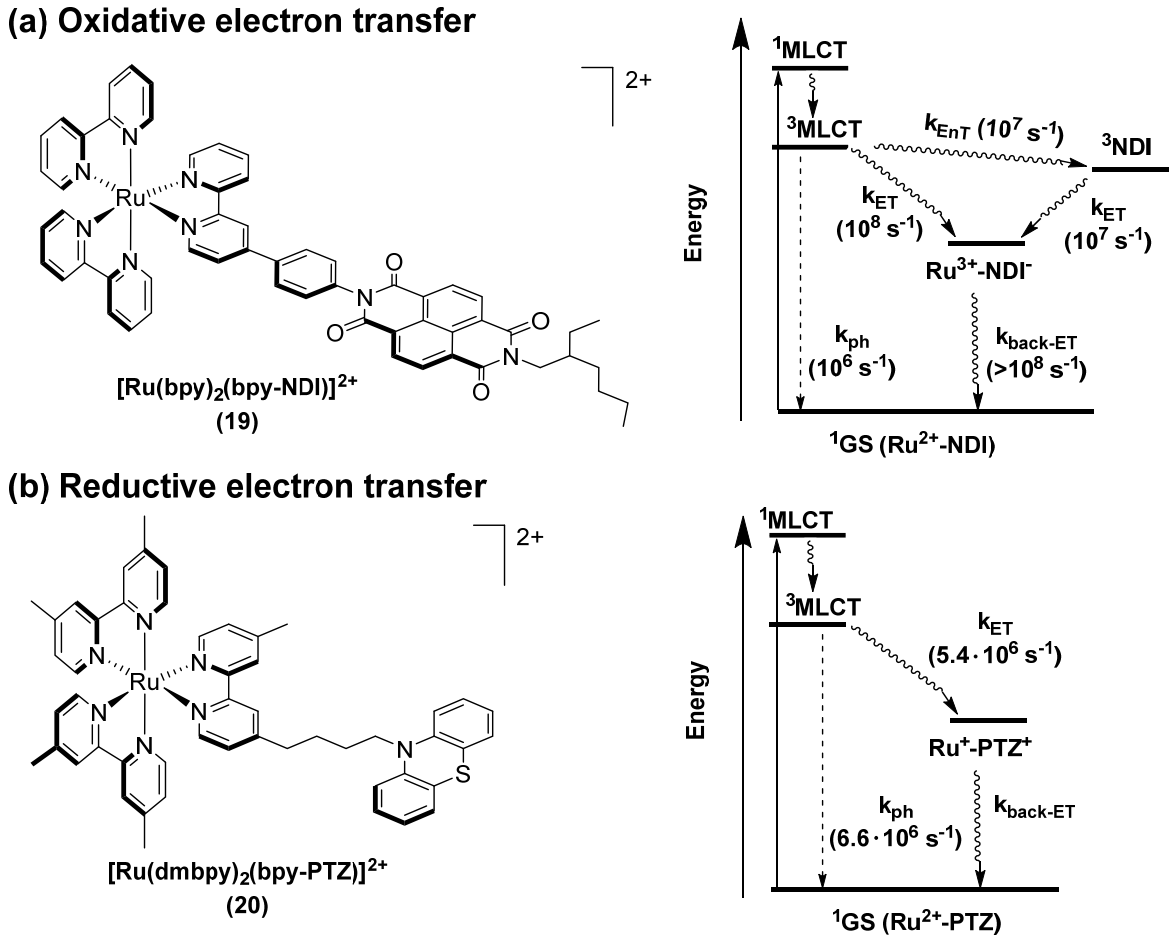

Figure 14 (a) Schematic representation of the dyad $[Ru(bpy)_2(bpy\text{-}NDI)]^{2+}$ **19** and its oxidative electron quenching mechanism.[107] (b) Schematic representation of the dyad $[Ru(dmbpy)_2(bpy\text{-}PTZ)]^{2+}$ **20** and its reductive electron quenching mechanism.[109]

2.3.2 Perylene bisimides as Co-Dyes in Ru(II) Polypyridyl Bichromophores

An alternative co-dye for bichromophoric ruthenium(II) polypyridyl systems is given by perylene chromophores. Especially the dye class of perylene bisimides (PBIs) has the reputation to be excellent chromophores due to their strong visible light absorption, high (photo)stability and unique fluorescence properties.[110, 111] The electron-withdrawing imide function at the PBI leads to very low-lying π and π^* orbitals, which make PBIs in particular attractive for reductive electron transfer processes (ET_{red}), in which the PBI gets itself photo-reduced and its counterpart photo-oxidized.

Although the number of metal-containing PBI assemblies is quite high,[112, 113] the combination with Ru(II) polypyridyl complexes is limited. The bi- and multichromophoric systems Ru-PBI **21-25** demonstrate well that the structural complexity of such systems can be high (**Chart 4**).[114, 115, 116, 117]

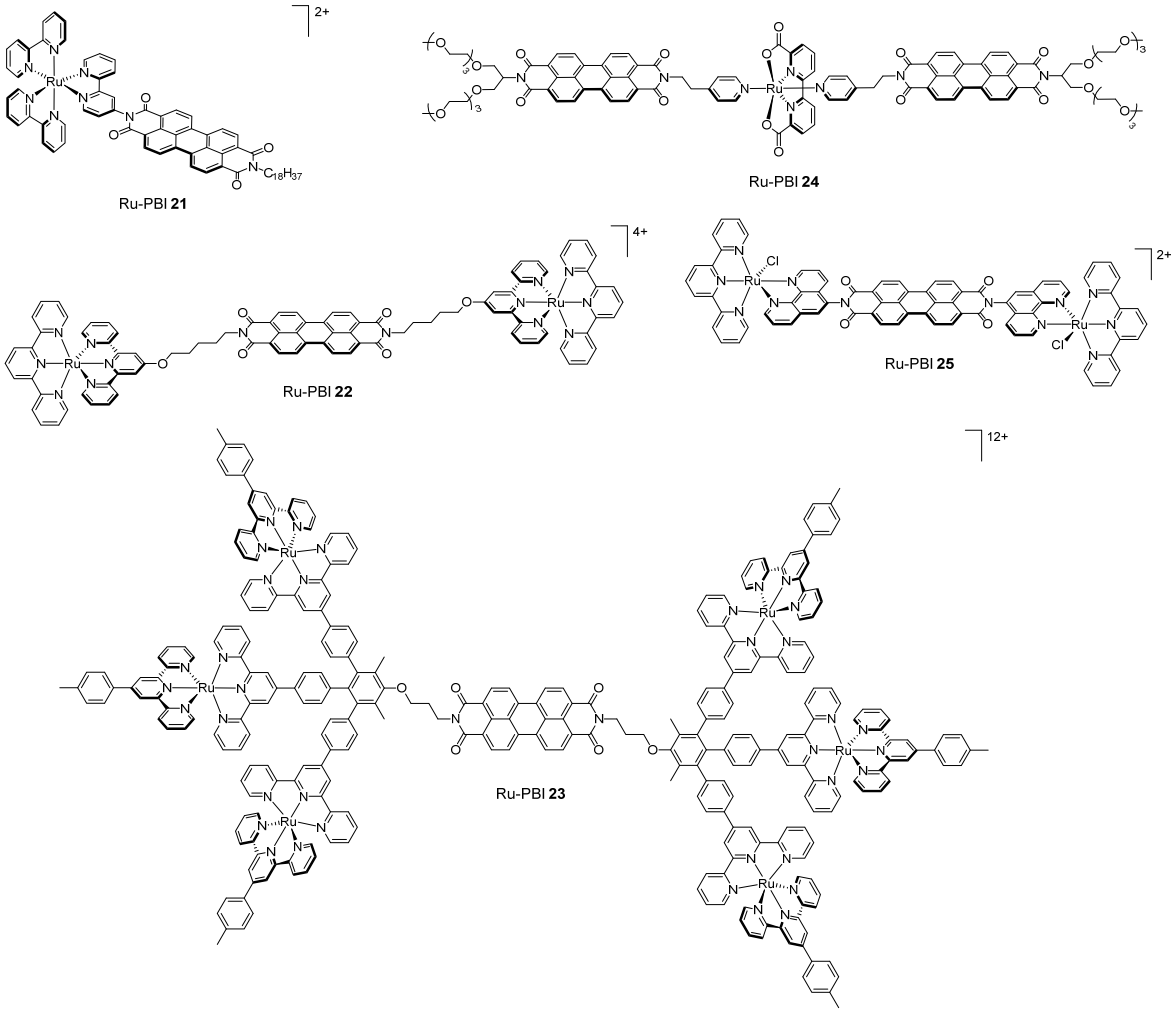

Chart 4 Bichromophoric systems Ru-PBI **21-25** containing perylene bisimide dyes which are attached to ruthenium(II) polypyridyl complexes via the imide position (Ru-PBI).

Particularly, the dendritic compound Ru-PBI **23** by Newkome *et al.* is structurally fascinating because it combines six ruthenium(II) complexes in one molecule with high optical absorptivity in the visible region of light ($\varepsilon^{tpy}_{313nm}$ = 178,000 M^{-1} cm^{-1}, $\varepsilon^{MLCT}_{497nm}$ = 83,000 M^{-1} cm^{-1} and $\varepsilon^{PBI}_{570nm}$ = 28,000 M^{-1} cm^{-1}). Unfortunately, the photophysical investigation of this impressive molecule is negligible and no systematic investigation for the reason of the quenched emission was conducted (also for Ru-PBIs **21**, **22** and **24**). Nevertheless, the emission quenching demonstrates an efficient new non-radiative deactivation process of ^{1}PBI* (*e.g.* energy transfer, electron transfer or ISC) dominates.

Singlet energy transfer in this bichromophoric systems can be generally excluded because the optical gap of PBI is smaller than the ^{1}MLCT energy of the ruthenium(II) polypyridyl complexes. The likeliest explanation for the emission quenching is that reductive electron transfer takes place and the excited PBI state is quenched by the metal complex. This assumption is supported by the triad Ru-PBI **25** by Gregg and coworkers, which combines two $[Ru(tpy)(phen)Cl]^+$ (phen = 1,10-phenanthroline) complexes *via* a perylene bisimide bridge (**Figure 15**).[118] Just after minutes of steady illumination of Ru-PBI **25**, the absorption spectra becomes dominated by new signals of the perylene radical anion (λ = 700, 800 and 950 nm). The perylene radical anion species was stable up to at least 30 min under inert conditions or went back to the neutral PBI after exposure to air.

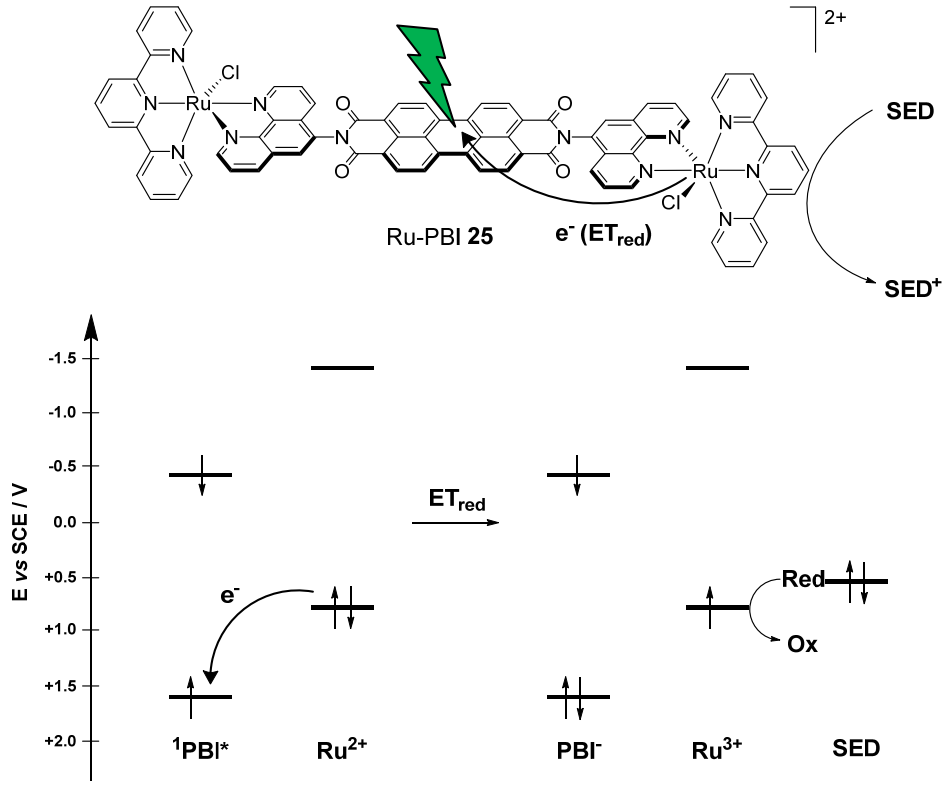

Figure 15 Schematic representation by Gregg *et al.* of the photophysical and photochemical processes of the triad Ru-PBI **25** by steady light illumination and in the presence of a SED.[118]

Gregg *et al.* argued that Ru-PBI **25** behaves differently to other Ru-PBI dyads because it has a more labile monodentate chloride ligand, which can initiate additional (photo)reactivity.[119, 120, 121] Subsequently, this coordination site opens up a chemical conversion pathway, by which the oxidized metal center can release its reactivity by a reaction with a sacrificial electron donor (SED, *e.g.* the solvent itself (here DMF) or impurities of the solvent (here *N,N*-dimethyl amine)). Consequently, the radical anion on the PBI is left behind and cannot be deactivated by the classic charge recombination

process and thus, the anion accumulates over time and finally becomes visible by spectroscopic techniques.

A detailed spectroscopic investigation of a successful electron transfer in a PBI dyad was published by Wasielewski and Rybtchinski *et al*. with the triad Ru-PBI **26** (**Figure 16**).[122] The linkage between perlyene bisimide and ruthenium(II) polypyridyl complex fragment was realized by an alkyne bridge between the perylene core of the PBI (bay-position) and the metal complex. Steady-state spectroscopy and electrochemical investigations revealed that Ru-PBI **26** can be considered as supramolecular multichromophoric assembly out of donor and acceptor fragments, which have a weak ground state electronic coupling. Therefore, after exclusive light excitation of the PBI moiety (λ = 550 nm) the excited ^{1}PBI* state is formed. Energy transfer to the complex subunit is an energetic uphill process and was consequently not found. In contrast, fast electron transfer from a Ru(d)-located HOMO electron to perylene bisimide takes place within 150 fs. The so formed charge-separated species Ru^{3+}-PBI^{-} undergoes either non-radiative charge recombination to the ground state (τ_{CR} = 63 ps) or a rapid radical-pair ISC followed by a charge recombination to the PBI triplet excited state ^{3}PBI*. The latter deceases very slowly back to the ground state by ISC (τ_{ISC} = 39 μs).

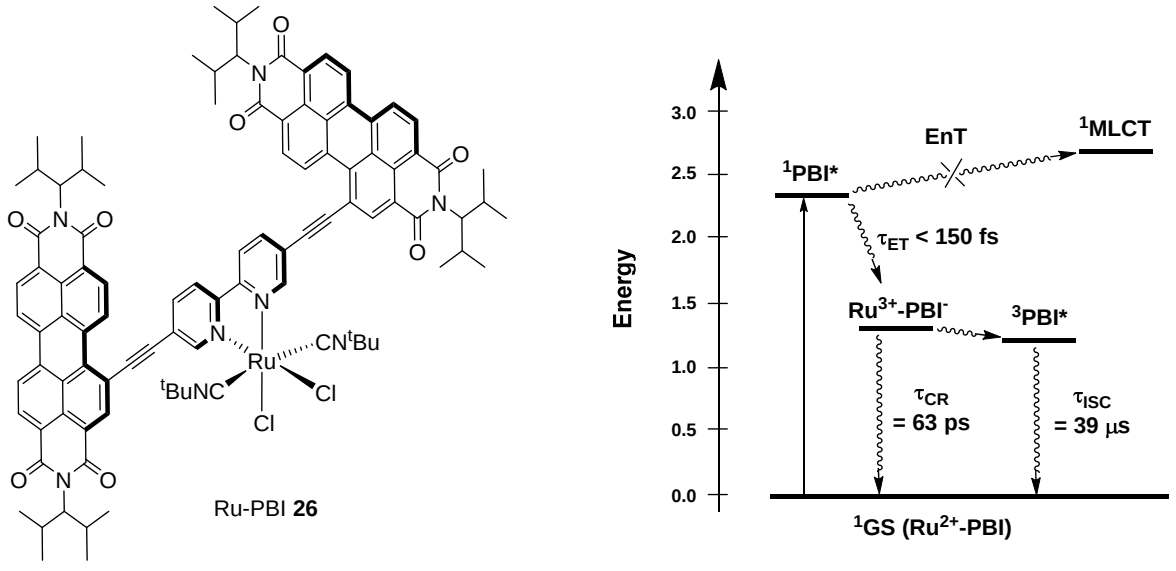

Figure 16 Schematic representation of the triad Ru-PBI **26** and the corresponding description of the photophysics in an energy level diagram after 550 nm PBI light excitation.

A phosphorescent emission from the ^{3}PBI* is not observed because the ruthenium metal center is most likely too far away from the perylene chromophore and thus, the required spin-orbit coupling to overcome the spin-forbidden radiative transition from ^{3}PBI* to the

^{1}GS is not given. Although, the charge-separated state Ru^{3+}-PBI^- is not very long-lived, the example demonstrates that perylene bisimides are potent strong photo-oxidants.

In 2013 Dubey *et al.* showed that PBIs are not only strong photo-oxidants and thus good electron acceptors, but also reasonable electron donors under the right conditions (**Figure 17**).[123] The two PBI dyads **27** and **28** consist of a $[Ru(bpy)_2(dppz)]^{2+}$ (dppz = dipyrido[3,2-*a*:2′,3′-c]phenazine)) subunit and a phenoxy- or pyrrolidinyl-substituted perylene bisimide. The photophysics of $[Ru(bpy)_2(dppz)]^{2+}$ are unusual and will be discussed in more detail in section **2.3.3**. Dyads **27** and **28** are characterized by two close-lying MLCT states of which only the $MLCT_1$ is spectroscopically visible and stands in equilibrium to the "dark" $MLCT_0$. Accordingly, after MLCT excitation in the dyad Ru-PBI **27** an oxidative electron transfer from the complex to the $PBI_{phenoxy}$ quenches the excited state $MLCT_0$.

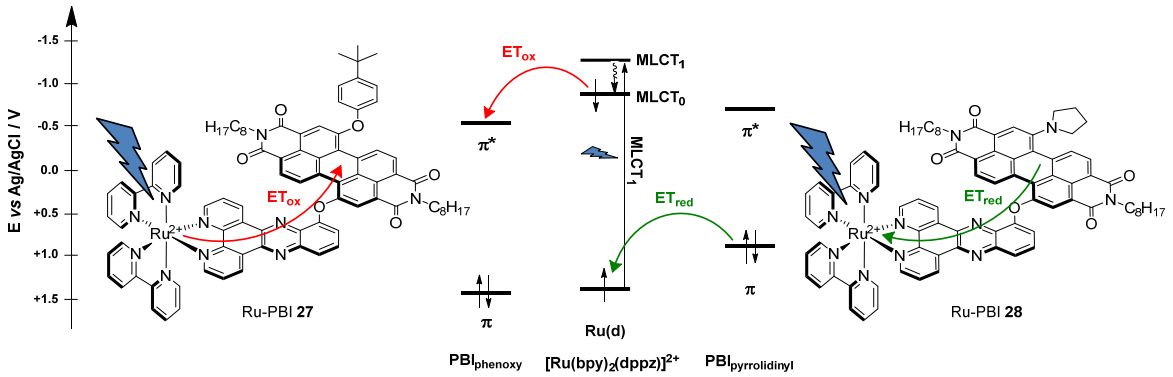

Figure 17 Energy level diagram of the dyads $[Ru(bpy)_2(dppz\text{-}PBI_{phenoxy})]^{2+}$ (Ru-PBI **27**) and $[Ru(bpy)_2(dppz\text{-}PBI_{pyrrolidinyl})]^{2+}$ (Ru-PBI **28**) and their photophysics after 450 nm light excitation in the $MLCT_1$ absorption band. The energies of the orbitals were estimated by electrochemical data and are referenced again Ag/AgCl.[123]

The $PBI_{pyrrolidinyl}$ dye in dyad **28** has higher lying π and π^* molecular orbitals so that the LUMO is nearly isoenergetic to the π^* of the dppz ligand, in which the electron is temporarily stored. Therefore, oxidative electron transfer has no or only low driving force in this case. In contrast, the HOMO is due to the electron-donating ability of the pyrrolidinyl substituent roughly 0.5 V higher in energy than the Ru(d)-centered orbital of $[Ru(bpy)_2(dppz)]^{2+}$ and thus, a high driving force for reductive electron transfer is given. As a consequence, Ru-PBI **28** is one of the rare cases, in which a ruthenium(II) polypyridyl complex in combination with a PBI dye acts as an electron acceptor and can be successfully reduced after light illumination. Notably, comparable electron transfer processes cannot be initiated by the excitation of the $PBI_{pyrrolidinyl}$ unit, which becomes evident from the energy level diagram showing that there is no driving force for

such a mechanism. However, unfortunately the charge-separated states Ru^{3+}-$PBI^{-}_{phenoxy}$ in dyad **27** and Ru^{+}-$PBI^{+}_{pyrrolidinyl}$ in dyad **28** have only a short lifetime of 1–100 ns and 53 ps, respectively, after they recombine to form the excited triplet $^{3}PBI^{*}$. This state deactivates non-radiatively because of the insufficiency of spin-orbit coupling of the too distant metal fragment to partly allow the spin-forbidden phosphorescent deactivation.

In summary, the energy and electron transfer processes of all shown supramolecular bichromophoric systems containing Ru(II) polypyridyl complexes can be well understood based on energy level diagrams. But the situation becomes more and more complicated as closer the dye and thus as larger the intercomponent electronic interaction becomes. The most extreme scenario in case of Ru(II) polypyridyl complexes is that the dye molecule is merged into the polypyridyl ligand as an intrinsic part, which will be discussed in the next subchapter.

2.3.3 Ru(II) Polypyridyl Complexes with Large π-Extended Ligands

The attachment of additional chromophores (with weak electronic ground state interaction) on an already existing working unit like $[Ru(bpy)_3]^{2+}$ as discussed before had the purpose to improve the light-harvesting properties of the core structure without changing intrinsic properties of the core unit. Scientists, who merge a second dye very closely in the coordination sphere of for instance Ru(II) polypyridyl complexes, have a completely different driving force – they want to change the specific properties of the centralRu bipyridine fragment. In this scenario, a modified and improved photosensitizer should be obtained, which (i) has a broad and intense absorption about the whole sun light spectrum, (ii) has the highest possible excited state energy to ensure high chemical driving force, (iii) has an excited state lifetime, which is long enough for a desired interaction, and (iv) has long-term (photo)stability of at least several days.

Known from literature, there are many hundreds of Ru(II) polypyridyl based bichromophoric assemblies, in which the second dye is closely approached to the metal complex so that the general complex properties change by moderate or strong intercomponent electronic interactions. Such systems can be classified due to different criteria like structure, electronic interaction, photophysical outcome or changed photosensitizer properties.

In the following, a structural classification based on different types of π-extension of the of 2,2′-bipyridine was chosen due to the fact that the *Results and Discussions* subchapters **3.2** and **3.3** deal with 2,2′-bipyridine-like and π-extended perylene ligand systems.

2,2′-Bipyridine itself only absorbs light in the ultraviolet region of light at around 280 nm and thus it does not contribute to the harvesting of visible light in ruthenium(II) polypyridyl complexes. By extending the π-system the absorption can be shifted into the visible part of the light, for instance 1,12-diazaperylene (dape) has an absorption maximum of around 440 nm. The conjugation of bpy can either be stretched as a whole to "perylene"-like molecules, along the back side at the 3-positions to "phenanthroline"-like molecules or along the side at the 5- and 6-position to "quinoline"-like molecules (**Scheme 4**).

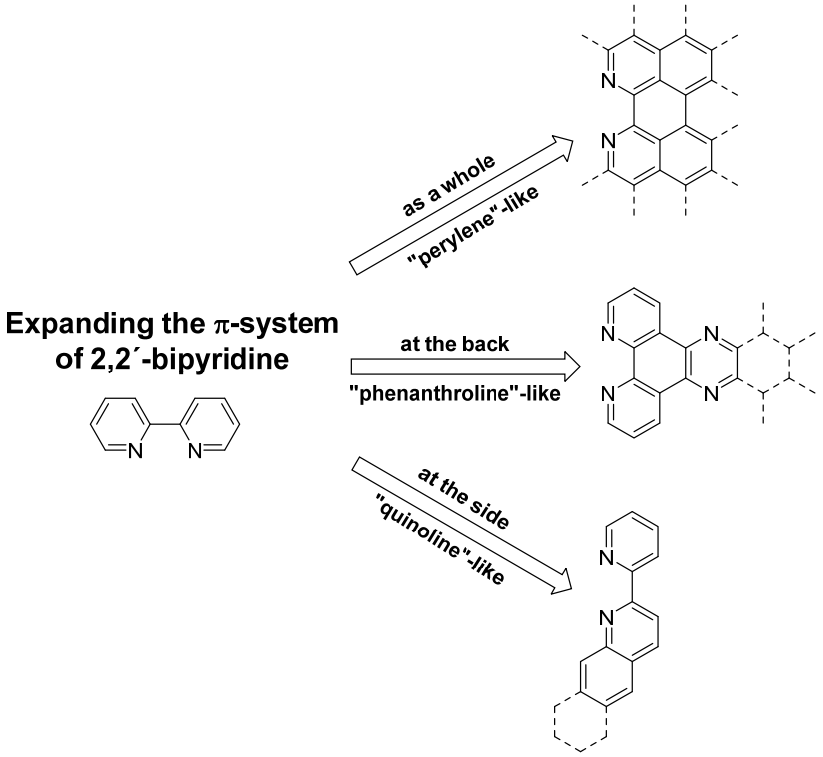

Scheme 4 Three different possibilities how the conjugated π-system of 2,2′-bipyridine can be extended.

"Perylene"-like ligands. The steady extension of the π-system of arenes leads to continuous convergence between the occupied π- and the unoccupied π^*-orbitals of the ligands and thus to a decrease of the HOMO-LUMO energy gap. As a consequence of the LUMO stabilization, the reduction of the polycyclic arenes becomes easier with increasing π-conjugation length. This phenomenon can be well seen for "perylene"-like ligands when they are compared to the polypyridyl standard ligand 2,2′-bipyridine (**Chart 5**, values in

brackets). Bpy can hardly be reduced (–2.47 V *vs* Fc^+/Fc) whereas 1,12-diazaperylene (dape)[124] and 1,6,7,12-tetraazaperylene (tape)[125] have an easier reduction by 0.8 and 1.2 V, respectively. In addition, the ligand family of the alkaloid eilatine (eil = eilatine,[126] ieil = isoeilatine[127] and dbneil = dibenzoeilatine[128]) receives an anodic potential shift by ~0.9 V. The highly conjugated "half-cyclized" and the "full-cyclized" nitrogen-heterosuperbenzene (N-1/2HSB[129] and N-HSB[130]) have a reduction potential of *ca* –1.6 V.

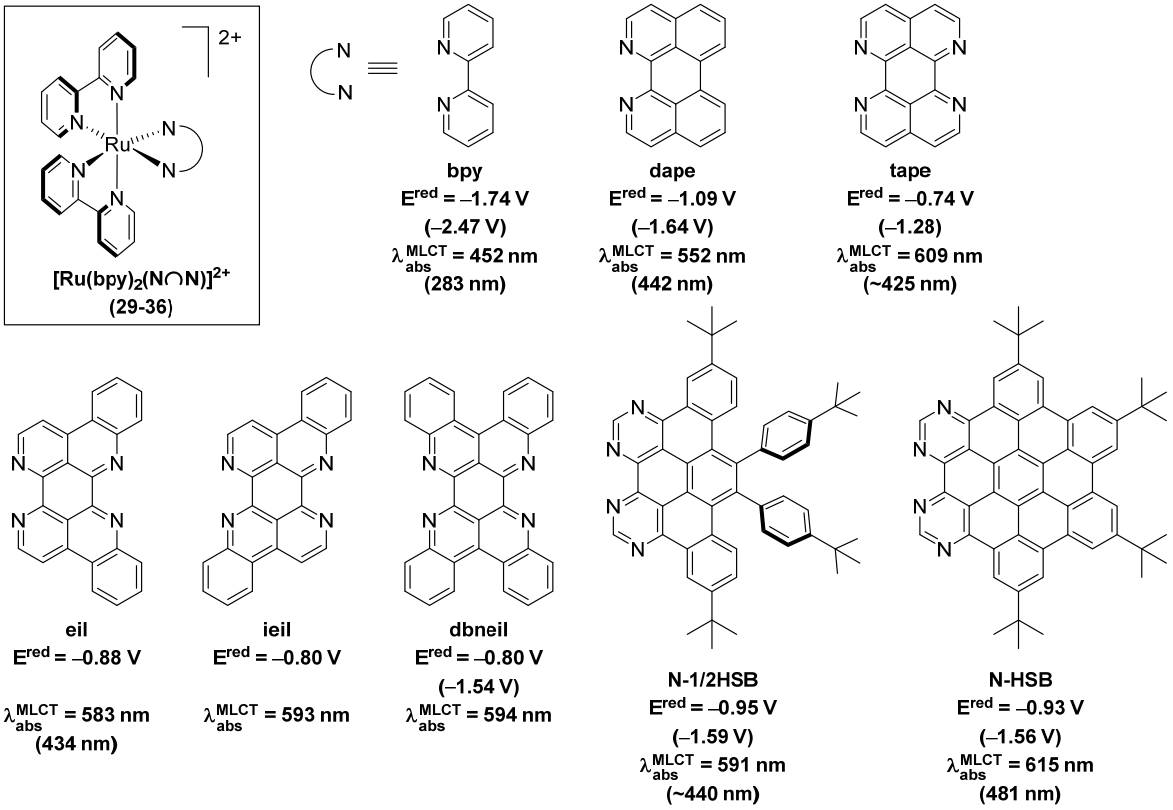

Chart 5 *N,N*-Bidentate ligands with a "perylene"-like motif creating "large surface" ligands. The given reduction potentials represent the first reduction of the respective $[Ru(bpy)_2(N\cap N)]^{2+}$ complexes **29-36** and are referenced against Fc^+/Fc. The value in brackets is the $N\cap N^{-/0}$ reduction of the free polypyridyl ligand. The wavelength of the absorption maxima belong to the lowest energetic MLCT absorption and the values in brackets represent the π–π^* absorption of free N∩N ligand.

Usually, the first reduction of Ru(II) polypyridyl complexes is placed on the easiest reducible ligand. Hence, in heteroleptic complexes of the type $[Ru(bpy)_2(N\cap N)]^{2+}$ containing two bipyridine and one polycyclic aromatic N∩N ligand, this reduction takes always place on the "large surface" N∩N ligand so that they strongly determine the electronic and optical properties of the complex. This behavior is well reflected by the heteroleptic complex series $[Ru(bpy)_2(N\cap N)]^{2+}$ **29-36** in **Chart 5**. The reduction potential of the ligands drops steadily from its free (values in brackets) to its coordinated form by a

potential between ~0.5 V (see tape) and ~0.7 V (see dbneil). This effect is caused by the decreased electron density on the ligand due to the ligation to a Lewis-acidic metal center. Because these potential decreases are well reproducible for the arenes in this series, the LUMO orbital of the complexes is consistently located on the "large surface" N∩N ligand. The MLCT state which leads also to a reduced ligand species is stabilized as well: the MLCT absorption maxima of $[Ru(bpy)_3]^{2+}$ is at 452 nm whereas the maximum of $[Ru(bpy)_2(dape)]^{2+}$ **30** and $[Ru(bpy)_2(tape)]^{2+}$ **31** is red-shifted to 552 nm and even to 609 nm, respectively.

The bichromophoric systems of the type $[Ru(bpy)_2(N\cap N)]^{2+}$ show weak MLCT emission ($\Phi = 10^{-4}$) between 700 and 1000 nm with an excited state lifetime shorter than 35 ns. Unfortunately, there are no in-depth photophysical investigations (like transient absorption spectroscopy, singlet oxygen sensing experiments or theoretical calculations), which could explain the reason for the quantum yield and lifetime drop or the real nature of the excited state. Hence, it can only be speculated if non-radiative deactivations cause the loss in the optical activity of the compounds due to the low energetic difference between the ground and the excited state ("energy-gap law" see section **2.2.2**).

"Phenanthroline"-like ligands. The MLCT transition is sometimes also represented as charge separated state $[Ru^{3+}(bpy)_2(bpy)^{-}]^{2+}$ with an oxidized ruthenium center and one reduced bpy ligand. Accordingly, there was an empiric linear correlation established over decades that the energy difference between the $Ru^{2+/3+}$ oxidation potential and the $N\cap N^{0/-}$ ligand reduction potential represents the optical energy gap of the MLCT transition. The complex series $[Ru(bpy)_2(N\cap N)]^{2+}$ **29-36** in **Chart 5** showcased that this empiric rule deserved a certain degree of validity. But especially the recent examples of complexes with "phenanthroline"-type ligands like dppz (dipyrido[3,2-*a*:2′,3′-*c*]phenazine) in $[Ru(bpy)_2(dppz)]^{2+}$ **37** differ from this established empiric rule (**Figure 18**). The first reduction in **37** is located on the dppz ligand at −1.28 V and thus, by comparing with the data of **Chart 5**, a MLCT absorption maximum of around 500 to 550 nm could be estimated.[131] However, the MLCT transition of $[Ru(bpy)_2(dppz)]^{2+}$ **37** is found to be at 445 nm; even 7 nm more blue-shifted than in $[Ru(bpy)_3]^{2+}$.[132] Other examples of ruthenium(II) complexes depicted that this observation is not unusual with "phenanthroline"-like polypyridyl ligands.[133] To understand this behavior, it is more appropriate to see the dppz ligand as a fusion of a bipyridine and a phenazine (phz) unit instead of a single fully conjugated system (**Figure 18a**).[134] In **37** the LUMO level lies

only on the phenazine part of the ligand framework, which is weakly coupled to the metal-based HOMO. Moreover, the LUMO+1 energy level is bpy-based and strongly coupled to the HOMO because of the chelating *N*-donors. As a consequence, there are two low-lying MLCT states, $MLCT_1$ located on the bpy and $MLCT_0$ on the phz subunit. The latter is spectroscopically invisible due to the weak frontier orbital coupling. The absorption at 445 nm corresponds to the $MLCT_1$, which is the second lowest but strongly coupled optical transition.

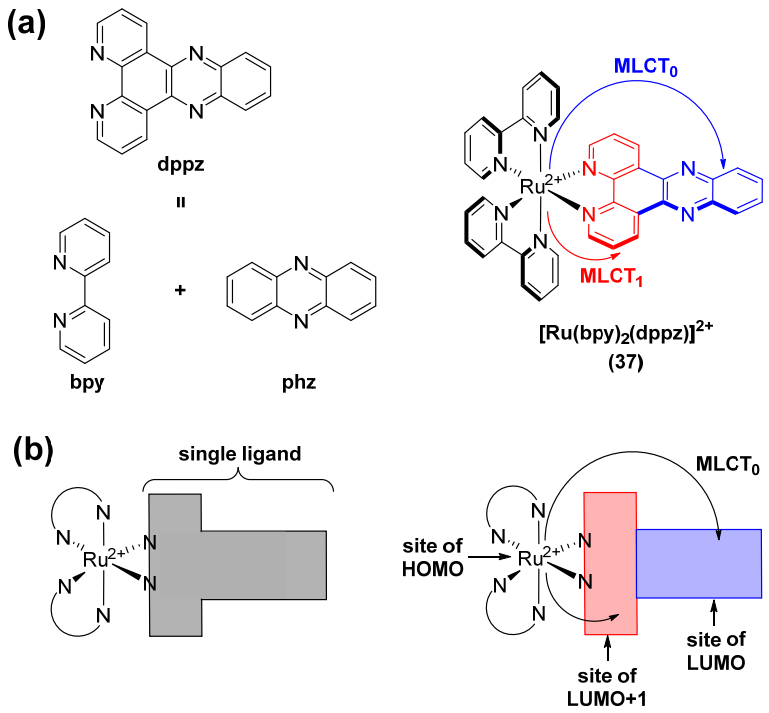

Figure 18 (a) Schematic representation of $[Ru(bpy)_2(dppz)]^{2+}$ **37** and the constitution of the dppz ligand by division into two subunits. (b) Ru(II) polypyridyl complex with one polypyridyl ligand having an extended large π-system in which two MLCT transitions are simultaneously possible (one proximal and one distal). Adapted from Campagna *et al.*[79]

In 2002, Meyer and Papanikolas and their coworkers unraveled the phenomenon of multiple low-lying MLCT states in $[Ru(bpy)_2(dppz)]^{2+}$ **37** based on temperature dependent luminescence lifetime measurements (**Figure 19a**). The temperature dependence of $[Ru(bpy)_3]^{2+}$ **8** can be understood with the already described Jablonski scheme in **Figure 11a**. At room temperature the lifetime of $[Ru(bpy)_3]^{2+}$ is ~1 µs. When the temperature is lowered, the thermal population of the high-lying and fast deactivating ^3MC state is reduced and thus, the lifetime increases to 2 µs at 150 K. In contrast heating leads to a shorter lifetime because of the opposite effect. The curve shape of $[Ru(bpy)_2(dppz)]^{2+}$ **37** in the high temperature range is exactly the same as for $[Ru(bpy)_3]^{2+}$ and therefore underlines the strong similarities between both complexes in regard to the overlying ^3MC

state. However, the overall graph of $[Ru(bpy)_2(dppz)]^{2+}$ **37** shows a maximum for the luminescence lifetime at medium temperatures instead of the sigmoidal shape for $[Ru(bpy)_3]^{2+}$. At low temperatures, the presence of the ^{3}MC can be neglected because it is not thermally accessible out of $^3MLCT_1$. But at that temperature range the additional "dark" $^3MLCT_0$ state in $[Ru(bpy)_2(dppz)]^{2+}$ **37** becomes important (**Figure 19b**), because it is in a fast equilibrium to the "bright" $^3MLCT_1$. At 150 K, the emissive $^3MLCT_1$ becomes more and more difficult to be populated by the low thermal energy and consequently, the non-radiative deactivation rate k^D_{ISC} through the $^3MLCT_0$ becomes dominant. Notably, these characteristics are quite similar to the reversible energy transfer of $[Ru(bpy)_2(bpy\text{-}pyr)]^{2+}$ **14b** in section **2.3.1**.

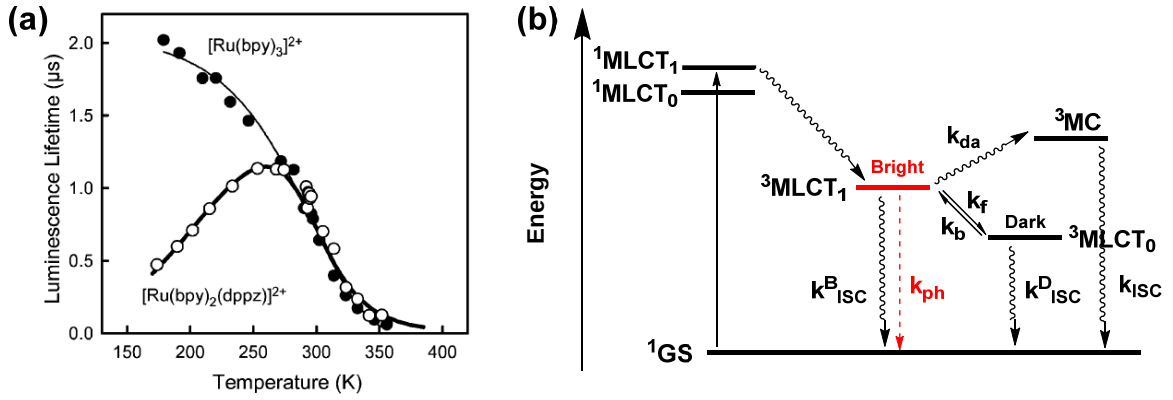

Figure 19 (a) Compilation of luminescence lifetimes as a function of temperature for $[Ru(bpy)_2(dppz)]^{2+}$ **37** (○) and $[Ru(bpy)_3]^{2+}$ **8** (●) measured in butyronitrile, taken from Meyer and Papanikolas.[134] Reprinted and adopted with permission from American Chemical Society. Copyright (2016). (b) Jablonski energy diagram of $[Ru(bpy)_2(dppz)]^{2+}$ **37** with its two ^{3}MLCT states, the "bright" $^3MLCT_1$ and the "dark" $^3MLCT_0$.

Besides the long excited state lifetime in the µs-timescale, Ru(II) polypyridyl complexes with "large" polycyclic arenes as ligands have also the possibility to interact with the base pairs of DNA due to their large hydrophobic π-system. This makes them especially desirable for specialized application like DNA targeting and subsequent light-triggered DNA destruction, *i.e.* photodynamic therapy (PDT).[62] During the search for other PDT reagents, Thummel and Turro *et al*. synthesized also tridentate polypyridyl ligands with even more extended π-systems than dppz.[135, 136] The examples of $[Ru(tpy)(pydppz)]^{2+}$ **38**, $[Ru(tpy)(pydppn)]^{2+}$ **39** and $[Ru(tpy)(pydbn)]^{+}$ **40** (pydppz = 3-(pyrid-2′-yl)dipyrido[3,2-*a*:2′,3′-*c*]phenazine, pydppn = 3-(pyrid-2′-yl)-4,5,9,16-tetraaza-dibenzo-[*a,c*]naphthacene, pyHdbn = 3-pyrid-2′-yl-4,9,16-triazadibenzo [*a,c*]naphthacene, **Figure 20**) demonstrate well that extended conjugated systems should be seen more often as a combination of

multiple divided localized π-systems. Consequently, these molecules tend to be more similar to the supramolecular bichromophoric systems discussed in section **2.3.1**. In $[Ru(tpy)(pydppz)]^{2+}$ **38**, the π-system is still small enough that the pydppz orbitals are lower in energy than the Ru(d)-centered HOMO.

In contrast, in $[Ru(tpy)(pydppn)]^{2+}$ **39** the pydppn-centered orbitals are elevated due to the larger π-conjugation and represents now the HOMO, whereas the Ru(d)-centered orbital becomes HOMO–1 and HOMO–2. The energy difference between HOMO and HOMO–1 is with 0.16 eV relatively small (**Figure 20b**). As a consequence, the character of the lowest electronic transition changes from a prior ^{1}MLCT nature in $[Ru(tpy)(pydppz)]^{2+}$ **38** to a $^1(\pi-\pi^*)$ nature in $[Ru(tpy)(pydppn)]^{2+}$ **39**. Notably, the $^1(\pi-\pi^*)$ absorption in $[Ru(tpy)(pydppn)]^{2+}$ **39** is strongly overlapping with the ^{1}MLCT. Because the singlet-triplet energy splitting of MLCT and $^1(\pi-\pi^*)$ are different (diverse interelectronic repulsion and spatial overlap of the orbitals), the situation in the lowest exciting state is less crowded and thus less competing. Therefore, $[Ru(tpy)(pydppz)]^{2+}$ **38** represents a weak triplet MLCT emitter and $[Ru(tpy)(pydppn)]^{2+}$ **39** has a non-emissive but long-lived ligand-centered triplet excited state.

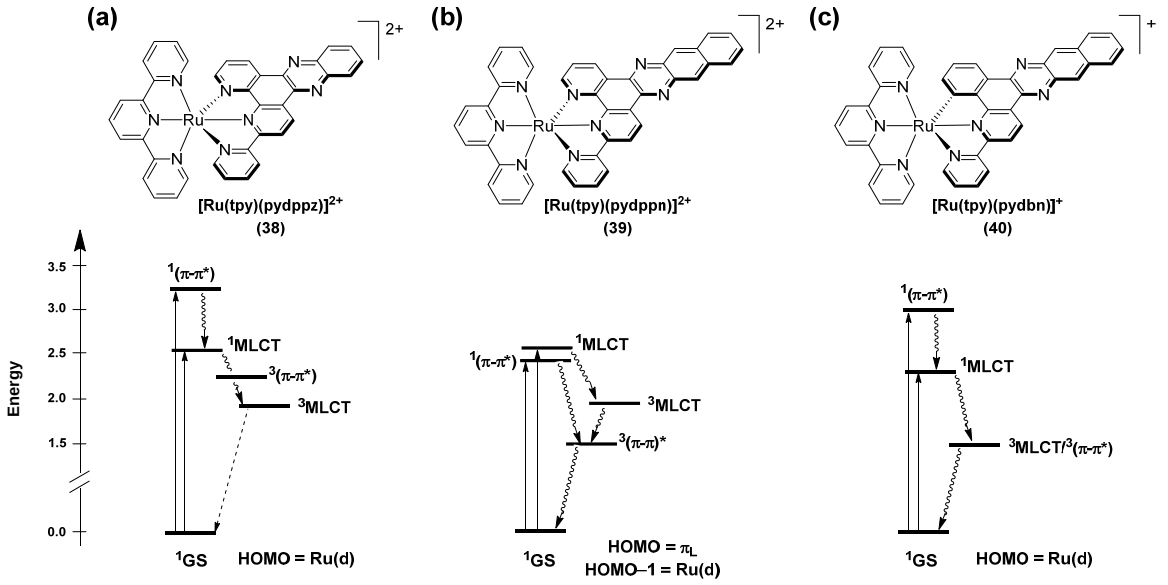

Figure 20 Ru(II) polypyridyl complexes containing tridentate ligands with extended π-systems. Generalized Jablonski energy diagrams of $[Ru(tpy)(pydppz)]^{2+}$ **38** (a), $[Ru(tpy)(pydppn)]^{2+}$ **39** (b) and $[Ru(tpy)(pydbn)]^{+}$ **40** (c) illustrating three cases of the specific interplay of the MLCT and $(\pi-\pi^*)$ energy levels.

$[Ru(tpy)(pydbn)]^{+}$ **40**, with a cyclometalated and thus the stronger σ-donor $pydbn^-$ ligand, represents a mixed situation between the two examples discussed above. The energy levels in the ligands $pydbn^-$ and pydppn are quite similar. In contrast, Ru(d) is the highest

occupied energy level (HOMO) because the cyclometalation increases mainly the energy of the metal-centered orbitals. Consequently, the lowest energetic absorption is the ^{1}MLCT and its corresponding triplet state, ^{3}MLCT, is nearly isoenergetic to the $^3(\pi-\pi^*)$ state of pydbn$^-$ (**Figure 20c**). The final result of this energy modulation is that $[Ru(tpy)(pydbn)]^+$ **40** shows neither luminescence at room temperature nor long-lived ligand-centered excited state behavior (most likely something in between).

"Quinoline"-like ligands. A comparison between "phenanthroline"-like and "quinoline"-like polypyridyl ligands in Ru(II) complexes can be exemplarily done in a complex series, in which both ligand types are mixed. Such an investigation was done by Wang and Zhang and coworkers with the complexes $[Ru(bpy)_2(dppn)]^{2+}$ **41**, $[Ru(bpy)_2(dpb)]^{2+}$ **42** and $[Ru(bpy)(dppn)(dppn)]^{2+}$ **43** (dppn = 4,5,9,16-tetraazadibenzo[*a,c*]naphthacene and dpb = 2,3-bis(2-pyridyl)benzoquinoxaline), in which dppn represents the "phenanthroline"-like and dpb the "quinoline"-like ligand (Figure 21).[137] The dppn ligand has a strong relationship to the pydppn ligand shown in **Figure 20b** and thus it is not surprising that $[Ru(bpy)_2(dppn)]^{2+}$ **41** has also a low-lying $^1(\pi-\pi^*)$ excited state and displays an extremely long excited state lifetime of 13 μs.

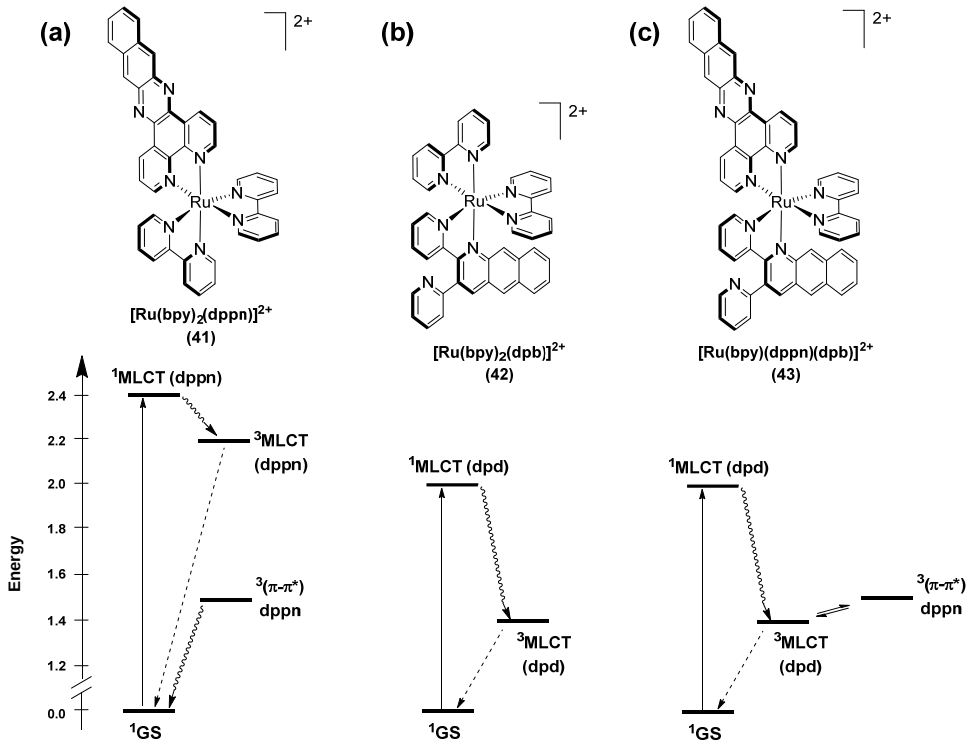

Figure 21 Ru(II) polypyridyl complexes with different polycyclic aromatic ligands, $[Ru(bpy)_2(dppn)]^{2+}$ **41** (a) has one "phenanthroline"-like ligand, $[Ru(bpy)_2(dpb)]^{2+}$ **42** (b) has one "quinolone"-like ligand and $[Ru(bpy)(dppn)(dppn)]^{2+}$ **43** has both types of ligands. The generalized Jablonski energy diagrams (below) depict three limiting cases.

In contrast, the ligand-centered orbitals of the "quinoline"-like dpb in $[Ru(bpy)_2(dpb)]^{2+}$ **42** are at lower energies than in dppn in general and the much shorter conjugation length stabilizes the π-orbital of the polypyridyl ligand even further. Therefore, the "classic" situation is again established: the HOMO is Ru(d)-centered and the LUMO is the ligand π*-orbital. The MLCT emission of $[Ru(bpy)_2(dpb)]^{2+}$ **42** is weak, short-lived (66 ns) and with a maximum at 927 nm strongly red-shifted into the near-infrared (NIR) region of light.

Taking all this information together $[Ru(bpy)(dppn)(dpb)]^{2+}$ **43** should represents a perfect mix of both systems and consequently should have two close-lying excited states, a ^{3}MLCT on the dpb ligand and a dppn-centered $^3(\pi-\pi^*)$ state. Fortunately, this scenario is found and $[Ru(bpy)(dppn)(dpb)]^{2+}$ **43** exhibits a excited-state lifetime of 229 ns with weak 926 nm emission. The intermediate situation of $[Ru(bpy)(dppn)(dpb)]^{2+}$ **43** is besides the emission properties also well reflected by singlet oxygen sensing experiments, in which the abundant triplet oxygen reacts by energy transfer with the excited triplet state to produce the emissive singlet oxygen (λ_{em} = 1275 nm). In this experiment the singlet oxygen sensing quantum yield of $[Ru(bpy)(dppn)(dpb)]^{2+}$ **43** with 43% lies between the 79% of $[Ru(bpy)_2(dppn)]^{2+}$ **41** and the 22% of $[Ru(bpy)_2(dpb)]^{2+}$ **42** – consequently a perfect mix.[137]

The outlined examples from literature have demonstrated that the bichromophoric approach to generate new and optimized ruthenium(II) polypyridyl photosensitizers is a balancing act. Of course, the usage of π-extended chromophores promises the possibility to increase the light absorption for an improved light-harvesting capability. But the implementation of additional energy levels of the dye into an established system interferes with already existing and favored energy or electron transfer processes. In particular, the complex $[Ru(bpy)_2(dppz)]^{2+}$ **37** has demonstrated the perturbation on the LUMO side. In **37**, two close-lying LUMO level exist and thus create two MLCT transitions of which one is emissive and the other is not. The non-emissive dark state hampers the general emission properties of the complex and occasionally leads to a complete phosphorescence loss like in aqueous solutions. In addition, the always further extension of the π-conjugation of chromophores can lead to the situation that π-orbitals of the ligand become the HOMO energy level instead of Ru(d) orbitals in ruthenium(II) polypyridyl complexes.

Consequently, $\pi-\pi^*$ states represent the lowest excited state instead of the preferred MLCT states. The latter have an already partly dissociated electron and hole pair and therefore, facilitate electron transfer processes.

Taking all these factors into account, it challenging to forecast the photophysical outcome of a certain modification on the framework of Ru(II) polypyridyl complexes. Accordingly, every system has to be explored independently and with the expectation of surprises.

CHAPTER 3 RESULTS AND DISCUSSION

3.1 Trinuclear Ruthenium Macrocycles[1]

As already pointed out in the introductory section **2.1**, the [Ru(bda)L_2] complex family are potent water oxidation catalysts reaching outstanding TOF values of up to 1,000 s^{-1} with the assistance of the I2M reaction pathway.[36] Interestingly, the [Ru(bda)L_2] catalysts accomplishing WO by the WNA mechanism are significantly less active with TOFs of 0.01 – 1 s^{-1}.[139, 140] In the following subchapter, it is demonstrated how the fixation of the Ru(bda) moiety into a metallosupramolecular macrocycle consisting of three metal centers influences not only the catalytic activity in general but also the underlying mechanism of the catalytic conversion. In such a supramolecular macrocycle TOF values above 100 s^{-1} are reached while the catalyst operates *via* the WNA mechanism.

3.1.1 Concept, Synthesis and Characterization in Organic Medium

The radical I2M coupling mechanism of [Ru(bda)L_2] requires the approach of two metal-oxide species in the rate-determining step.[37] Furthermore, dissociation of the axial pyridyl ligands L followed by diffusion of the cleaved ligands into the solution is accepted as the main degradation pathway of the [Ru(bda)L_2] catalyst class.[141] Accordingly, a metallosupramolecular concept was created in which the two axial ligands are connected to each other *via* a macrocyclic chelating ligand (**Scheme 5**). The benefit of such an assembly is that after cleavage of an axial pyridyl moiety the ligand is still tethered to the whole system. Consequently, it is feasible to re-coordinate to the ruthenium center and thus recreate the original species, *i.e.* self-healing. In addition, the gathering of multiple redox centers in close proximity is considered to be a promising approach to artificial photosynthesis due to similarities to natural photosynthesis in plants – nature accomplishes water oxidation by assembling four manganese redox centers in the manganese-calcium

[1] This section has been communicated in:
[138] M. Schulze, V. Kunz, P. D. Frischmann, F. Würthner, *Nature Chem.* **2016**, *8*, 576-583.

cluster (Mn_4O_5Ca) of photosystem II.[142] However, the latter aspect is highly dependent on the intrinsic properties of the bridging unit like flexibility and length.

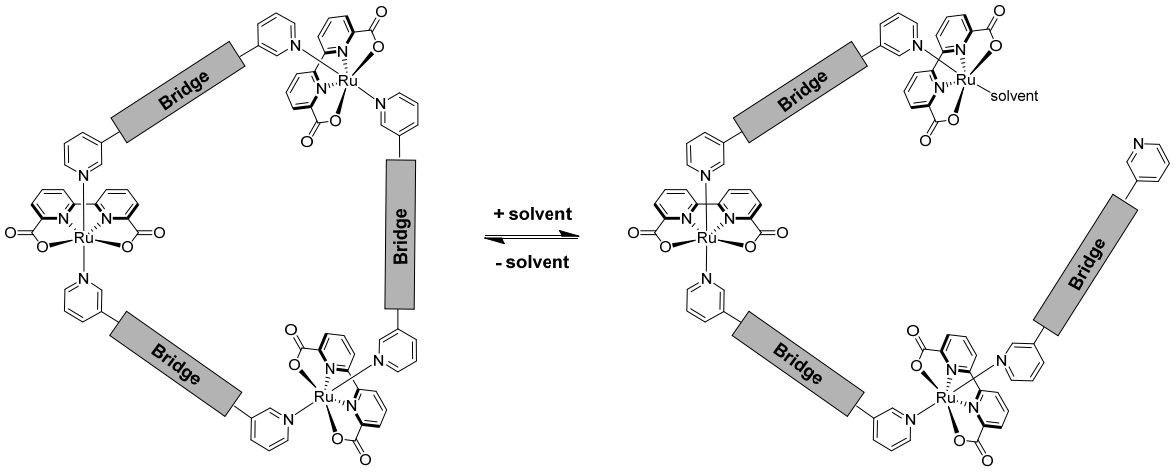

Scheme 5 Schematic representation of a trinuclear metallosupramolecular macrocycle consisting of three Ru(bda)-subunits and its feasible reversible self-healing mechanism after replacement of an axial ligand by a solvent molecule.

Obviously, the Ru(bda) subunit represents a linear 180° building block. Therefore, the construction of a self-assembled trigonal [3+3] macrocycle requires a ditopic ligand with a 60° angle between the donor nitrogens. A suitable bridging unit to construct such a macrocyclic structure is the ditopic ligand 1,4-bis(pyrid-3′-yl) benzene **45** (bpb). The $[Ru(bda)bpb]_3$ macrocycle **46** was obtained by a simple self-assembly process from an equimolar mixture of the precursor $[Ru(bda)((CH_3)_2SO)_2]$ **44** and bpb **45** (**Scheme 6**). Considering the relatively inert nature of ruthenium coordination complexes disfavoring the self-error checking given in other metallosupramolecular architectures,[5, 143, 144] the 55% yield of the [3+3] macrocycle $[Ru(bda)bpb]_3$ is remarkably high and obviously encoded in the bpb structure-directing ligands.

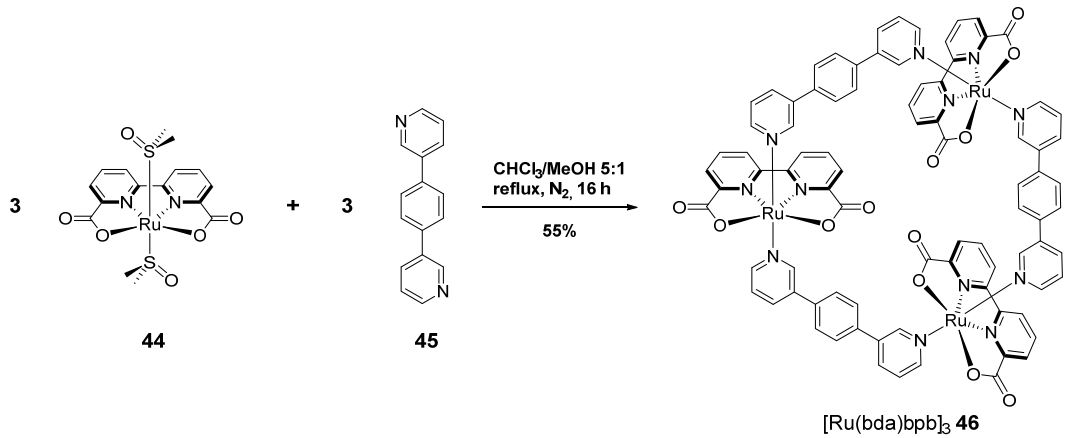

Scheme 6 Synthesis of the macrocycle $[Ru(bda)bpb]_3$ **46** by a self-assembly process from an equimolar mixture of the precursor $[Ru(bda)((CH_3)_2SO)_2]$ **44** and bpb **45**.

Structural confirmation of the macrocyclic assembly is provided by NMR spectroscopy and high-resolution electrospray ionization mass spectrometry (HR-ESI-MS). The symmetry of the $[Ru(bda)bpb]_3$ macrocycle **46** is immediately evident in the ^1H NMR spectrum (**Figure 22a**) exhibiting only three signals for the bda backbone unit (blue) and five signals for the bpb linker (red) in a 1:1 ratio. In particular, the sharp singlet H^t for the four protons of the central benzene ring of bpb is a strong proof of a D_{3h} symmetric macrocycle. The chemical shifts of the other signals are in good agreement to the spectrum of the reference $[Ru(bda)(pic)_2]$ **5** reported in literature.[49] The dominant peak in the HR-ESI mass spectrum is found at 1727.12 *m/z*, assigned to the macrocyclic cation $\mathbf{46}^+$, and matches perfectly with its predicted isotope pattern further supporting the presence of three Ru centers in the macrocycle (**Figure 22b**). No higher order oligomers are found by either ESI or MALDI (matrix-assisted laser desorption/ionization) mass spectrometry

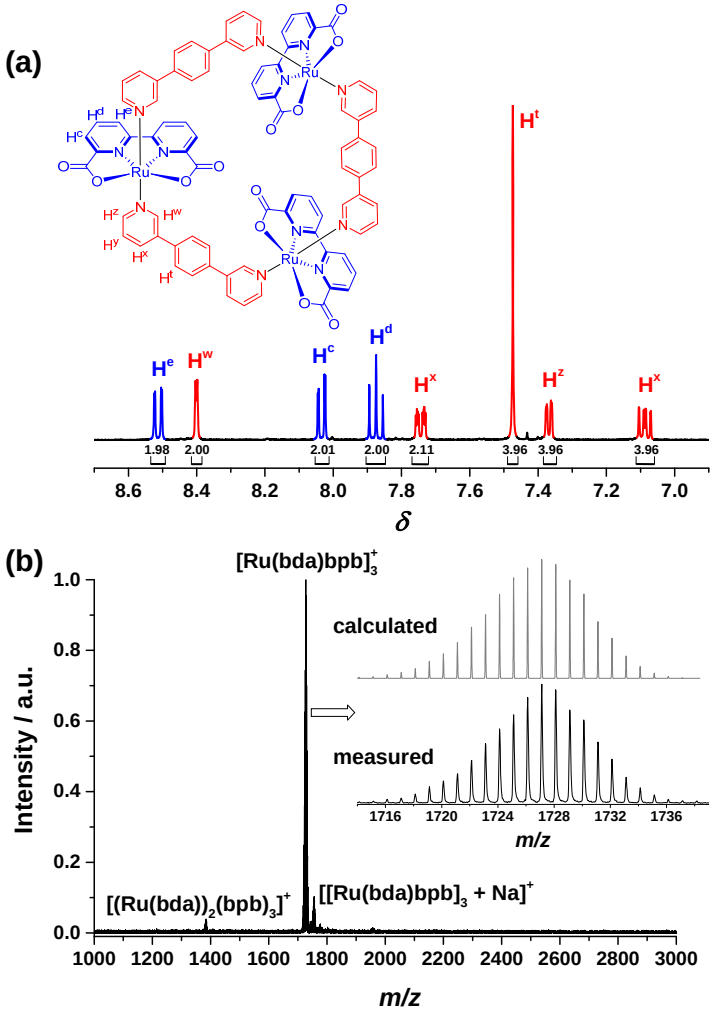

Figure 22 (a) 400 MHz ^1H NMR spectrum of $[Ru(bda)bpb]_3$ **46** in 5:1 CD_2Cl_2:MeOD (blue = [Ru(bda)], red = bpb). (b) HR-ESI mass spectrum of **46** (c = $1 \cdot 10^{-6}$ M in 5:1 $CHCl_3$:CH_3CN). Inset: Experimentally observed ESI-MS (black, bottom) and simulated isotopic distributions (gray, top) of $[Ru(bda)bpb]_3^+$ $\mathbf{46}^+$.

Having confirmed the macrocyclic structural assignment, electrochemical and optical properties in organic medium were investigated (**Figure 23**) to ensure that the characteristics of the [Ru(bda)]-unit were not adversely perturbed by replacing the common axial 4-picoline ligands with bpb. The UV/Vis absorption spectrum of $[Ru(bda)bpb]_3$ **46** in a 4:1 mixture of dichloromethane and methanol displays broad spin-allowed ^{1}MLCT absorptions between 350 and 600 nm. Based on theoretical calculations of Murata and co-workers the lower energetic shoulder at 500 nm is assigned to an Ru(d)–π^*_{bda} optical HOMO-LUMO transition.[145] Accordiningly, the position of this band in the macrocycle is at the same wavelength as in $[Ru(bda)(pic)_2]$ **5**. The second MLCT maximum at 390 nm is composed of Ru(d)–π^*_{axial} transitions and thus differs between both complexes to a certain extent. In addition to the MLCTs, π–π^* absorptions between 250 and 300 nm are also observable. The preservation of the frontier orbitals in $[Ru(bda)bpb]_3$ in comparison to other [Ru(bda)]-complexes is also confirmed by electrochemical measurements in dichloromethane (**Figure 23b**). In the organic solvent one oxidation at -0.06 V *vs* $Fc^{0/+}$ is observed which is assigned to the $Ru^{2+/3+}$ redox couple and is in perfect agreement with the value of $[Ru(bda)(pic)_2]$ from literature.[49]

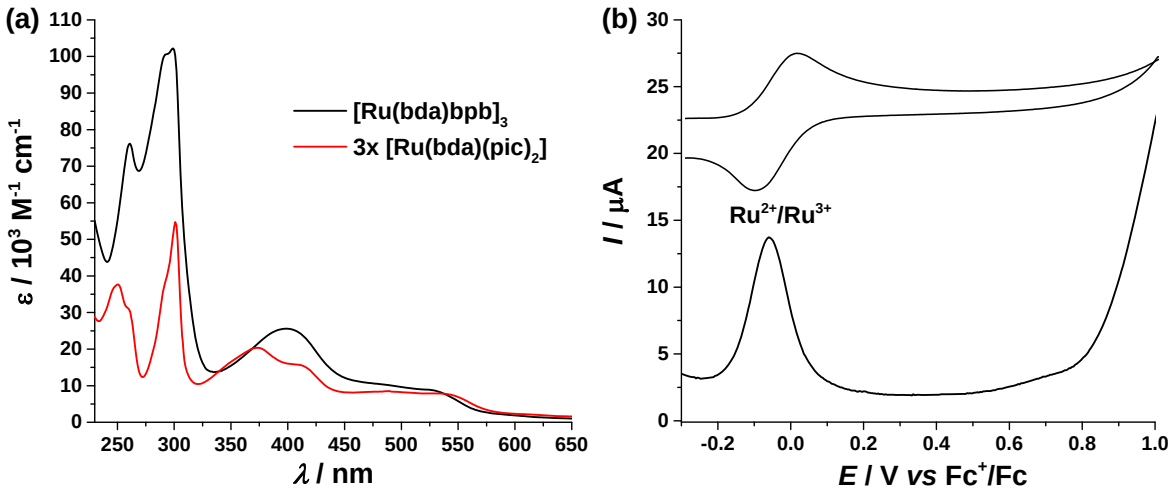

Figure 23 (a) Absorption spectra of $[Ru(bda)bpb]_3$ **46** (black) and $[Ru(bda)(pic)_2]$ **5** (3x, red) in 4:1 dichloromethane/methanol mixture ($c = 1 \cdot 10^{-5}$ M). (b) Cyclic- and squarewave voltammogram of **46** in dichloromethane and a trace of methanol for solubility (0.1 M *n*-Bu_4PF_6).

3.1.2 Electrochemical and Optical Properties in Aqueous Solution

Electrochemistry of [Ru(bda)bpb]$_3$ in aqueous solutions. To provide first insights into the capability of the macrocycle **46** to catalyze the oxidation of water, aqueous electrochemical investigations were carried out. The differential pulse voltammogram in aqueous pH 1 solution with 50% 2,2,2-trifluoroethanol as co-solvent for solubility displayed three ruthenium oxidation events (**Figure 24a**). The oxidation potentials appear at +0.72, +1.17 and +1.36 V *vs* NHE, respectively, and correspond to the formal oxidations of $Ru^{2+/3+}$, $Ru^{3+/4+}$ and $Ru^{4+/5+}$. The three redox states of **46** are roughly 0.1 V harder to oxidize than in the mononuclear reference compound [Ru(bda)(pic)$_2$] **5** (+0.60, +1.07, +1.25 V) likely due to the proximity of the three Ru ions.[37] Evidence for the simultaneous oxidation of the three ruthenium centers can be obtained by spectroelectrochemistry (*vide infra*).

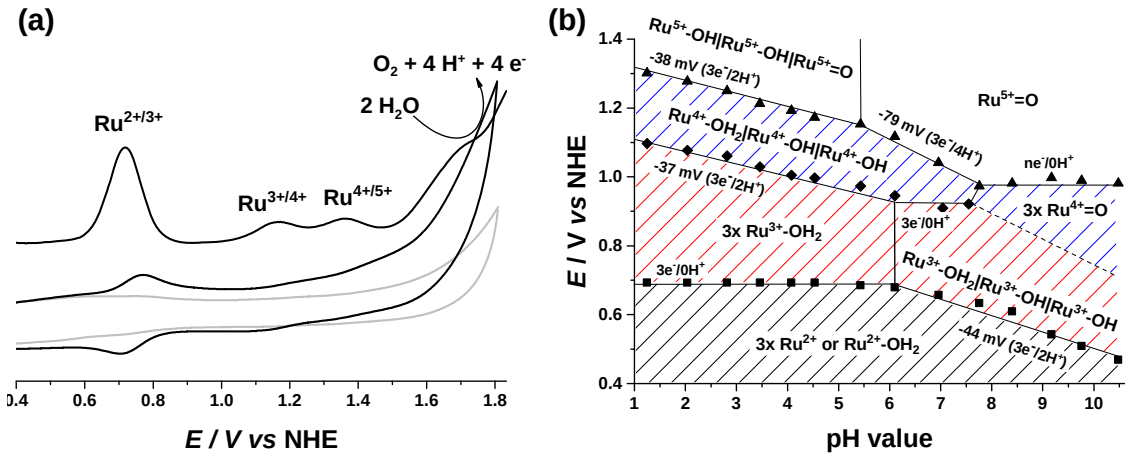

Figure 24 (a) Cyclic and differential pulse voltammograms of the macrocycle [Ru(bda)bpb]$_3$ **46** (black, $c = 2.5 \cdot 10^{-4}$ M) with a corresponding blank measurement (greay) in 1:1 2,2,2-trifluoroethanol/water (pH 1, acid: trifluoromethane sulfonic acid). (b) Pourbaix (E-pH) diagram of **46**. The potentials were obtained from differential pulse voltammetry at certain pH values which were adjusted by stepwise addition of NaOH solutions to a 1:1 2,2,2-trifluoroethanol/water (pH 1) solution. The colored and shaded areas correspond to the stability regions of different Ru oxidation states.

The pH dependency of the $Ru^{2+/3+}$, $Ru^{3+/4+}$ and $Ru^{4+/5+}$ redox couples in the macrocyclic framework (Pourbaix diagram (plot of *E vs* pH) in **Figure 24b**) is somewhat more complex in comparison to [Ru(bda)(pic)$_2$] **5** because the three Ru centers mutually influence each other. In contrast to other well established mononuclear [Ru(bda)] complexes no simple $1e^-/1H^+$ or $3e^-/3H^+$ proton-coupled electron transfer (PCET) processes can be observed for [Ru(bda)bpb]$_3$ **46** between pH = 1 and pH = 11.[146] In acidic solutions (pH 1 to 5) the

alterations of the $Ru^{3+/4+}$ and $Ru^{4+/5+}$ redox potentials exhibit slopes of -37 and -38 mV, respectively, indicative for $3e^-/2H^+$ transfer processes (Nernstian ideal 39 mV) whereas the $Ru^{2+/3+}$ oxidations ($3e^-$) are completely proton-uncoupled.[46] Altogether, 9 electrons and 4 protons are transferred within the water oxidation processes resulting in a catalytically active species containing Ru^{5+}-OH|Ru^{5+}-OH|Ru^{5+}=O metal centers. However, after the oxidation to the Ru^{5+} species the current strongly increases in comparison to a blank measurement without catalyst. This increase in current is attributed to the water oxidation process. The required fourth oxidation cannot be observed under these conditions because of the signal overlap with the water oxidation current and thus was not included in the Pourbaix diagram.

Later catalytic water oxidation experiments were performed with acetonitrile as co-solvent due to its oxidation stability.[147, 148] Accordingly, the aqueous electrochemistry of $[Ru(bda)bpb]_3$ with acetonitrile as co-solvent was also investigated (**Figure 25**).

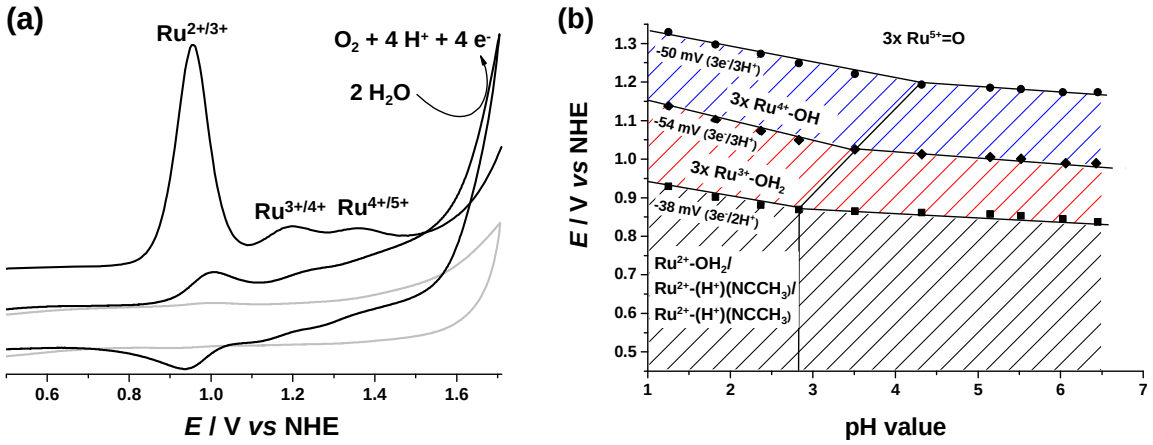

Figure 25 (a) Cyclic- and differential pulse voltammograms of the macrocycle $[Ru(bda)bpb]_3$ **46** (c = 0.25 mM) in 1:1 acetonitrile/water (pH 1, acid: trifluoromethane sulfonic acid) with a corresponding blank measurement (gray). (b) Pourbaix diagram (redox potential as a function of the pH value) of **46** in 1:1 acetonitrile/water solutions. The potentials were obtained from differential pulse voltammograms at certain pH values which were adjusted by stepwise addition of NaOH solutions to a 1:1 acetonitrile/water (pH 1) solution.

In general, the redox chemistry of both co-solvents is comparable. The most important difference is that acetonitrile has the capability to bind to metal centers *via* its nitrile group in contrast to TFE.[51] Therefore, CH_3CN can compete with H_2O for the seventh coordination site in the complex. Accordingly, the first oxidation is ~0.2 V harder to accomplish in aqueous mixtures with acetonitrile than with TFE.[51, 146] Fortunately, this effect nearly vanishes at higher oxidation states because water binds then as hydroxide and oxide, respectively, due to its ability to trigger PCET processes. Consequently, the $Ru^{3+/4+}$

and $Ru^{4+/5+}$ redox potentials are nearly equivalent in both solvent mixtures at pH 1 (TFE: +1.17 and +1.36 V; CH_3CN: +1.20 and +1.36 V). Also the Pourbaix diagram becomes more complex by this effect and the redox active species can only be satisfyingly assigned in the acidic pH range.

In summary, although the electrochemical properties of the metallosupramolecular macrocycle are more complex compared to the mononuclear [Ru(bda)(pic)$_2$] catalyst **5**, the general electrochemical characteristics are similar to the reference system and thus [Ru(bda)bpb]$_3$ **46** appears to be a suitable catalyst for water oxidation.

Spectroelectrochemistry of different ruthenium redox states in [Ru(bda)bpb]$_3$. To establish if the three Ru centers are simultaneously oxidized, spectroelectrochemistry was performed to assign the redox state of the Ru centers at a given potential as each Ru oxidation state exhibits a signature optical absorption (**Figure 26a** and **b**). Upon increasing the potential to +0.97 V the MLCT absorptions between 380 and 550 nm are bleached and a new band at 668 nm emerges. This new absorption is assigned to the Ru^{3+} species in agreement with examples known from literature that attribute the origin of this transition to the presence of a Ru^{3+}-species based on UV/Vis experiments and theoretical calculations.[47, 149]

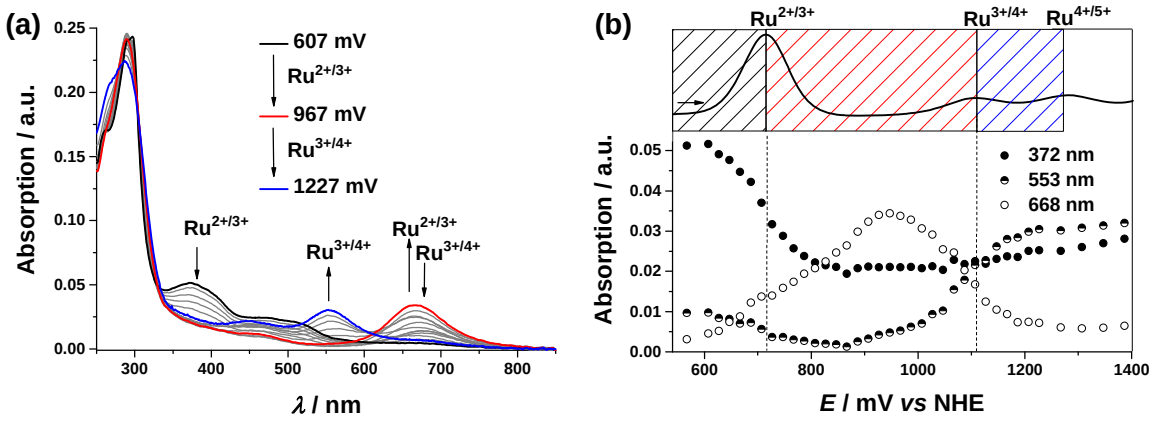

Figure 26 (a) Spectroelectrochemistry of [Ru(bda)bpb]$_3$ **46** (c = 0.1 mM) in 1:1 TFE/water pH 1. (b) Plot of the absorption changes at 372, 553 and 668 nm *vs* the applied potential in the electrochemical cell. Above the differential pulse voltammogram of the macrocycle is depicted.

When the potential is further increased from +0.97 V to +1.23 V in the spectroelectrochemical titration the Ru^{3+} band at 668 nm of **46** decreases and an absorption arises at 553 nm indicating the formation of Ru^{4+} species. Concepcion *et al.* observe the same spectral band formations at very similar wavelengths and postulate a dinuclear Ru^{4+} species.[149] No further spectral changes were observed upon increasing the potential beyond the $Ru^{4+/5+}$ redox couple because the formed Ru^{5+} species immediately catalyzes the oxidation of water and thus no Ru^{5+} can be accumulated.

UV/Vis redox titration of [Ru(bda)bpb]$_3$. Similar absorption changes indicating an alteration of the redox states of the ruthenium centers in the macrocycle [Ru(bda)bpb]$_3$ **46** can be triggered by chemical oxidants like oxygen from air or cerium(IV) ammonium nitrate (CAN). A freshly prepared solution of the macrocycle in a 1:1 mixture CH_3CN/water (pH 1) has a brownish color and turns slowly to green over time due to the oxidation by oxygen in air (**Figure 27**). The greenish color is caused by the increase of the 668 nm absorption band; simultaneously, the MLCT absorption bleaches with the same rate.

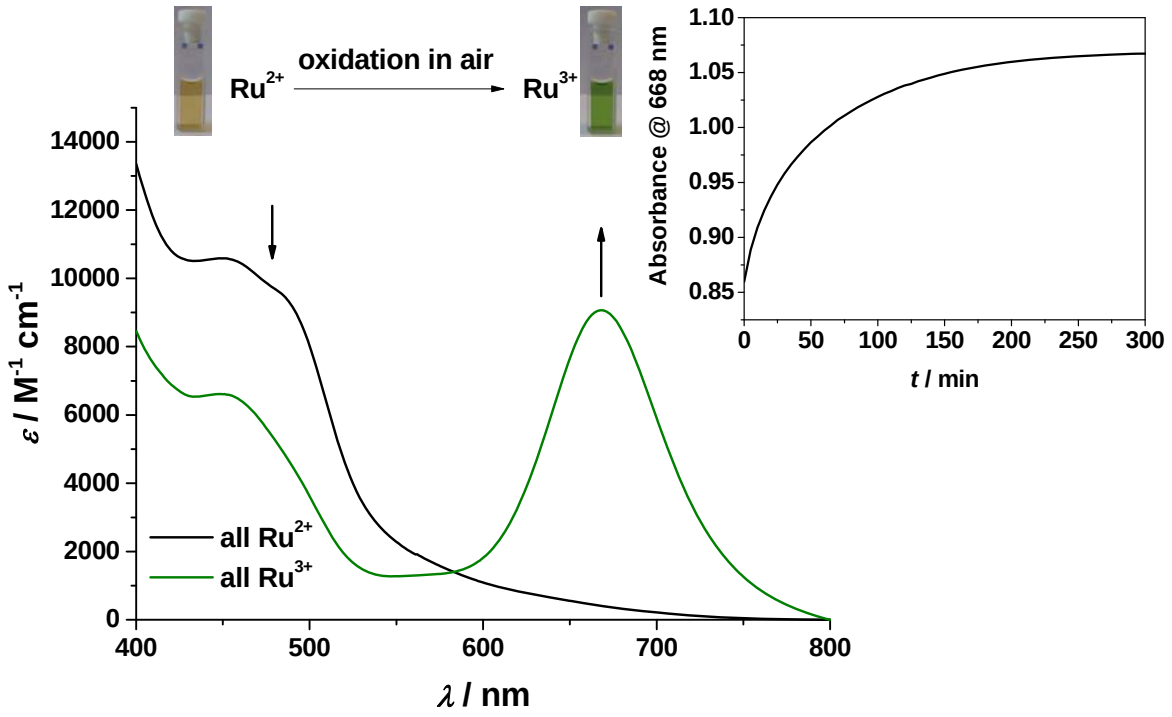

Figure 27 UV/Vis absorption spectra of [Ru(bda)bpb]$_3$ **46** in 1:1 CH_3CN/water (pH 1) in which all ruthenium centres of the macrocycle are in the Ru^{2+} or the Ru^{3+} oxidative state ([**46**] = 0.1 mM), inset: monitoring the Ru^{3+} absorbance at 668 nm over time. The $Ru^{2+}\rightarrow Ru^{3+}$ oxidation is finished after ~5 h under ambient conditions.

A further oxidation to the 4+ oxidation state cannot be accomplished by oxygen but can be conducted by the stronger oxidant CAN (**Figure 28**). By the stepwise addition of stoichiometric equivalents of CAN to a $[Ru^{3+}–OH_2(bda)bpb]_3^{3+}$ $\mathbf{46}^{3+}$ solution, the three metal centers can be continuously oxidized to Ru^{4+}. Accordingly, the 668 nm absorption decreases and the 553 nm absorption of Ru^{4+} increases, which goes along with a color, change from green to violet.

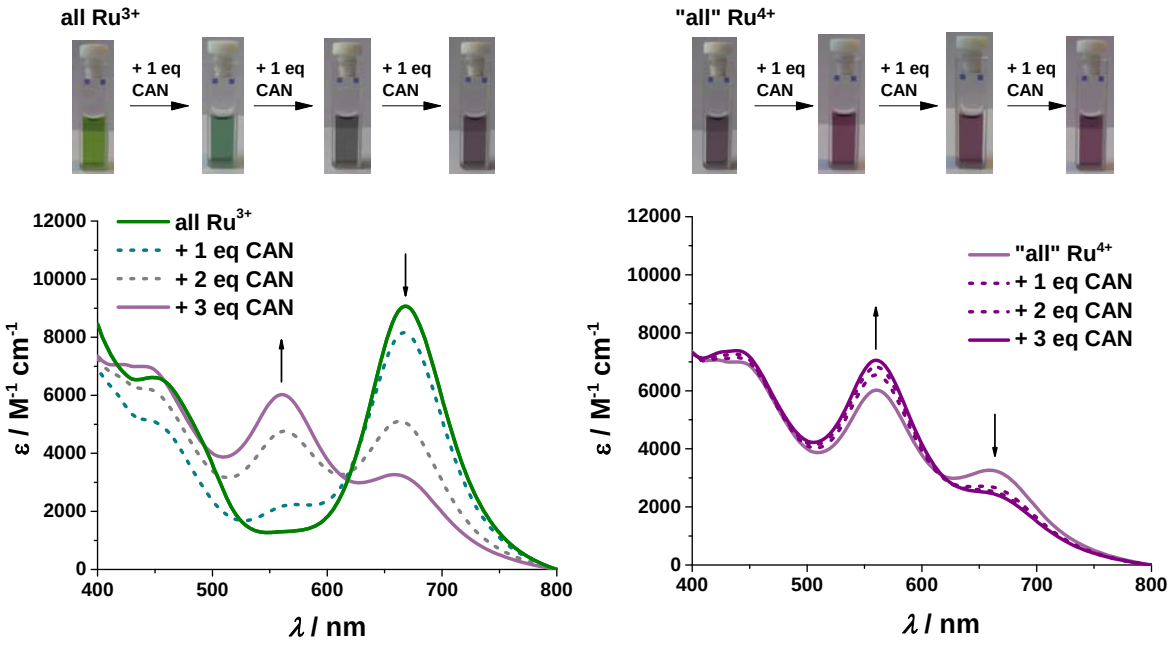

Figure 28 Spectral changes in the process of the redox titration of $[Ru^{3+}–OH_2(bda)bpb]_3^{3+}$ $\mathbf{46}^{3+}$ (fully oxidized to Ru^{3+} by air, see **Figure 27**) with cerium(IV) ammonium nitrate (CAN) as oxidant. Conditions: in 2 mL 1:1 CH_3CN/water (pH 1),[$\mathbf{46}^{3+}$] = 0.1 mM, [CAN] = 20 mM, 10 µL CAN corresponds to 1 equiv. CAN with regard to $\mathbf{46}^{3+}$.

Subsequent CAN equivalents lead to no further changes in the absorption spectrum. This behavior indicates that the $[Ru^{4+}–OH]_3^{3+}$–species represents a resting state in the system and the following oxidation step to Ru^{5+}=O is rate-determining (see section **3.1.4**) which is supported by the fact that the Ru^{5+}-species could not be accumulated in the spectroelectrochemical experiment after +1.23 V.

ESI measurement of catalyst solutions with different equivalents of CAN supports the previous results of the spectroelectrochemical and redox titration (**Figure 29**). At pH 7 the macrocycle is always ionized by the oxidation of one ruthenium center to Ru^{3+}.

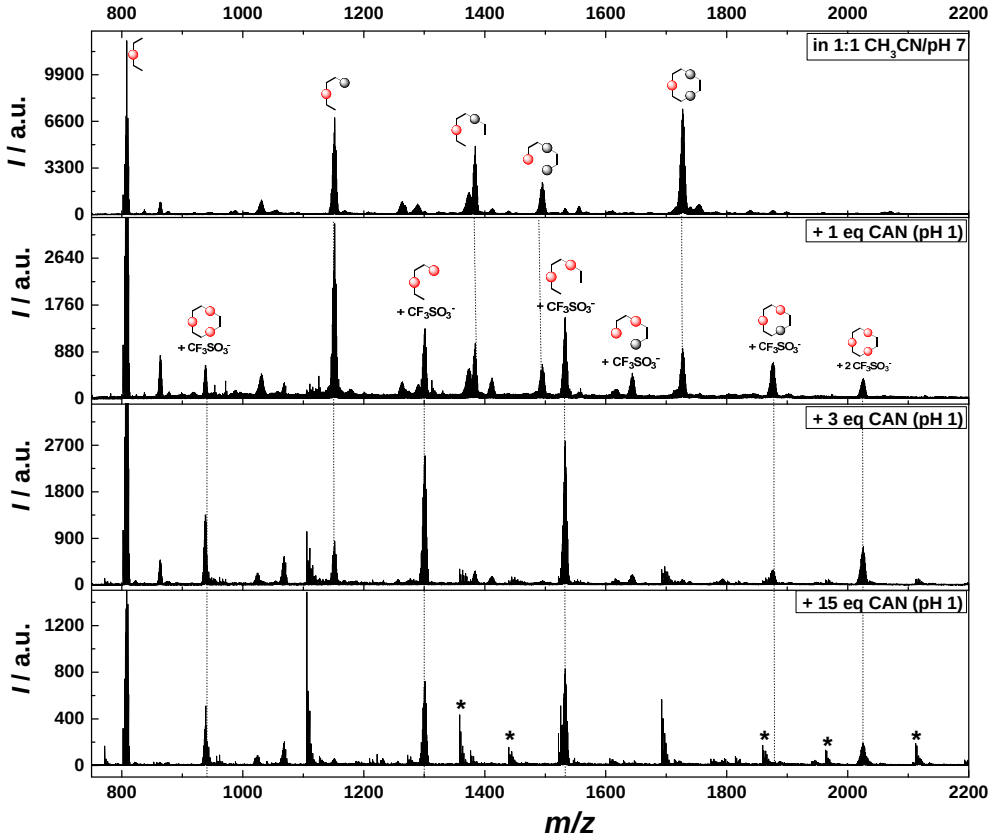

Figure 29 ESI mass spectra of $[Ru(bda)bpb]_3$ **46** in 1:1 CH_3CN/water (pH 7) water after defined addition of freshly prepared cerium(IV)ammonium nitrate (CAN) solution in pH 1 water (acid: trifluoromethane sulfonic acid). Signals assigned with * belong to CAN. Gray spheres represent Ru^{2+} and red spheres indicate Ru^{3+} centers.

After addition of pH 1 CAN solution (acid: trifluoromethane sulfonic acid) multiple oxidized Ru centers in the macrocycle are observed in which all charges higher than one are compensated by triflate counter anions. Unfortunately, the Ru^{4+} species seems to be unstable under the experimental electrospray conditions and thus cannot be observed. However, the UV/Vis and ESI-MS results of either electrochemical or chemical oxidation experiments provide strong evidence for stepwise conversion of all metal centers in the macrocycle first to Ru^{3+} followed by Ru^{4+}.

3.1.3 Catalytic Water Oxidation by a Sacrificial Oxidant

Chemically driven water oxidation was studied with cerium(IV) ammonium nitrate as the sacrificial electron acceptor in aqueous pH 1 solutions (**Figure 30**). The catalyst $[Ru(bda)bpb]_3$ **46** was first dissolved in aqueous pH 7 mixtures with a certain amount of co-solvent. In a separate Schlenk reaction vessel 3 mL of a pH 1 CAN solution (same co-solvent content) were placed. Afterwards, 400 µL of the catalyst solution were injected into the Schlenk vial *via* a septum. Subsequently, a vigorous gas evolution occurred. To quantify the evolved gas amount during the reaction, the Schlenk tube was connected to a commercial pressure sensor. After the gas evolution had ceased, an aliquot of the gas headspace was taken out of the reaction vessel and injected into the gas chromatograph to determine the gas composition at the end of the reaction (**Figure 30c**).

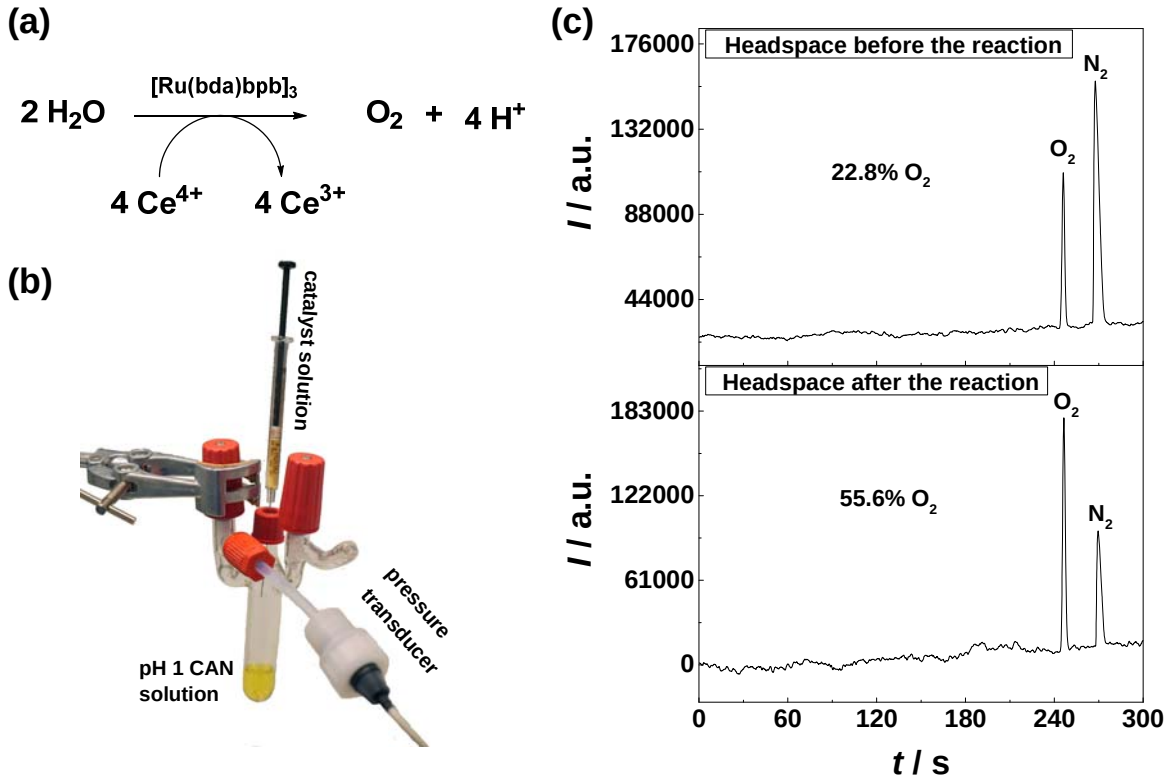

Figure 30 (a) Catalytic water oxidation with $[Ru(bda)bpb]_3$ **46** as catalyst and cerium(IV) ammonium nitrate as sacrificial oxidant. (b) Experimental setup: A commercial pressure transducer measures the pressure increase in the Schlenk reaction vessel caused by the oxygen evolution during the water oxidation reaction. (c) Headspace-GC analysis of the gas volume of the Schlenk tube before and after the reaction.

Due to the low solubility of $[Ru(bda)bpb]_3$ in pure water, acetonitrile was chosen as co-solvent due to its oxidative stability. [147, 148] Various acetonitrile/water ratios were screened, and in all experiments vigorous oxygen evolution was detected (**Figure 31a**).

The highest catalytic activity was reached with 59% acetonitrile addition (**Figure 31b**), whereas higher acetonitrile percentages lead to reduced activity because CH_3CN acts as a competitive binder to the seventh coordination site of the ruthenium.[147] Visible precipitation was observed after the oxygen evolution had ceased for solutions with CH_3CN content below 40% possibly due to the generation of catalytic intermediates with lower solubility.

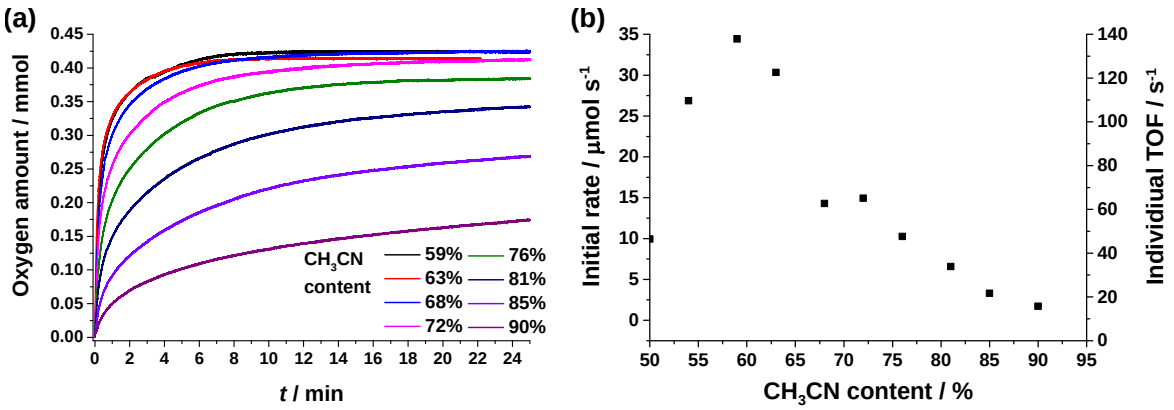

Figure 31 (a) Oxygen evolution *vs* time during the water oxidation with [Ru(bda)bpb]$_3$ **46** as a catalyst in aqueous pH 1 solutions with varying acetonitrile content using CAN as a sacrificial oxidant. (b) Plot of the individual reaction rates in the first 3 s of the water oxidation with **46** as catalyst against the acetonitrile content. Catalysis conditions: 400 µL of a catalyst solution (pH 7) with a certain acetonitrile amount were injected into 3 mL of a pH 1 CAN solution (1 g, 1.82 mmol) with the same acetonitrile content. Resulting catalysis conditions: [**46**] = 75.5 µM, [CAN] = 0.54 M, V_{ges} = 3.4 mL.

To benchmark the catalytic performance of [Ru(bda)bpb]$_3$ **46** the TON and TOF values of our system were compared with the structurally similar mononuclear [Ru(bda)(pic)$_2$] complex known from literature (**Table 1**).[37] Varying the concentration of **46** in 59% CH_3CN (all other parameters kept constant) to optimize the performance gave TON_{max} and a TOF_{max} values of 7400 and 155 s^{-1}, respectively, for the macrocyclic system and a TON_{max} of 970 and TOF_{max} of 8.4 s^{-1} for the [Ru(bda)(pic)$_2$] reference **5**. Notably, higher values for [Ru(bda)(pic)$_2$] are obtained in nearly pure water solutions (1% CH_3CN, TON_{max} of 1690 and TOF_{max} of 33.3 s^{-1}) to which our macrocyclic system cannot be compared due to insolubility. Consequently, the macrocyclic structure imparts enhanced catalytic activity by more than one order of magnitude and it preserves its activity even in the presence of considerable amounts of acetonitrile (59%).

In addition, [Ru(bda)bpb]$_3$ **46** exhibits increased stability when comparing the TON_{max} values of 7400 (~2500 per Ru) for the macrocycle and the TON_{max} of 970 for the single unit in [Ru(bda)(pic)$_2$]. Dissociation of axial pyridyl ligands followed by diffusion of the cleaved ligands into the solution was already discussed in section **3.1.1** to be one of the

main degradation pathways of [Ru(bda)L_2] type catalysts.[141] Accordingly, the macrocyclic nature of **46** imparts a better stability through the chelate effect of the bpb ligand that mitigates deleterious pyridyl ligand dissociation; if a pyridyl unit of the bidentate bpb dissociates it is still tethered to the macrocyclic catalyst *via* the second pyridyl binding site thus greatly enhancing the probability of intramolecular re-association *i.e.* self-healing.

This assumption is supported by MALDI mass spectrometry after *ca* 40 catalytic cycles which displayed nearly no fragmentation of the macrocycle and thus underlines the robustness of the self-assembled architecture (not figured).

Table 1 Summary of the catalytic benchmark numbers (TON and TOF) of the catalysts [Ru(bda)bpb]$_3$ **46** and [Ru(bda)(pic)$_2$] **5** in the chemically driven water oxidation reaction.[a]

CH_3CN content	Remarks	[Ru(bda)(pic)$_2$] 5			[Ru(bda)bpb]$_3$ 46		
		c **/ μM**	**TON**	**TOF / s^{-1}**	***c*** **/ μM**	**TON**	**TOF / s^{-1}**
1%	conditions for TON_{max}	54 (59)[b]	1690 (2010)[b]	6.9 (14.7)[b]	76	Precipitation occurred	
	conditions for TOF_{max}	240 (216)[b]	490 (–)[b]	33.3 (32.8)[b]			
59%	conditions for TON_{max}	128	970	3.6	11.8	7400	85
	conditions for TOF_{max}	510	245	8.4	47	2600	155
	Equal amount of substance	~80	930	2.1	~80	1600	135
	Equal amount of Ru	~80	930	2.1	24	5130	127

[a] Conditions: 400 μL of a catalyst solution (varying CH_3CN/water (pH 7) content) was injected into 3 mL of a CH_3CN/water (pH 1) solution containing 1 g CAN (1.82 mmol). [b] Comparison with values from literature see ref [37].

3.1.4 Mechanistic Investigations

Kinetic analysis of the water oxidation catalysis. A more detailed picture of the kinetic rate law behind the water oxidation is obtained by concentration dependent catalytic investigations. The general form of the oxygen formation rate law is given by equation (7):

$$\frac{d[O_2]}{dt} = k_{cat} \cdot [H_2O]^x \cdot [[Ru(bda)bpb]_3]^y \cdot [Ce^{4+}]^z \qquad (7)$$

The water concentration dependent part of (6), $[H_2O]^x$, can be neglected because the catalysis takes place in water and thus a huge excess is given so that the concentration change is irrelevant. In the studies, which cover the concentration dependency of the

catalyst, the catalytic activity of [Ru(bda)bpb]$_3$ **46** is observable to a catalyst concentration of 5.9 µM whereas [Ru(bda)(pic)$_2$] demonstrates negligible oxygen evolution at a concentration level of 34 µM.

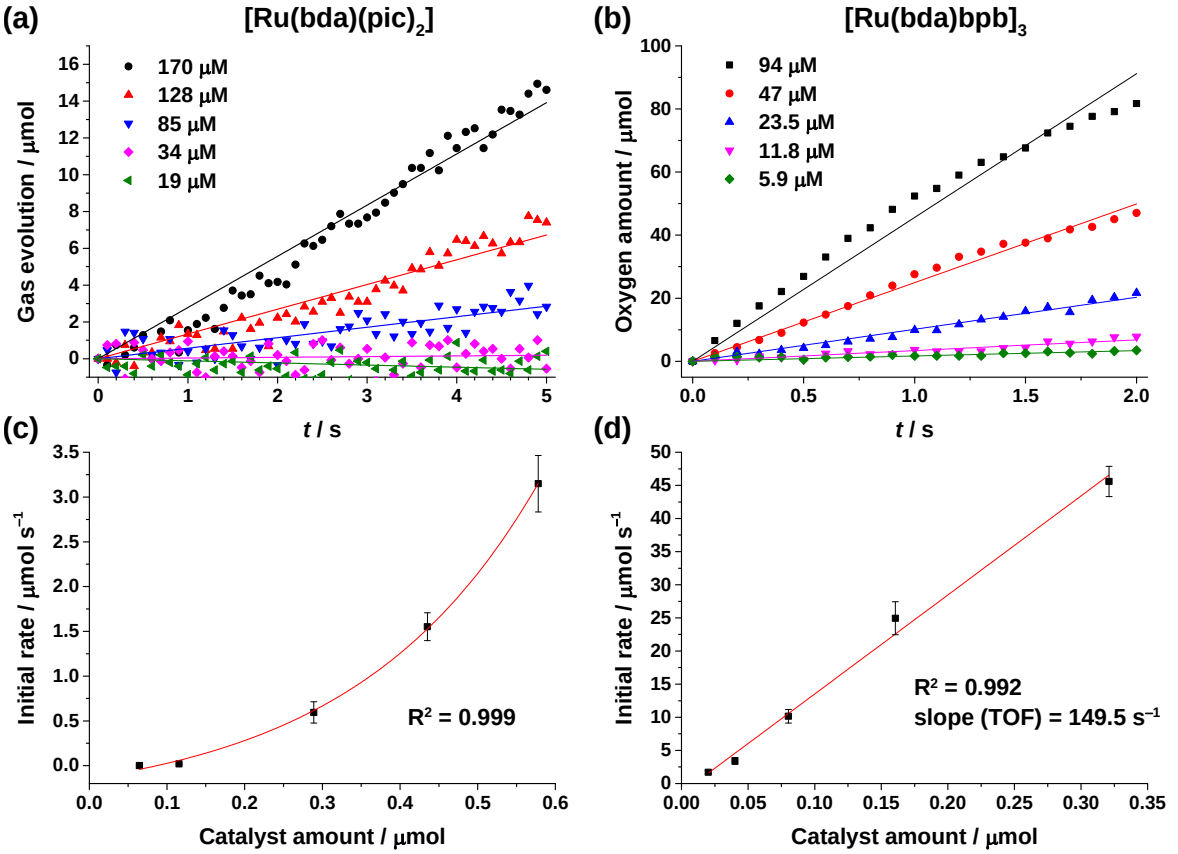

Figure 32 (a) Oxygen evolution curves of the first 5 s of the catalysis with varying [Ru(bda)(pic)$_2$] **5** concentrations (170 – 19 µM). (b) Oxygen evolution curves of the water oxidation in the first 2 s with varying [Ru(bda)bpb]$_3$ **46** concentrations (94 – 5.9 µM). (c) and (d) Plots of the initial catalysis rate *vs* the catalyst amount with a corresponding linear regression fit. The individual reaction rates were obtained by a linear fitting procedure of the first 5 s and 2 s, respectively, of the catalysis. Catalysis conditions: 400 µL of a catalyst solution (pH 7 water with 59% acetonitrile) were injected into 3 mL of a pH 1 CAN solution (1 g, 1.82 mmol) with the same acetonitrile content. V_{ges} = 3.4 mL. Resulting concentrations: [**46**] = varying, [CAN] = 0.54 M. The error bars were estimated by the maximum volumetric error during solution preparation and catalyst injection.

The initial rate of the catalysis is evaluated in the first few seconds of the oxygen evolution by a linear regression analysis because at that point the sacrificial electron acceptor CAN is still in large access and thus its concentration change in the rate law is negligible (**Figure 32a** and **b**). The plot of the different initial rates at different catalyst loadings delivers a valuable methodology to determine the order of the rate law with regard to the catalyst concentration (**Figure 32c** and **d**). Interestingly, a linear dependency on catalyst concentration is observed for [Ru(bda)bpb]$_3$ **46** providing evidence for first-order reaction kinetics in the rate-determining step (RDS) of oxygen evolution. These findings are in

strong contrast to the second-order reaction kinetics of reference [Ru(bda)(pic)$_2$] **5** which evolves oxygen *via* a dimeric ruthenium-oxo species (I2M mechanism). Therefore, the rate-determining steps for catalytic water oxidation differ between the two systems. The kinetics in regard to the oxidant under this experimental setup was found to be of zeroth-order as expected for such a high oxidant excess (>1·10^5 CAN equiv., not figured).

The pressure transducer setup requires large evolved gas amounts and thus is not suitable to determine smaller stoichiometric CAN quantities and thus the dependency of the rate low on [Ce^{4+}]. Therefore, the methodology was changed to a "Ce^{4+} absorption decay" assay in which the Ce^{4+} absorption at 360 nm is monitored over time to follow the Ce^{4+} concentration. In a typical experiment a freshly prepared CAN solution is placed in a cuvette, afterwards a certain amount of catalyst **46** in a negligible amount of solvent is added, shaken and immediately positioned into the UV/Vis spectrometer to determine the absorbance at 360 nm overt time. Due to the ongoing water oxidation catalysis in the cuvette the absorption of Ce^{4+} decreases (**Figure 33a**).

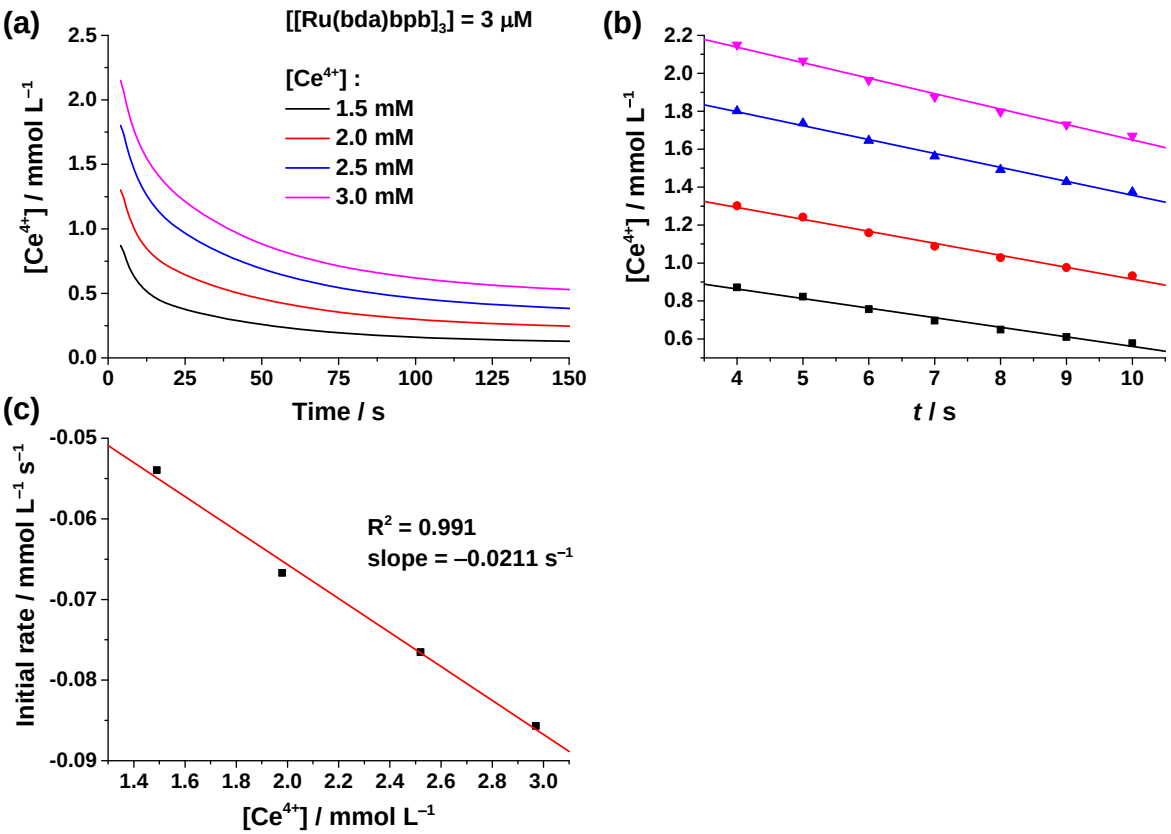

Figure 33 Ce^{4+} absorbance decay at 360 nm depending on different Ce^{4+} concentrations over 150 s (a) and between 4 and 10 s (b). Conditions: [[Ru(bda)bpb]$_3$] = 3 µM in 1:1 CH_3CN/water (pH 1) at 25 °C. (c) Initial rate of the Ce^{4+} consumption *vs* Ce^{4+} concentration with the corresponding linear regression fit. The change of absorbance was transferred to the consumption of Ce^{4+} according to the Lambert-Beer law (λ_{360} = 760 M^{-1} cm^{-1}, 1 cm path length of cuvette).

The concentration of Ce^{4+} can be calculated with the help of the Lambert-Beer law ($A=\lambda\cdot\varepsilon\cdot d$, d = path length of the cuvette). Accordingly, at moderate Ce^{4+} concentrations (excess of 200 to 1000 eq) the water oxidation catalysis for $[Ru(bda)bpb]_3$ **46** becomes first-order both in catalyst and in cerium(IV) ammonium nitrate concentration ($[Ce^{4+}]$ variation is shown in **Figure 33**, [**46**] variation is not figured).

Kinetic isotope effect. To verify whether a proton-coupled process is involved in the RDS of the catalytic cycle, the rates for water oxidation of both catalysts in H_2O and D_2O were compared. Primary kinetic isotope effects (KIE) which result from direct O–H/D bond breaking during the RDS of the catalytic process normally exhibit reaction rates that differ at least by a factor of 2 in H_2O and D_2O.[150] By quantifying the initial rates at different catalyst concentrations the reaction velocities in H_2O (k_{H2O}) and D_2O (k_{D2O}) were determined (**Figure 34**).

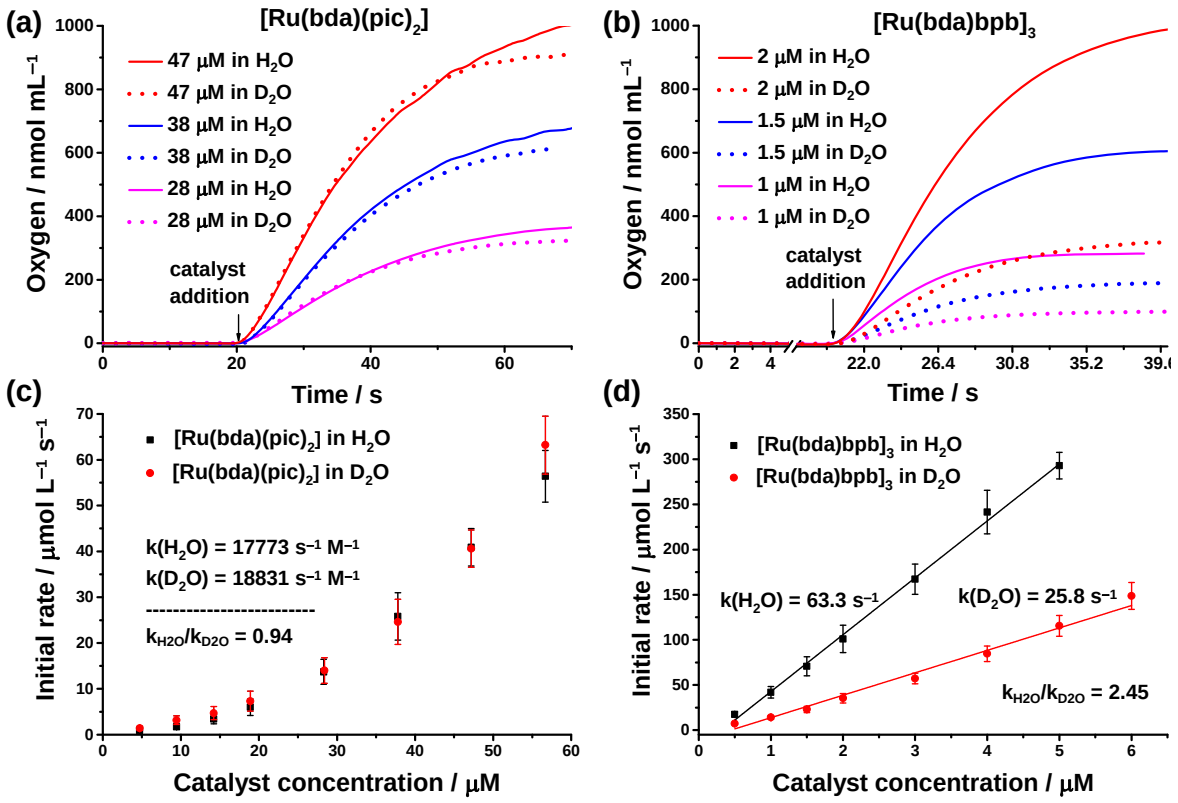

Figure 34 (a) and (b) Oxygen evolution *vs* time during the water oxidation with $[Ru(bda)(pic)_2]$ **5** and $[Ru(bda)bpb]_3$ **46** , respectively, as catalyst at varying catalyst concentrations in 2.0 mL aqueous pH 1 solutions (H_2O or D_2O) with 59% CH_3CN content using CAN (0.525 M) as a sacrificial oxidant measured with a Clark-type electrode setup. (c) Plot of the initial catalytic rates *vs* the concentration of **5**. The individual reaction rates k_{H2O} and k_{D2O} were obtained by plotting the initial rate *vs* the square of catalyst concentration (not figured). (d) Plot of the initial catalytic rates *vs* the concentration of **3** with the corresponding linear regression fits to determine the reaction rates k_{H2O} and k_{D2O}. The error bars were estimated by the maximum volumetric error during sample preparation and catalyst injection.

The initial rate *vs* catalyst concentration plot of [Ru(bda)(pic)$_2$] **5** displays the expected quadratic curve typical for bimolecular reactions (**Figure 34c**) confirming the previously established I2M mechanism.[37] Linearization of the rate dependence on [Ru(bda)(pic)$_2$] concentration was achieved by plotting the initial rate *vs* the square of catalyst concentration (not figured). The resulting linear regressions are equivalent to reaction rates (in s^{-1} M^{-1}) and the KIE quotient of k_{H2O}/k_{D2O} is 0.94 for [Ru(bda)(pic)$_2$] proving no proton involvement in the RDS. In contrast, for [Ru(bda)bpb]$_3$ **46** the measured oxygen evolution rates in heavy water are significantly reduced giving rise to a KIE of 2.45 (**Figure 34b** and **d**), providing unequivocal evidence for the direct hydrogen abstraction in the RDS.

Mechanistic scheme of the two possible pathways of water oxidation, WNA and I2M. According to the kinetic and H/D isotope labeling experiments the RDS of the water oxidation using macrocyclic [Ru(bda)bpb]$_3$ **46** as the catalyst is (i) first-order in catalyst concentration, (ii) first-order in Ce^{4+} concentration and (iii) characterized by an O–H bond breaking process. These findings are opposed to the water oxidation reaction catalyzed by [Ru(bda)(pic)$_2$] **5** which is (i) second-order in catalyst, (ii) zeroth-order in oxidant and (iii) proton uncoupled in the rate-determining step.[36] Accordingly, the RDS with [Ru(bda)(pic)$_2$] as catalyst can only be the bimolecular reaction step (4´) in **Scheme 7** summarizing the possible reaction pathways of the water oxidation, WNA and I2M.

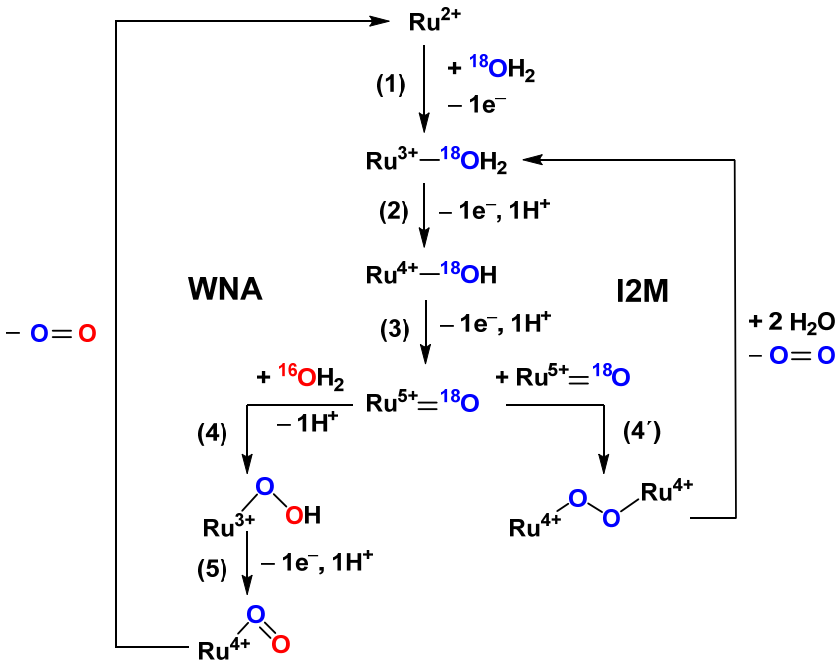

Scheme 7 Mechanistic representation of the possible reaction pathways of the catalytic water oxidation, WNA and I2M, with [Ru(bda)bpb]$_3$ **46** as catalyst. The color code of the oxygens represents a simplified ^{18}O-labeling experiment which was performed and evaluated in **Table 2**.

In contrast, in the case of $[Ru(bda)bpb]_3$ as catalyst the reaction steps (2), (3) and (5) fulfil the formal requirements outlined before. Interestingly, this implies that the common rate-determining steps of water nucleophilic attack (4) as well as the bimolecular coupling of two Ru^{5+}=O centers (4′) can be excluded.

In the optical redox titration experiment (**Figure 28**) it was observed that an additional oxidation of Ru^{4+} centers in the macrocycle by excess of CAN oxidant leads to no further change in the absorption indicating that a $[Ru^{4+}–OH]_3^{3+}$-resting state is very likely. Accordingly, the reaction step (3) in the catalytic scheme would be rate-determining. To support this assumption an experiment similar to the optical redox titration was performed in which not the absorption change but the real evolved oxygen amount is analyzed. In a Clark-type electrode setup which measures directly the amount of produced oxygen by an electrochemical method (for details see *Experimental Section*) a freshly prepared $[Ru^{3+}–OH_2(bda)bpb]_3^{3+}$ solution (green) was stepwise titrated by the addition of one equivalent of CAN per entire macrocycle (**Figure 35**).

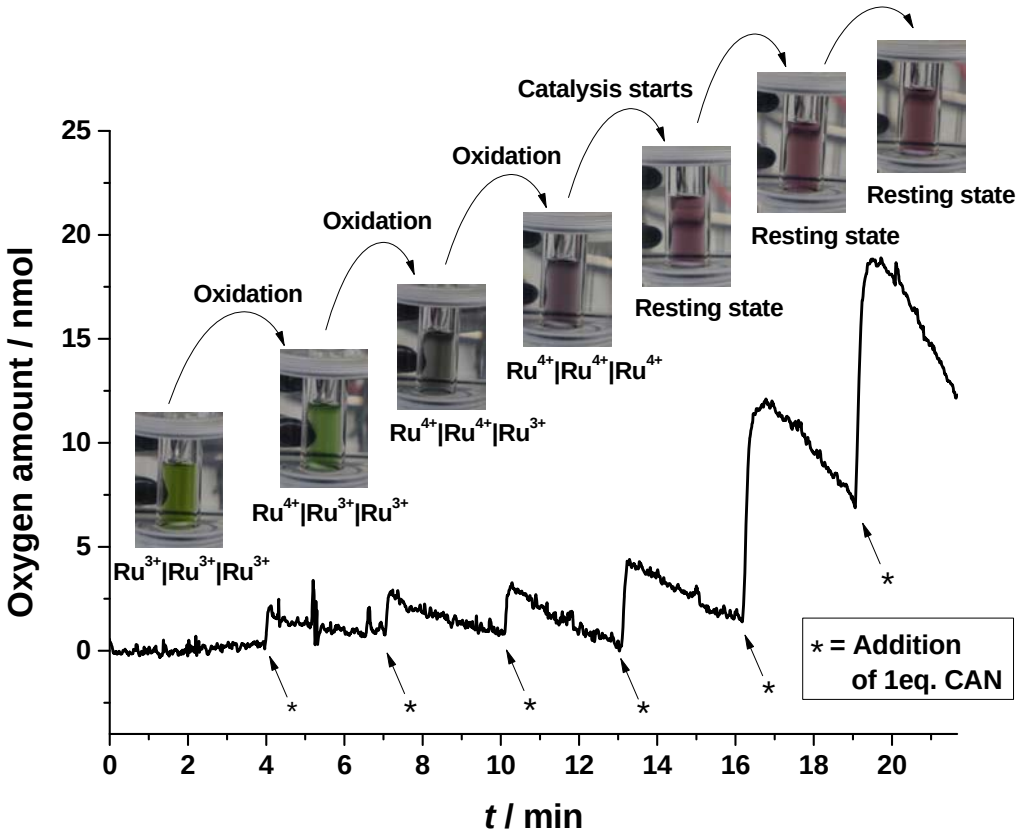

Figure 35 Monitoring of the oxygen evolution (detection by a Clark-type electrode) in the process of a redox titration of $[Ru^{3+}–OH_2(bda)bpb]_3^{3+}$ $\mathbf{46}^{3+}$ (fully oxidised to Ru^{3+} by air, see **Figure 27**) with cerium(IV) ammonium nitrate (CAN) as oxidant. Conditions: in 2 mL 1:1 CH_3CN/water (pH 1), [$\mathbf{46}^{3+}$] = 0.1 mM, [CAN] = 20 mM, 10 μL CAN corresponds to 1 equiv. CAN with regard to $\mathbf{46}^{3+}$.

The first three Ce^{4+} additions lead to only minor oxygen formations caused by local overoxidation at the injection spot. However, after the violet $[Ru^{4+}–OH]_3^{3+}$-species is generated the oxygen production per CAN addition increases strongly and becomes reproducible after every injection. This observation confirms that the $[Ru^{4+}–OH]_3^{3+}$-species is the last stationary state before the O-O forming water oxidation takes place. Therefore, the unambiguous differentiation between the WNA and I2M mechanism becomes obviously more elaborate since reaction step (3) is shared by both catalytic pathways and thus kinetic investigations cannot distinguish between the two mechanisms.

^{18}O isotope labeling experiment. The $[Ru^{4+}–OH]_3^{3+}$-resting state provides the possibility to distinguish the WNA and I2M mechanism by an ^{18}O-labeling experiment. The realization of such a labeling experiment is depicted in **Scheme 7** in a simplified way. In a typical experiment the procedure is as followed: First the catalyst is dissolved in almost quantitative ^{18}O-labeled water and then oxidized by an excess of CAN oxidant. Due to the stability of the metal hydroxide bond in the Ru^{4+} state the catalyst is quantitatively transformed into a persistent $[Ru^{4+}–{}^{18}OH]_3^{3+}$-species. Afterwards, additional oxidant which is dissolved in purely ^{16}O-labeled water is added to the catalyst so that only one catalytic cycle per macrocycle (1/3 of the Ru centers) can take place. Accordingly, in the case of water oxidation under I2M nearly 100% $^{36}O_2$ should be evolved and in the case of water oxidation under WNA a statistical mixture of the different oxygen isotopes depending on the ^{18}O-labeling degree of the resulting solvent mixture should be formed (see **Table 2**).

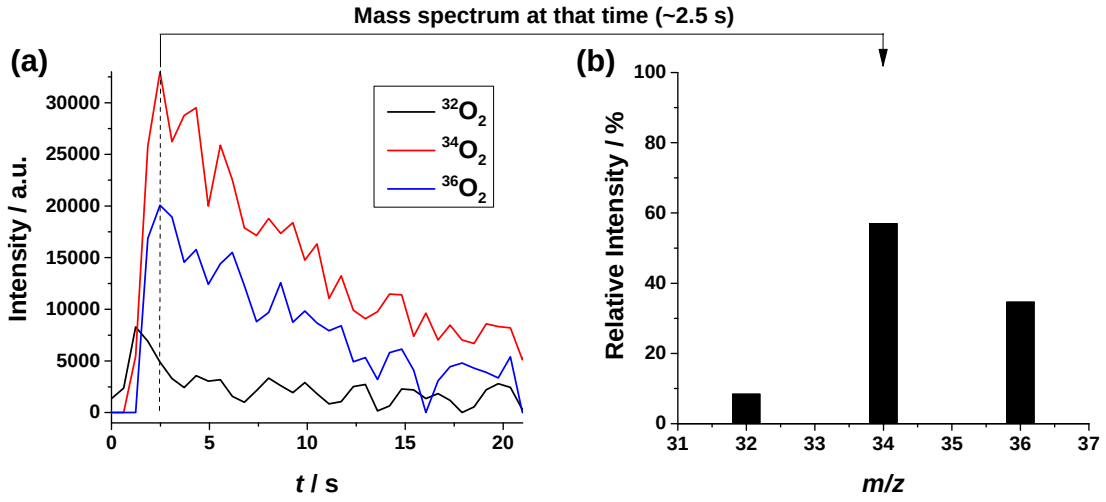

Figure 36 (a) Ion counts of the oxygen isotopes $^{32}O_2$, $^{34}O_2$ and $^{36}O_2$ obtained by mass spectrometry after the Schott Produran® tap was opened which separated the reaction vessel and the mass spectrometer. (b) The mass spectrum in the range between 31 and 37 *m/z* at 2.5 s which corresponds to the time after the Schott Produran® tap was opened. For experimental details see *Experimental Section*.

The resulting gas mixture can be analyzed by mass spectrometry and delivers the relative concentrations of the three oxygen isotopes (**Figure 36**, for details see *experimental section*). The experimentally found results of [Ru(bda)bpb]$_3$ are in close proximity to the theoretical values of WNA (**Table 2**) and thus demonstrate that this mechanism is the only operable reaction pathway for the macrocyclic architecture. In contrast, the analogous experiment with the reference catalyst [Ru(bda)(pic)$_2$] **5** showed that the Ru^{4+}–^{18}OH label is not stable in this case and no mechanistic conclusions can be obtained.

Table 2 Relative isotopic ratios of O_2 evolved from the first catalytic cycle at a certain degree of ^{18}O-labeling of the catalyst and the solvent, along with the calculated values assuming different reaction mechanisms.[a]

^{18}O-labeling / %[b]		Entry (catalyst)	Isotope ratios		
Catalyst	Solution		$^{16}O_2$	$^{16}O^{18}O$	$^{18}O_2$
97	43	**Fast label exchange**[c]	35.5	49	18.5
		WNA[d]	1.7	56.6	41.7
		I2M[e]	0.1	5.8	94.1
		1 ([Ru(bda)bpb]$_3$ **46**)	5.6	61.9	32.4
		2 ([Ru(bda)bpb]$_3$ **46**)	9.5	57.8	32.7
		3 ([Ru(bda)bpb]$_3$ **46**)	7.7	58.8	33.5
		∅	7.6	59.5	32.9
		4 ([Ru(bda)(pic)$_2$] **5**)	35.2	46.8	18.0

[a] See *Experimental Section* for experimental details. [b] These values indicate the degree of ^{18}O-labeling of the catalyst and the solvent. [c] Expected ratios in case of a fast O atom exchange between the catalyst and the solvent. [d] Expected ratios for the mechanism involving a nucleophilic attack of a solvent water to the O atom at the Ru^{5+}=O group. [e] Expected ratios for the mechanism involving a bimolecular mechanism with an oxygen-oxygen coupling from two Ru^{5+}=O groups of different catalyst molecules.

Classification of the results and theoretical considerations. Although this is not the first example of a structural modification to the [Ru(bda)L$_2$] catalyst instigating a change from the I2M to WNA oxygen evolution mechanism, the tremendous acceleration of the rate from 0.04 – 0.1 s^{-1} typically found for WNA-[Ru(bda)L$_2$] catalysts to 155 s^{-1} (chemically driven at pH 1) is unprecedented.[139, 140] Therefore, [Ru(bda)bpb]$_3$ **46** obviously enables a very low activation barrier water nucleophilic attack (step (4) in the WNA mechanism in **Scheme 7**) by activating a water molecule and thus the rate-determining step is shifted from the nucleophilic attack of water at Ru^{5+}=O to an earlier reaction step. This closely resembles many enzymatic processes in which natural systems like the oxygen-evolving complex of photosystem II (OEC-PSII) modulate the reactivity of water molecules for particular reactions by pre-organizing them appropriately.

When a proton coupled electron transfer process is involved in the rate-limiting step of a reaction it is possible to enhance the catalytic activity by adding a base to accept protons.[146] Nature´s water oxidation system OEC-PSII makes use of this principle where the protein residue acts as a proton-accepting unit.[24, 27] Therefore, it is hypothesized that within the macrocyclic cavity of $[Ru(bda)bpb]_3$ **46** a defined arrangement of water molecules exists where adjacent subunits are involved in the catalytic pathway by pre-organizing water molecules and/or acting as a proton acceptor. A DFT geometry optimized structure of the macrocycle **46** with three Ru^{4+}-OH units containing water molecules inside its cavity rationalizes this assumption (**Figure 37** , for details see *experimental section*). Based on the structure it could be estimated that up to 10 water molecules fit into the void and roughly three water molecules are required to bridge the gap between two [Ru(bda)] units. Interestingly, Llobet and co-workers identified a similar hydrogen bond network consisting of three water molecules to significantly lower the transition state energy in the rate-limiting O–O bond formation step of a WNA operating ruthenium WOC with quantum theoretical calculations.[151]

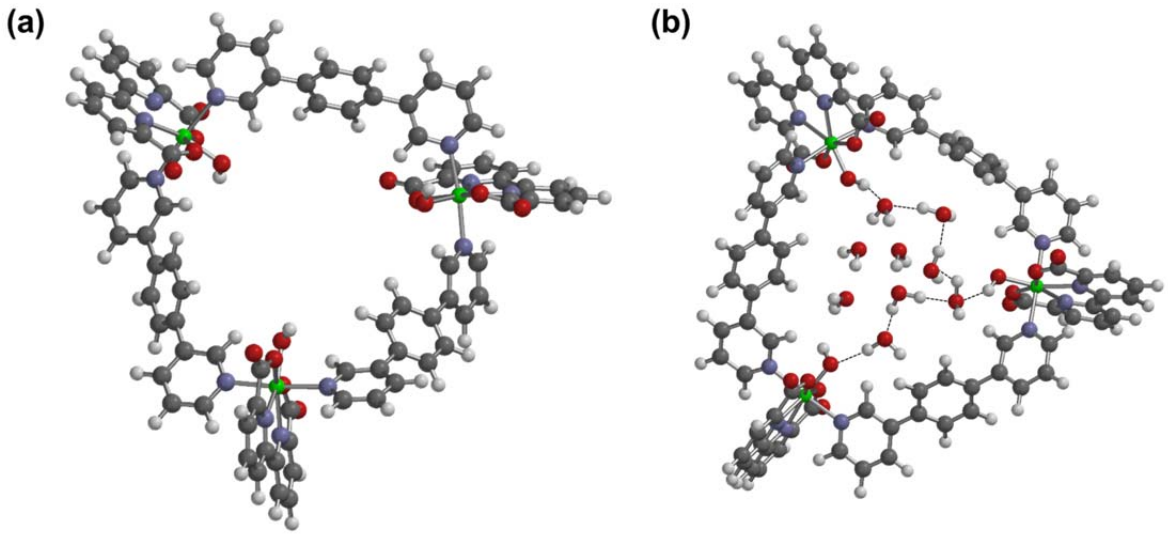

Figure 37 DFT optimized structure of $[Ru^{4+}\text{-}OH(bda)bpb]_3^{3+}$ without (a) and with cavity-embedded water molecules (b). Color code for DFT optimized structures: carbon: grey, hydrogen: white, oxygen: red, nitrogen: purple, ruthenium: green. For details see *Experimental Section*.

3.1.5 Photocatalytic Water Oxidation

Having established the superior catalytic activity of $[Ru(bda)bpb]_3$ **46** with Ce^{4+} as oxidant, the macrocycle was next applied to photocatalytic water oxidation which is of particular interest for sustainable energy production because sun light provides an inexhaustible energy source.[5] Hence, the water oxidation capability of **46** was investigated under photo-driven oxidation conditions with $[Ru(bpy)_3][Cl]_2$ as the photosensitizer and $Na_2S_2O_8$ as the sacrificial electron acceptor. The mechanistic details of this three-component light-driven water oxidation are illustrated in **Figure 38a** and indeed relate closely introductory the mononuclear catalyst $[Ru(bda)pic_2]$ **5** discussed in the introduction (**Figure 8**).

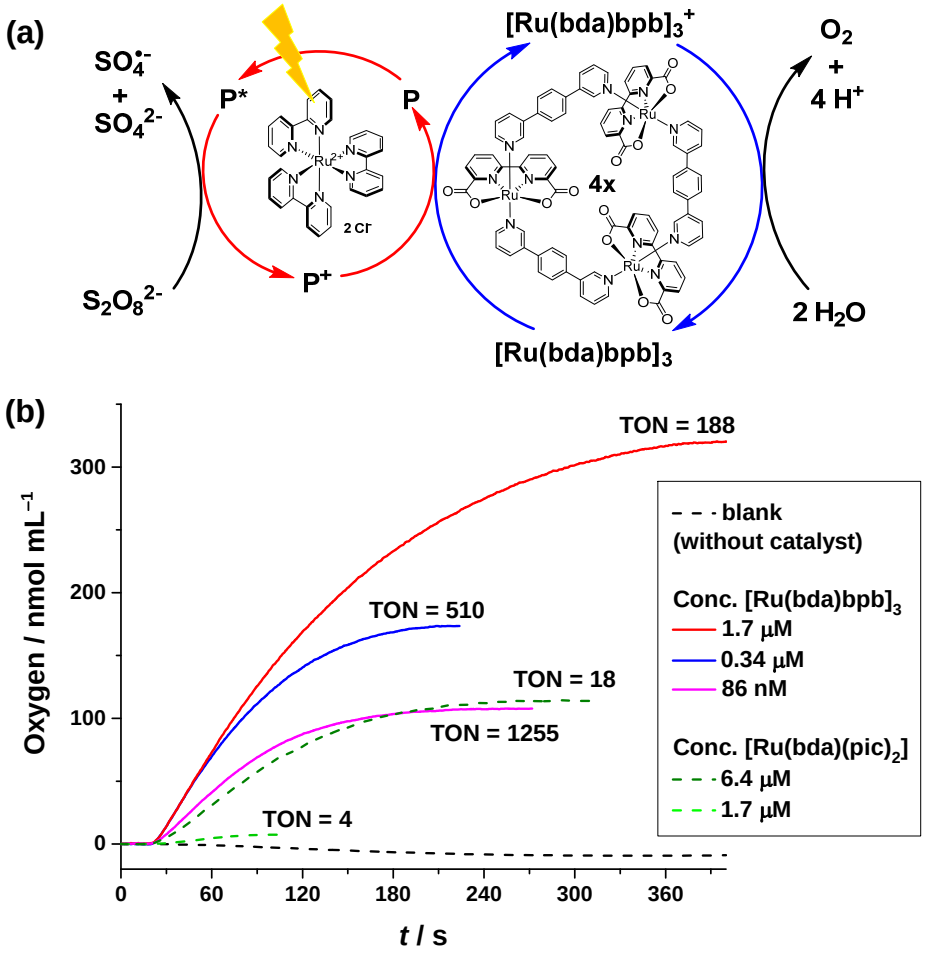

Figure 38 (a) Scheme of light-induced water oxidation with $[Ru(bda)bpb]_3$ **46** as WOC, $[Ru(bpy)_3][Cl]_2$ **8** as photosensitizer (P) and $Na_2S_2O_8$ as sacrificial electron acceptor. To preserve the simplicity of the schematic representation, the oxidation cycle of $[Ru(bda)bpb]_3$ **46** contains only the two redox states $[Ru^{2+}(bda)bpb]_3$ and $[Ru^{3+}(bda)bpb]_3^+$. A more appropriate scheme has to include the proton-coupled electron transfer processes of the higher oxidation states of ruthenium (Ru^{3+}, Ru^{4+} and Ru^{5+}) in which water is coordinated to the ruthenium center as well. (b) Oxygen evolution curves of photocatalytic water oxidation experiments with varying $[Ru(bda)bpb]_3$ **46** and $[Ru(bda)(pic)_2]$ **5** concentrations measured with a Clark-type electrode set-up in 2 ml 1:1 CH_3CN/phosphate buffer (pH 7.2) solution ($[Na_2S_2O_8]$ = 37 mM, $[[Ru(bpy)_3][Cl]_2$ = 1.5 mM, λ_{irr} >380 nm at 230 mW cm^{-2}). Irradiation of the sample started after 25 s.

Gratifyingly, evolution of oxygen bubbles was immediately evident upon illuminating a solution containing all three components in a 1:1 acetonitrile/phosphate buffer (pH 7.2) mixture. Catalytic activity of the macrocycle **46** is observed down to a nM concentration regime (~90 nM), and under such conditions remarkable TON and TOF values of >1255 and >13.1 s^{-1}, respectively, are obtained (**Figure 38b**). No gas evolution was detected at similar dilutions within the same photocatalytic experiment using the mononuclear [Ru(bda)(pic)$_2$] **5** complex. At a concentration of 6.4 μM, roughly two orders of magnitude higher than in the case of [Ru(bda)bpb]$_3$ **46**, the reference catalyst gives a maximum TON of 18 and a TOF of 0.13 s^{-1}. This extreme performance difference under dilute conditions is a consequence of the unimolecular WNA reaction mechanism accessible solely to the macrocyclic system. Only unimolecular catalytic systems are capable of such activity under high dilution because diffusion-limited collision of two catalytic subunits, essential for bimolecular mechanisms, becomes unnecessary. Therefore, **46** shows its exceptional potential as water oxidation catalyst best under light-driven conditions at high dilution.

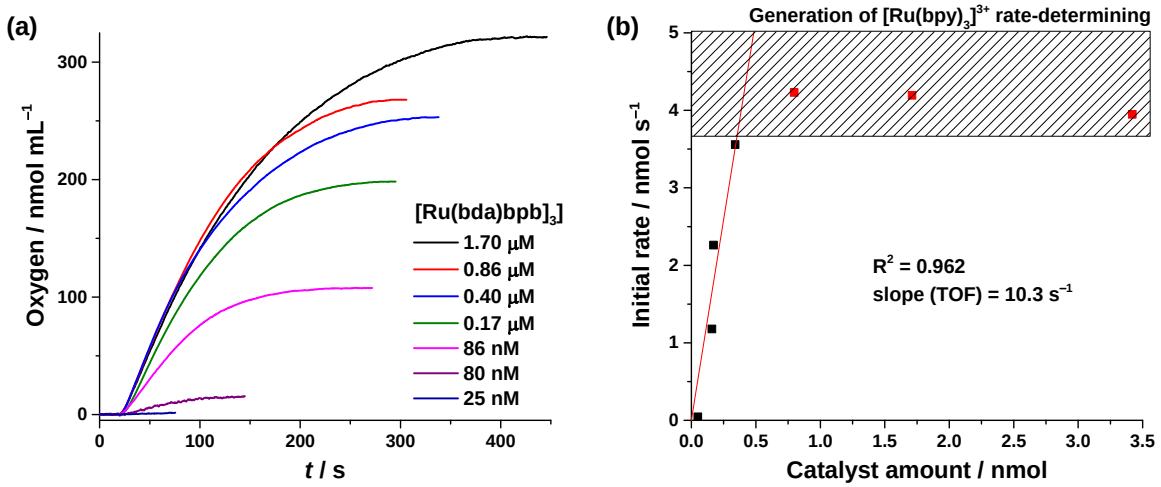

Figure 39 (a) Oxygen evolution curve of the photocatalytic water oxidation with varying [Ru(bda)bpb]$_3$ **46** concentrations measured with a Clark-type electrode setup in 2 mL 1:1 CH_3CN/phosphate buffer (pH 7.2) solution ([$Na_2S_2O_8$] = 37 mM, [[Ru(bpy)$_3$][Cl]$_2$] = 1.5 mM, λ_{irr} >380 nm with 230 mW/cm^2). Irradiation of the sample started after 25 s. (b) Plots of the initial catalysis rate *vs* the catalyst amount. The individual reaction rates were obtained by a linear fitting procedure of the first 20 s of the catalysis (not figured). The first four data points were fitted by a linear regression to determine the TOF value. The shaded rectangular marks the zone where the generation of [Ru(bpy)$_3$]$^{3+}$ becomes rate-determining.

Additionally, concentration dependent photocatalytic water oxidation experiments were performed to verify the WNA mechanism not only by the improved dilution behavior of the macrocyclic catalyst but also by its reaction order in the rate-law (**Figure 39a**). Below a concentration of 0.17 μM the initial rate is not limited by the photogeneration of the

oxidant $[Ru(bpy)_3]^{3+}$ anymore but by the turnover rate of the catalyst itself.[152] The linear regression of this concentration range delivers first-order kinetics (**Figure 39b**) like for the chemically driven water oxidation experiments with CAN as an oxidant confirming the unimolecular rate-determining step in the catalysis. By this procedure the unprecedented high TOF (here 10.3 s^{-1}) can be reproduced making $[Ru(bda)bpb]_3$ one of the most active homogenous photocatalytic ruthenium water oxidation catalysts containing organic ligands reported to date.[11, 153, 154]

3.2 Azabenz-Annulated Perylene Derivatives[2]

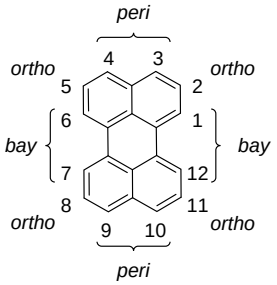

The reasons for hybrid systems out of organic dyes and inorganic metal complexes were sufficiently explained in section **2.2.3**. Perylene bisimide dyes are interesting candidates for the organic part in such hybrid conjugates. There are two main possibilities how to couple these dyes to metal centers: either in the PBI imide positions or in the *bay*-positions of the perylene core. In the following subchapter, the azabenz-annulation (ab) of the *bay*-position of perylene derivatives is presented as one option to create polypyridyl-fashioned perylene ligands for metal coordination.

3.2.1 Monoazabenz-Annulated Perylenes with Symmetric *peri*-Substitution[3]

The key step for the synthesis of azabenz-annulated perylene derivatives presented in this thesis is the Pictet-Spengler (PiSp) reaction (**Scheme 8**).

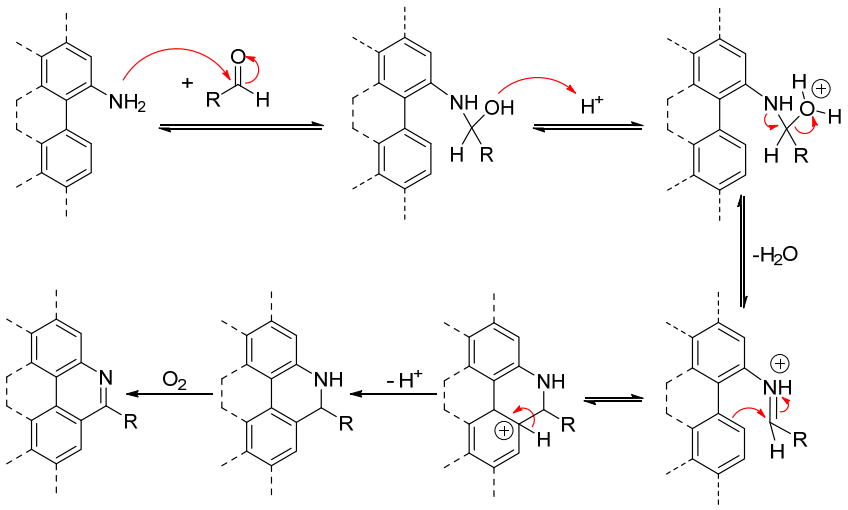

Scheme 8 Mechanism of the Pictet-Spengler reaction. The perylene core is indicated by the dashed lines.

Starting from amino-substituted perylene derivatives and the corresponding aldehydes, this Mannich-type transformation is initiated by an iminium ion formation followed by an intramolecular electrophilic aromatic substitution of the aromatic system by this iminium

[2] This section has been partly communicated in:
[155] M. Schulze, M. Philipp, W. Waigel, D. Schmidt, F. Würthner, *J. Org. Chem.* **2016**, doi:10.1021/acs.joc.1026b01573.

[3] The synthesis of ab-PBI **49c** was performed by Waldemar Waigel, Bachelor Thesis, Universität Würzburg **2014**.

ion.[156] After annulation of the perylene core, an oxidative rearomatization takes place to generate the fully π-extended system.[31]

The respective amino-functionalized perylene precursors can be obtained by well-established sequences of perylene core nitration (1- or 2-fold) and nitro group reduction to the amines.[157, 158, 159] However, for the synthesis of ab-PBIs **49a-f** (**Scheme 9**) containing up to three coordinating pyridyl subunits, a slightly modified procedure was developed because the synthetic PiSp protocol described in literature does not work for less reactive aldehydes. Therefore, (i) the equilibrium of iminium ion formation was shifted toward the product side by using dry *N,N*-dimethylformamide and adding molecular sieves (3 Å) to remove the released water; and (ii) after completion of iminium ion formation (~30 min) the inert atmosphere was exchanged by pure oxygen to facilitate the oxidative rearomatization. Thus, ab-PBIs **49a-f** could be obtained in yields of up to 57%, which is remarkably high for such systems.

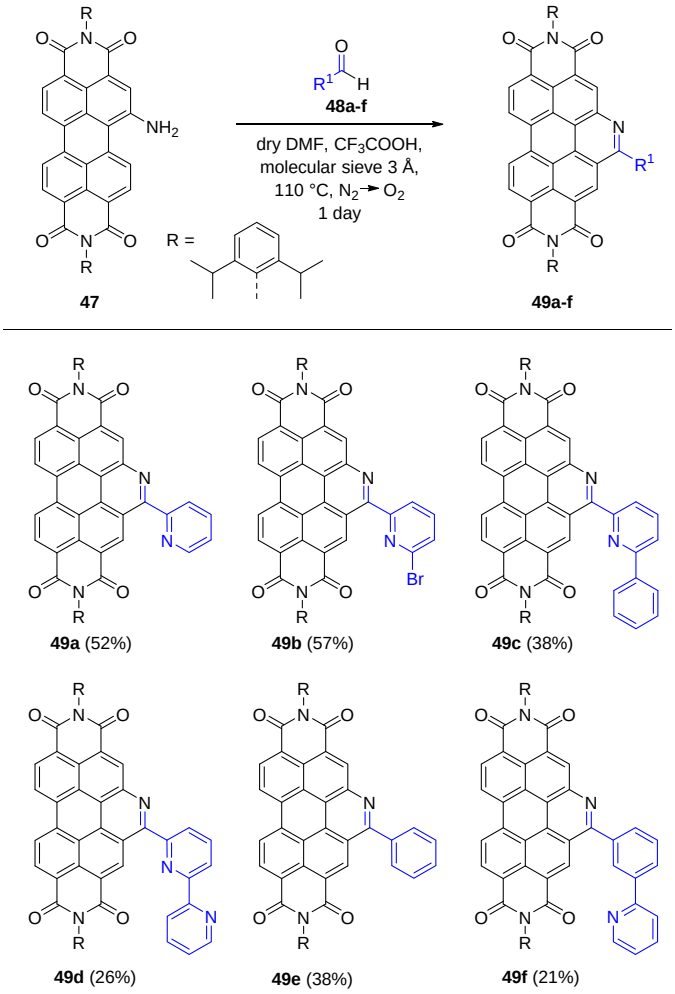

Scheme 9 Synthesis of ab-PBIs **49a-f** by Pictet-Spengler reaction of amino-PBI **47** with different aldehydes **48a-f**.

Whereas the functional properties of perylene bisimides are primarily encoded in the core substituents, the imide subunits are often used to manipulate properties like solubility or aggregation behavior in organic and aqueous media.[110] Frequently, the synthesis of such customized imide substituents is even more elaborate than the construction of the PBI framework itself because the substituent might be prone to oxidation, reduction and/or labile under PiSp reaction conditions. And if the preparation is successful, the amount of material can often be limited to a few milligram. Therefore, an alternative synthetic procedure (**Scheme 10**) for the preparation of ab-PBIs bearing complex functional imide substituents in which the imidization is the final step of the entire synthesis was established.

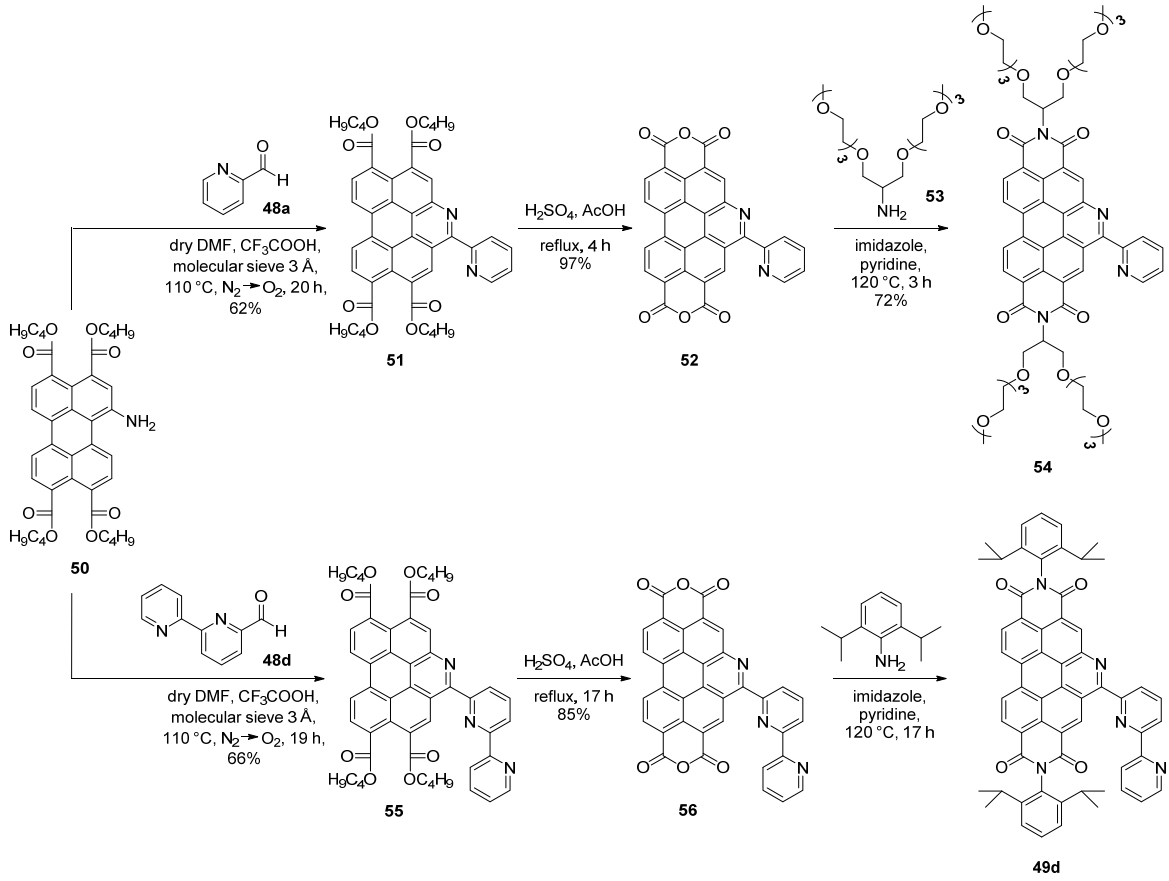

Scheme 10 Synthetic protocol for the preparation of the azabenz-annulated perylene bisanhydrides ab-PBA **52** and **56** and their imidizations using the customized amine derivative **53** and 2,6-diisopropylaniline, respectively.

The key intermediate of this pathway is the azabenz-annulated perylene bisanhydride (*e.g.* ab-PBA **52**) which constitutes a versatile starting material in this route. However, anhydride formation can be a tedious procedure starting from perylene bisimides (usually strong bases like KOH in refluxing alcohols are required) and is much more efficient from

perylene tetraesters (PTE, usually organic acids in refluxing hydrocarbons are utilized).[160, 161] Thus, using the modified PiSp reaction protocol described above, the amino-PTE **50**[162] known from literature was converted with pyridine-2-carboxaldehyde **48a** into the bright-yellow ab-PTE **51** in 62% yield. Subsequently, the ester groups of **51** were hydrolyzed under acidic conditions to yield almost quantitatively the azabenz-annulated bisanhydride ab-PBA **52**. Like many other perylene bisanhydrides, **52** is nearly insoluble in common organic solvents and is therefore difficult to characterize. However, ^{1}H and ^{13}C NMR spectroscopy in D_2SO_4 proved the absence of any aliphatic protons with an appropriate number of aromatic signals for the protons of the perylene core and the pyridyl functionality.

An exemplary imidization reaction of ab-PBA **52** with an oligoethylene glycol-functionalized amine **53** was used to demonstrate the advantages of this synthetic pathway. After reacting **52** with two equivalents of **53** in a mixture of molten imidazole and pyridine at 120 °C ab-PBI^{OEG} **54** could be isolated in a good yield of 72%. Starting from commercially available perylene bisanhydride, this protocol illustrates even more its superiority by virtue of a total yield of 27% for compound **54** that drops down to an overall yield of only 2% using the conventional procedure described in **Scheme 9**. That this route is also applicable to other terminal azabenz-annulated functionalities is outlined by the synthesis of ab-PBI **49d** *via* the ab-PBA **56**. Here the reaction steps were realizable in good yields of 66 and 85%, respectively.

3.2.2 Monoazabenz-Annulated Perylenes with Unsymmetric *peri*-Substitution[4]

To extend the scope of such azabenz-annulated perylene derivatives a synthetic procedure for the preparation of unsymmetrically *peri*-substituted analogues like the ab-perylene monoimide diester (ab-PMIDE) **60** was developed. These coordinating chromophores should be interesting starting materials for the fabrication of photoactive hybrid materials upon fixation to semiconducting surfaces like TiO_2. Accordingly, the regioselective nitration of unsymmetric perylene monoimide diester **57**[163] (**Scheme 11**) using cerium(IV)ammonium nitrate (CAN) and nitric acid as nitronium ion source[164, 165] yielded 1-nitro-PMIDE **58** in an excellent yield of 86% (for the numbering of the perylene core see

[4] The syntheses of 1-nitro-PMIDE **58**, 1-amino-PMIDE **59**, ab-PMIDE **60** and ab-PMIMA **61** were performed by Michael Philipp, Bachelor Thesis, Universität Würzburg **2015**.

PMIDE **57** in **Scheme 11**). Interestingly, under the applied reaction conditions (15 min at room temperature), only traces of 2-fold nitrated byproducts could be detected by mass spectrometry.

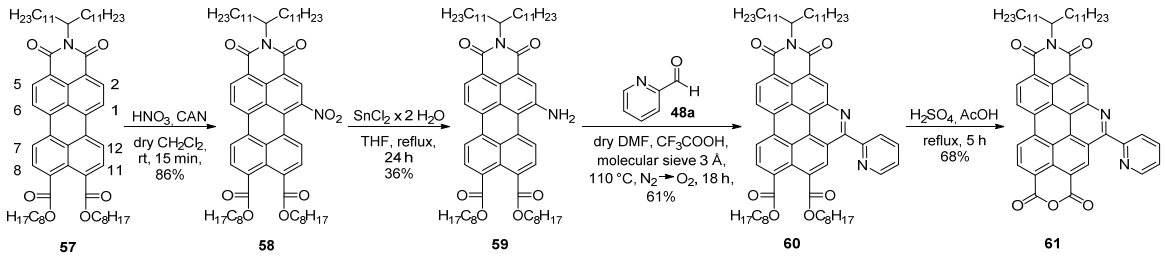

Scheme 11 Synthesis of unsymmetric ab-PMIDE **60** and ab-PMIMA **61** by regioselective nitration, nitro reduction and PiSp transformation of PMIDE **57**.

Besides the excellent yield, an exclusive regioselectivity could be confirmed for the mono-nitrated 1-nitro-PMIDE **58** by 1D and 2D NMR spectroscopy (**Figure 40**). It is noteworthy that the rotation of the "swallowtail" 12-tricosanyl ($CH(C_{11}H_{23})_2$) imide substituent around the C–N^{imide} bond is somewhat restricted at room temperature giving rise to broad resonances for the protons at the 2 and 5 positions.[166] Although this signal broadening usually hampers the interpretation of NMR data, it can here be used as a sensitive probe for the correct assignment of the regioselectivity. Accordingly, for the 1-nitro-substituted PMIDE isomer, broad resonances can be detected for the hydrogen atoms at the 2 and 5 positions beside sharp doublets for the protons at the 6, 7, 8, 11 and 12 positions (see ^{1}H NMR trace in **Figure 40a**), which exhibit appropriate $^3J_{HH}$ cross-signals. In contrast, for the corresponding 7-nitro-substituted regioisomer, a sharp singlet was expected for the hydrogen atom at the 8-position, which is absent in the proton NMR spectrum. Further evidence is provided by two-dimensional correlation spectra (^{1}H,^{13}C-HMBC and ^{1}H,^{1}H-NOESY, **Figure 40b** and **c**) where cross-signals between H^8/H^{11} and the carbonyl carbon atoms in the ^{1}H,^{13}C-HMBC spectrum and between H^8/H^{11} and H^c in the ^{1}H,^{1}H-NOESY spectrum confirm the structural assignment.

After reduction of the nitro group using tin(II)chloride as reductant, 1-amino-PMIDE **59** can be subjected to a PiSp transformation to isolate ab-PMIDE **60** in 61% yield. Subsequently, the ester functionalities of **60** can be hydrolyzed under acidic conditions to generate the corresponding anhydride ab-perylene monoimide monoanhydride (ab-PMIMA) **61**. Both diester **60** and monoanhydride **62** are versatile starting materials for the preparation of unsymmetrically imide-substituted azabenz-annulated perylene bisimides and can additionally be used to anchor such dye molecules onto semiconducting

surfaces.[167, 168, 169] These chromophores were fully characterized by ^{1}H and ^{13}C NMR spectroscopy, high-resolution mass spectrometry and UV/Vis spectroscopy, and their regioselective integrity was substantiated by 2D NMR spectroscopy.

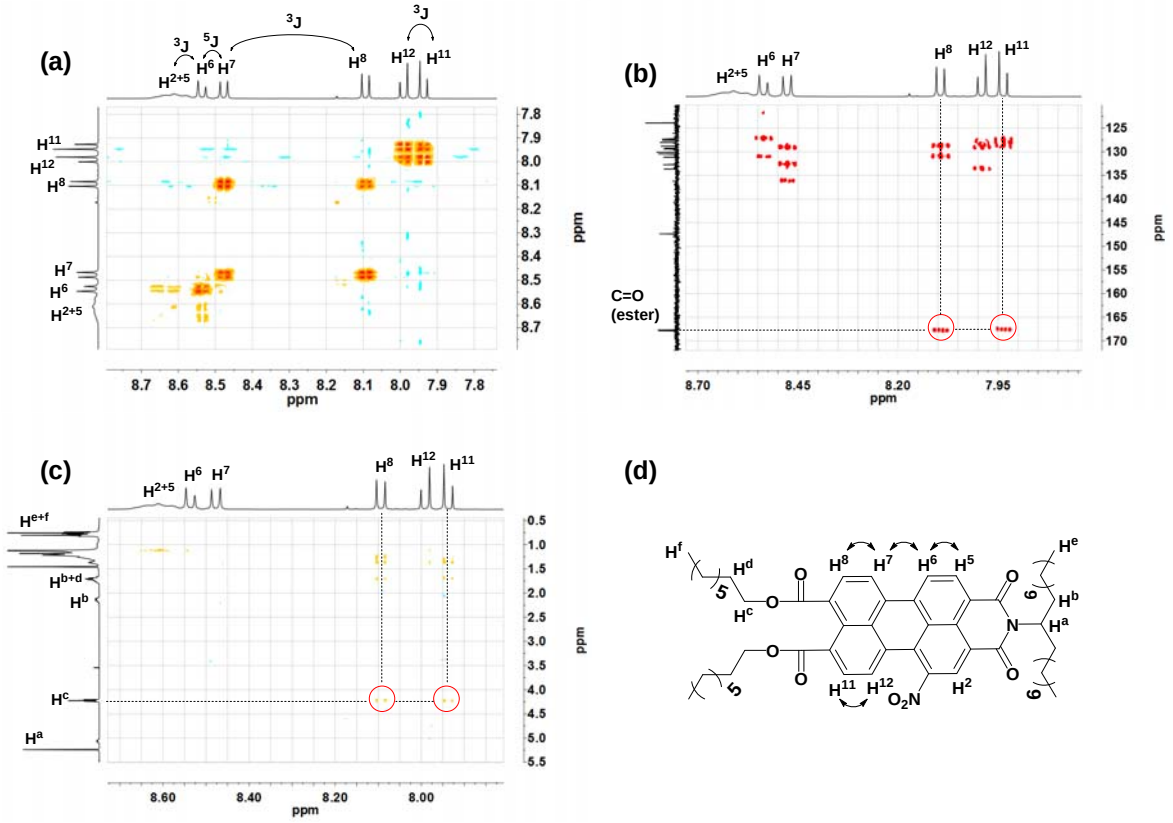

Figure 40 2D NMR correlation spectra of 1-nitro-PMIDE **58** in CD_2Cl_2 at room temperature (400 MHz). (a) $^{1}H,^{1}H$-COSY spectrum with assigned J_{HH} couplings. (b) $^{1}H,^{13}C$-HMBC spectrum. (c) $^{1}H,^{1}H$-NOESY spectrum. In the structure of **58** (d), the curved arrows indicate the cross couplings.

3.2.3 Bisazabenz-Annulated Perylenes

Whilst the azabenz-annulated perylene derivatives mentioned so far are capable of coordinating single transition metal centers, they do not provide access to multinuclear transition metal complexes with multiple redox active subunits.[112, 170, 171, 172] Therefore, the focus was put on bisazabenz-annulated systems, which have rarely been reported in the literature so far.[173] Starting from a 3:2 mixture of 1,7- and 1,6-diamino-substituted perylene bisimides **62** (**Scheme 12**, left), *anti*-(ab)$_2$-PBI **63** and *syn*-(ab)$_2$-PBI **64**[173] can easily be prepared according to the PiSp protocol described in subchapter **3.2.1**, and the regioisomers can be separated by column chromatography. Because of an elaborate purification process both molecules were isolated in only moderate yields of 23% and 14%, respectively, pursuant to the isomeric ratio of the diamino-substituted precursor. Similarly, the bisazabenz-annulated perylene tetraester *syn*-(ab)$_2$-PTE **66** was synthesized

by PiSp transformation of isomerically pure 1,6-diamino-PTE **65** in 37% yield (the corresponding 1,7-isomer could not be prepared as analytically pure material). After hydrolysis, the corresponding bisanhydride *syn*-(ab)$_2$-PBA **67** can be converted into any type of bisazabenz-annulated perylene bisimide as it has been illustrated by the imidization reaction with 2,6-diisopropylaniline to the corresponding *syn*-(ab)$_2$-PBI **64** (**Scheme 12**, right).

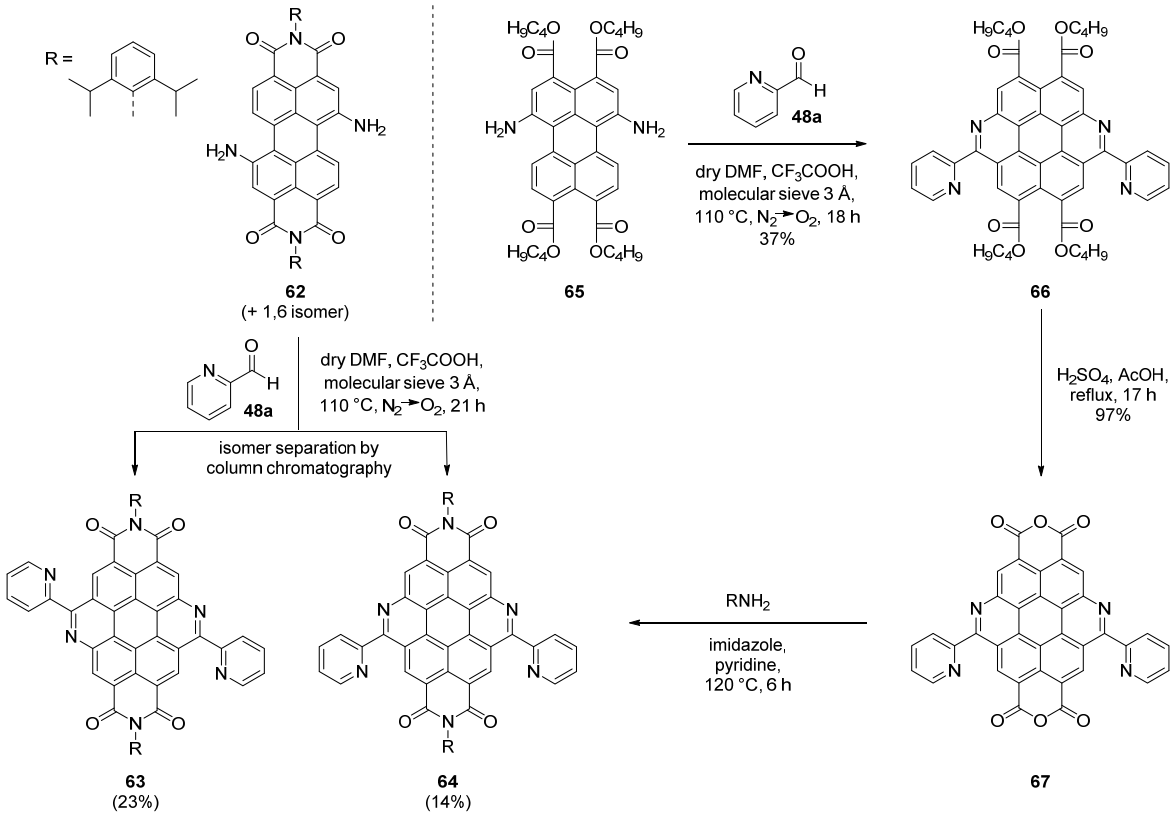

Scheme 12 Synthetic access to bisazabenz-annulated perylene derivatives (ab)$_2$-PBI **63** and **64** (left) and (ab)$_2$-PTE **66** (right).

Although *anti*-(ab)$_2$-PBI **63** and *syn*-(ab)$_2$-PBI **64** cannot be distinguished by high-resolution ESI mass spectrometry both isomers exhibit completely different dynamic behavior in solution revealed by temperature-dependent NMR spectroscopy in deuterated THF (**Figure 41**). Whereas *syn*-(ab)$_2$-PBI **64** is characterized by well-resolved NMR signals even at room temperature (295 K, **Figure 41** top), strongly broadened resonances can be detected for *anti*-(ab)$_2$-PBI **63** (middle), presumably due to the restricted rotation of the peripheral pyridine substituents. However, upon cooling to 233 K (bottom), the aromatic resonances sharpened gradually facilitating an unambiguous structural assignment.

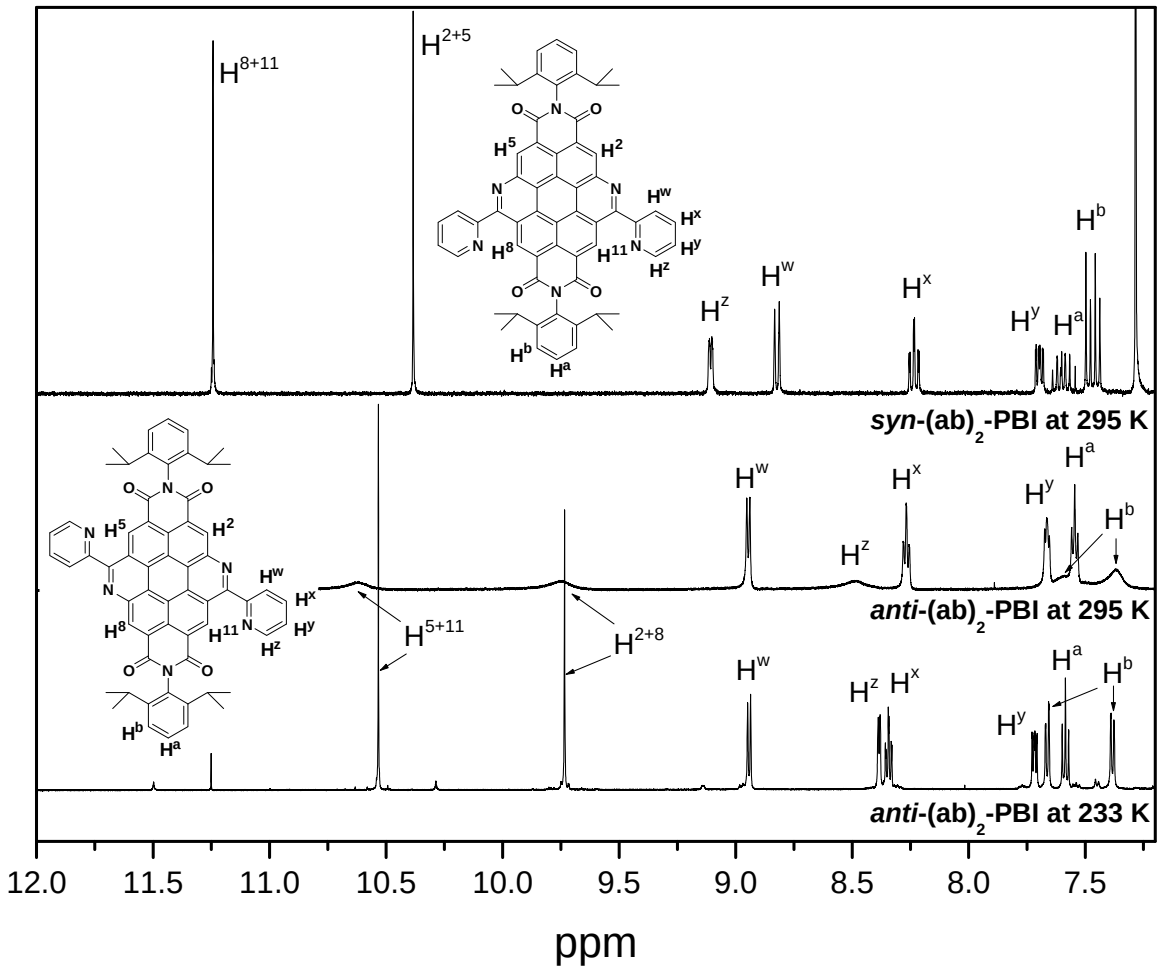

Figure 41 Comparison of the ^{1}H NMR spectra of *syn*-(ab)$_2$-PBI **64** at 295 K (top), *anti*-(ab)$_2$-PBI **63** at 295 K (middle) and 233 K (bottom) in d_8-THF (400 MHz).

Explicit structural evidence for the *anti*-bisazabenz-annulation in (ab)$_2$-PBI **63** is provided by X-ray diffraction experiments performed on single crystals grown from THF solutions (**Figure 42**).

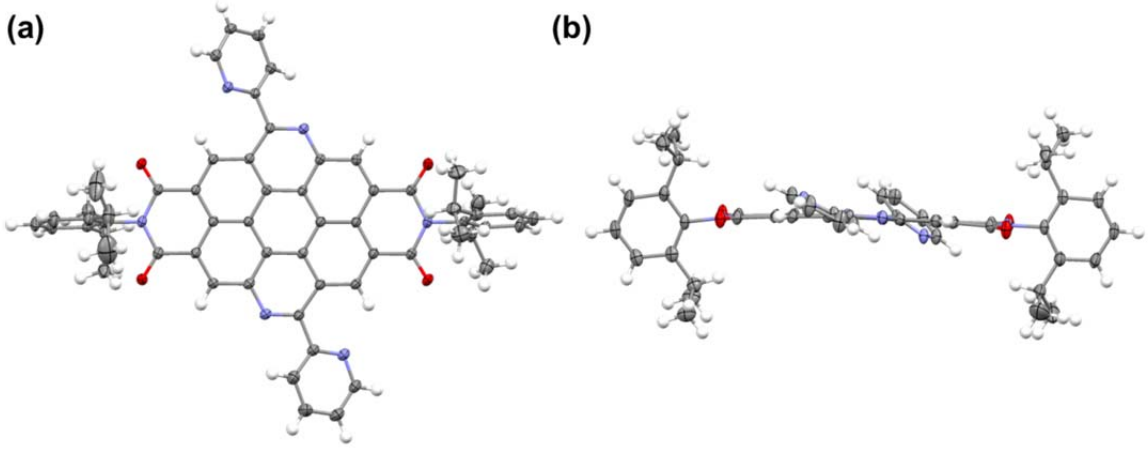

Figure 42 Crystal structure of *anti*-(ab)$_2$-PBI **63** in the solid state from top (a) and side views (b, ellipsoids set at 50% probability level; THF solvent molecules are omitted for clarity).

Apart from the *anti*-arrangement, $(ab)_2$-PBI **63** exhibits a completely flat aromatic core with both pyridyl substituents oriented out of the π-surface by 25° and 36°, respectively. Moreover, each bipyridine-like subunit is characterized by *transoid* oriented nitrogen atoms to minimize the electronic repulsion between the bipyridyl lone pairs. The length of the C–C bonds, which connect the pyridine substituents to the aromatic core (1.49 Å), is comparable with those of other 2,2′-bipyridine (~1.49 Å).[174] The whole single crystalline material is composed of well THF-solvated PBI dimers with no further extended π–π-stacking due to the perpendicular oriented 2,6-diisopropylphenyl imide functionalities, which efficiently prevent columnar π–π-stacking arrangements.

3.2.4 Functional Characterization of Ab-Perylene Derivatives

The variety of different azabenz-annulated perylene derivatives accomplished in this work enables a systematic comparison of their optical and redox properties (**Table 3)**. Two distinct effects can accordingly be studied based on this library of compounds: (i) The effect of perylene core-extension (1- and 2-fold) along the short molecular axis. (ii) The influence of the *peri*-substituents (imide, anhydride and ester functionalities) on the optoelectronic properties of monoazabenz-annulated perylenes.

Table 3 Summary of the optical and electrochemical data of different azabenz-annulated perylene derivatives.[a]

Compounds	λ_{abs} / nm (ε / 10^3 M^{-1} cm^{-1})		λ_{em} / nm	Φ_F	$E_{1/2}^{1st\ red}$ / V[b]	$E_{1/2}^{2nd\ red}$ / V[b]	E^{LUMO} / eV[c]	E^{HOMO} / eV[d]
	S_0–S_1	S_0–S_x	S_1–S_0					
PTE	471 (40.6)	353 (2.4)	486	0.98	–1.54	–1.79	–3.26	–5.85
ab-PTE (**51**)	430 (25.7)	319 (43.4)	440	0.41	–1.60	–1.88	–3.20	–6.06
syn-ab_2-PTE (**66**)	445 (1.8)	336 (119)	450	0.09	–1.68	–1.98	–3.12	–5.89
PBI	527 (94.7)	370 (5.8)	532	0.96	–0.99	–1.22	–3.91	–6.25
ab-PBI (**49a**)	475 (68.4)	333 (29.2)	484	0.69	–1.06	–1.34	–3.74	–6.33
anti-ab_2-PBI (**63**)	485 (20.5)	354 (85.0)	493	0.23	–1.13	–1.43	–3.67	–6.21
syn-ab_2-PBI (**64**)	478 (4.8)	355 (83.0)	485	0.22	–1.16	–1.44	–3.64	–6.21
ab-PBI (**49a**)[e]	475 (68.4)	333 (29.2)	484	0.69	–1.06	–1.34	–3.74	–6.33
ab-PMIMA (**61**)	469 (41.7)	322 (33.4)	478	0.50	–1.05	–1.31	–3.75	–6.37
ab-PMIDE (**60**)	454 (36.9)	318 (32.3)	468	0.77	–1.35	–1.64	–3.45	–6.15
ab-PTE (**51**)[e]	430 (25.7)	319 (43.4)	440	0.41	–1.60	–1.88	–3.20	–6.06

[a] Measured in dichloromethane at 298 K. [b] Measured with 0.1 M *n*-Bu_4NPF_6 and with Fc^+/Fc as a reference. [c] Energy of the lowest unoccupied molecular orbital E^{LUMO} in eV as calculated considering the energy level of Fc^+/Fc with respect to the vacuum level by using $E^{LUMO} = [-(E_{1/2}^{1st\ red}) - 4.8]$ eV. [d] Energy of the highest occupied molecular orbital E^{HOMO} in eV was calculated by using $E^{HOMO} = [E^{LUMO} - E^{opt.gap}]$, $E^{opt.gap}$ determined at the intersection of the absorption and emission spectra with the latter being normalized with respect to the lowest-energy absorption. [e] For comparison within a series, the data are repeated.

Absorption spectroscopy. Obviously, upon core extension, a hypsochromic shift of the S_0–S_1 transition band, referred to the parent PBI, can be observed that is less pronounced for the bisazabenz-annulated PTE **66** and its PBI analogues **63** and **64** (for PTE series see **Figure 43a**, PBI series not figured). Simultaneously, the oscillator strengths and the intensities of the S_0–S_2 transitions strongly increase with core extension because the S_0–S_2 transition dipole moments are aligned along the laterally elongated molecular axes. Therefore, the UV/Vis absorption spectra of *syn*-$(ab)_2$-PTE **66**, *syn*-$(ab)_2$-PBI **64** and *anti*-

$(ab)_2$-PBI **63** are not predominated anymore by the lowest energy S_0–S_1 transitions but by higher energy absorption bands with extinction coefficients of up to $\varepsilon = 119 \cdot 10^3$ M^{-1} cm^{-1}. Similar observations (hypsochromic shift of the absorption maximum and intensification of the S_0–S_2 transition) have already been reported by the groups of Nijegorodov, Adachi and Müllen for core-extended perylene derivatives (Nijegorodov: perylene, 1,12-benzoperylene and coronene; Adachi and Müllen: perylene bisimide, benzo[*g,h,i*]-perylene bisimide and coronene bisimide).[175, 176, 177] However, for the monoazabenz-annulated compounds ab-PBI **49a**, ab-PMIMA **61**, ab-PMIDE **60** and ab-PTE **51**, the S_0–S_1 transitions (longitudinally polarized along the N–N molecular axes) still exhibit enough oscillator strength, giving rise to intensive lowest energy absorption bands with well-resolved vibronic progressions (**Figure 43b**). Both chromophores **49a** and **61** have nearly the same conjugation length and are therefore characterized by similar absorption spectral features with a minor spectral shift of only 6 nm that can be ascribed to slightly different electronic properties (see electrochemistry below). However, the size of the fully π-conjugated system is gradually reduced from ab-PBI **49a** to ab-PMIDE **60** and ab-PTE **51**, resulting in hypsochromically shifted absorption spectra with lowest energy UV/Vis transitions located at 475, 454 and 430 nm, respectively. Thus, a blue-shift of approximately 23 nm per introduced diester functionality can be ascertained for the S_0–S_1 transitions with nearly unaffected higher energetic UV/Vis absorptions.

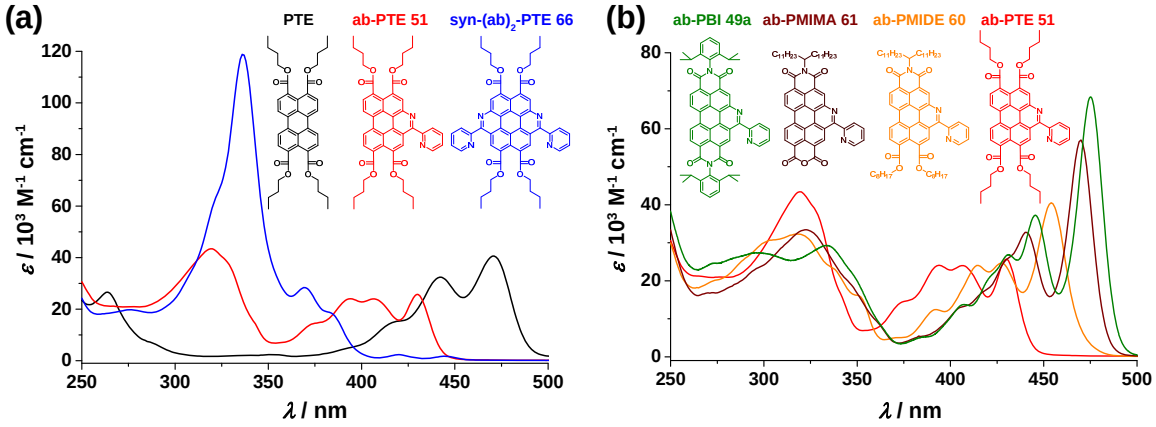

Figure 43 UV/Vis absorption spectra ($c = 1 \cdot 10^{-5}$ M) of the core-extended perylene tetraester series (a) and of the monoazabenz-annulated perylenes derivative series (b). All measurements were performed in dichloromethane at room temperature.

Fluorescence spectroscopy. The present perylene derivatives exhibit fluorescence emission out of the first excited singlet state with mirror images of the absorption vibronic fine structures and comparatively small Stokes shifts (**Figure 44**). However, azabenz-

annulation reduces the fluorescence quantum yield by 30–40% per annulation step due to reduced S_1–S_0 transition probabilities (*vide supra*).[178] Therefore, the bright fluorescence of PTE and PBI (quantum yields close to unity) is reduced to 41–69% for monoazabenz-annulated chromophores and diminishes to 9–23% for the bisazabenz-annulated derivatives (see **Table 3**). Interestingly, the ab-perylenes have emission lifetimes of ~3 ns except for the *syn*-configured molecules *syn*-(ab)$_2$-PBI **64** and *syn*-(ab)$_2$-PTE **66** with τ of 7.5 and 11 ns, respectively.

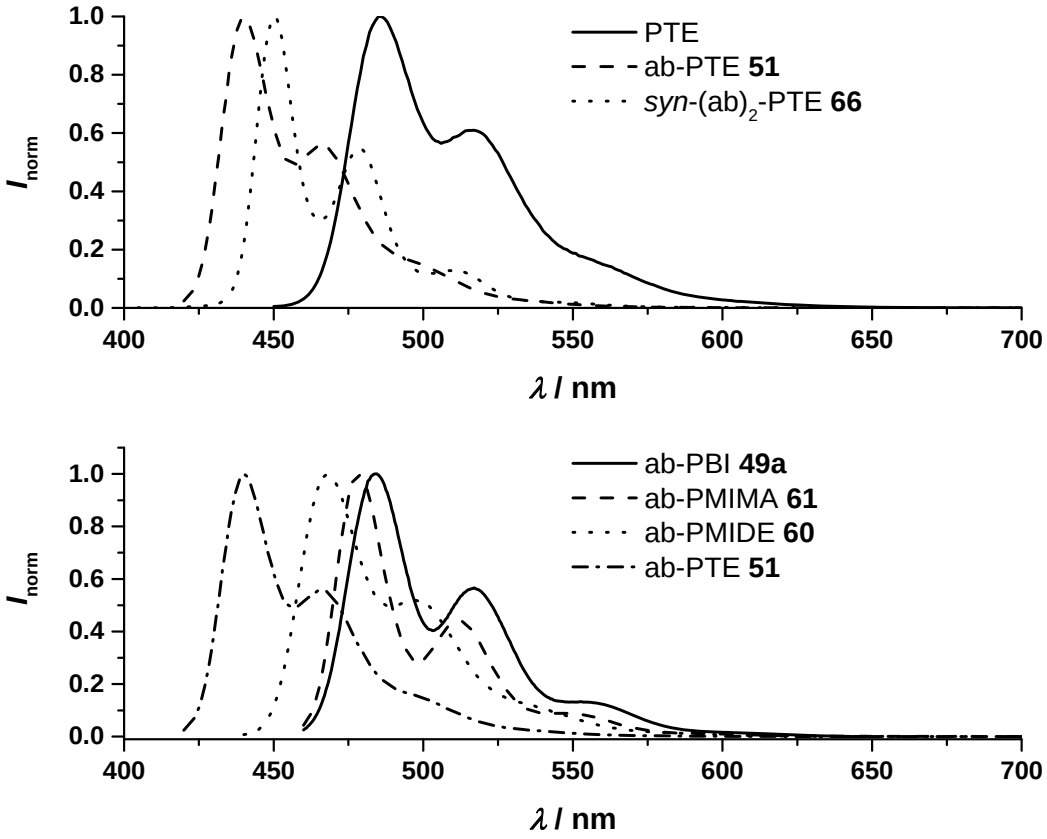

Figure 44 Normalized emission spectra of core-extended perylene tetraesters (top) and of the monoazabenz-annulated perylene derivatives (bottom) measured in dichloromethane at room temperature.

Electrochemistry. To experimentally assess the energies of the frontier molecular orbitals as a function of perylene core extension and *peri*-substitution, the reduction potentials of the individual chromophores were determined by cyclic voltammetry in dichloromethane using *n*-Bu_4NPF_6 as electrolyte and ferrocene as internal standard (see **Table 3**). Apparently, upon core annulation both reduction processes $E_{1/2}^{1st\ red}$ and $E_{1/2}^{2nd\ red}$ become gradually shifted to more negative values. Accordingly, azabenz-annulation disfavors reduction to mono- and dianionic species as it becomes evident by comparing both, the PTE (PTE, ab-PTE **51**, *syn*-(ab)$_2$-PTE **66**, **Figure 45a**) and the PBI series (PBI, ab-PBI

49a, *anti*-(ab)$_2$-PBI **63**, *syn*-(ab)$_2$-PBI **64**, not figured). In contrast, the reduction potentials of the monoazabenz-annulated systems are highly dependent on the electron accepting properties of the respective *peri*-substituents. Thus, with an increasing number of coplanar electron withdrawing subunits (ab-PTE **51** < ab-PMIDE **60** < ab-PMIMA **61** ≈ ab-PBI **49a**, **Figure 45b**) the two reduction processes are gradually shifted to more positive potentials. Altogether, an electrochemical window of 690 and 760 mV for the first and second reduction, respectively, can be covered by this library of azabenz-annulated perylene derivatives.

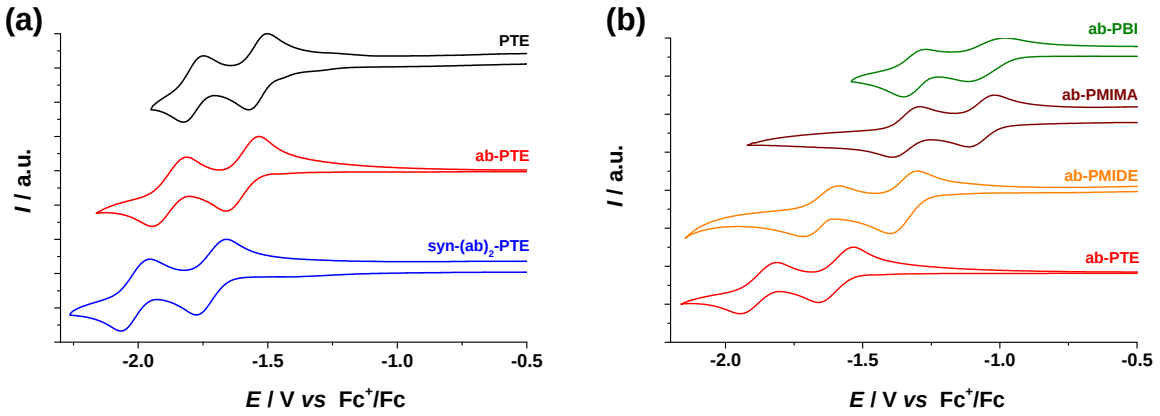

Figure 45 Cyclic voltammograms (c = 2.5·10^{-4} M, electrolyte: 0.1 M n-Bu$_4$NPF$_6$) of the core-extended perylene tetraesters (a) and of the monoazabenz-annulated perylene derivatives (b). The electrochemical values were corrected *vs* ferrocenium/ferrocene (Fc$^+$/Fc) as an internal standard. The measurements were performed in dichloromethane at room temperature.

Energies of frontier molecular orbitals and DFT calculations. Considering the energy level of ferrocenium/ferrocene (Fc$^+$/Fc) with respect to the vacuum level (–4.8 eV), the LUMO levels of the azabenz-annulated perylene derivatives can readily be estimated using their experimentally determined reduction potentials according to $E^{\mathrm{LUMO}} = -[E_{1/2}^{1\mathrm{st\ red}} + 4.8]$ eV (see **Table 3**). The order of the LUMO energies thus obtained is well-reproduced by our DFT calculations on a B3LYP/def2SVP level of theory (**Figure 46** black and grey marks). The energetic offset of up to 0.5 eV can presumably be ascribed to solvent effects, which were not implemented in our theoretical considerations. In contrast, the HOMO levels of these chromophores cannot be estimated following the same approach because the oxidation potentials of many derivatives are not covered by the electrochemical window of our experimental setup. However, on the basis of the assumption that the lowest energetic optical transition directly reflects the HOMO-LUMO energy gap, the HOMO energies should in principle be accessible by subtracting the

optical band gap from the respective LUMO level ($E^{HOMO} = E^{LUMO} - E^{opt.gap}$, **Table 3** and **Figure 46** red marks).

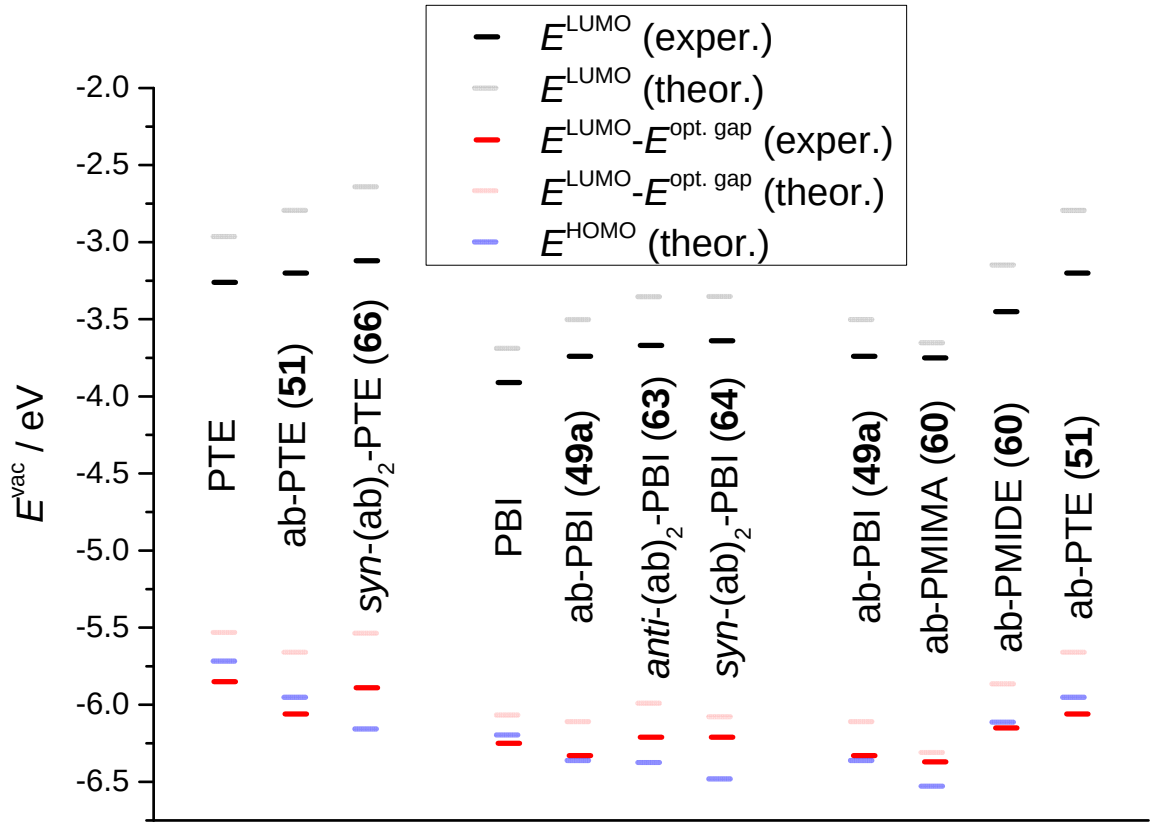

Figure 46 Schematic representation of the frontier molecular orbital energies of azabenz-annulated perylene derivatives. The experimentally determined values are obtained from electrochemical and absorption properties (see **Table 3**). The theoretical data are based on DFT calculations at the B3LYP/Def2SVP level of theory (for details see *experimental section*).

Although the energetic order of these values is in good agreement with the corresponding ones obtained by DFT methods (**Figure 46** pink marks), there is an obvious deviation from the directly calculated values (**Figure 46** blue marks). This divergence can be explained by the fact that especially for the bisazabenz-annulated perylene derivatives, transitions between other molecular orbitals like HOMO–1 and LUMO+1 contribute to the lowest energetic UV/Vis absorption bands. Therefore, such simple approximations should be handled carefully and only be applied to systems where these perturbations do not result in serious misinterpretations. Apart from this, the HOMO and LUMO values of the materials presented in this work can readily be adjusted and should therefore be of interest for many desirable applications.

3.2.5 Azabenz-Annulated Perylene Bisimide Dimers[5]

Synthesis of ab-PBI dimers. The combination of monoamino-PBIs and dialdehydes should straightforwardly generate ab-PBI dimers of the form "PBI-ab-X-ab-PBI" (X = spacer). Indeed, such dimers were achieved with the modified PiSp reaction protocol and the right choice of the dialdehyde (**Scheme 13a**). The twofold transformation of two equivalents of amino-PBI **47** with one equivalent of glyoxal and pyridine-2,6-dicarboxaldehyde resulted in the synthesis of the ab-PBI dimers **68** ("PBI-ab–ab-PBI") and **69** ("PBI-ab–py–ab-PBI") with moderate yields of 18% – 48%. Creation of higher homologues like "PBI-ab–py-py–ab-PBI" **70** is limited by the proper preparation of the respective dialdehydes. Besides this outlined route, there is also the alternative methodology to couple the bromo-functionalized ab-PBI **49b** *via* transition metal catalyzed coupling reactions to itself or appropriate coupling partners (**Scheme 13**, bottom route). Therefore, **49b** was homocoupled under Negishi-type reaction conditions ($NiBr_2(PPh_3)_2$ and Zn powder) in excellent yields of 92% to afford dimer **70**.

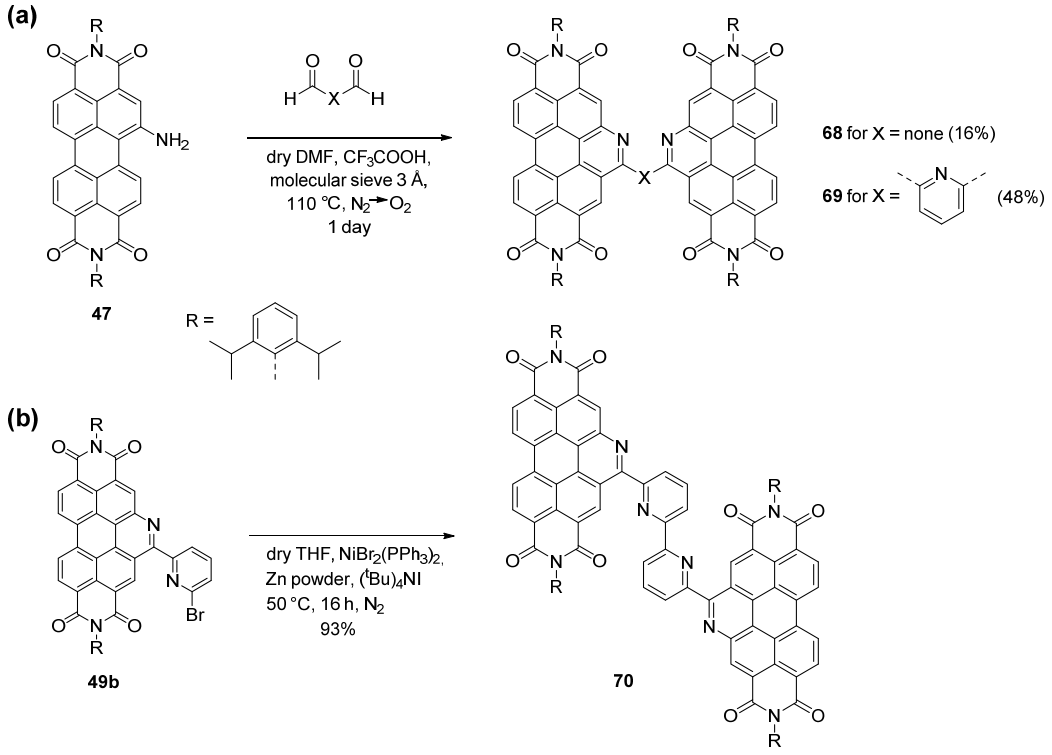

Scheme 13 (a)Synthesis of the ab-PBI dimers **68** and **69** by a twofold Pictet-Spengler reaction of amino-PBI **47** with the dialdehydes glyoxal and pyridine-2,6-dicarboxaldehyde. (b) Preparation of the higher homologue ab-PBI dimer **70** *via* a Negishi-type cross-coupling of two bromo-functionalized molecules ab-PBI **49b**.

[5] The synthesis of ab-PBI dimer **69** was performed by Waldemar Waigel, Bachelor Thesis, Universität Würzburg **2014**.

The structural integrity of the dimers was confirmed by 1D and 2D NMR spectroscopy, MALDI-TOF and high-resolution ESI mass spectrometry. NMR spectra in the good PBI-solvating solvent dichloromethane displayed no inter- and intramolecular aggregation or folding processes. Nevertheless, the close proximity of the chromophore units leads occasionally to peak splitting of before chemically equivalent protons in the monomer reference dyes due to a certain electronic perturbation of the proton environment in the dimer arrangement.

Optical and redox properties of ab-PBI dimers. Besides the structural investigations of the dimers also the basic optical and electronic properties in dichloromethane at room temperature were studied by absorption and emission spectroscopy and by electrochemical measurements (summarized in **Table 4**). In general, the optical and redox data of the dimers in dichloromethane are comparable to the monomeric derivatives and thus the electronic ground state interactions between the chromophores are weak.

Table 4 Summary of the optical and electrochemical data of the azabenz-annulated perylene bisimide dimers **25**–**27**.[a]

Compounds	λ_{abs} / nm (ε / 10^3 M^{-1} cm^{-1})		λ_{em} / nm	Φ_F	$E_{1/2}^{1st\ red}$ / V[b]	$E_{1/2}^{2nd\ red}$ / V[b]
	S_0–S_1	S_0–S_x	S_1–S_0			
Dimer **68**	470 (90.9)	342 (37.3)	477	0.56	–1.05	–1.33
Dimer **69**	476 (134.3)	350 (66.4)	483	0.66	–1.09	–1.39
Dimer **70**	477 (107.2)	420 (68.4)	486	0.53	–1.10	–1.41
Monomer **49a**	475 (68.4)	333 (29.2)	484	0.69	–1.06	–1.34

[a] Measured in dichloromethane at 298 K. [b] Measured with 0.1 M *n*-Bu_4NPF_6 and with Fc^+/Fc as a reference.

However, a first indication of the supramolecular as well as the excited state interactions can be estimated by the slightly different optical properties, which are much more sensitive to such interactions than the redox values. Accordingly, these data reveal a general trend in the dimer series: The dimer **69** with a middle-sized spacer length of the pyridyl group comes closest to resemble the properties of two perfectly isolated and non-interacting ab-PBI monomers **49a**. The extinction coefficient of the S_0–S_1 transition band of **69** is $134.3 \cdot 10^3$ M^{-1} cm^{-1} and thus is roughly twice as high as for monomer **49a** ($\varepsilon = 68.4 \cdot 10^3$ M^{-1} cm^{-1}, **Figure 47**).

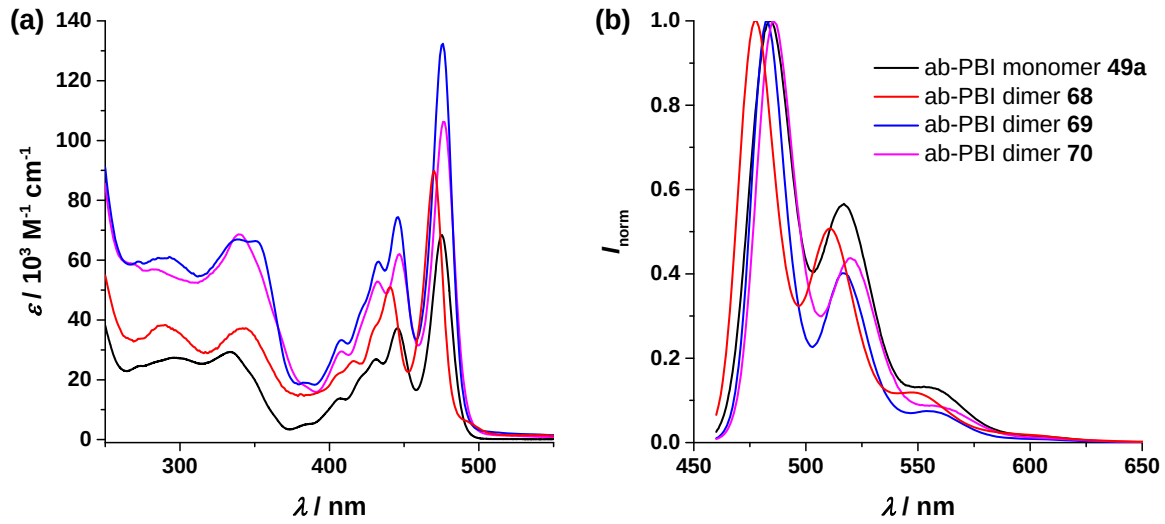

Figure 47 Absorption (a) and emission spectra (b) of azabenz-annulated perylene monomer **49a** and the dimers **68–70** in dichloromethane at room temperature ($c = 1 \cdot 10^{-5}$ M).

In contrast, the shorter and longer separated chromophores in the dimers **68** and **70** lead to a decreased extinction coefficient indicating electronic coupling between both dye subunits. Furthermore, the fluorescence quantum yield of **69** (66%, see **Table 4**) is higher than those of **68** and **70**, respectively, again resembling the monomer value of 69%. Although these findings represent only weak criteria, they testify different supramolecular and/or excited state interactions in the dimer series. Such PBI dimers have gained much attention in the context of non-fullerene *n*-type materials in organic photovoltaics[179, 180] and thus a deeper investigation of their aggregation and thin film properties could be of worth.

3.3 Ruthenium(II) and Iridium(III) Metal Complexes of ab-PBIs[6]

Ruthenium(II) and iridium(III) complexes with polypyridyl ligands like 2,2′-bipyridine constitute one of the most widespread classes of photosensitizers nowadays.[182] The light absorption of such complexes is normally placed in the high-energy part of the sun light (250 – 450 nm) and is quite weak ($\varepsilon_{450\,nm}^{MLCT}$ ($[Ru(bpy)_3]^{2+}$) = 12,300 M^{-1} cm^{-1}). Consequently, their potential to drive chemical reactions with long-wavelength light is limited. To increase the absorptivity of the sun light spectrum, the bichromophoric approach, in which an additional chromophore is attached to the polypyridyl complexes, is often used.

An azabenz-annulation with a 2′-pyridyl substituent mimics closely 2,2′-bipyridine – the mostly utilized polypyridyl ligand in coordination chemistry. Accordingly, also ab-PBIs can be easily applied as ligand systems for metal-organic complexes. In such new PBI-based metal complexes, the metal fragment is most intimately merged to the perylene chromophore. Consequently, these hybrids should not be considered as supramolecular bichromophoric systems (section **2.3.1**) but as metal complexes with an additional largely extended and fused polypyridyl ab-PBI ligand (section **2.3.2**). In the following chapter, the synthesis and characterization of such hybrid materials with ruthenium(II) and iridium(III) metal centers are presented. The close proximity of the organic chromophore and the metal complex allows strong spin-orbit coupling, which is sufficiently strong to not only facilitate the $S_n \rightarrow T_n$ intersystem crossing of the ab-PBI dye, but also the radiative $T_1 \rightarrow S_0$ transition, known as phosphorescence. Finally, the photosensitizer capability of this new complex class is evaluated in organic and aqueous medium.

3.3.1 Synthesis and Structural Characterization

The preparation of the metal complexes based on azabenz-annulated perylene ligands proceeds analogous to the coordination chemistry of the 2,2′-bipyridine. Hereto, the bipyridine-like ab-PBI ligand **49a** (R^1 = 2,6-diisopropyl phenyl) was reacted with $[Ru(bpy)_2Cl_2]$ and an excess of $AgClO_4$, and subsequent anion exchange with NH_4PF_6 afforded the complex $[Ru(bpy)_2(ab\text{-}PBI)][PF_6]_2$ **71** in 65% yield (**Scheme 14**). The iridium

[6] This section has been partly communicated in:
[181] M. Schulze, A. Steffen, F. Würthner, *Angew. Chem. Int. Ed.* **2015**, *54*, 1570-1573.

complex [Cp*Ir(ab-PBI)Cl][PF_6] **72** was prepared by the reaction of ab-PBI **49a′** (R^2 = 3-pentyl) with half an equivalent of [Cp*$IrCl_2$]$_2$ and subsequent anion exchange with NH_4PF_6 in 67% yield.

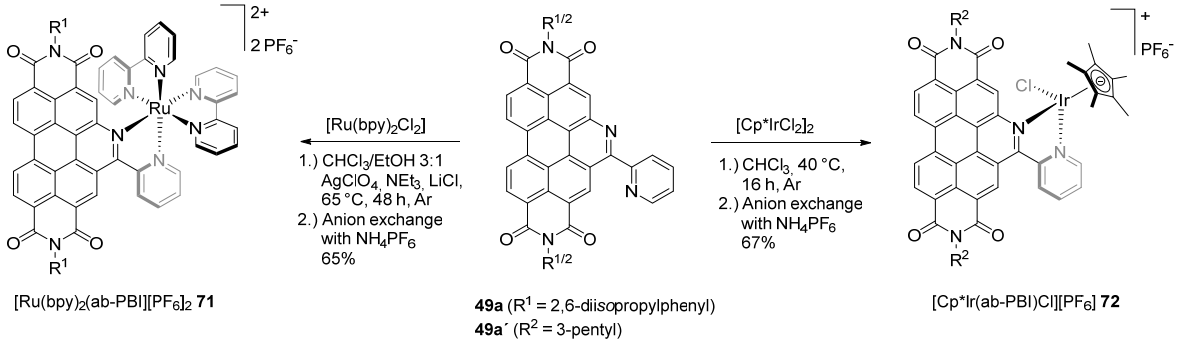

Scheme 14 Synthesis of the monometallic complexes [Ru(bpy)$_2$(ab-PBI)][PF_6]$_2$ **71** and [Cp*Ir(ab-PBI)Cl][PF_6] **72** based on ab-PBI ligands.

The preparation of the ruthenium complexes **73**–**76** started with the (ab)$_2$-PBI ligands *anti*-(ab)$_2$-PBI **63** and *syn*-(ab)$_2$-PBI **64** which have a second coordination pocket to ligate also two metal fragments (**Scheme 15**). Therefore, the respective ligand was reacted with half of an equivalent of the [Ru(bpy)$_2$$Cl_2$] precursor to obtain a mixture of the mono- and bimetalated ruthenium(II) complexes. Afterwards, the complex mixture was separated by column chromatography (SiO_2, 40:4:1 acetonitrile/water/saturated potassium nitrate solution) and subsequent anion exchange with NH_4PF_6 gave the hexafluorophosphate salts of the complex.

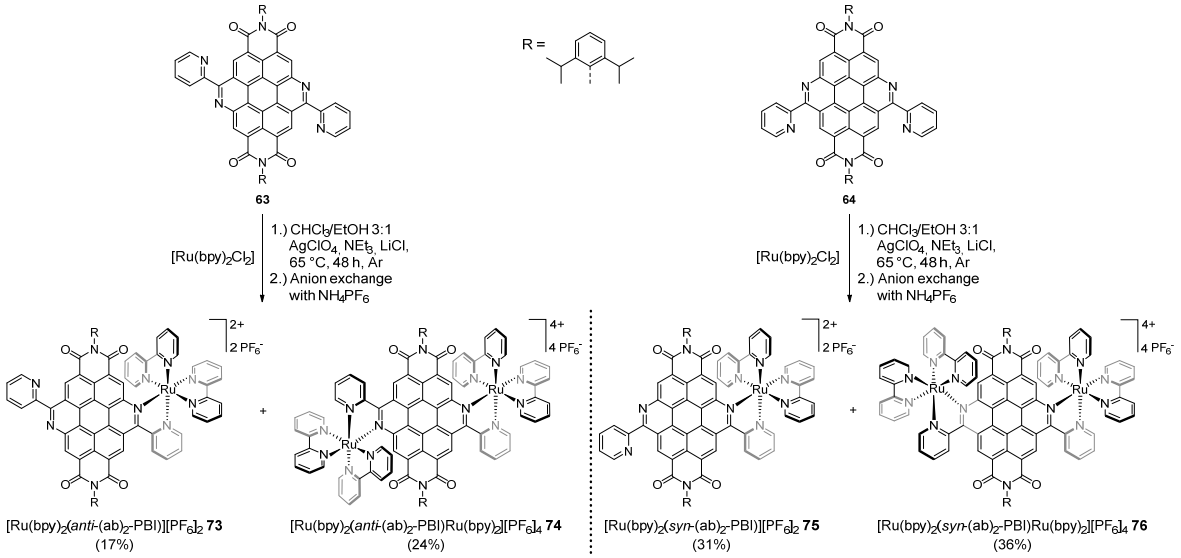

Scheme 15 Synthesis of mono- and bimetallic complexes **73**–**76** based on the (ab)$_2$-PBI ligands *anti*-(ab)$_2$-PBI **63** and *syn*-(ab)$_2$-PBI **64**.

In case of the ligand **63**, the mono-ruthenium complex $[Ru(bpy)_2(anti\text{-}(ab)_2\text{-}PBI)][PF_6]_2$ **73** and the bis-ruthenium complex $[Ru(bpy)_2(anti\text{-}(ab)_2\text{-}PBI)Ru(bpy)_2][PF_6]_4$ **74** were obtained in a yield of 17 and 24%, respectively; for the ligand **64**, the complexes $[Ru(bpy)_2(syn\text{-}(ab)_2\text{-}PBI)][PF_6]_2$ **75** and $[Ru(bpy)_2(syn\text{-}(ab)_2\text{-}PBI)Ru(bpy)_2][PF_6]_4$ **76** were isolated with 31 and 36% yield, respectively.

The complexes were characterized by NMR spectroscopy, MALDI, high-resolution ESI mass spectrometry as well as elemental analysis for the two monometallic complexes $[Ru(bpy)_2(ab\text{-}PBI)][PF_6]_2$ **71** and $[Cp^*Ir(ab\text{-}PBI)Cl][PF_6]$ **72**. Furthermore, the molecular structure of **72** was confirmed by single-crystal X-ray diffraction studies (**Figure 48**). The iridium(III) center is coordinated in a "piano-stool" conformation, in which the Cp^* ligand occupies three of the six possible coordination sites. The bong lengths and angles of **72** are in agreement with the corresponding reference compound $[Cp^*Ir(bpy)Cl]Cl$,[183] except the iridium(III) nitrogen bond Ir–N5 (2.138(5) Å) and the Ir–Cp^* distance (1.803(8) Å). For both, elongations compared to the reference (d (Ir–bpy) = 2.076(8)/2.090(9) and d (Ir–Cp^*) = 1.786 Å) are observed and attributed to the electron-withdrawing character of the PBI moiety. In addition, the pyridyl ring is twisted out of the flat PBI plane (φ (C4–C5–C8–C9) = 3.80°) with 18.3° due to the steric constraint between the C23 and C62 hydrogens.

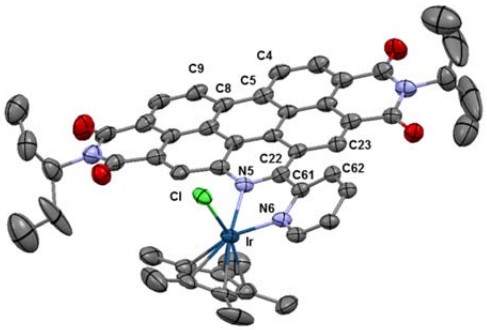

	[Cp*Ir(ab-PBI)Cl][PF$_6$] **72**	[Cp*Ir(bpy)Cl][Cl]
d (Ir–N6)	2.086(5) Å	2.076(8) Å
d (Ir–N5)	2.138(5) Å	2.090(9) Å
d (Ir–Cl)	2.3790(15) Å	2.404(2) Å
d (Ir–Cp*)	1.803(8) Å	1.786 Å
∢ (N5–Ir–N6)	75.12(19)°	76.2(3)°
φ (C4–C5–C8–C9)	3.80(10)°	-
φ (N5–C22–C61–N6)	18.3(7)°	9(1)°

Figure 48 Molecular structure of $[Cp^*Ir(ab\text{-}PBI)Cl][PF_6]$ **72** in the solid state (ellipsoids drawn at 50% probability level; hydrogen atoms and counter ion omitted for clarity). The table summarizes important binding parameters of **72** and of the reference compound $[Cp^*Ir(bpy)Cl][Cl]$.[183]

3.3.2 Redox and Optical Properties in Organic Medium

Redox properties. The newly synthesized PBI-based metal complexes **71**–**76** have revealed extensive redox chemistry. The complexes of the monoazabenz-annulated ligands **49a** and **49a′** $[Ru(bpy)_2(ab\text{-}PBI)][PF_6]_2$ **71** and $[Cp^*Ir(ab\text{-}PBI)Cl][PF_6]$ **72** revealed an anodic shift of the two reversible PBI reductions in comparison to the free ab-PBI ligands

(both ligands have identical redox potentials, see **Table 5**). The both reductions, $PBI^{0/-}$ and $PBI^{-/2-}$, moved from −1.06 V and −1.34 V *vs* Fc^+/Fc, respectively, in the free ab-PBI to −0.85 V and −1.23 V in **71** and to −0.82 V and −1.22 V in **72** upon complexation (**Figure 49a**). The further bpy-centered reductions in **71** are located at comparable potentials than in the parent $[Ru(bpy)_3][PF_6]_2$ complex.

Table 5 Summary of the redox data of azabenz-annulated PBI-based metal complexes **71**–**76** and the respective ligands **49a**, **49a′**, **63** and **64**.

Compounds	$E_{1/2}$ / V[a]					
	$PBI^{0/-}$	$PBI^{-/2-}$	$bpy^{0/-}$	$Ru^{2+/3+}$	$Ir^{3+/4+}$	$Ir^{3+/+}$
ab-PBI **49a**	−1.06	−1.34	–	–	–	–
Ruthenium complex **71**	−0.85	−1.23	−1.86 −2.15	+1.02	–	–
$[Ru(bpy)_3][PF_6]_2$ **8**[b]	–	–	−1.73 −1.93 −2.15	+0.90	–	–
ab-PBI **49a′**	−1.06	−1.34	–	–	–	–
Iridium complex **72**	−0.82	−1.22	–	–	+1.46[c]	−1.42
$[Cp^*Ir(bpy)Cl][BF_4]$[184]	–	–	−2.67	–	+1.40[c]	−1.17
anti-$(ab)_2$-PBI **63**	−1.08	−1.41	–	–	–	–
Mono-ruthenium complex **73**	−0.87	−1.24	−1.73 −2.07	+1.10	–	–
Bis-ruthenium complex **74**	−0.70	−1.01	−1.54 −1.85 −2.06 −2.19	+1.11 +1.13	–	–
syn-$(ab)_2$-PBI **64**	−1.16	−1.44	–	–	–	–
Mono-ruthenium complex **75**	−0.87	−1.24	−1.73 −2.08	+1.11	–	–
Bis-ruthenium complex **76**	−0.72	−1.01	−1.53 −1.84 −2.04 −2.18	+1.10 +1.12	–	–

Measured in dichloromethane at 298 K. [a] Measured with 0.1 M *n*-Bu_4NPF_6 and with Fc^+/Fc as a reference. [b] Measured in acetonitrile. [c] Irreversible redox event.

Furthermore, the easier reduction of ab-PBI upon coordination to the Lewis-acidic metal ion centers is accompanied by a more difficult oxidation of the metal centers in the complexes **71** and **72**. The reversible $Ru^{2+/3+}$ redox couple appears at +1.02 V in **71** (+0.90 V in $[Ru(bpy)_3]^{2+}$ **8**) and the irreversible $Ir^{3+/4+}$ oxidation at +1.46 V in **72** (+1.40 V in $[Cp^*Ir(bpy)Cl]^+$).[184] This redox behavior is related to the electron-withdrawing nature

of the electron-poor PBI unit, which destabilizes the higher oxidized state of the metal centers.

The monometallic ruthenium(II) complexes **73** and **75** of the ligands *anti*-(ab)$_2$-PBI **63** and *syn*-(ab)$_2$-PBI **64** behave very similar in comparison to [Ru(bpy)$_2$(ab-PBI)][PF$_6$]$_2$ **71**. With the exception of a 0.1 V anodic potential shift of the $Ru^{2+/3+}$ oxidation and the two bpy-centered reductions (in **Figure 49b** only the complex series of *syn*-(ab)$_2$-PBI **64** depicted). Both bimetallic complexes **74** and **76** can be sixfold reversibly reduced and twofold reversibly oxidized, so that in total eight electrons can be shuttled in these complexes. The six reductions are composed of four bpy and two PBI reductions, whereas the two oxidations are located on each ruthenium metal center. The small potential splitting of the two metal oxidations by 0.02 V is only visible in the differential-pulse voltammograms revealing a slight electronic communication between the two complex moieties. Interestingly, due to the ligation of the second Lewis-acidic metal fragment in **74** and **76** only the position of the first three reductions ($PBI^{0/-}$, $PBI^{-/2-}$ and the first $bpy^{0/-}$) is further shifted to lower potentials than in the monometallic complexes **71**, **73** and **75**, whereas the remaining bpy-centered reductions stay unchanged. For instance, the first PBI reduction relocates in the *syn*-(ab)$_2$-PBI complex series from −1.16 V for the free ligand **64** to −0.87 V for the mono-ruthenium complex **74** and to −0.72 V for the bis-ruthenium complex **76**.

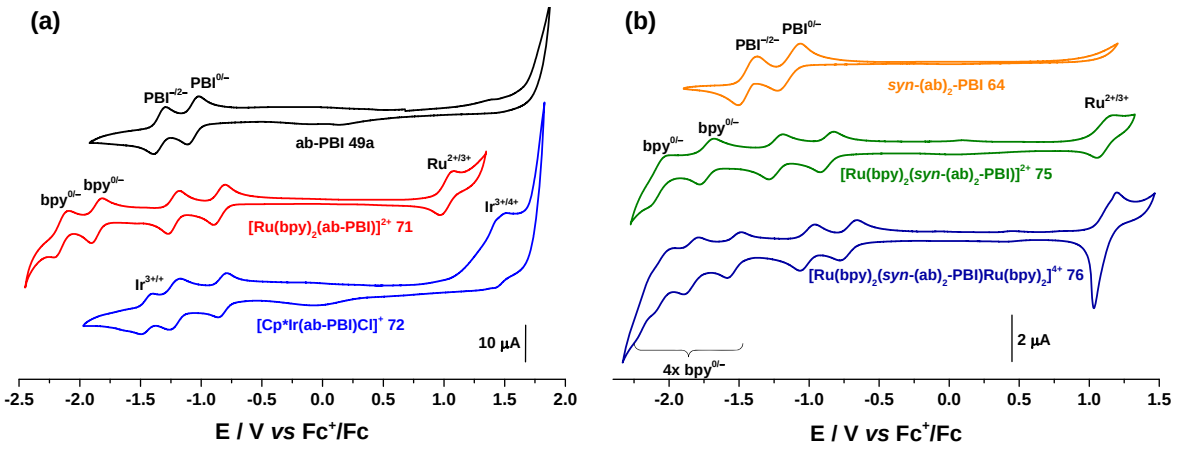

Figure 49 Cyclic voltammograms of the two monometallic complexes **71** and **72** of the ab-PBI ligands **49a** and **49a′** (a) and the two ruthenium complexes **75** and **76** of ligand *syn*-(ab)$_2$-PBI **64** (b). The measurements were performed in dry dichloromethane at room temperature at a concentration of $2.5 \cdot 10^{-4}$ mol/L (electrolyte: 0.1 M *n*-Bu$_4$NPF$_6$). The values were corrected *vs* ferrocene as an internal standard.

Absorption spectroscopy. In the new ab-PBI based complexes $[Ru(bpy)_2(ab\text{-}PBI)][PF_6]_2$ **71** and $[Cp^*Ir(ab\text{-}PBI)Cl][PF_6]$ **72** the optical properties of the ab-PBI ligands (**49a** and **49a′**) with its strong π–π* band ($\lambda_{abs}^{ab\text{-}PBI}$ = 470 nm, $\varepsilon \approx 65{,}000\ M^{-1}\ cm^{-1}$) and the corresponding vibronic progressions are fairly recognizable (**Figure 50**). These characteristics are maintained in both complexes except for a small 5 nm hypsochromic shift, a broadening of the vibrational fine structure and thus a loss in absorptivity. However, the ruthenium complex **71** shows an additional broad absorption band at around 516 nm, which is assigned to a bathochromically shifted MLCT transition in analogy to the MLCT state of $[Ru(bpy)_3]^{2+}$ at 450 nm.[63] The iridium compound **72** exhibits several new bands between 370 to 420 nm, which are apparently arising from MLCT transitions, and thus leading to a nearly constant absorptivity from 250 to 470 nm with an extinction coefficient of ~30,000 $M^{-1}\ cm^{-1}$.

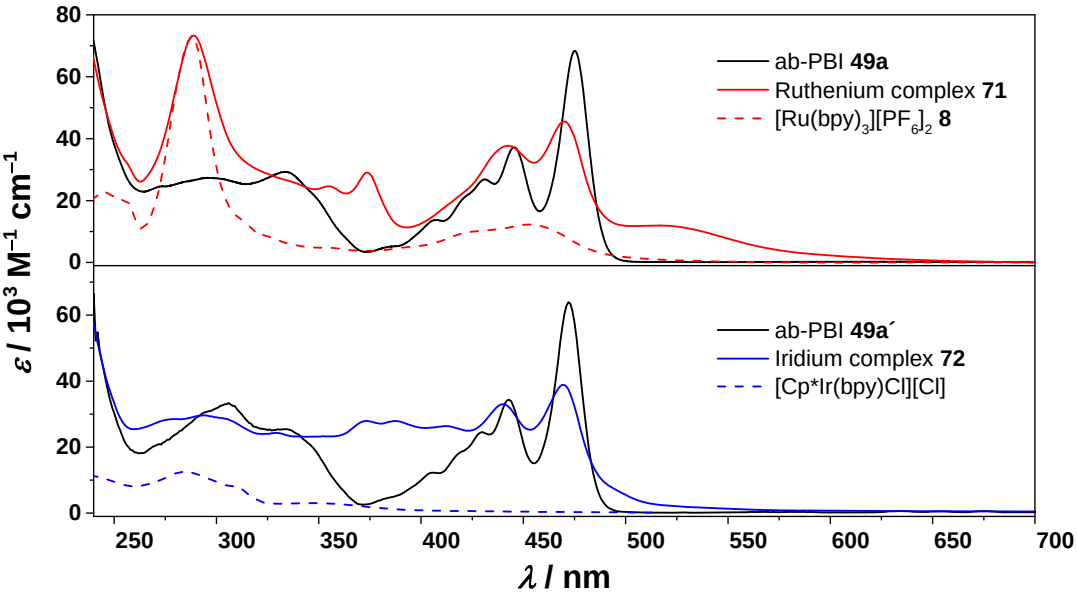

Figure 50 Absorption spectra of the monometallic complexes $[Ru(bpy)_2(ab\text{-}PBI)][PF_6]_2$ **71** (top) and $[Cp^*Ir(ab\text{-}PBI)Cl][PF_6]$ **72** (bottom) along with the corresponding references **49a**, **49a′**, $[Ru(bpy)_3][PF_6]_2$ and $[Cp^*Ir(bpy)Cl]Cl$[185] in dichloromethane at room temperature ($c = 1{\cdot}10^{-5}$ M).

The ruthenium(II) complexes **73**–**76** show also a broad MLCT absorption (**Figure 51**). The position of the maximum and the extinction coefficient is strongly dependent on the number of coordinated metal centers; for instance, the MLCT of the monometallic complex **73** to the bimetallic complex **74** of the ligand *anti*-$(ab)_2$-PBI **63** shifts from 527 nm (ε = 11,200 $M^{-1}\ cm^{-1}$) to 573 nm (ε = 18,100 $M^{-1}\ cm^{-1}$). In addition, the spectrum between 330 and 480 nm of the complexes **73**–**76** is dominated by PBI-centered π–π*

transitions. The π–π^* absorptions of the bipyridine ligands are localized at 290 nm and their extinction coefficient increase with the number of these units in the complex. In **Table 6** (see below) the absorption data of the complexes and respective references are summarized.

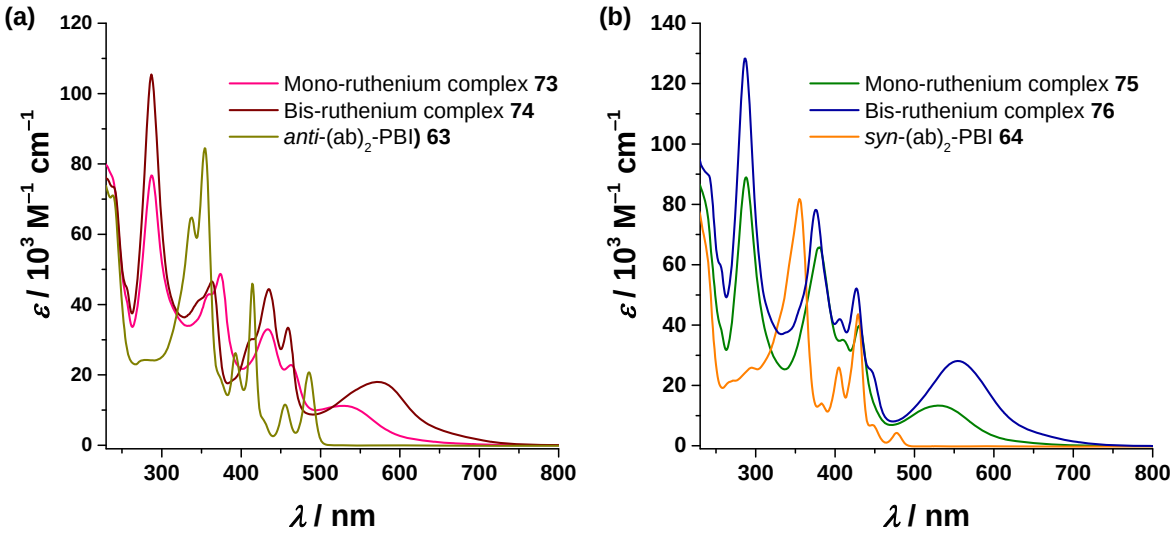

Figure 51 Absorption spectra of the ruthenium metal complexes based on *anti*-(ab)$_2$-PBI **63** (a) and *syn*-(ab)$_2$-PBI **64** (b) in dichloromethane at room temperature (c = 1–2·10^{-5} M).

Emission spectroscopy. The emission spectra of the ruthenium(II) and iridium(III) complexes **71**–**76** show an almost quantitative quenching of the ab-PBI or (ab)$_2$-PBI fluorescence at 484 and ~492 nm, respectively. Instead, the compounds reveal a long-lived emission in the NIR regime between 700 and 1100 nm in degassed dichloromethane at room temperature (**Figure 52**). In detail, the ruthenium complexes display an unstructured broad emission, while the iridium complex **72** has a well resolved band with an energetic separation between the submaxima of 1400 cm^{-1}, which is typical for C–C stretching modes of the PBI aromatic core[186] indicating PBI-centered emission. The emission peak maximum of iridium complex **72** is at 745 nm (for ruthenium complex **71** at 780 nm) and correlates to an energy of 1.66 eV (for **71** of 1.59 eV). Like the MLCT absorption maximum, the emission is also shifted to lower energies by ligation of the second metal center (λ_{em} (**74**) = 839 nm and λ_{em} (**76**) = 836 nm). However, the excitation spectra of **71** and **72** are nearly identical to the absorption spectra and thus demonstrate that all parts of the molecule contribute to the newly found NIR emission (**Figure 52**, dashed lines, λ_{em} = emission maximum).

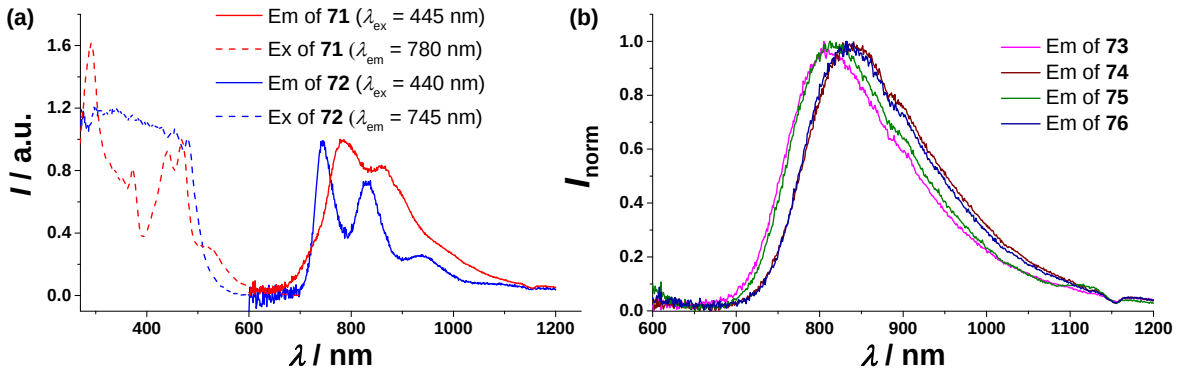

Figure 52 (a) Emission (solid) and excitation spectra (dashed) of the complexes $[Ru(bpy)_2(ab\text{-}PBI)][PF_6]_2$ **71** and $[Cp^*Ir(ab\text{-}PBI)Cl][PF_6]$ **72**. (b) Normalized emission spectra of the complexes **73**–**76** After 430 nm light excitation. The spectra were measured in degassed dichloromethane at room temperature.

The emission lifetimes of ab-PBI complexes **71** and **72** were found to be 4.2 µs and 33 µs, respectively, in degassed dichloromethane at room temperature. These timeframes are typical for radiative emissions out of a triplet state, known as phosphorescence. Representative phosphorescence lifetimes of purely organic PBIs are around 100 µs[187] and thus, the shorter lifetimes of both compounds indicate a strong spin-orbit coupling contribution of the metal centers. This effect seems to be stronger for the ruthenium complex **71** than for $[Cp^*Ir(ab\text{-}PBI)Cl][PF_6]$ **72**, although iridium is a heavier 5d-metal. Furthermore, **71** displays a higher phosphorescence quantum yield (Φ_{ph} = 11%, λ_{ex} = 375 nm) than the iridium compound **72** (Φ_{ph} ~0.2%), and in addition shows a more efficient phosphorescence than found for other ruthenium polypyridyl complexes,[188] exceeding even the 6% efficiency of $[Ru(bpy)_3]^{2+}$ itself (see **Table 6**).

With the emission lifetime τ_{em} and the quantum yield Φ_{em} in hand the radiative and non-radiative rate constants can be estimated. The radiative rate constant is given with $k_r = \tau_{em} \cdot \Phi_{em}^{-1}$ and the non-radiative rate constant is defined as $k_{nr} = (1-\tau_{em}) \cdot \Phi_{em}^{-1}$. Interestingly, the values of k_r are steadily reduced by orders of magnitude from the ab-PBI ligand **49a** ($2.2 \cdot 10^8$ s^{-1}) to Ru(II) complex **71** ($1.8 \cdot 10^4$ s^{-1}) and to Ir(III) compound **72** ($6.0 \cdot 10^1$ s^{-1}). In contrast, k_{nr} shows a slower decrease from $9.7 \cdot 10^7$ for **49a**, to $1.1 \cdot 10^6$ for **71** and to $3.0 \cdot 10^4$ s^{-1} for **72**. Accordingly, the non-radiative pathways are less dependent on the type of the metal center, whereas radiative deactivation is highly influenced by the metal fragment. Notably, in case of the ligand the values correspond to a fluorescence emission, whereas for the complexes they are associated to a phosphorescence phenomenon.

The mono- and bimetallic ruthenium complexes **73**–**76** of the $(ab)_2$-PBI ligands **63** and **64** show comparable Φ_{ph} after 435 nm excitation ranging from 4.6 to 7% in comparison the ab-PBI based complex **71** (Φ_p (**71**) = 7.7%). In contrast, the phosphorescence lifetimes are reduced by one order of magnitude varying at around 200 ns. Accordingly, both rate constants, radiative and non-radiative, have to be accelerated by one order of magnitude from the ab-PBI complex **71** to the $(ab)_2$-PBI ruthenium(II) complexes **73**–**76** (see **Table 6**). Because both rate constants are facilitated by roughly the same factor, the quantum yield of the phosphorescence stays on a comparable level for all ruthenium complexes.

Table 6 Summary of the optical data of azabenz-annulated PBI-based metal complexes **71**–**76** and the respective ligands **49a**, **49a′**, **63** and **64**.[a]

Compounds	λ_{abs} / nm (ε / 10^3 M^{-1} cm^{-1})[b]	λ_{em} / nm[c]	Φ_{em} / %[d]	τ_{em} / µs[e]	k_r / s^{-1} [f]	k_{nr} / s^{-1} [g]
ab-PBI **49a**	475 (68.4)	484	69	$3.15\cdot10^{-3}$	$2.2\cdot10^{8}$	$9.7\cdot10^{7}$
Ruthenium complex **71**	516 (11.9)	780	7.7 (11)[h]	4.2	$1.8\cdot10^{4}$	$2.2\cdot10^{5}$
$[Ru(bpy)_3][PF_6]_2$ **8**	453 (12.3)	602	6.0	0.89	$6.7\cdot10^{4}$	$1.1\cdot10^{6}$
ab-PBI **49a′**	472 (63.9)	482	54	$3.12\cdot10^{-3}$	$1.7\cdot10^{8}$	$1.5\cdot10^{8}$
Iridium complex **72**	469 (38.8)	745	0.2	33	$6.0\cdot10^{1}$	$3.0\cdot10^{4}$
[Cp*Ir(bpy)Cl]Cl[185]	349 (3.0)	–	–	–	–	–
anti-$(ab)_2$-PBI **63**	485 (20.5)	493	23	$3.34\cdot10^{-3}$	$7.0\cdot10^{7}$	$2.3\cdot10^{8}$
Mono-ruthenium complex **73**	527 (11.2)	809	6.2	$215\cdot10^{-3}$	$2.9\cdot10^{5}$	$4.4\cdot10^{6}$
Bis-ruthenium complex **74**	573 (18.1)	839	5.7	$198\cdot10^{-3}$	$2.9\cdot10^{5}$	$4.8\cdot10^{6}$
syn-$(ab)_2$-PBI **64**	478 (4.8)	485	22	$7.50\cdot10^{-3}$	$2.9\cdot10^{7}$	$1.0\cdot10^{8}$
Mono-ruthenium complex **75**	531 (13.3)	817	4.6	$190\cdot10^{-3}$	$2.4\cdot10^{5}$	$5.1\cdot10^{6}$
Bis-ruthenium complex **76**	554 (28.1)	836	7.0	$178\cdot10^{-3}$	$2.9\cdot10^{5}$	$5.2\cdot10^{6}$

[a] Measured in dichloromethane at 298 K. [b] The wavelength represents the lowest energetic absorption maximum. [c] The wavelength represents the highest energetic emission maximum. [d] The values were determined by an integrating sphere (λ_{ex} = 435 nm for all PBI-based metal complexes). [e] For all PBI-based metal complexes: λ_{ex} = 419 nm and λ_{em} = 800 nm. [f] $k_r = \tau_{em} \cdot \Phi_{em}^{-1}$. [g] $k_{nr} = (1-\tau_{em}) \cdot \Phi_{em}^{-1}$. [h] λ_{ex} = 375 nm.

3.3.3 The PBI Excited Triplet State in Organic Medium

In subchapter **3.3.2** PBI-based transition metal complexes **71**–**76** were characterized and showed a remarkable intense NIR phosphorescence with Φ_{ph} up to 11% for the complex $[Ru(bpy)_2(ab\text{-}PBI)][PF_6]_2$ **71**. This is a tremendous improvement compared to literature examples, in which NIR phosphorescence of PBI-based hybrid materials could only be measured at 77 K and was never quantified.[189, 190] That these systems can rather be considered as metal organic hybrids with a largely extended and fused polypyridyl ab-PBI ligand (section **2.3.2**) instead of supramolecular bichromophoric assemblies (section **2.3.1**) can already be derived from the newly formed MLCT absorption states and the strongly shifted NIR emission of these complexes. Furthermore, also first indications for the PBI-centered character of the excited state have appeared: (i) The NIR emission of ab-PBI complexes with different metal centers is similar (see complexes of **71** and **72**). (ii) The vibronic energy splitting of the emission of the iridium complex **72** matches to a prominent C-C stretching mode of the perylene ligand itself.
In the following, the nature of this state and the emission out of it is further characterized. The complex $[Ru(bpy)_2(ab\text{-}PBI)][PF_6]_2$ **71** was hereby investigated as reference for the whole complex series due to the many parallels between all complexes.

Time-dependent transient absorption spectroscopy. Before the nanosecond pump-probe spectroscopy can be applied to reveal further insights into the photophysics of **71**, it is necessary to gather information about possible intermediate species, which can occur in the course of the pump-probe spectroscopy. Therefore, spectroelectrochemistry was performed to extract the optical features of the reduced and oxidized form of $[Ru(bpy)_2(ab\text{-}PBI)][PF_6]_2$, which can be relevant if charge-separated states are involved in the photophysics.
In the spectroelectrochemical experiment, absorption spectra are recorded at a certain applied electrochemical potential. The reduced or oxidized substance increases in the solution and thus, their contribution to the absorption spectra rises, if the applied potential matches a redox event of the substance. Hence, in case of a fully reduced or oxidized species, the characteristic absorption spectrum of the respective moiety is obtained. However, the $PBI^{0/-}$ reduction in $[Ru(bpy)_2(ab\text{-}PBI)][PF_6]_2$ **71** is passed between the potential of +200 and –300 mV (**Figure 53a**). In this process, the PBI π–π^*-transition at 475 nm vanishes and the typical three absorption bands at 650, 725 and 850 nm for the PBI

radical anion appear.[191, 192] Furthermore, the MLCT absorption at 516 nm does not shift its position and increases slightly in intensity. This fact indicates that the PBI core unit is not directly involved into the MLCT transition but more the azabenz-annulated subpart.

The $Ru^{2+/3+}$ oxidation event is passed between the potential of +1100 and +1240 mV and goes along with a steady bleach of the MLCT absorption (**Figure 53b**). In addition, the bpy π–π^*-transition obtain a bathochromic shift from 289 to 310 nm and a new broad unstructured absorption peak at around 750 nm arises, which matches well to the low-energetic LMCT in oxidized ruthenium(III) polypyridyl complexes.[193, 194] Unsurprisingly, the PBI absorption is only weakly affected by the ruthenium oxidation.

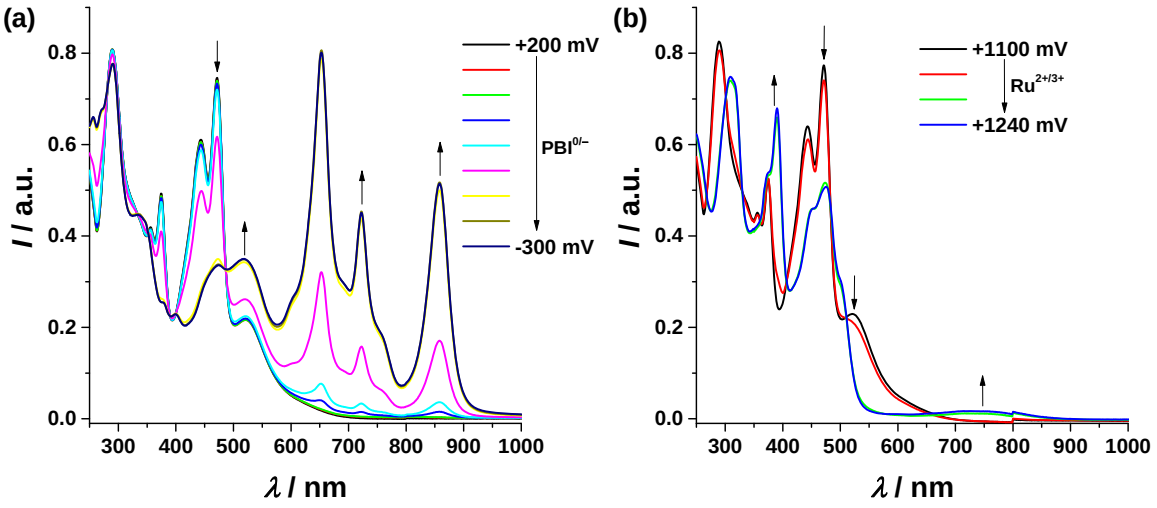

Figure 53 Spectroelectrochemistry of $[Ru(bpy)_2(ab\text{-}PBI)][PF_6]_2$ **71** (c = 0.1 mM) in dichloromethane (0.2 M n-Bu_4NPF_6, 298 K). (a) UV/Vis absorption spectral changes upon electrochemical $PBI^{0/-}$ reduction at potentials from +200 to –300 mV. (b) UV/Vis absorption spectral changes upon electrochemical $Ru^{2+/3+}$ oxidation at potentials from +1100 to +1240 mV.

The nanosecond transient absorption spectroscopy gave no evidence for such a charged intermediate species, which were prior spectroelectrochemically characterized. Nevertheless, a different optical active intermediate with a strong absorption at 550 nm could be detected (**Figure 54a** and **b**). After 50 ns this positive signal has fully built-up and starts to decrease again with a lifetime of 744 ns. In parallel, a ground state bleach signal between 425 and 480 nm has risen, which vanishes with nearly the same lifetime as the positive signal at 550 nm. Furthermore, after purging the sample with nitrogen both lifetimes increase to ~1.9 µs (not figured) and thus, gets close to the phosphorescence lifetime of 4.2 µs. Accordingly, this transient absorption process reflects the same deactivation of the excited state as the phosphorescence. Based on transient optical data of several other research groups, the 550 nm feature can be assigned to the PBI $T_1 \rightarrow T_n$

absorption.[195, 196, 197] Hence, this transient absorption represents the optical signature of the T_1 state and can be assigned with high certainty to the PBI triplet state.

The time regime from 0 to 32 ns in the ns-transient absorption spectroscopy displays the formation of the PBI triplet state (**Figure 54c** and **d**). Again, the formation of the 550 nm band and the ground state bleach behave equal and have a lifetime of ~6 ns (fit of the black (440 nm) or the green data points (550 nm)). During this process, the monitoring of the 475, 480 and 485 nm wavelength reveals that an additional process with a maximum after 8 ns takes place in the meanwhile. However, this event does not directly affect the steady formation of the triplet state and the scope of the data allows no further interpretations. Notably, this fast processes is unaffected by the presence or absence of oxygen.

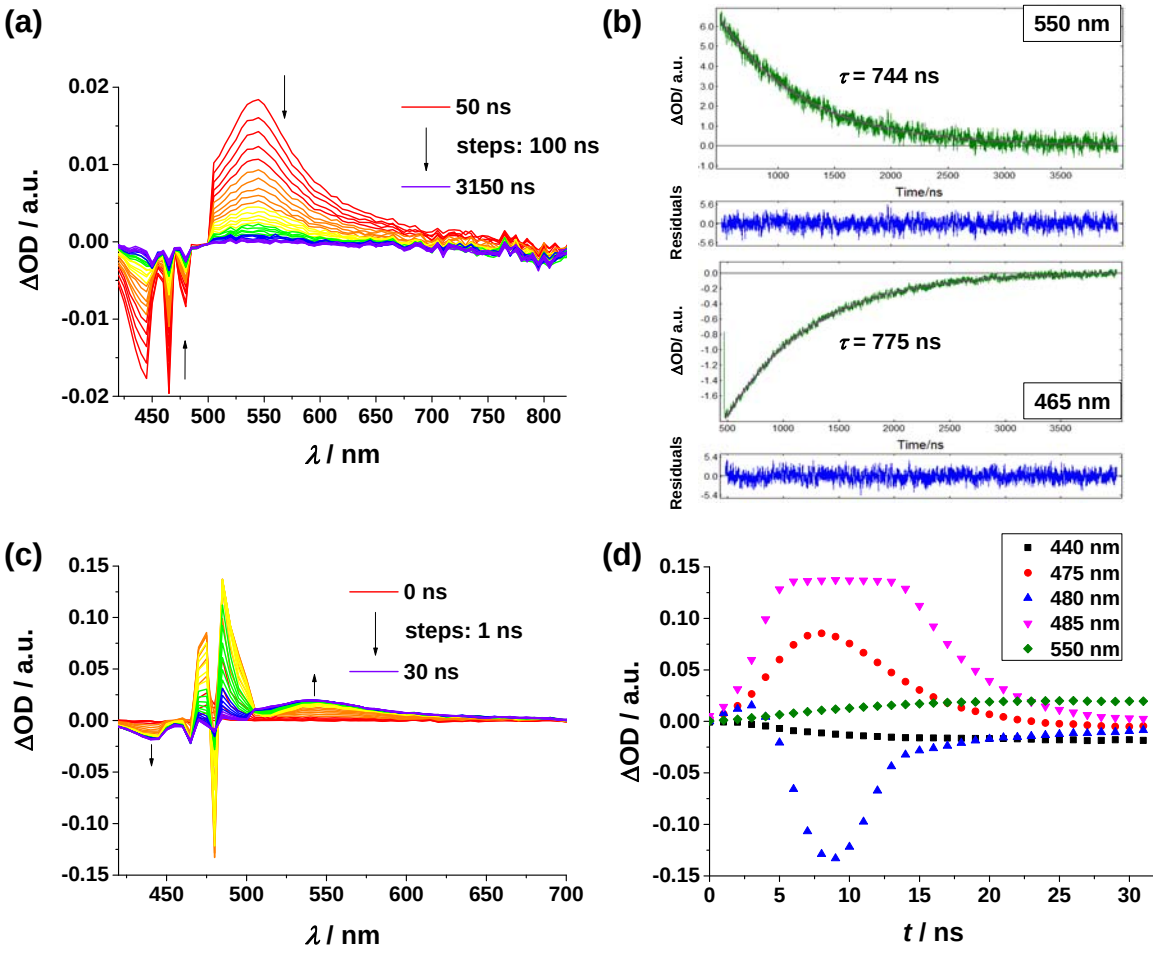

Figure 54 (a) Nanosecond transient absorption spectra of $[Ru(bpy)_2(ab\text{-}PBI)][PF_6]_2$ **71** in the time regime of 50 to 3150 ns after the 416 nm light pulse under ambient conditions in dichloromethane. The spectral resolution is 5 nm. (b) Monoexponential fit of the 550 nm absorption decay and the 465 nm absorption rise with the corresponding residual analyses. (c) Nanosecond transient absorption spectra of $[Ru(bpy)_2(ab\text{-}PBI)][PF_6]_2$ **71** in the time regime of 0 to 32 ns under the same experimental conditions. (d) Evolution of significant wavelengths during the first 32 ns after light excitation.

DFT calculations.[7] The electrochemical and absorption spectroscopic results are rationalized by DFT and TD-DFT studies (BHandHLYP-D3BJ/def2-TZVP, gas-phase), which suggest that the HOMO and HOMO−1 of $[Ru(bpy)_2(ab\text{-}PBI)][PF_6]_2$ **71** and $[Cp^*Ir(ab\text{-}PBI)Cl][PF_6]$ **72** are metal-centered Ru(d) or Ir(d) orbitals (**Figure 55**). Notably, the HOMO of the iridium complex **72** has a certain contribution of the Cp^* and chloride ligand. The LUMO is in both cases mainly PBI-centered and the LUMO+1 is localized on the azabenz-annulated subpart of the organic ligand. Furthermore, the LUMOs of **72** are less confined and have again Cp^* or Cl^- contributions.

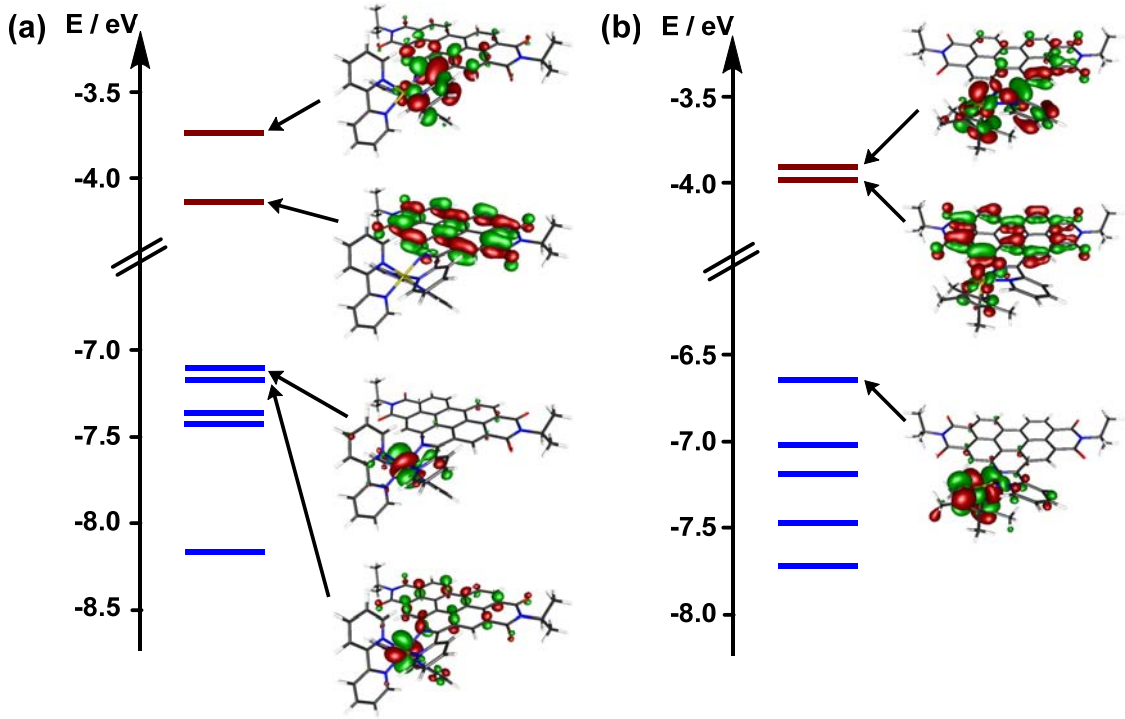

Figure 55 MO scheme of $[Ru(bpy)_2(ab\text{-}PBI)][PF_6]_2$ **71** (a) and $[Cp^*Ir(ab\text{-}PBI)Cl][PF_6]$ **72** (b) with selected frontier orbitals. Blue: occupied molecular orbitals; red: unoccupied molecular orbitals.

There are three interesting optical transitions in the lower energetic part of the ruthenium complex **71** (S_3, S_6 and S_9), which have a different nature to each other (**Figure 56**). Firstly, the lower energetic band S_3 has a MLCT character, which shifts a metal-centered electron to the PBI core unit. However, the oscillator strength of it is very weak because of the missing orbital overlap of the corresponding orbitals. Secondly, a much stronger MLCT absorption (S_6) is found between a ruthenium d-orbital and an azabenz-annulated bipyridine-localized orbital of ab-PBI. Finally, there is the PBI $^1(\pi\text{–}\pi^*)$ absorption S_9, also

[7] Dr. Andreas Steffen (Inorganic Department, University of Würzburg) performed the theoretical calculations and created the graphical illustrations of this subsection.

sometimes called intraligand charge transfer (ILCT). Based on the π–π^* transition which can be reliably assigned in both, the theoretical and experimental data, the calculated values have to be shifted by 40–50 nm to lower energies to match the experimentally determined wavelengths. Accordingly, the calculated MLCT absorptions on the azabenz-annulation subunit S_6 would be relocated from 478 nm to ~520 nm, which is quite close to the experiment value of 516 nm. Furthermore, the other (invisible) MLCT S_3 would be pushed to ~600 nm (≙ 2.0 eV). Interestingly, this energy is near the energy difference between the redox events of the PBI reduction and the metal center oxidation (~1.9 V), which corresponds by empiric observations very often to the MLCT energy band gap. All in all, the orbital situation is quite comparable to the electronic circumstances in $[Ru(bpy)_2(dppz)]^{2+}$ **37** (see subchapter **2.3.3**) in which the lowest energetic absorption has also negligible oscillator strength and thus, is not observable in the absorption spectrum. A more detailed discussion can be found later in subchapter **3.3.4**.

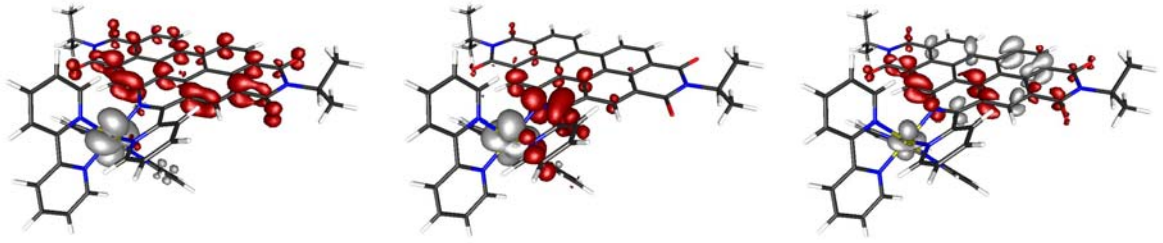

Figure 56 Most important low-energy absorptions of $[Ru(bpy)_2(ab\text{-}PBI)][PF_6]_2$ **71** with considerable oscillator strength.

A similar analysis to the singlet state can also be applied to the triplet excited state T_1. In both discussed metal complexes **71** and **72**, the T_1 can be described as a charge separated species in which the electron is placed on the perylene unit of the metal-organics, whereas the hole is located on the complex fragment (**Figure 57**). The main difference between **71** and **72** is the extent of the direct contribution of the metal center. In $[Ru(bpy)_2(ab\text{-}PBI)][PF_6]_2$ **71** the hole is predominately situated on a d-orbital of the ruthenium center (**Figure 57a**); in contrast, the hole in the iridium complex **72** has a significant contribution of the Cp^* and the chloride ligand (**Figure 57b**). Accordingly, the spin-orbit input of the ruthenium center is much higher than that of the iridium one.

This fact is well reflected by experimental observations: (i) The phosphorescence lifetime of **72** (33 µs) is one orders of magnitude longer than of **71** (4.2 µs). (ii) The emission profile of all ruthenium compounds are significantly broadened in contrast to the sharp profile of [Cp*Ir(ab-PBI)Cl][PF_6] **72**.

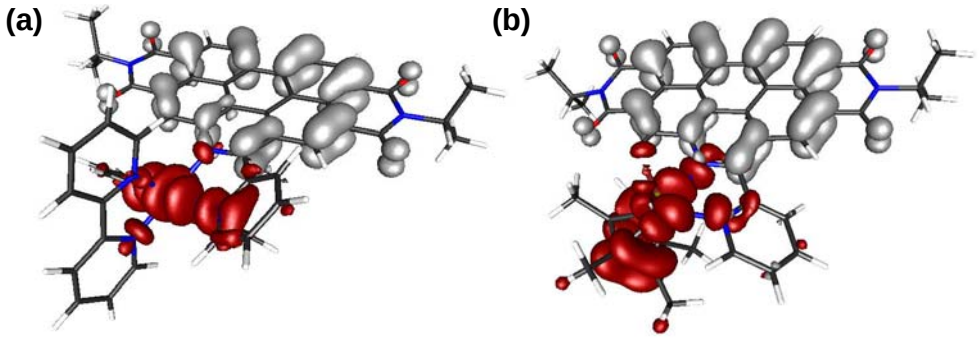

Figure 57 Electron (grey) and hole (red) in the optimized T_1 state of [$Ru(bpy)_2$(ab-PBI)][PF_6]$_2$ **71** (a) and [Cp*Ir(ab-PBI)Cl][PF_6] **72** (b), respectively, at the BHandHLYP-D3BJ/def2-TZVP level of theory.

Photocatalytic conversion in organic medium – ab-PBI metal complexes as photoreductants.[8] The experimental and theoretical results emphasize that the excited state character of ab-PBI based transition metal complexes contain a significant MLCT character. Accordingly, these compounds could be of interest as photosensitizers (PS) in electron and energy transfer processes (for general considerations see subchapter **2.2.3**). The complexes [$Ru(bpy)_2$(ab-PBI)][PF_6]$_2$ **71** and [Cp*Ir(ab-PBI)Cl][PF_6] **72** were tested against the established photosensitizer [$Ru(bpy)_3$][PF_6]$_2$ in an organic photocatalytic test reaction to evaluate their photosensitizer capability. In this case, the conversion of the photocatalytic dimerization of 4-nitrobenzyl bromide to 1,2-bis(4-nitrophenyl)ethane was selected as an exemplary reaction (**Figure 58a**). The dimerization of 4-nitrobenzyl bromide was chosen because of the existence of an already established and standardized experimental protocol in the group of Prof. Lambert satisfying the desired proof of principle character of the experiment.

Unfortunately, the thermodynamic characteristics of this reaction are less energetically favored for the ab-PBI metal complexes than for $[Ru(bpy)_3]^{2+}$ **8** (**Figure 58b**). For the desired transformation, it is essential that the reduced photosensitizer is higher in energy than the reduction potential of the 4-nitrobenzyl bromide to realize a resulting driving force for the reaction. Obviously, the low-lying ab-PBI orbital, on which the first reduction of

[8] The experiments were performed in the group of Prof. Lambert with the help of Dr. Guillaume Grelaud.

the complexes is localized, is by ~0.9 V lower in energy than the relevant reduction of $[Ru(bpy)_3]^{2+}$ at −1.73 V. However, the reduction potential is still above the 4-nitrobenzyl bromide reduction window, which is between −0.77 and −0.45 V.[198]

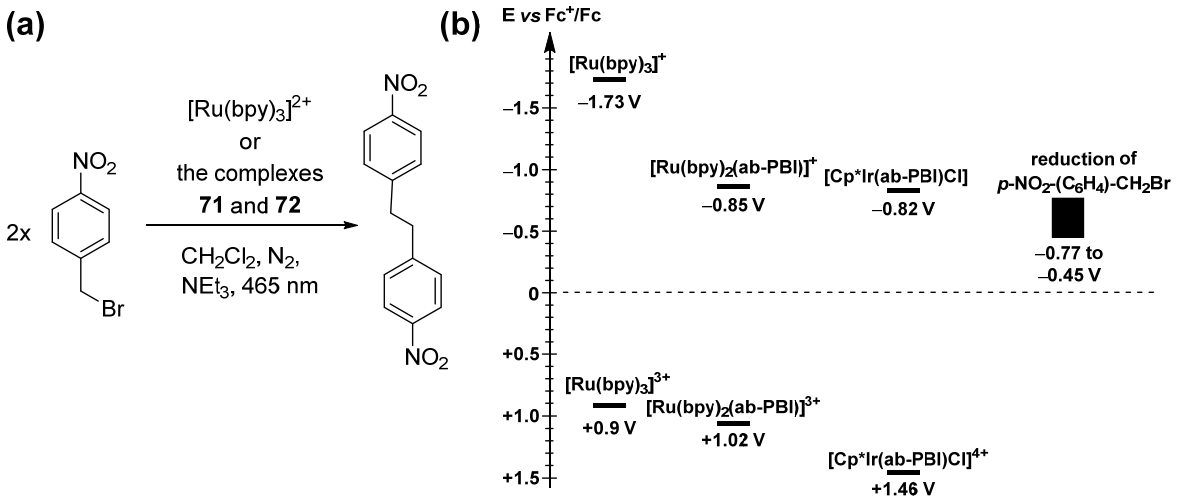

Figure 58 (a) Photocatalytic dimerization of 4-nitrobenzyl bromide to 1,2-bis(4-nitrophenyl)ethane with $[Ru(bpy)_3][PF_6]_2$ or the ab-PBI based transition metal complexes $[Ru(bpy)_2(ab\text{-}PBI)][PF_6]_2$ **71** and $[Cp^*Ir(ab\text{-}PBI)Cl][PF_6]$ **72** as photosensitizers. (b) Energy scheme of the oxidation and reduction potentials (*vs* Fc^+/Fc) of participating compounds in the photocatalytic conversion of 4-nitrobenzyl bromide.

The photocatalysis starts with the absorption of a 465 nm light photon by the photosensitizer and the subsequent formation of the photoexcited photosensitizer (**Scheme 16**). Afterwards, the excited state is reductively quenched by triethylamine to obtain the reductant of the reaction, *e.g.* $[Ru(bpy)_3]^+$. The *in situ* generated reductant reduces the 4-nitrobenzyl bromide. The reduced organic compound stabilizes itself by a carbon-bromine bond breaking and thus, forms a bromide ion and a 4-nitrobenzyl radical. This radical has now two general reaction pathways: (i) It encounters a second reductant molecule to form the 4-nitrobenzyl anion, which reacts afterwards with a 4-nitrobenzyl bromide to produce 1,2-bis(4-nitrophenyl)ethane (**Scheme 16**). (ii) The 4-nitrobenzyl radical homocouples with another radical of its kind to generate 1,2-bis(4-nitrophenyl)ethane (not figured).

The photosensitizer $[Ru(bpy)_2(ab\text{-}PBI)][PF_6]_2$ **71** reaches a yield of 10% of produced 1,2-bis(4-nitrophenyl)ethane at a PS/educt ratio of 1:100. Regarding that two reduction equivalents are necessary for each product formation, the number of catalytic cycles totals up to 20 (≡ TON, turnover number). Under the same conditions PS $[Ru(bpy)_3][PF_6]_2$ **8** reaches an educt conversion of 82%, which is four times higher than for **71**. The iridium complex **72** achieves a conversion of only 4%. This decrease in photocatalytic activity is

less surprising because of the 0.9 V loss of driving force in the ab-PBI complexes **71** and **72**. Nevertheless, both ab-PBI based transitions metal compounds have proven that their excited state is photocatalytically active and thus, the compounds exhibit photosensitizer qualities.

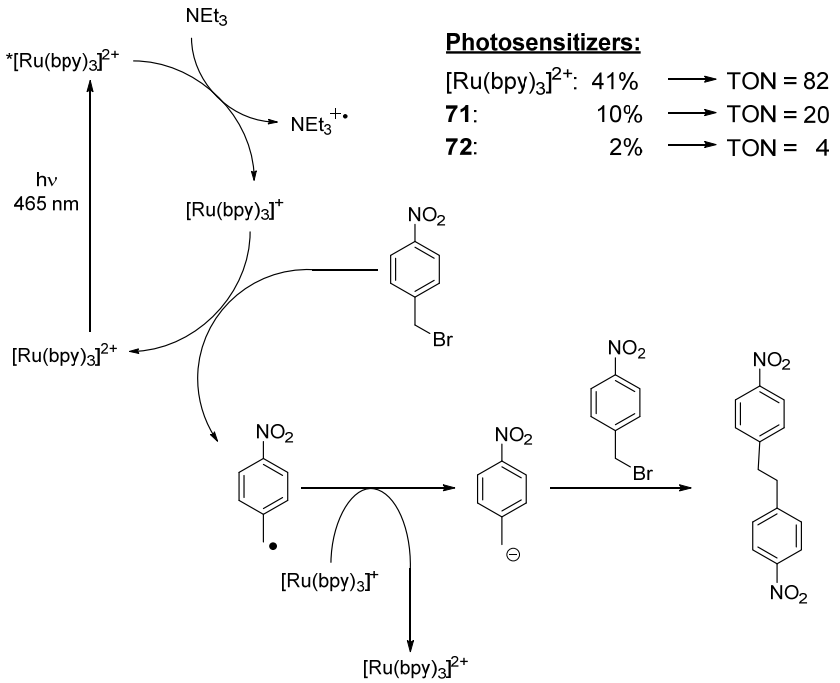

Scheme 16 Mechanism of the dimerization of 4-nitrobenzyl bromide to 1,2-bis(4-nitrophenyl)ethane with $[Ru(bpy)_3][PF_6]_2$ as photosensitizer and 465 nm light excitation in dichloromethane at 25 °C. In the right upper corner the yield of 1,2-bis(4-nitrophenyl)ethane and the turnover number of the three experiments with different photosensitizers is depicted. Catalytic conditions: 1 mol 4-nitrobenzyl bromide, 2 mol triethylamine, 0.01 mol photosensitizer.

3.3.4 The PBI Excited Triplet State in Aqueous Medium

Ab-PBI metal complexes represent stronger photooxidants than $[Ru(bpy)_3]^{2+}$ based on the oxidation potential data (E (**71**) = +1.02 V and E ($[Ru(bpy)_3][PF_6]_2$) = +0.90 V) and thus, their preferred application field are photocatalytic oxidation processes like water splitting instead of transformations initiated by reductive dehalogenation.

Photocatalytic conversion in aqueous medium – ab-PBI metal complexes as photooxidant. The potential of ab-PBI metal complexes to act as photosensitizers for the water oxidation (WO) was evaluated based on a three-component WO setup which was already described in section **2.1.4** (**Figure 8**). Hereby, the polypyridyl metal complexes $[Ru(bpy)_3]^{2+}$, **71** and **72** act as photosensitizers, $[Ru(bda)(pic)_2]$ is the WOC and $Na_2S_2O_8$ plays the role as sacrificial electron acceptor. As already outlined in the introduction,

the oxidized photosensitizer has to be a stronger oxidant than the [Ru(bda)(pic)$_2$] catalyst to guarantee a continuous oxidation. For the combination of $[Ru(bpy)_3]^{2+}$ (E ($Ru^{2+/3+}$) = +1.21 V *vs* NHE)[44] and [Ru(bda)(pic)$_2$] (water oxidation onset in pH 7 water = +0.98 V)[50] this criterion is fulfilled. The electrochemistry of ab-PBI complexes **71–76** could not be measured in aqueous medium due to the minor solubility in pure water. However, it can be expected that the oxidation potential of all synthesized complexes in aqueous solutions is more positive than for $[Ru(bpy)_3]^{2+}$ because of the oxidation potential trend in the solvent dichloromethane (see **Table 5**). Because of the solubility issue, the performance of the reaction requires a 1:1 solvent mixture of acetonitrile and phosphate buffer (pH 7.2) instead of pure water.

To establish the general experimental conditions for the water oxidation with this three-component system, the reaction was optimized with the reference photosensitizer $[Ru(bpy)_3]^{2+}$ **8** at first. Good oxygen productions in the chosen solvent mixture were obtained with a catalyst/PS/SEA ratio of 1:33:655 (**Figure 59**, black trace). Unfortunately, all efforts to produce oxygen with the photosensitizers [Ru(bpy)$_2$(ab-PBI)][PF_6]$_2$ **71** and [Cp*Ir(ab-PBI)Cl][PF_6] **72** failed. Changes like the variation of the concentrations, the used buffer salt, the solvent mixture, the SEA from $Na_2S_2O_8$ to $[Co(NH_3)_5Cl][Cl]_2$ and the excitation wavelength lead to no improvement.

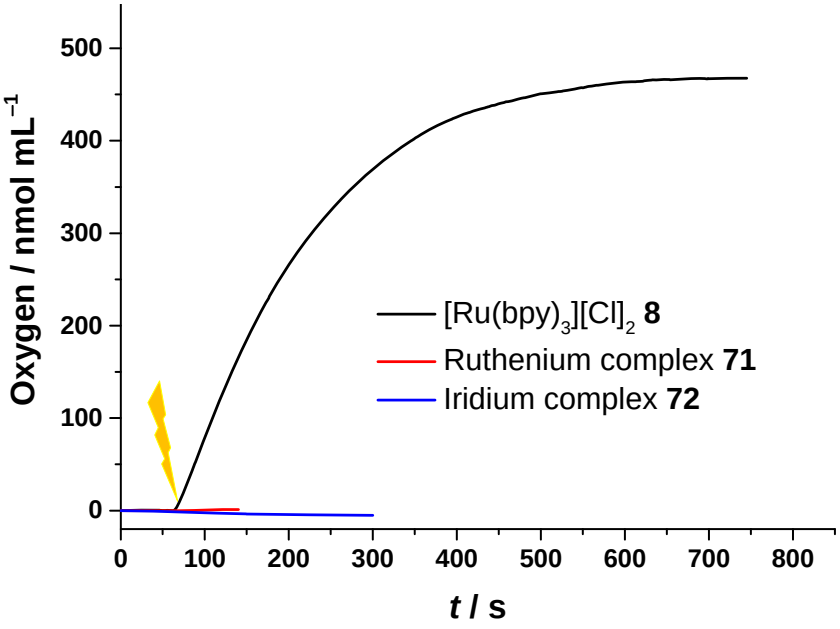

Figure 59 Oxygen evolution *vs* time during photocatalytic water oxidation with [Ru(bda)pic$_2$] as catalyst, [Ru(bpy)$_3$][Cl]$_2$ **8**, [Ru(bpy)$_2$(ab-PBI)][PF_6]$_2$ **71** or [Cp*Ir(ab-PBI)Cl][PF_6] **72** as photosensitizer and $Na_2S_2O_8$ as sacrificial electron acceptor. The measurements were performed in a Clark-type electrode setup to detect the oxygen amount in solution. Catalytic conditions: 2 mL 1:1 acetonitrile/phosphate buffer (pH 7.2), [$Na_2S_2O_8$] = 13.1 mM, [[Ru(bda)(pic)$_2$]] = 0.02 mM, [photosensitizer] = 0.65 mM, λ_{irr} >400 nm with 230 mW/cm^2.

Absorption and emission spectroscopy. The failure of the photocatalytic water oxidation demonstrates that the transfer of a photosensitizer from one solvent into another one with different polarity is critical and premature without a thorough evaluation of the fundamental properties in the new solvent. Accordingly, the absorption and the emission properties of $[Ru(bpy)_2(ab\text{-}PBI)][PF_6]_2$ **71** were investigated by measurements in different polar solvents starting from dichloromethane ($\varepsilon = 9.1$) over acetonitrile ($\varepsilon = 37.5$) to 1:1 acetonitrile/water mixtures ($\varepsilon = 58.6$).[199]

The general shape of the absorption spectra of **71** does not change by increasing solvent polarity except that the π–π^* PBI transitions increase hyperchromically by up to ~25% in comparison to the corresponding MLCT absorptions (**Figure 60a**). Furthermore, the absorption maxima of the bpy π–π^*, the PBI π–π^* and the MLCT transitions were plotted against the solvent polarity revealing that the latter has the strongest polarity dependency, whereas the π–π^* of bpy has nearly none and the π–π^* of PBI has only a weak one (**Figure 60b**). This finding supports once again the MLCT character of the 520 nm absorption and its similarities to the 450 nm MLCT of $[Ru(bpy)_3]^{2+}$ **8**.[200]

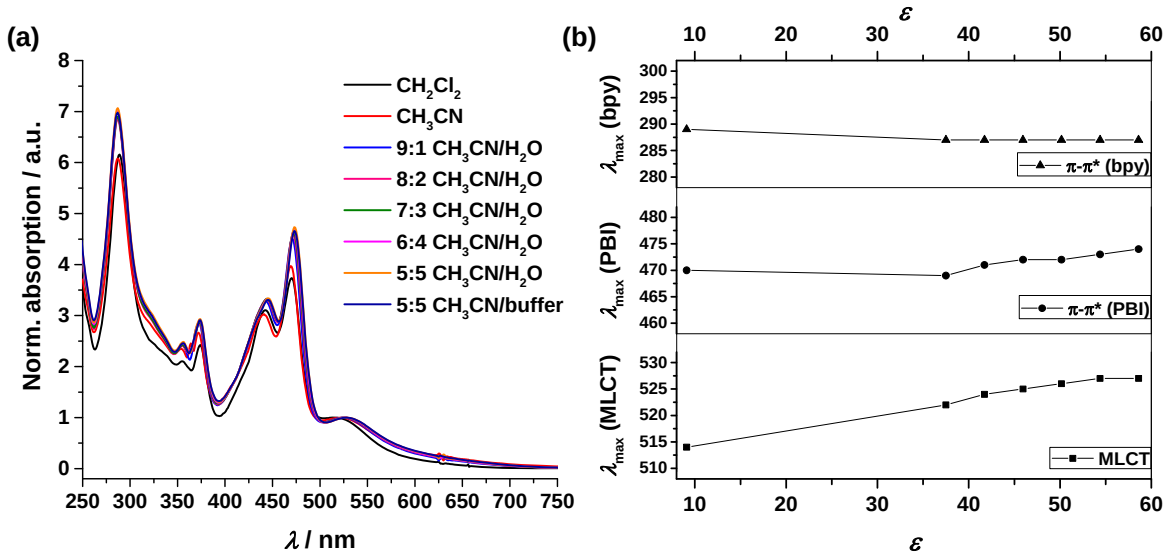

Figure 60 (a) Normalized absorption spectra of $[Ru(bpy)_2(ab\text{-}PBI)][PF_6]_2$ **71** in solvents of different polarity ($c = 1 \cdot 10^{-5} - 1 \cdot 10^{-6}$ M). (b) Progression of the absorption maxima (top: π–π^* of bpy, middle: π–π^* of PBI, bottom: MLCT) against the solvent polarity. Dielectric constants of the solvents at 20 °C: $\varepsilon(CH_2Cl_2) = 9.1$, $\varepsilon(CH_3CN) = 37.5$, $\varepsilon(H_2O) = 79.7$.[199] The dielectric constants of CH_3CN/H_2O solvent mixtures (v/v %) were estimated by $\varepsilon_{mix} = \phi(CH_3CN) \cdot \varepsilon(CH_3CN) + \phi(H_2O) \cdot \varepsilon(H_2O)$.

In contrast to the absorption spectra, there is a much stronger response of the emission spectra to the different solvent polarities. In addition, the ab-PBI metal complex $[Ru(bpy)_2(ab\text{-}PBI)][PF_6]_2$ **71** (**Figure 61c** and **d**) behaves differently in comparison to the

parent $[Ru(bpy)_3]^{2+}$ **8** (**Figure 61a** and **b**). Firstly, the emission of the reference $[Ru(bpy)_3]^{2+}$ was measured under ambient and inert (N_2-purged) conditions because the emission shows high sensitivity against oxygen (for detailed discussion see singlet oxygen sensing experiments below). $[Ru(bpy)_3]^{2+}$ displays an intense emission signal under all measurement conditions. The intensities vary among each solvent due to varying oxygen uptake levels of the solvents. After purging the $[Ru(bpy)_3]^{2+}$ solutions with nitrogen, all emission intensities increase significantly because of the reduced oxygen concentration acting as a emission quencher. Interestingly, all emission intensities approach to a similar maximum level indicating that the photophysics and the corresponding emission of $[Ru(bpy)_3]^{2+}$ is solvent-independent.

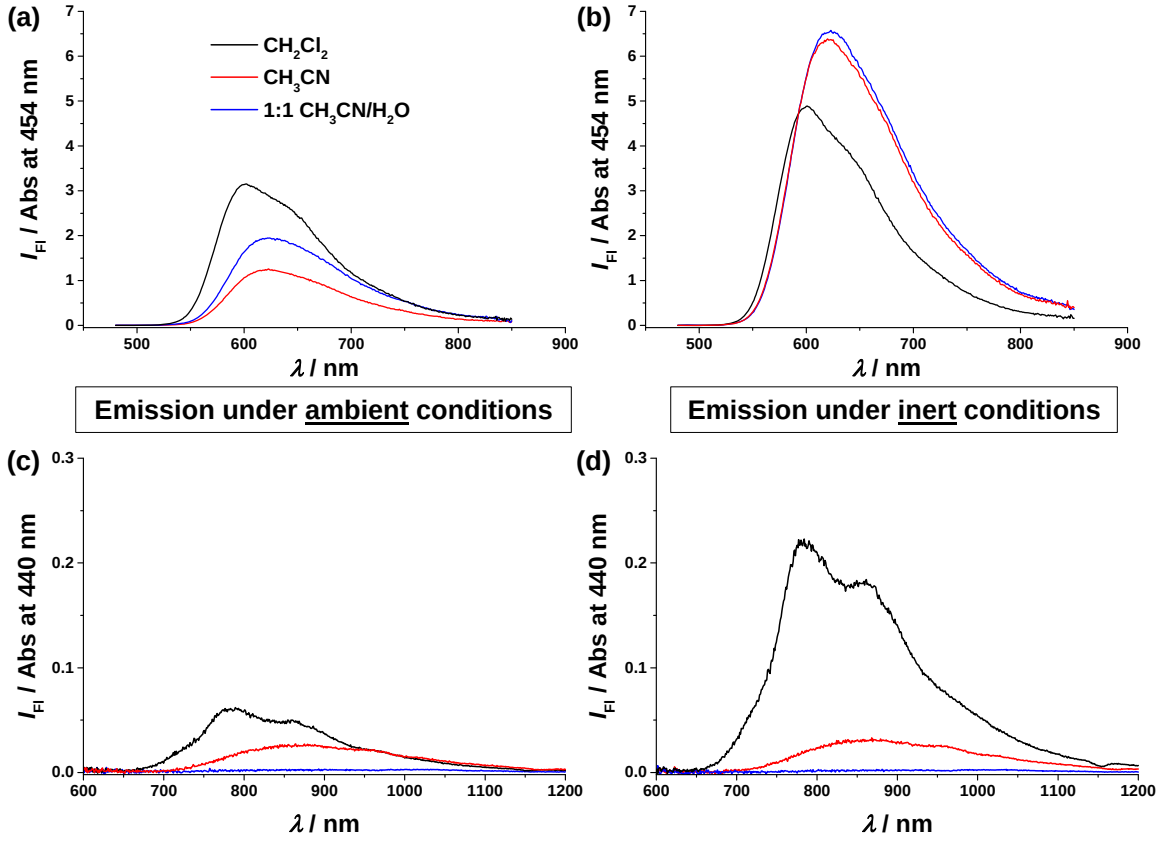

Figure 61 Emission spectra of $[Ru(bpy)_3][PF_6]_2$ **8** in three different solvents (CH_2Cl_2, CH_3CN and 1:1 CH_3CN/H_2O) measured under ambient (a) and inert conditions (b). The analogous experiment was also performed for $[Ru(bpy)_2(ab\text{-}PBI)][PF_6]_2$ **71** (c and d). The emission intensity was divided by the absorption intensity at 454 nm for **8** and at 440 nm for **71** to get a term which correlates to the quantum yield.

The behavior of **71** in the unpolar solvent dichloromethane is comparable to $[Ru(bpy)_3]^{2+}$, whereas it changes completely in polar solvents (**Figure 61c** and **d**). In dichloromethane, the emission intensity is sufficiently strong enough for the detection limit of the NIR detector and can be significantly increased by N_2-purging. Measurements in the more polar

acetonitrile reveal weak phosphorescence, which cannot be increased by removal of disturbing oxygen. Unsurprisingly, in even more polar solvents like 1:1 acetonitrile/water mixtures the emission under both conditions is fully disappeared.

Triplet state population – singlet oxygen sensing experiments.[9] Up to this point, it is not clear if the solvent dependency of the emission behavior of $[Ru(bpy)_2(ab\text{-}PBI)][PF_6]_2$ **71** results from a non-populated triplet state or from an acceleration of additional existing non-radiative deactivation pathways of this state. A classic experiment to investigate the triplet state population of a system after light excitation is the singlet oxygen sensing experiment. In this regard, the excited triplet state reacts in an energy transfer process with triplet oxygen $^3O_2$ – the energetically most stable form of molecular oxygen (**Figure 62a**).[202, 203] Accordingly, both triplet states annihilate each other to form a deactivated photosensitizer molecule and singlet oxygen $^1O_2$. Besides its high reactivity, $^1O_2$ can also be detected by its unique NIR emission at 1275 nm (**Figure 62b**).

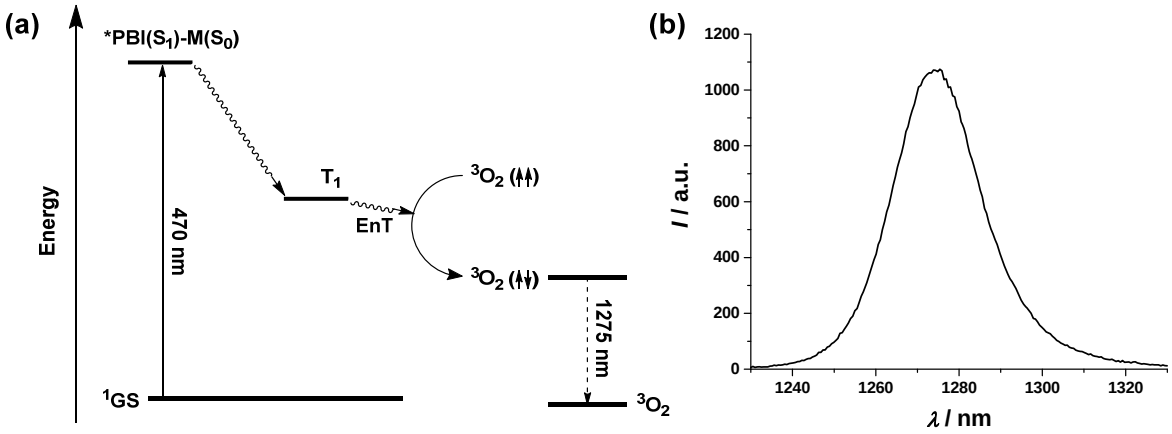

Figure 62 (a) Simplified Jablonski energy scheme of the formation of the T_1 triplet state in ab-PBI based metal complexes like **71** or **72** and the subsequent quenching of this state by triplet oxygen ($^3O_2$), which leads to the formation of singlet oxygen ($^1O_2$). (b) Exemplary emission spectrum of singlet oxygen after 470 nm light excitation of $[Cp^*Ir(ab\text{-}PBI)Cl][PF_6]$ **72** in an oxygen-purged dichloromethane solution at room temperature.

Both, the reactivity and the emission of singlet oxygen, can be used to quantify the amount of $^1O_2$, whereas the former is an indirect and the latter a direct method.[204, 205] In the direct method, upon irradiation of the compound in the solvent of choice, the luminescence of $^1O_2$ is detected. In the indirect method, the produced $^1O_2$ is trapped by an imidazole derivative to form an adduct, which quenches the absorbance of a probe molecule (for

[9] The singlet oxygen sensing experiments in acetonitrile and aqueous media were performed in the group of Prof. Gilles Gasser and were communicated in [201] C. Mari, H. Huang, R. Rubbiani, M. Schulze, F. Würthner, H. Chao, G. Gasser, *Eur. J. Inorg. Chem.* **2016**, doi:10.1002/ejic.201600516.

details see *Experimental Section*). For both methods, phenalenone can be used as a reference.

Generally, the amount of produced singlet oxygen correlates to the triplet quantum yield, but there are some pitfalls to this simplification. Firstly, if the lifetime of the excited triplet state decreases under the diffusion limit of the oxygen (dependent on the concentration of photosensitizer and oxygen, the type of the solvent and so on), the yield of singlet oxygen (Φ_Δ) can drop although the triplet quantum yield is still at 100%. Furthermore, energetic intermediates on the way to the triplet state can also react with $^3O_2$ to $^1O_2$ and thus, the Φ_Δ can overestimate the real triplet quantum yield. Nevertheless, a trend in singlet oxygen quantum yields can give valuable information about the excited triplet state formation.

The measured singlet oxygen quantum yields of the two complexes $[Ru(bpy)_2(ab\text{-}PBI)][PF_6]_2$ **71** and $[Cp^*Ir(ab\text{-}PBI)Cl][PF_6]$ **72** and the respective ab-PBI ligands **49a** and **49a′** by both methods are summarized in **Table 7**.[201] Both methods show comparable data and a good reproducibility. In general, in acetonitrile the Φ_Δ's are at least 29% except the directly determined value of **71**, which cannot be exactly defined because the detection limit of the setup of around 30%. Surprisingly, also the ab-PBI ligands show singlet oxygen sensing behavior in acetonitrile. Going to aqueous phosphate buffer solutions, Φ_Δ is strongly reduced to 4% for the ruthenium complex **71** and to 21% for the iridium one **72**. Interestingly, **72** has always higher Φ_Δ than the corresponding ruthenium complex although the phosphorescence quantum yields behave *vice versa*.

Table 7 $^1O_2$ quantum yields (Φ_Δ) measured upon irradiation at 420 nm for the complexes $[Ru(bpy)_2(ab\text{-}PBI)][PF_6]_2$ **71** and $[Cp^*Ir(ab\text{-}PBI)Cl][PF_6]$ **72** and their respective ab-PBI ligands **49a** and **49a′**.[a]

Compounds	Direct method[b]	Indirect method[c]	
	CH_3CN	CH_3CN	Phosphate buffer
ab-PBI **49a**	33%	36%	Not soluble
$[Ru(bpy)_2(ab\text{-}PBI)][PF_6]_2$ **71**	<30%[d]	29%	4%
ab-PBI **49a′**	31%	33%	Not soluble
$[Cp^*Ir(ab\text{-}PBI)Cl][PF_6]$ **72**	87%	85%	21%

[a] The data were provided by the group of Prof. Gilles Gasser.[201] [b] Upon 420 nm irradiation of the compound in the solvent of choice, the luminescence of $^1O_2$ is detected (reference: phenalenone). [c] The produced $^1O_2$ is trapped by an imidazole derivative to form an adduct, which quenches the absorbance of a probe molecule (reference: phenalenone, for experimental details see *experimental section*). [d] The detection limit of the instrumental setup is ~30%.

Both ligands are not soluble under these polar conditions and thus cannot be evaluated. Although the correlation between this singlet oxygen and triplet quantum yield have to be done carefully (see above), the triplet population of the iridium complex **72** seems to be very high and significantly improved than in the ruthenium complex **71**. Accordingly, the heavier 5d-metal iridium seems to have a stronger spin-orbit coupling for the intersystem crossing $S_n \rightarrow T_n$.

To elucidate that all spectral absorption parts of the ab-PBI complexes **71** and **72** contribute to the singlet oxygen sensing in the same way, the excitation spectra were recorded (λ_{em} = 1275 nm, **Figure 63**). Both excitation spectra match well to the absorption spectra and demonstrate strong parallels to the excitation spectra obtained by recording the emissive phosphorescence (λ_{ph} = 745 and 780 nm, **Figure 52**). All in all, the singlet oxygen sensing experiments have demonstrated that the triplet states in the ab-PBI metal complexes are still populated to a certain degree also in polar solvents. However, an additional deactivation process seems to outpace the existing pathways like phosphorescence and photosensitization of water oxidation catalysts.

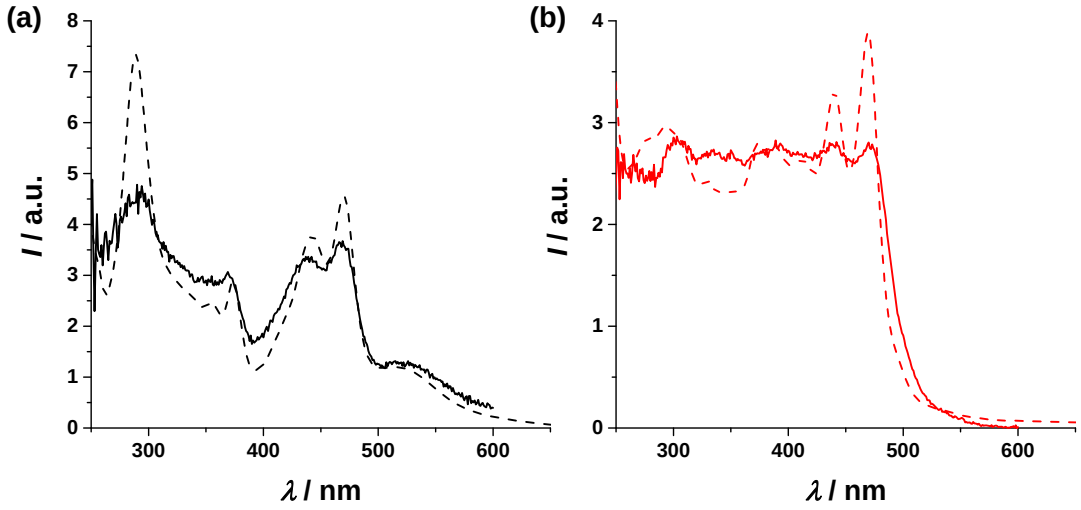

Figure 63 Excitation (λ_{em} = 1275 nm, oxygen-purged solution, solid) and normalized absorption spectra of $[Ru(bpy)_2(ab\text{-}PBI)][PF_6]_2$ **71** (a) and $[Cp^*Ir(ab\text{-}PBI)Cl][PF_6]$ **72** (b) in dichloromethane at room temperature.

Comparison of photosensitizer properties in organic and aqueous medium. There are three important requirements for a proper photosensitizer: (i) Strong absorption in the visible region of light, (ii) appropriate reduction or oxidation power of the excited state and (iii) enough longevity of the excited state. While the non-compliance of the first fact leads only to an efficiency loss of the photosensitizers, the failure of one of the other criteria results in the loss of any photocatalytic activity of the PS. **Table 8** summarizes the

photosensitizer properties of $[Ru(bpy)_2(ab\text{-}PBI)][PF_6]_2$ **71**, which represents the reference system for the ab-PBI metal complex series **71**–**76**.

Table 8 Summary of the photosensitizer properties of $[Ru(bpy)_2(ab\text{-}PBI)][PF_6]_2$ **71** in unpolar and polar solvent medium and their consequences for the realization of photocatalytic conversions.

Criteria for photosensitizers	Properties of ruthenium complex 71	
	in organic medium	in aqueous medium
Visible light absorption	Absorption up to 600 nm	Absorption up to 600 nm
Sufficient potential driving force	0.12 V stronger oxidation potential than $[Ru(bpy)_3]^{2+}$ **8**	Stronger oxidation potential than $[Ru(bpy)_3]^{2+}$ **8**[a]
Longevity of the excited state	μs lifetime	Strongly reduced lifetime
Realization of a photocatalytic conversion	Successful photocatalytic dimerization of 4-nitrobenzyl bromide	Failed photocatalytic water oxidation

[a] The oxidation potential of **71** was not determined in aqueous medium. However, it is expected that the same trend of the $Ru^{2+/3+}$ oxidation potentials between $[Ru(bpy)_3]^{2+}$ **8** and **71** in dichloromethane exists also in polar aqueous medium.

The first criterion of a valuable photosensitizer, namely the strong visible light absorption, is clearly given for the ruthenium complex **71**, which absorbs efficiently light up to 600 nm.

In addition, also the requirement of a sufficient driving force for a chemical conversion in organic medium is fulfilled but with some restrictions. The reduction power of **71** in dichloromethane is reduced by ~0.9 V in comparison to $[Ru(bpy)_3][PF_6]_2$ **8**, whereas the oxidation power is increased by 0.12 V compared to the parent complex, which makes the ab-PBI metal complexes more interesting for photooxidation processes. Although the electrochemistry of the complexes **71**–**76** was only performed in dichloromethane, it can be expected that the trend of the $Ru^{2+/3+}$ oxidation potentials between $[Ru(bpy)_3]^{2+}$ **8** and **71** in dichloromethane (see **Table 5**) exists similarly also in polar aqueous medium.

Criterion three, the longevity of the excited state, makes the real difference between the two media for the photosensitizer **71**. In organic solvents, a μs phosphorescence lifetime exists and thus, a long-lived excited triplet state. In contrast, in polar solvents there is no observable phosphorescence anymore leading to the conclusion that the excited state of **71** is much more short-lived than in organic solutions. Accordingly, it is less surprising that the photocatalytic conversion of 4-nitrobenzyl bromide to 1,2-bis(4-nitrophenyl)ethane in organic medium is successful, whereas the photocatalytic water oxidation reaction in aqueous mixtures fails completely.

Tentative Jablonski term scheme. The main observation during the evaluation of the triplet state can be summarized as followed: The excited state properties like the NIR phosphorescent emission of $[Ru(bpy)_2(ab\text{-}PBI)][PF_6]_2$ **71** are immediately switched off by changing from unpolar to polar solvent conditions. Interestingly, this behavior shows striking similarities to the complex $[Ru(bpy)_2(dppz)]^{2+}$ **37** (see **Figure 18** and **Figure 19**) in which the dppz ligand constitutes of a bipyridine and a phenazine subunit. In **37** there are two close-lying MLCT transitions: The first one is situated on the proximal bipyridine, whereas the second is located on the distal phenazine. The latter of both is invisible by absorption spectroscopy due to the missing orbital overlap between the respective Ru(d) and the ligand phenazine orbital. In the sum, there is on the one hand a proximal MLCT showing significant absorption and responsible for the observed emission and on the other hand there is a distal MLCT, which is invisible by absorption and facilitates the depopulation of the excited state by non-radiative deactivation processes.

Recapitulating the DFT calculations of $[Ru(bpy)_2(ab\text{-}PBI)][PF_6]_2$ **71**, a similar situation in **71** like in ruthenium complex **37** is found (**Figure 56**): There is an energetic low optical transition S_3, which is a MLCT from a Ru(d) orbital to a PBI core orbital with a weak oscillator strength. In contrast, the energetically higher-lying MLCT transition S_6 from the ruthenium metal center to the azabenz-annulated ligand moiety has much higher oscillator strength and fits well to the experimental data. According to the similarities to $[Ru(bpy)_2(dppz)]^{2+}$, an energy level scheme of **71** was tentatively outlined (**Figure 64**), which satisfies the experimental and theoretical results.

After 520 nm light excitation, the $^1MLCT_{ab}$ is populated with a localized electron on the azabenz-annulated subpart of ab-PBI. Afterwards, a charge-shift of the electron from the azabenz-annulated part to the PBI core unit and intersystem crossing to the $^3MLCT_{PBI}$ takes place. The triplet $^3MLCT_{PBI}$ state of **71** is formed after excitation with a rate constant k_{ISC} of $\sim 1.7 \cdot 10^8$ s^{-1} based on transient ns absorption spectroscopy in dichloromethane. These processes should be comparable in all solvents due to their fast nature. However, an additional dark state is postulated in ab-PBI metal complexes, which lead to the modulated emission behavior in different solvent polarities. In dichloromethane, the dark state is higher lying than the bright $^3MLCT_{PBI}$ and thus, does not influence the intrinsic radiative (k_{ph}) as well as the non-radiative deactivation (k^B_{ISC}) of the bright state. In the more polar solvent acetonitrile, the dark state becomes thermodynamically accessible at room temperature and an equilibrium between bright and dark state is established. Accordingly,

the population of the emissive state and thus, the phosphorescence are additionally influenced by the non-radiative rate constant k^{D}_{ISC} of the dark state. The accelerated deactivation of the excited state leads also to the independence from the $^{3}O_{2}$ quencher because non-radiative depopulation outcompetes the $^{3}O_{2}$ quenching rate. In the polar environment of aqueous solutions, the dark state is even more stabilized and thus, it is mainly populated without any repopulation of the bright state. Consequently, the emissive properties and photocatalytic activity of the ruthenium complex **71** vanish completely in the course of the excitation.

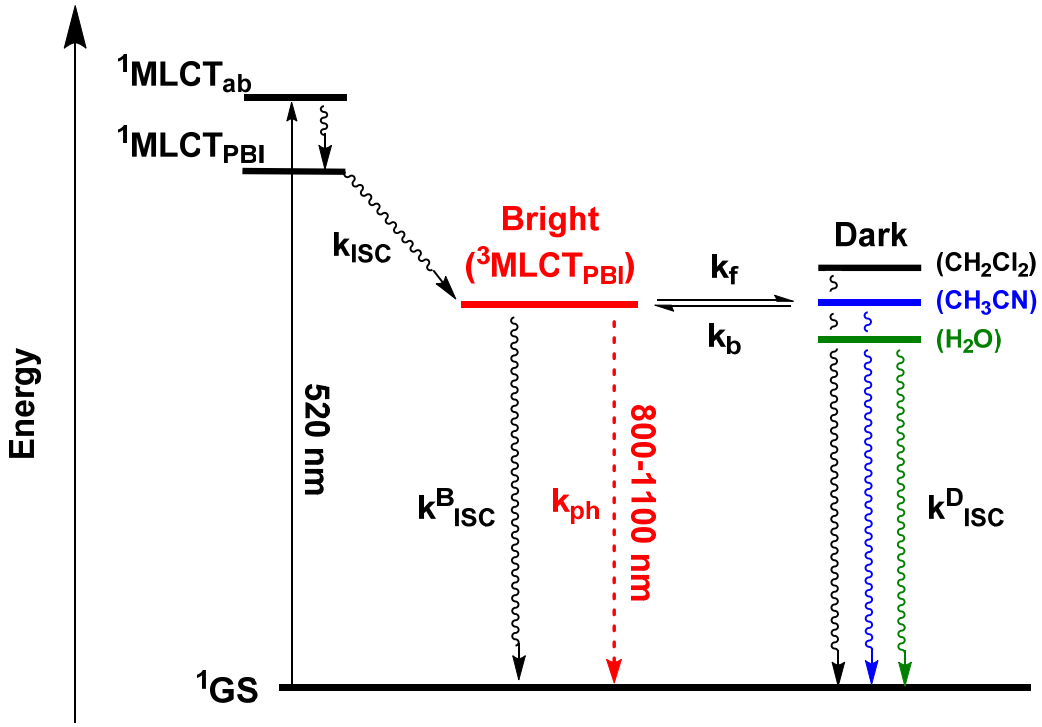

Figure 64 Tentatively constructed energy level diagram of the complex $[Ru(bpy)_2(ab\text{-}PBI)][PF_6]_2$ **71** with assigned relaxation pathways.

On the basis of the collected data, a further assignment on the nature of the dark state is not possible and would clearly exceed the scope of the data. Although the described scenario in **Figure 64** is tentatively constructed, it is an appropriate starting point to design new experiments to unravel the intrinsic photophysical properties of the ab-PBI metal complexes **71**–**76** and thus, to deny or verify the given hypothesis. One of such experiments would be temperature-dependent emission measurements to control the thermal population of the dark state *via* certain temperatures. This experiment was also applied by Meyer and Papanikolas to clarify the energetic situation in $[Ru(bpy)_2(dppz)]^{2+}$ **37**.[134] Faster transient absorption methods like fs pump-probe spectroscopy could elucidate the photophysical intermediates prior to the ns time regime.

In addition, the developed optical and electronic tunability of ab-perylene ligands in subchapter **3.2** allows also a synthetic approach to clarify the photophysics of these metal complexes. The $MLCT_{PBI}$ can be energetically elevated by the variation of the *peri*-groups from imide to diester functions. By electron-withdrawing or electron-donating substituents at single pyridyl ring at the ab subunit, the $MLCT_{ab}$ energy level is accessible and can be modified. In total, all relevant energies are systematically and independently addressable which opens up many starting points to overcome the photophysical shortages of the ab-perylene metal complexes also in aqueous solutions.

CHAPTER 4 SUMMARY

4.1 Summary

The transformation from fossil fuel-based to renewable energy generation is and will be a central and ongoing question in the energy industry. In this regard, light-driven chemical transformations like the reduction of protons and CO_2 as well as the oxidation of water are promising possibilities to achieve this goal. The aim of this thesis was to study different molecular aspects of the light-driven oxidation of water, which is the anodic half-reaction of water splitting.

The first focus of this thesis was the synthesis as well as the characterization of the water oxidation (WO) activity of the metallosupramolecular catalyst $[Ru(bda)bpb]_3$ **46** (**Figure 65a**). At the beginning the conceptual thoughts behind the supramolecular arrangement of the single catalyst units into a supramolecular network and the synthetic self-assembly strategy to obtain such macrocycles were discussed.

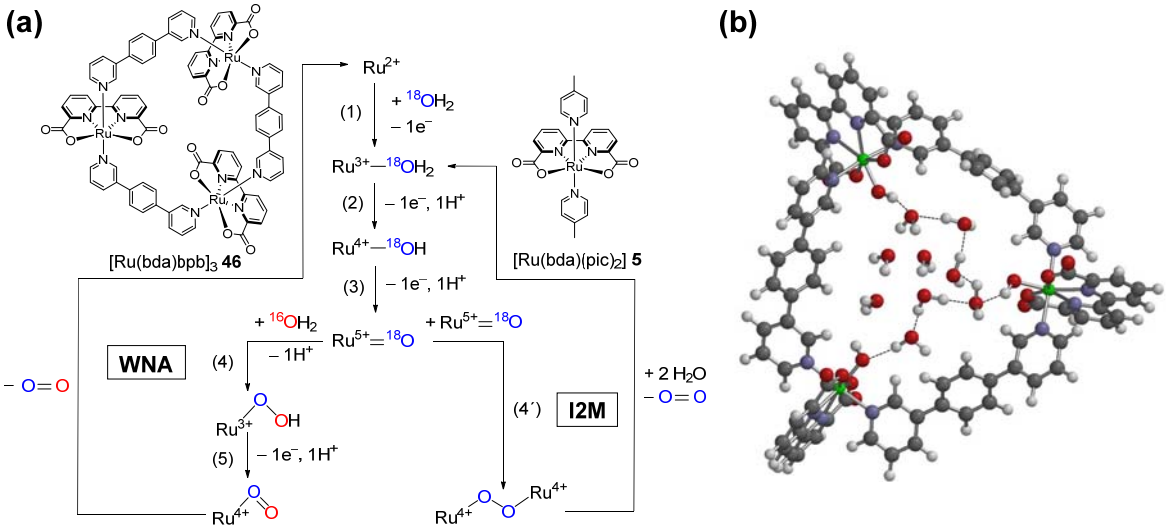

Figure 65 (a) Mechanistic representation of the WNA and I2M reaction pathways of catalytic water oxidation, of which the former is proceeded by the trinuclear ruthenium catalyst $[Ru(bda)bpb]_3$ **46** and the latter by the mononuclear reference catalyst $[Ru(bda)(pic)_2]$ **5**. The color code of the oxygen atoms/molecules represents a simplified ^{18}O-labeling experiment which was essential to confirm the mechanism in the macrocyclic system. (b) DFT-optimized structure of $[Ru^{4+}\text{-}OH(bda)bpb]_3^{3+}$ with cavity-embedded water molecules rationalizing the hydrogen-bonding network inside the interior of the macrocycle which leads to water nucleophilic attack with a low activation barrier.

The structural characterization proved the closed cyclic form of the trinuclear complex. Subsequently, the potentiostatic investigations revealed that the general electrochemical features of the mononuclear reference complex [Ru(bda)(pic)$_2$] **5** are maintained in macrocyclic [Ru(bda)bpb]$_3$ **46**. Spectroelectrochemistry and UV/Vis redox titration with cerium(IV) ammonium nitrate confirmed that the three ruthenium metal atoms act as separate redox centers and can be independently oxidized until the ruthenium oxidation stage +IV. After the electrochemical oxidation of water was proven, the chemically driven WO was investigated with Ce^{4+} as sacrificial oxidant at pH 1. An unprecedented high catalytic activity of 150 s^{-1} (TOF_{max}) and a good TON_{max} value of 7400 for the macrocyclic structure were observed, which is a one order of magnitude higher catalytic activity than for the parent mononuclear catalyst. Furthermore, an in-depth kinetic WO investigation was depicted and the results were compared to the parent [Ru(bda)(pic)$_2$]. In this process it was found that the rate-determining step (RDS) of the WO, using the macrocycle as catalyst, is first-order in catalyst and Ce^{4+} concentration as well as characterized by an O–H bond breaking process. These RDS findings were opposed to the water oxidation reaction catalyzed by [Ru(bda)(pic)$_2$] which is second-order in catalyst concentration, zeroth-order in oxidant concentration and proton uncoupled. Additional catalytic and UV/Vis experiments with stoichiometric Ce^{4+} amounts revealed that there is a $[Ru^{4+}–OH]_3^{3+}$-resting state formed for the macrocycle. Consequently, the reaction step afterwards, the $Ru^{4+/5+}$ oxidation, becomes rate-limiting for the oxidation of water. Because both mechanistic pathways, WNA and I2M, pass through this intermediate stage, only ^{18}O labeling experiments could help to distinguish between the mechanisms (**Figure 65a**). The performed catalytic experiments with ^{18}O-labeled water, in which the different oxygen isotopes were analyzed by mass spectrometry, unambiguously proved the WNA mechanism to be operative for the macrocycle [Ru(bda)bpb]$_3$.

The mechanistic investigation indicates that the macrocycle [Ru(bda)bpb]$_3$ **46** enables a water nucleophilic attack with a very low activation barrier by preorganizing water molecules inside its cavity. Consequently, the rate-determining step shifts from the nucleophilic attack of water at Ru^{5+}=O (reaction step (4) in **Figure 65a**) to the earlier oxidation step (3). This closely resembles many enzymatic processes in which natural systems – like the oxygen-evolving complex of photosystem II – modulate the reactivity of water molecules for particular reactions by pre-organizing them appropriately. The experimental proof for this hypothesis could not be provided within this work; therefore,

theoretical calculations on a DFT level of theory were performed. A DFT-optimized molecular structure with cavity-embedded water molecules showed that a hydrogen-bond network exists in the interior of the macrocycle and that only three water molecules are required to bridge efficiently the distance between two catalyst centers (**Figure 65b**).

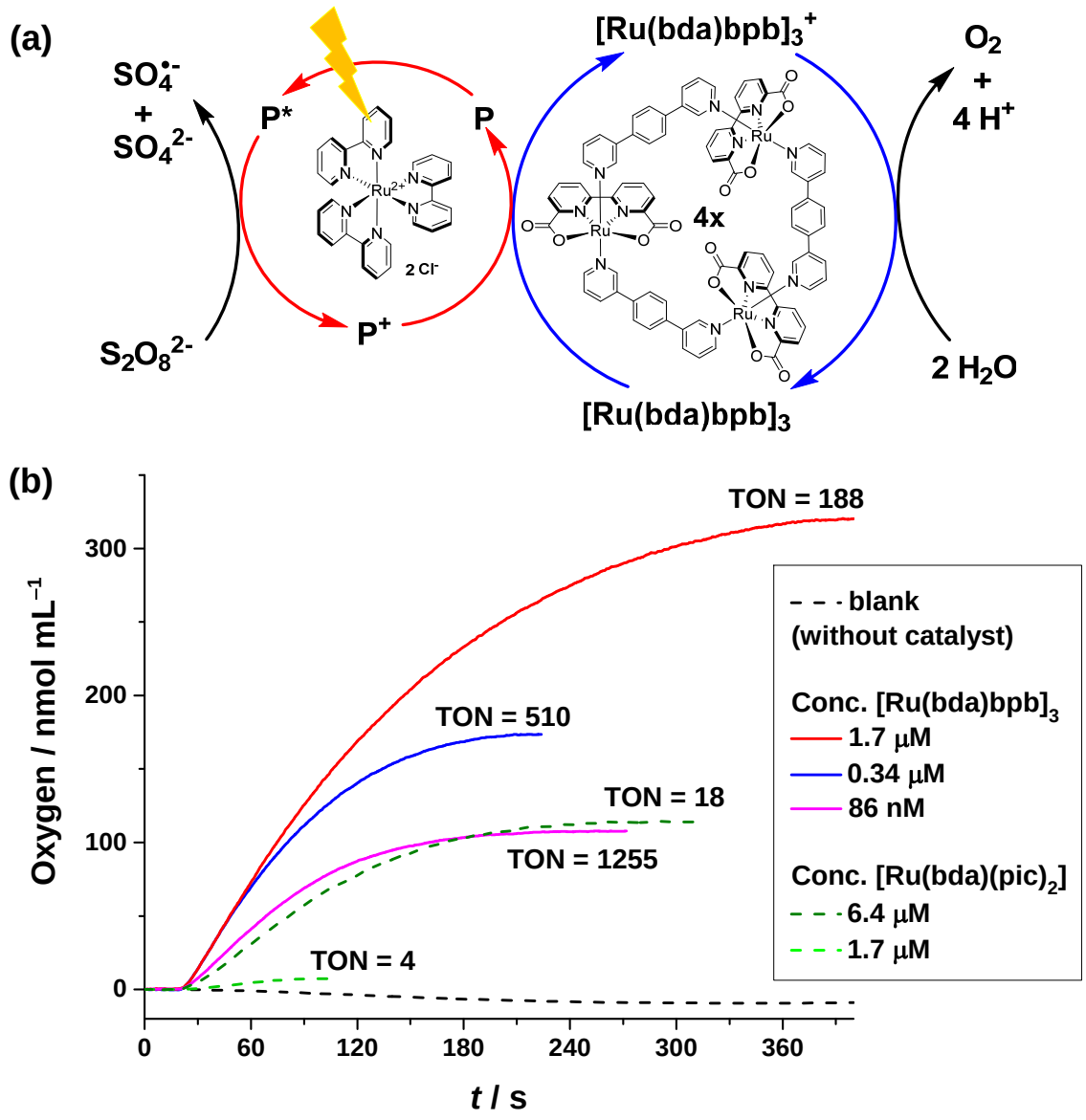

Figure 66 (a) Scheme of light-induced water oxidation with $[Ru(bda)bpb]_3$ **46** as WOC, $[Ru(bpy)_3][Cl]_2$ **8** as photosensitizer (P) and $Na_2S_2O_8$ as sacrificial electron acceptor. To preserve the simplicity of the schematic representation, the oxidation cycle of $[Ru(bda)bpb]_3$ **46** contains only the two redox states $[Ru^{2+}(bda)bpb]_3$ and $[Ru^{3+}(bda)bpb]^{+}_{3}$. A more appropriate scheme has to include the proton-coupled electron transfer processes of the higher oxidation states of ruthenium (Ru^{3+}, Ru^{4+} and Ru^{5+}) in which water is coordinated to the ruthenium center as well. (b) Comparison of the oxygen evolution curves of the photocatalytic water oxidation between the trinuclear macrocycle $[Ru(bda)bpb]_3$ **46** and mononuclear reference complex $[Ru(bda)(pic)_2]$ **5**.

The mechanistic differences between the trinuclear macrocyclic $[Ru(bda)bpb]_3$ **46** and the mononuclear reference catalyst $[Ru(bda)(pic)_2]$ has also application-oriented relevance as it can be seen in light-driven water oxidation experiments. Three-component light-driven water oxidation studies with $[Ru(bda)bpb]_3$ **46** or $[Ru(bda)(pic)_2]$ **5** as catalyst, $[Ru(bpy)_3][Cl]_2$ as photosensitizer and $Na_2S_2O_8$ as sacrificial electron acceptor (**Figure 66**) showed that the macrocycle $Ru(bda)bpb]_3$ has high catalytic activity even in the nM concentration regime (TON >1255 and TOF = 13.1 s^{-1}). In comparison, $[Ru(bda)(pic)_2]$ revealed only a low TON of 18 and a TOF of 0.13 s^{-1}. This extreme performance difference under dilute conditions is a consequence of the unimolecular WNA reaction mechanism accessible solely to the macrocyclic system. Only unimolecular catalytic systems are capable of such activity under high dilution because diffusion-limited collision of two catalytic subunits, which is essential for bimolecular mechanisms like I2M, becomes unnecessary. This behavior makes the macrocycle also attractive for surface applications in which the molecular mobility is strongly reduced by the covalent surface attachment.

The second part of this thesis was concerned about photosensitizers for light-driven chemical conversions. In this regard, azabenz-annulated perylene bisimide (ab-PBIs) derivatives, a new type of polypyridyl ligands with an integrated perylene moiety, were prepared. Therefore, an existing Pictet-Spengler protocol was improved and new preparation methods were developed to extend the versatility and scope of this ligand class (**Scheme 17**). The modified Pictet-Spengler procedure allowed the conversion of 1-amino-perylene bisimide **47** with a variety of aldehydes (highlighted in green). The so synthesized ab-PBIs **49a-f** provide diverse donor functionalities for the complexation of different metal complex fragments. Furthermore, the reaction of **47** with bisaldehydes created the dimeric ab-PBI compounds **68** and **69**. Next to the 2,6-diisopropylphenyl imide substituent also other solubilizing imide substituents like oligoethyleneglycol chains could be introduced by a synthetic route *via* the azabenz-annulated perylene bisanhydride **52** (highlighted in red). In this process, the imidization can be placed as final step in the reaction cascade. The exclusive regioselective nitration of perylene monoimide diester **57** to 1-nitro-PMIDE **58** enabled as well the preparation of unsymmetric *peri*-substituted ab-perylenes (ab-PMIDE **60** and ab-PMIMA **61**, highlighted in orange). Besides monofunctionalized perylene derivatives, also the bisazabenz-annulated perylene compounds $(ab)_2$-PBI (*anti*-$(ab)_2$-PBI **63** and *syn*-$(ab)_2$-PBI **64** highlighted in blue) and $(ab)_2$-PTE could be realized providing a

second coordination pocket for the construction of multinuclear metal complexes. The optical, electronic and theoretical investigations revealed that the properties of these dyes can be widely tuned (*e.g.* shift of the two PBI-centered reductions by ~0.7 V). Furthermore, the outlined chemical modifications allow a high flexibility for future applications like the chemisorption of perylene anhydrides onto TiO_2 surfaces by anhydride opening.

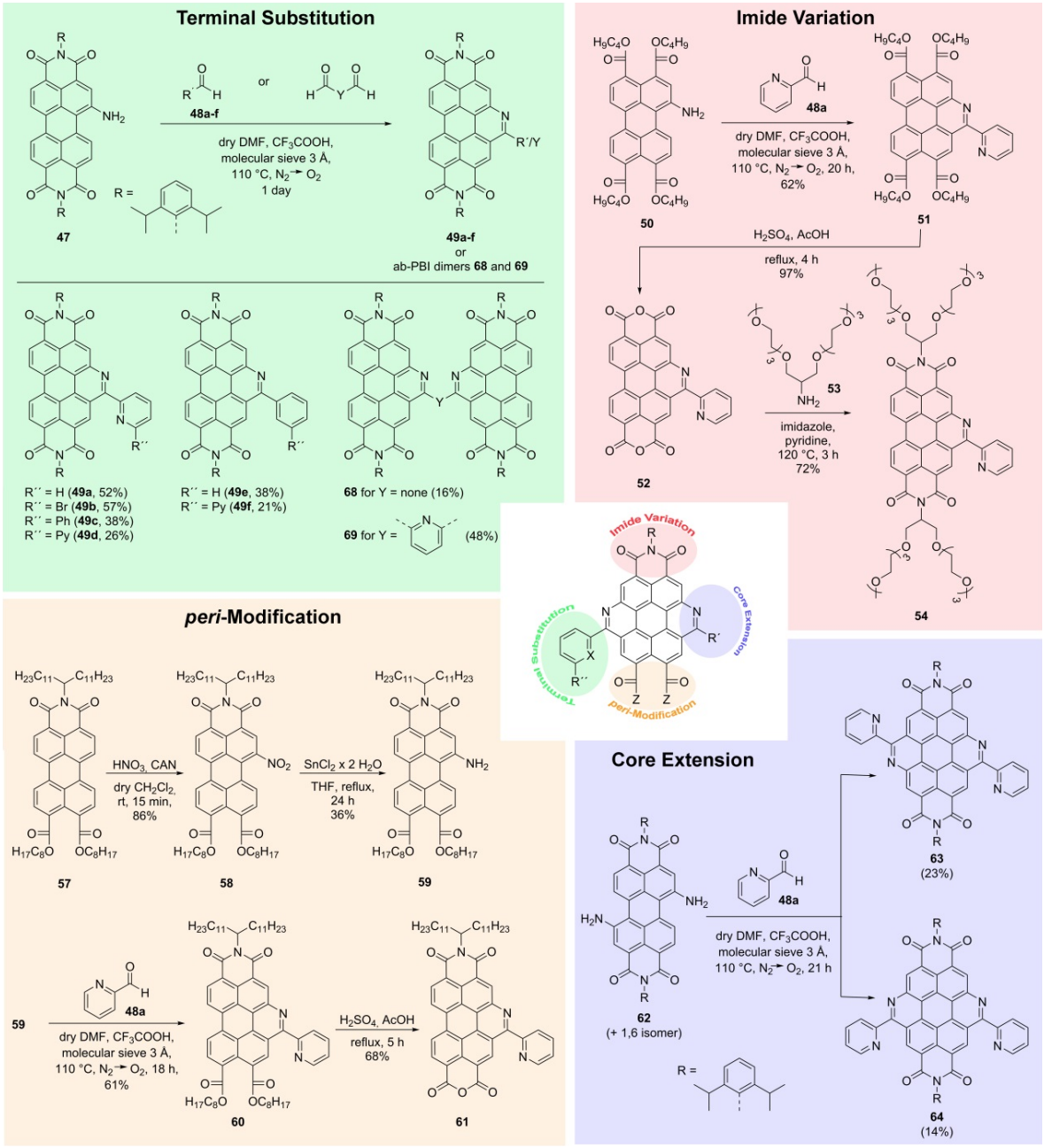

Scheme 17 Overview about the manifold possibilities to functionalize the azabenz-annulated perylene core fragment with the synthetic procedures outlined in this thesis.

Hereafter, the PBI-metal complexes were described, which were obtained by coordination of the azabenz-annulated perylene bisimides to metal complex fragments. The used metal centers were either the transition metal ruthenium, as in the complex $[Ru(bpy)_2(ab\text{-}PBI)][PF_6]_2$ **71** (**Chart 6**), or the transition metal iridium ($[Cp^*Ir(ab\text{-}PBI)Cl][PF_6]$ **72**). Besides the monoazabenz-annulated PBI **49a**, the bisfunctionalized perylenes *anti*-$(ab)_2$-PBI **63** and *syn*-$(ab)_2$-PBI **64** were also used as ligands to construct mono- and bimetallic complexes (**73**–**76**). After successful synthesis, the ground state properties of the complexes, like light absorption and electrochemistry, demonstrated that the ab-PBI based metal complexes are not only the sum of their single components but that additional states are formed as well, like for example the bathochromically shifted MLCT states in the ruthenium complexes.

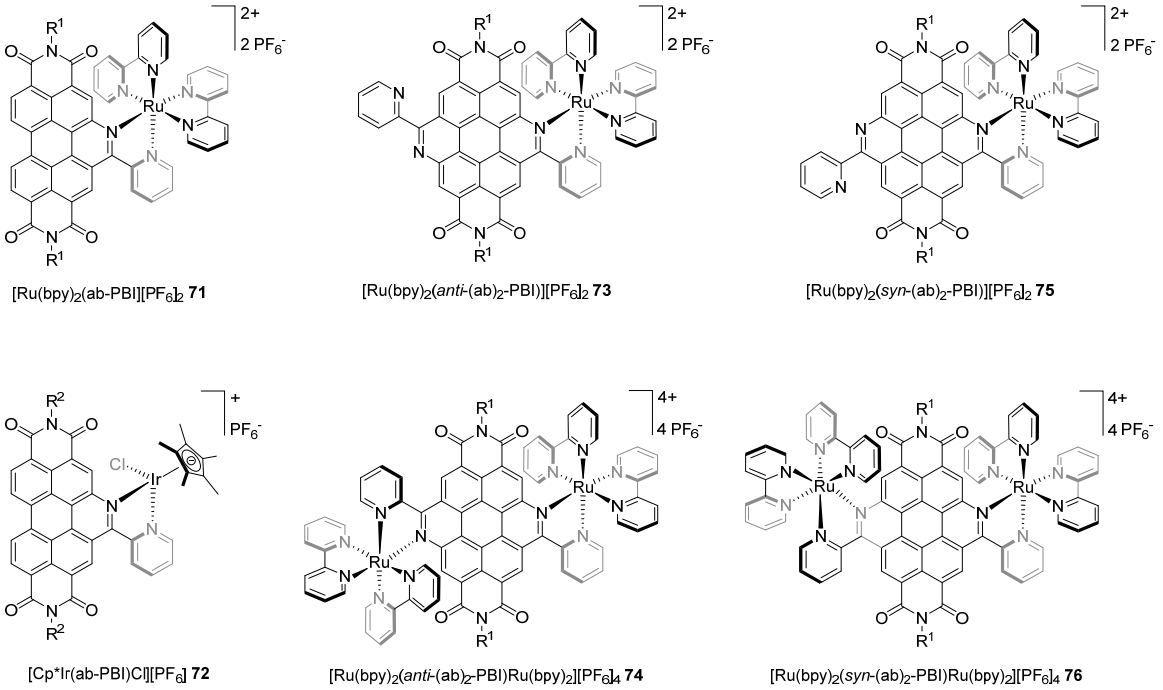

Chart 6 Overview of the ab-PBI based meal complexes **71**–**76** which have been synthesized in this thesis (R^1 = 2,6-diisopropylphenyl und R^2 = 3-pentyl).

The emission features of the complexes **71**–**76** displayed a complete quenching of the perylene fluorescence, whereas a new phosphorescence (Φ_{ph} up to 11%) in the NIR region became observable in degassed dichloromethane (**Figure 67**). Nanosecond transient absorption spectroscopy, DFT calculations and singlet oxygen generation experiments revealed that the excited state of these complexes is PBI-centered and has a strong MLCT character. Consequently, the complexes $[Ru(bpy)_2(ab\text{-}PBI)][PF_6]_2$ **71** and $[Cp^*Ir(ab\text{-}PBI)Cl][PF_6]$ **72** exhibit photosensitizer potential in organic media as for instance in the

photocatalytic dimerization of 4-nitrobenzyl bromide to 1,2-bis(4-nitrophenyl)ethane. Unfortunately, this promising photosensitizer capability vanished once the solvent medium was changed from organic to aqueous solutions. All attempts to drive photocatalytic water oxidation with the photosensitizer complexes **71**–**76** failed. Furthermore, luminescent and singlet oxygen sensing studies in aqueous medium demonstrated that phosphorescence diminishes as well, and the triplet state population changes. Based on theoretical calculations on $[Ru(bpy)_2(ab\text{-}PBI)][PF_6]_2$ **71** and the similarities to the complex $[Ru(bpy)_2(dppz)]^{2+}$ **37** which is known from literature, it is assumed that there is an additional excited dark state in **71**. This state is energetically close to the emissive $^3MLCT_{PBI}$ state, causing quenching of the NIR phosphorescence (**Figure 67**). With increasing solvent polarity the energy level of this dark state is decreasing so that the excited state energy can rapidly be dissipated to the ground state by intersystem crossing with the non-radiative rate constant k^D_{ISC}.

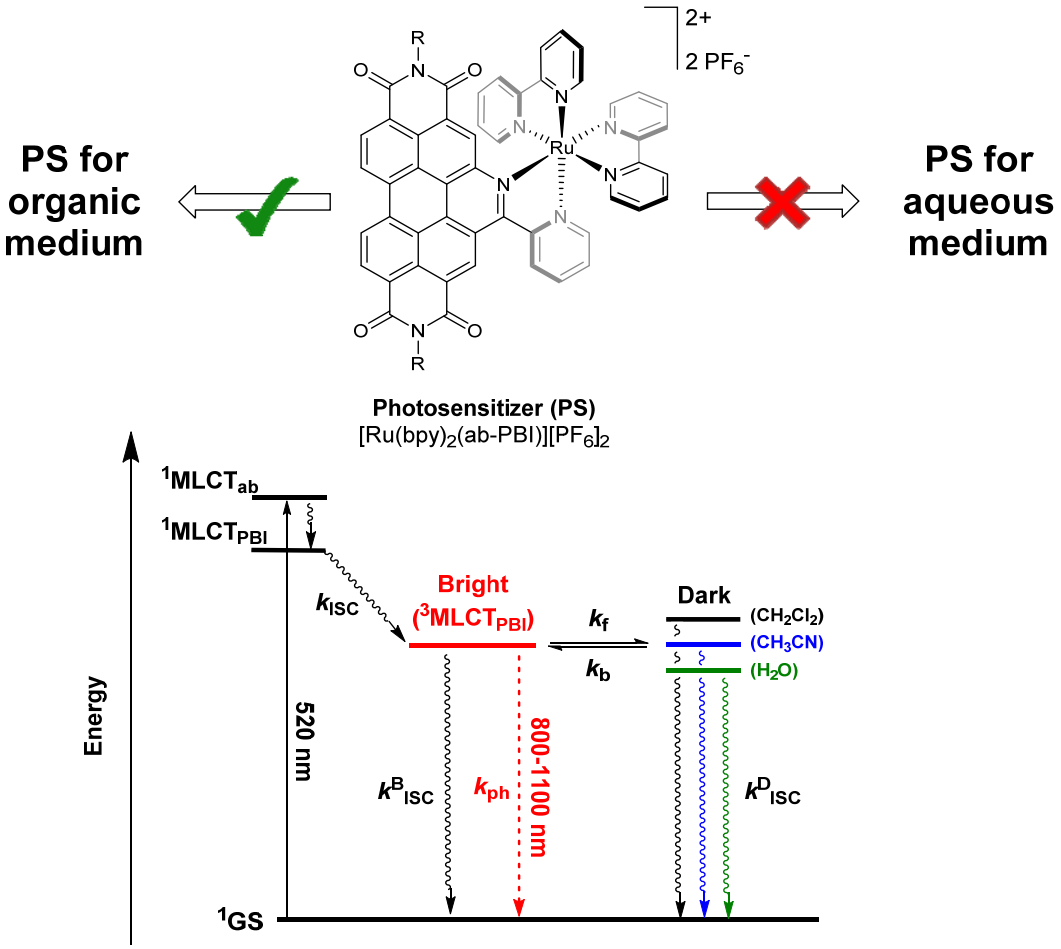

Figure 67 Schematic representation of the photosensitizer properties and summary of the photophysical processes after light excitation of ab-PBI based ruthenium(II) polypyridyl complexes in different polar solvents. $[Ru(bpy)_2(ab\text{-}PBI)][PF_6]_2$ **71** is exemplarily depicted as representative of the whole substance class.

In conclusion, this thesis elaborated that metallosupramolecular assemblies such as the trinuclear macrocycle [Ru(bda)bpb]$_3$ **46** are promising catalyst systems for the oxidation of water. The metallosupramolecular structure increase the catalytic activity in comparison to the parent mononuclear complex with an unexpected mechanistic change from the I2M to the WNA pathway. On the other hand, the ab-PBI based metal complexes **71**–**76** demonstrated that the realization of the light-driven oxidation of water remains an enormous challenge. The photosensitizers based on ab-PBI ligands and {Ru(bpy)$_2$} and {IrCp*Cl} complex fragments like [Ru(bpy)$_2$(ab-PBI)][PF$_6$]$_2$ **71** are strong light absorbers with a remarkable NIR phosphorescence that can drive photocatalytic conversions in organic media. In aqueous environment these promising features vanish concomitant with the loss of the luminescence properties prohibiting the photocatalytic oxidation of water.

Mimicking the water oxidation efficiency of the natural PSII can be realized quite well as this thesis has demonstrated with a TON value 7400 and TOF value of 150 s^{-1} (comparison to the natural PSII: TON = $1.8 \cdot 10^5$, TOF = 100–400 s^{-1}). However, the proper connection of the individual molecular components for an efficient artificial photosynthesis is difficult to achieve and there is still some way to go. Large-scale solar fuel production is a long-term energy strategy and will most likely not be achieved within the next 10 to 20 years even with extensive efforts. But once accomplished, mankind will have overcome one of its greatest challenges to ensure a reliable and sustainable energy supply.

4.2 Zusammenfassung

Die Umstellung der Energieerzeugung von fossilen Brennstoffen hin zu erneuerbaren Energien ist derzeit eine zentrale Problemstellung in der Energiewirtschaft und wird dies wahrscheinlich auch noch lange Zeit sein. Lichtgetriebene chemische Umsetzungen wie zum Beispiel die Reduktion von Protonen oder Kohlendioxid sowie die Oxidation von Wasser spielen bei der Lösung des Energieproblems eine wichtige und vielversprechende Rolle. Daher beschäftigt sich die vorliegende Arbeit mit unterschiedlichen molekularen Aspekten der lichtgetriebenen Wasseroxidation – der anodischen Halbreaktion der Wasserspaltung.

Der erste Arbeitsschwerpunkt bestand in der Synthese sowie der Charakterisierung der Wasseroxidationseigenschaften des metallosupramolekularen Katalysators $[Ru(bda)bpb]_3$ **46** (**Abbildung 1a**). Zunächst wurde die konzeptionelle Motivation hinter der supramolekularen Anordnung einzelner Katalysatoren in einem Komplexverbund sowie die Selbstassemblierungs-Strategie, mit welcher der Makrozyklus hergestellt werden konnte, beschrieben. Die nachfolgende strukturelle Charakterisierung bewies die geschlossen-zyklische Natur des dreikernigen Komplexes. Potentiostatische Untersuchungen verdeutlichten, dass sich die grundlegenden elektrochemischen Merkmale des einkernigen Referenzkomplexes $[Ru(bda)(pic)_2]$ **5** auch im supramolekularen $[Ru(bda)bpb]_3$ **46** wiederfinden. Anschließend bestätigten spektroelektrochemische Untersuchungen sowie UV/Vis-Redoxtitrationen mit Cer(IV)-ammoniumnitrat, dass die drei Rutheniummetallatome als unabhängige Redoxzentren agieren und getrennt voneinander bis zur Rutheniumoxidationsstufe +IV oxidiert werden können. Nach dem Beweis der elektrochemischen Wasseroxidation (WO), wurde die chemisch getriebene WO mit dem Opferoxidationsmittel Ce^{4+} bei pH 1 untersucht. In diesem Zusammenhang konnte eine unerwartet hohe katalytische Aktivität von 150 s^{-1} (TOF_{max}) und ein guter TON_{max}–Wert von 7400 für die makrozyklische Struktur beobachtet werden – dies ist eine um eine Größenordnung höhere Aktivität als im zugrundeliegenden einkernigen Referenzkomplex. Im weiteren Verlauf wurden ausführliche kinetische WO-Untersuchungen durchgeführt, bei welchen der artverwandte einkernige Katalysator in allen Experimenten als Referenz diente.

Es zeigte sich, dass der geschwindigkeitsbestimmende Schritt (engl. rate-determining step = RDS) der Wasseroxidation, mit dem Makrozyklus als Katalysator, erster Ordnung in Bezug auf die Konzentration des Katalysators und nullter Ordnung bezüglich der Oxidationsmittelkonzentration, sowie durch einen O-H Bindungsbruch charakterisiert ist. Interessanterweise waren diese RDS-Befunde entgegengesetzt zu denen der Wasseroxidation mit dem Katalsyator $[Ru(bda)(pic)_2]$, welche zweiter Ordnung bezüglich der Katalysatorkonzentration, nullter Ordnung in Bezug auf die Oxidationsmittelkonzentration und Protonen-ungekoppelt ist. Katalyse- und UV/Vis-Experimente mit stöchiometrischen Mengen Ce^{4+} bewiesen, dass für $[Ru(bda)bpb]_3$ ein stationärer $[Ru^{4+}–OH]_3^{3+}$-Zwischenzustand existiert. Weil beide Mechanismen – WNA und I2M – diesen Zustand durchlaufen, verblieben als Unterscheidungskriterium nur noch ^{18}O-isotopenmarkierte Untersuchungen (**Abbildung 1a**). Die dazu durchgeführten Experimente, in welchen die Sauerstoffisotopenverteilung mittels Massenspektrometrie analysiert wurde, zeigten eindeutig, dass der Makrozyklus $[Ru(bda)bpb]_3$ über den WNA-Reaktionspfad verläuft.

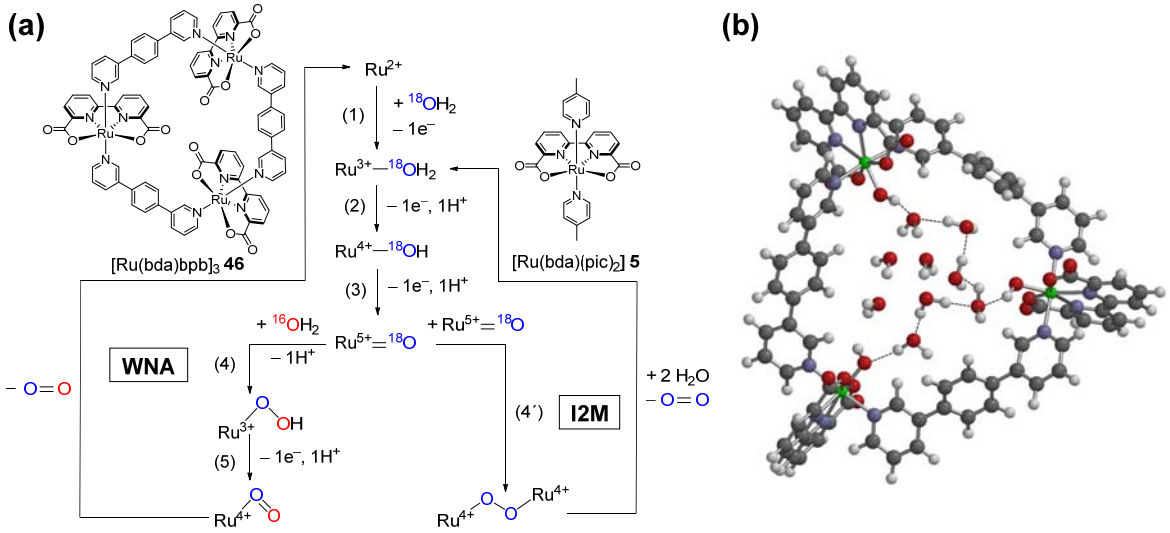

Abb. 1 (a) Mechanistische Darstellung des WNA und I2M Reaktionsweges der katalytischen Oxidation von Wasser. Die Wasseroxidation durch den dreikernige Rutheniumkatalysator $[Ru(bda)bpb]_3$ **46** verläuft hierbei über den WNA-Mechanismus, wohingegen der einkernige Referenzkatalysator $[Ru(bda)(pic)_2]$ **5** den I2M-Reaktionspfad benutzt. Der angegebene Farbcode der Sauerstoffatome veranschaulicht ein vereinfachtes ^{18}O-Markierungsexperiment, welches im Falle des Makrozyklus für die mechanistische Aufklärung von zentraler Bedeutung war. (b) DFT-optimierte Struktur des oxidierten Makrozyklus $[Ru^{4+}\text{-}OH(bda)bpb]_3^{3+}$ mit im Innenraum eingeschlossenen Wassermolekülen, welche ein Wasserstoffbrückennetzwerk ausbilden und somit einen nukleophilen Wasserangriff mit niedriger Aktivierungsbarriere ermöglichen.

Zusammengefasst weisen die mechanistischen Untersuchungen darauf hin, dass der Makrozyklus $[Ru(bda)bpb]_3$ **46** einen nukleophilen Angriff eines Wassermoleküls auf $Ru^{5+}=O$ mit einer niedrigen Aktivierungsbarriere erlaubt, wobei wahrscheinlich Wassermoleküle im Innenraum des Zyklus für den Angriff besonders vororientiert werden. Folgerichtig verschiebt sich der geschwindigkeitsbestimmende Schritt vom nukleophilen Angriff des Wassers an $Ru^{5+}=O$ (Reaktionsschritt (4) in **Abbildung 1a**) auf den vorgelagerten Oxidationsschritt (3). Ein solches Verhalten findet sich in vielen enzymatischen Prozessen, in welchen natürliche Systeme – wie der Sauerstoff-entwickelnde Komplex des Photosystems II (PSII) – ebenfalls die Reaktivität des Wassers durch entsprechende Vororganisation modifizieren. Der experimentelle Beweis für diese Hypothese konnte im Rahmen dieser Arbeit nicht geliefert werden, weshalb theoretische Berechnungen auf DFT-Niveau durchgeführt wurden. In einer DFT-optimierten Molekülstruktur mit eingebetteten Wassermolekülen im Innenraum des Makrozyklus zeigte sich, dass einerseits ein Netzwerk aus Wasserstoffbrückenbindungen existiert und des Weiteren nur drei Wassermoleküle notwendig sind, um den Abstand zwischen zwei Katalysatorzentren zu überbrücken (**Abbildung 1b**).

Der mechanistische Unterschied zwischen dem dreikernigen metallosupramolekularen Makrozyklus $[Ru(bda)bpb]_3$ **46** und dem einkernigen Referenzkomplex $[Ru(bda)(pic)_2]$ **5** hat auch anwendungsbezogene Relevanz, wie das Beispiel der lichtgetriebenen Wasser-oxidation eindrucksvoll demonstriert hat. In photokatalytischen Wasseroxidations-experimenten mit $[Ru(bda)bpb]_3$ **46** bzw. $[Ru(bda)(pic)_2]$ **5** als Wasseroxidations-katalysator, $[Ru(bpy)_3][Cl]_2$ als Photosensibilisator und $Na_2S_2O_8$ als Elektronenakzeptor (**Abbildung 2**) zeigte $[Ru(bda)bpb]_3$ ausgezeichnete Aktivitäten bis in den nM-Konzentrationsbereich (TON >1255 und TOF = 13.1 s^{-1}). Im Vergleich hierzu erreichte $[Ru(bda)(pic)_2]$ nur einen maximalen TON von 18 und eine TOF von 0.13 s^{-1}. Dieser extreme Leistungsunterschied unter verdünnten Bedingungen ist eine Folge des unimolekular ablaufenden WNA-Mechanismus. Nur so operierende Katalysatoren können bei solch hoher Verdünnung noch hervorragende Ergebnisse erzielen, da hierfür keine diffusionskontrollierte Kollision von Reaktionsintermediaten wie im Falle des I2M-Mechanismus notwendig ist. Dieser Befund macht den Makrozyklus auch für oberflächen-basierende Anwendungen interessant, in welchen die molekulare Beweglichkeit durch die kovalente Oberflächenanknüpfung eingeschränkt ist.

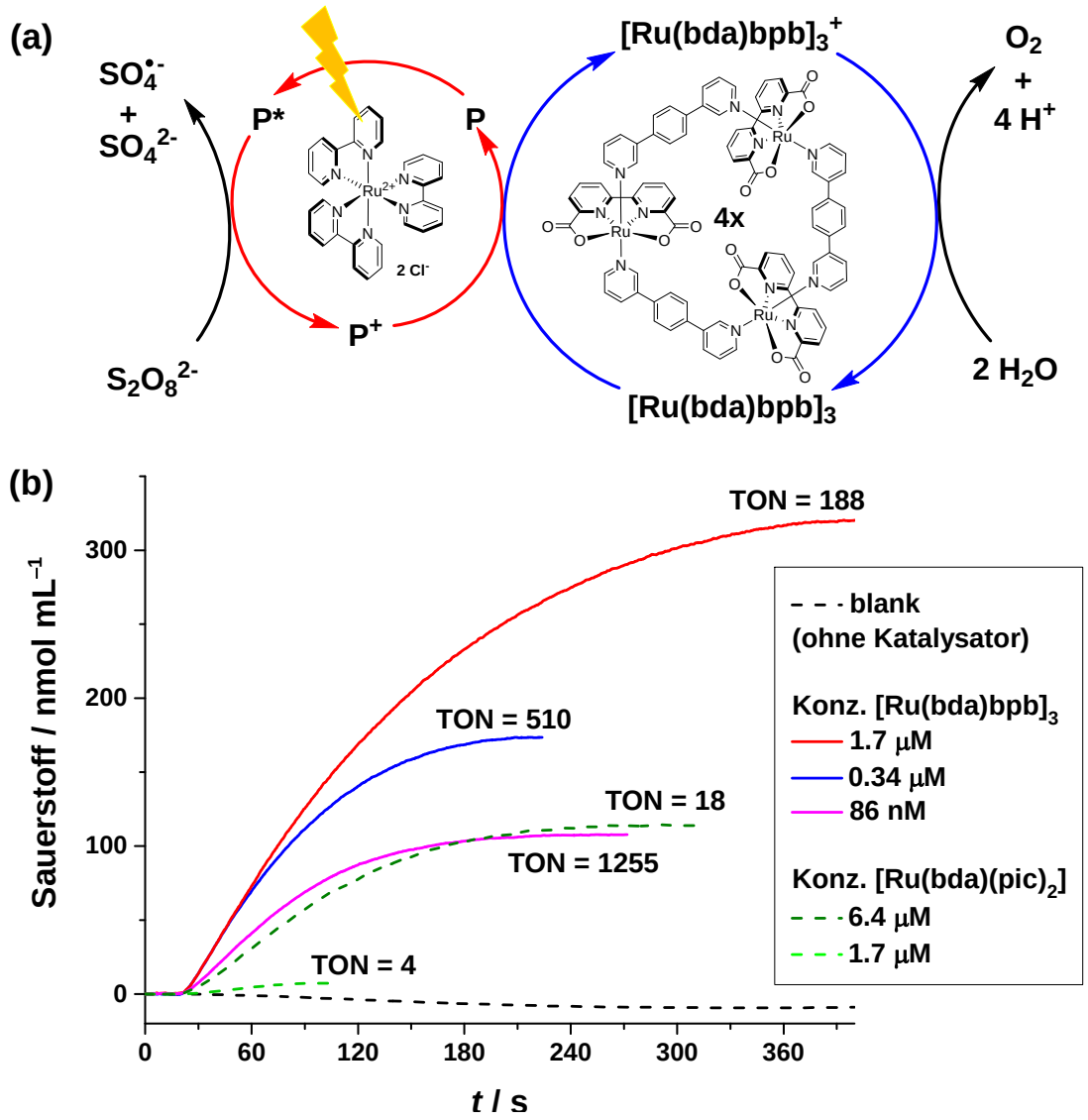

Abb. 2 (a) Schema der photokatalytischen Wasseroxidation mit $[Ru(bda)bpb]_3$ **46** als Wasseroxidationskatalysator, $[Ru(bpy)_3][Cl]_2$ **8** als Photosensibilisator (P) und $Na_2S_2O_8$ als Elektronenakzeptor. Um die Einfachheit der schematischen Darstellung zu bewahren, wurden im Oxidationskreislauf von $[Ru(bda)bpb]_3$ **46** nur die beiden Redoxzustände $[Ru^{2+}(bda)bpb]_3$ und $[Ru^{3+}(bda)bpb]_3^+$ angegeben. Ein genaueres Schema müsste des Weiteren die Proton-gekoppelten Elektronentransferprozesse der höhere Oxidationsstufen des Rutheniums (Ru^{3+}, Ru^{4+} und Ru^{5+}), bei welchen Wasser an das Metallzentrum koordiniert ist, beinhalten. b) Vergleich der Sauerstoffentwicklung im photokatalytischen Wasseroxidationsexperiment zwischen dem dreikernigen Makrozyklus $[Ru(bda)bpb]_3$ **46** und dem einkernigen Referenzkomplex $[Ru(bda)(pic)_2]$ **5**.

Der zweite Teil der Doktorarbeit befasste sich mit Chromophoren beziehungsweise Photosensibilisatoren für lichtgetriebene chemische Umwandlungen. Hierzu wurden azabenz-anellierte Perylenbisimidderivate (ab-PBIs) hergestellt, welche eine neue Klasse von Polypyridyl-Liganden mit einer integrierten Perylenuntereinheit darstellen. Die Vielseitigkeit sowie die Anwendungsbreite dieses Ligandentyps wurde durch die Weiterentwicklung einer bestehenden Pictet-Spengler-Synthese und die Erarbeitung neuer Herstellungsmethoden ausgebaut (**Schema 1**). Das modifizierte Pictet-Spengler-Protokoll erlaubte die Umsetzung des 1-Amino-Perylenbisimids **47** mit einer Vielzahl verschiedener Aldehyde (grün hervorgehoben). Hierbei konnten verschiedene ab-PBIs (**49a-f**) erhalten werden, welche durch ihre unterschiedlichen Donorfähigkeiten die Komplexierung verschiedener Metallkomplexfragmente ermöglichen. Des Weiteren konnten durch die Reaktion von **47** mit Bisaldehyden die dimere PBI-Strukturen **68** und **69** hergestellt werden. Neben dem 2,6-Diisopropylphenyl-Imidsubstituent konnten auch andere löslichkeitsvermittelnde Imidsubstituenten wie Oligoethylenglykolketten mit Hilfe einer Syntheseroute, die über das azabenz-anellierte Perylenbisanhydrid **52** verläuft, leicht eingeführt werden (rot hervorgehoben). Hierbei stellt die Imidisierung den letzten Schritt der Reaktionskaskade dar. Die regioselektive Nitrierung des Perylenmonoimiddiesters **57** zu 1-Nitro-PMIDE **58** erlaubte des Weiteren die Herstellung von ab-Perylenen mit unsymmetrischen *peri*-Modifikationen (ab-PMIDE **60** und ab-PMIMA **61**, orange hervorgehoben). Neben den monofunktionalisierten Perylenderivaten konnten auch die bisazabenz-anellierten Perylenverbindungen $(ab)_2$-PBI (*anti*-$(ab)_2$-PBI **63** und *syn*-$(ab)_2$-PBI **64** (blau hervorgehoben) und $(ab)_2$-PTE realisiert werden, welche aufgrund einer zweiten Koordinationsmöglichkeit die Herstellung von mehrkernigen Metallkomplexen erlauben.

Die optischen, elektronischen und theoretischen Untersuchungen ergaben, dass die Eigenschaften dieser Farbstoffe in großem Umfang angepasst werden können (z.B. Verschiebung der beiden PBI-zentrierten Reduktionen um ~0.7 V). Zusätzlich führen die aufgezeigten chemischen Veränderungen zu einer hohen Flexibilität für zukünftige Anwendungen, wie zum Beispiel die Chemisorption von Perylenanhydridderivaten auf TiO_2-Oberflächen mittels einer entsprechenden Anhydridöffnung.

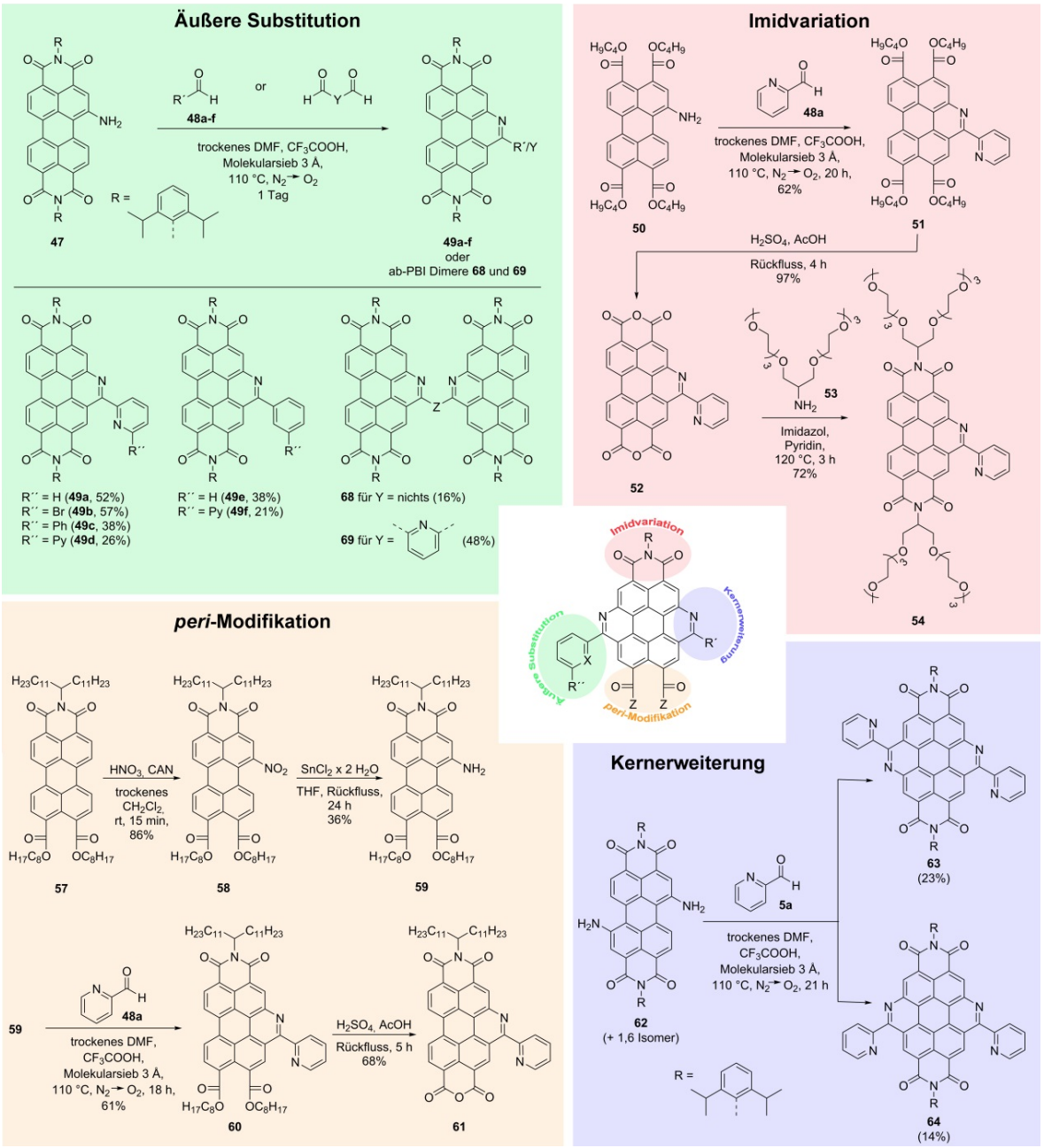

Schema 1 Überblick über die vielfältigen Funktionalisierungsmöglichkeiten der azabenz-anellierten Perylenfarbstoffe, welche in dieser Arbeit beschrieben wurden.

Anschließend wurden PBI-Metallkomplexe beschrieben, welche durch Koordination der azabenz-anellierten Perylenbisimide an Metallkomplexfragmente erhalten wurden. Bei den verwendeten Metallzentren handelte es sich entweder um das Übergangsmetall Ruthenium, wie im Komplex $[Ru(bpy)_2(ab\text{-}PBI)][PF_6]_2$ **71** (**Tafel 1**), oder das Übergangsmetall Iridium ($[Cp^*Ir(ab\text{-}PBI)Cl][PF_6]$ **72**). Neben dem monoazabenz-anellierten PBI **49a** wurden auch die zweifach funktionalisierten Perylene *anti*-$(ab)_2$-PBI **63** und *syn*-$(ab)_2$-PBI **64** zur Herstellung von mono- und bimetallischen Rutheniumkomplexen (**73**–**76**) verwendet.

Die Eigenschaften des Grundzustands dieser Komplexe – Lichtabsorption und Elektrochemie – verdeutlichten, dass die ab-PBI basierenden Koordinationsverbindungen nicht bloß die Summe der Eigenschaften ihrer Einzelbestandteile aufweisen, sondern dass auch neue zusätzliche Zustände wie die bathochrom-verschobenen MLCT-Zustände in den Rutheniumkomplexen vorhanden sind.

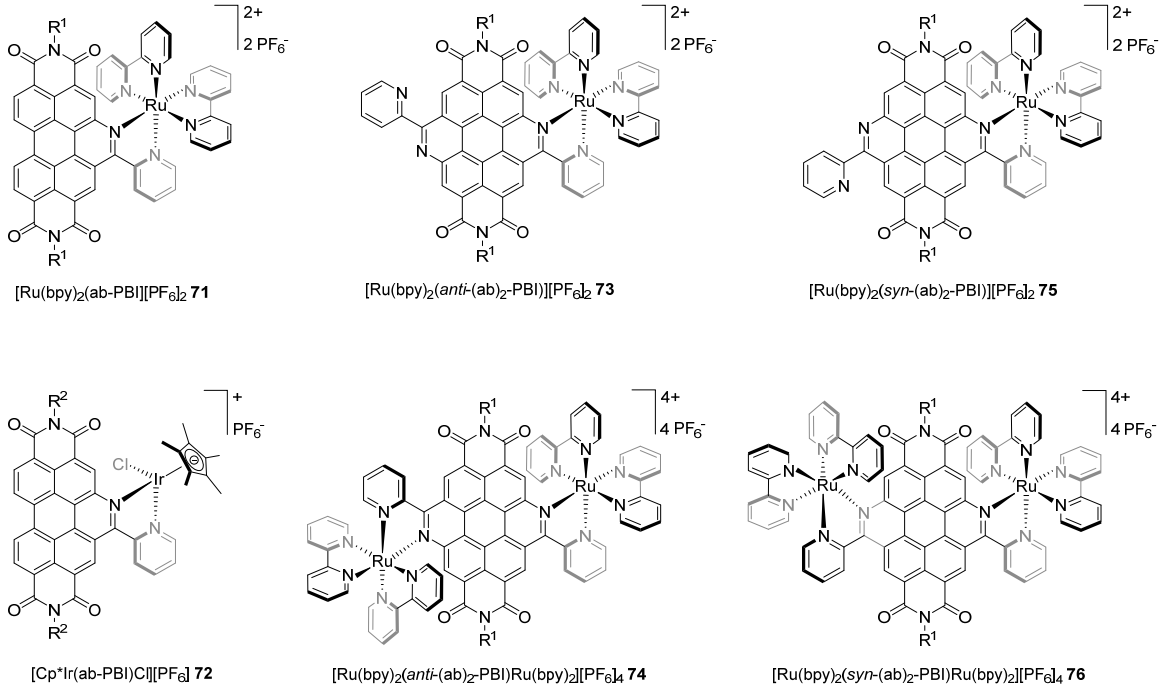

[Ru(bpy)$_2$(ab-PBI)][PF$_6$]$_2$ **71** [Ru(bpy)$_2$(*anti*-(ab)$_2$-PBI)][PF$_6$]$_2$ **73** [Ru(bpy)$_2$(*syn*-(ab)$_2$-PBI)][PF$_6$]$_2$ **75**

[Cp*Ir(ab-PBI)Cl][PF$_6$] **72** [Ru(bpy)$_2$(*anti*-(ab)$_2$-PBI)Ru(bpy)$_2$][PF$_6$]$_4$ **74** [Ru(bpy)$_2$(*syn*-(ab)$_2$-PBI)Ru(bpy)$_2$][PF$_6$]$_4$ **76**

Tafel 1 Übersicht über die ab-PBI Metallkomplexe **71**–**76**, welche in dieser Arbeit hergestellt wurden (R^1 = 2,6-diisopropylphenyl und R^2 = 3-pentyl).

Die Emissionsmessungen der Komplexe **71**–**76** zeigten eine vollständige Löschung der Perylenfluoreszenz, wobei eine neuartige Phosphoreszenz im NIR-Bereich des Lichts in entgastem Dichlormethan beobachtet werden konnte (**Abbildung 3**). Transiente Absorptionsspektroskopie im Nanosekundenbereich, DFT-Berechnungen und Experimente mit Singulett-Sauerstoff bewiesen, dass der angeregte Zustand dieser Komplexe PBI-zentriert ist und einen starken MLCT-Charakter besitzt. Folgerichtig zeigten die Komplexe [Ru(bpy)$_2$(ab-PBI)][PF$_6$]$_2$ **71** und [Cp*Ir(ab-PBI)Cl][PF$_6$] **72** ihr Potential als Photosensibilisatoren in organischem Medium wie beispielsweise bei der photokatalytischen Dimerisierung von 4-Nitrobenzylbromid zu 1,2-Bis(4-nitrophenyl)ethan.

Leider ging die Photosensibilisator-Fähigkeit verloren, sobald anstatt eines organischen Lösungsmittels ein wässriges verwendet wurde. Es war daher nicht möglich mit den Photosensibilisatorkomplexen **71**–**76** eine photokatalytisch getriebene Wasseroxidation zu realisieren.

Lumineszenz- und Singulett-Sauerstofferzeugungs-Studien in wässrigen Lösungen haben gezeigt, dass die Phosphoreszenz beim Mediumwechsel ebenfalls verschwindet und sich die Population des Triplettzustands verändert. Basierend auf den theoretischen Berechnungen zu $[Ru(bpy)_2(ab\text{-}PBI)][PF_6]_2$ **71** und den Gemeinsamkeiten mit dem literaturbekannten Komplex $[Ru(bpy)_2(dppz)]^{2+}$ **37**, wird angenommen, dass ein zusätzlicher, besetzbarer „Dunkel-Zustand“ in **71** existiert. Dieser liegt energetisch nah am emittierenden $^3MLCT_{PBI}$-Zustand und verursacht den Verlust der NIR-Phosphoreszenz (**Abbildung 3**). Eine erhöhte Polarität des Lösungsmittels führt zu einer Energieerniedrigung des „Dunkel-Zustands“, sodass die angeregte Zustandsenergie mittels Intersystem Crossing (k^D_{ISC}) sehr schnell abgegeben werden kann.

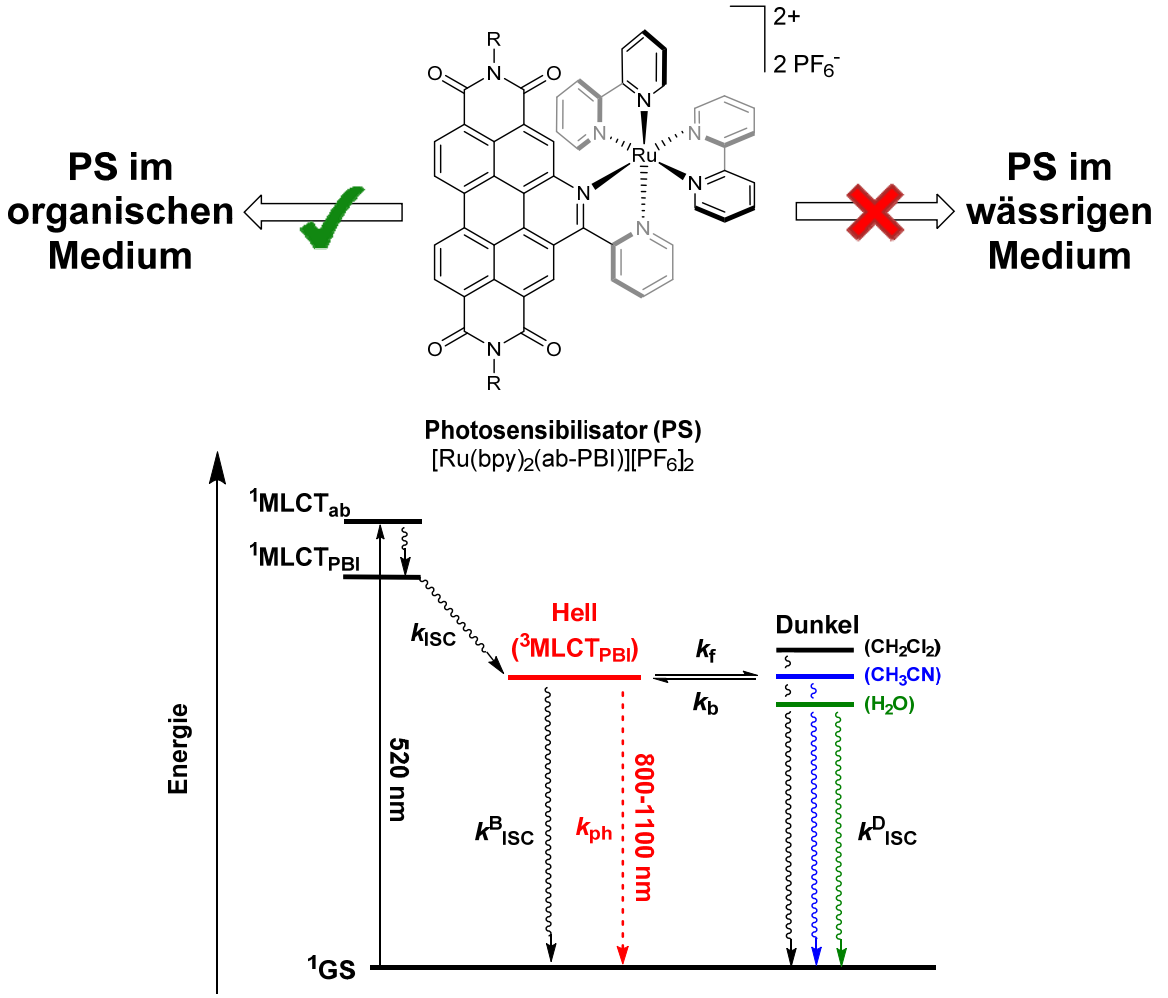

Abb. 3 Schematische Darstellung zur Eignung des ab-PBI Metallkomplexes $[Ru(bpy)_2(ab\text{-}PBI)][PF_6]_2$ **71** als Photosensibilisatormolekül im organischen beziehungsweise wässrigem Medium sowie eine Zusammenfassung der photophysikalischen Relaxationspfade.

Die vorliegende Arbeit zeigt auf der einen Seite, dass metallosupramolekulare Strukturen wie der dreikernige Makrozyklus $[Ru(bda)bpb]_3$ **46** eine vielversprechende Möglichkeit darstellen, die katalytische Aktivität im Vergleich zu einem einkernigen artverwandten Komplex zu erhöhen. Hierbei wurde ein unerwarteter Wechsel des Mechanismus von I2M zu WNA beobachtet. Auf der anderen Seite deuten die ab-PBI basierenden Metallkomplexe **71**–**76** an, dass die Realisierung der lichtgetriebenen Oxidation von Wasser mit großen Schwierigkeiten verbunden ist. Die Photosensibilisatoren auf Basis von ab-PBI-Liganden und $\{Ru(bpy)_2\}$- sowie $\{IrCp^*Cl\}$-Komplexfragmenten wie $[Ru(bpy)_2(ab\text{-}PBI)][PF_6]_2$ **71** sind starke Lichtabsorber, zeigen eine bemerkenswerte NIR-Phosphoreszenz und treiben photokatalytische Umsetzungen im organischen Medium an. Allerdings verlieren sie einige der vielversprechenden Eigenschaften beim Wechsel ins wässrige Medium. Dies äußert sich im Verlust der Lumineszenz und der photokatalytischen Inaktivität bezüglich der Wasseroxidation.

Die Nachahmung der Wasseroxidation des natürlichen PSII ist in dieser Arbeit mit TON-Werten von 7400 und TOF-Werten von 150 s^{-1} (vgl. natürliches PSII: TON = $1.8 \cdot 10^5$, TOF = 100–400 s^{-1}) schon recht gut gelungen. Andererseits stellt die optimale Verbindung der molekularen Einzelbestandteile für eine effiziente künstliche Photosynthese immer noch eine große Herausforderung dar. Die Produktion von solaren Brennstoffen im großtechnischen Maßstab ist eine langfristige Strategie zur Energiegewinnung und wird in den nächsten 10 bis 20 Jahren wahrscheinlich trotz hoher Investitionen nur schwer zu erreichen sein. Sollte dies aber einmal gelingen, dann wird die Menschheit eines ihrer größten Probleme hinsichtlich einer verlässlichen und nachhaltigen Energieversorgung bewältigt haben.

CHAPTER 5 EXPERIMENTAL SECTION

5.1 Materials and Methods

Chemicals:

[Ru(bda)(pic)$_2$] (**5**),[49] [Ru(bda)((CH$_3$)$_2$SO)$_2$] (**44**),[49] *N,N*′-Bis(2′,6′-diisopropylphenyl)-1-amino-perylene-3,4:9,10-tetracarboxylic acid bisimide (**47**, amino-PBI),[158] 6-phenyl-pyridine-2-carboxaldehyde (**48c**),[206] 6-pyridin-2′-yl-pyridine-2-carboxaldehyde (**48d**),[207] 1-amino-perylene-3,4,9,10-tetracarboxylic acid tetrabutyl ester (**50**, amino-PTE),[162] 2,5,8,11,15,18,21,24-octaoxapentacosan-13-amine (**53**),[208, 209] *N*-(12′-tricosanyl)-perylene-3,4-dicarboxylic acid monoimide-9,10-dicarboxylic acid dioctyl ester (**57**, PMIDE),[163] a 1,6- and 1,7-isomeric mixture of *N,N*′-bis(2′,6′-diisopropylphenyl)-diamino-perylene-3,4:9,10-tetracarboxylic acid bisimide (**62**, 1,7- and 1,6-diamino-PBI),[158] 1,6-diamino-perylene-3,4,9,10-tetracarboxylic acid tetrabutyl ester (**65**, 1,6-diamino-PTE),[162] [Ru(bpy)$_2$Cl$_2$][210] and [Cp*IrCl$_2$]$_2$[211] were synthesized according to procedures known from literature. All other starting materials were purchased from commercial sources and used as obtained, unless otherwise noted. Dichloromethane, *N,N*-dimethylformamide and tetrahydrofuran were dried with a commercial solvent purification system.

Chromatography:

Column chromatographic separations were performed either on silica gel 60M (0.04–0.063 mm) or on aluminum oxide (neutral, "ICN", deactivation degree V). For thin-layer chromatography (TLC) aluminum sheets precoated with silica gel 60 F254 were used. Preparative size-exclusion chromatography was performed using Bio-Beads S-X3 (mesh size: 200-400, molar mass operation range: up to 2,000 g/mol) swollen with a 9:1 dichloromethane/methanol solution.

NMR spectroscopy:

NMR spectra were recorded on a Bruker Avance spectrometer (400 MHz) in deuterated solvents at 25 °C. Chemical shifts are reported in parts per million (ppm, δ scale) relative to the signal of the residual undeuterated solvent. The following abbreviations were used to

describe nuclear spin coupling: s = singlet, d = doublet, t = triplet, sept = septet, m = multiplet and b = broad.

Mass spectrometry:

MALDI-ToF MS spectra were measured on Bruker Autoflex II spectrometer. The MS spectra were measured either in the positive or the negative reflector mode using *trans*-2-[3-(4-*tert*-butylphenyl)-2-methyl-2-propenylidene]malononitrile (DCTB) as a matrix. High-resolution mass spectra (ESI) were recorded on Bruker ESI MicrOTOF Focus mass spectrometer.

Elemental analysis:

Elemental analyses were carried out on a vario MICRO cube (Elementar Analysensysteme GmbH) elemental analysis system at the Institute of Inorganic Chemistry, University of Würzburg.

Melting point:

Melting points (Mp) were determined on an Olympus BX41 polarization microscope and are uncorrected.

UV/Vis/NIR absorption spectroscopy:

UV/Vis absorption spectra were measured on commercial spectrophotometers (JASCO V-670 or Perkin Elmer Lambda 35) at 25 °C in 1 cm quartz cuvettes with spectroscopic grade solvents.

"Ce^{4+} absorption decay" assay: The Ce^{4+} consumption was monitored by the absorption decay at 360 nm. The studies were performed in 1:1 CH_3CN/water (pH 1, acid: nitric acid) solution as followed: 1.99 mL of a freshly prepared cerium(IV) ammonium nitrate solution was mixed with 10 µL of the catalyst solution. Afterwards the cuvette was shaken and put inside the spectrometer (~4 s) and the Ce^{4+} absorption (360 nm, λ_{360} = 760 M^{-1} cm^{-1}) was monitored over 300 s.

Electrochemistry:

Standard measurements in dichloromethane: Electrochemical measurements were performed on an EC Epsilon instrument (BAS Instruments Ltd. UK) with a standard three-electrode configuration (reference electrode: Ag/AgCl, working electrode: Pt disc, auxiliary electrode: Pt wire). The applied scan rates ranged from 20 to 1,000 mV/s. The

experiments were carried out in dry (distillation over CaH_2) and degassed dichloromethane at a concentration of $2.5 \cdot 10^{-4}$ M containing tetra-*n*-butylammonium hexafluorophosphate (0.1 M) as electrolyte. Ferrocene (Fc) was added at the end of each experiment as an internal standard. The potentials are referred to the ferrocenium/ferrocene reference couple (Fc^+/Fc).

Measurements in aqueous solutions: Measurements in aqueous solutions were executed on the same setup with a different three-electrode configuration: Ag/AgCl (3M KCl) as reference electrode, glassy carbon as working electrode, Pt wire as auxiliary electrode. The solutions were either measured in 1:1 CH_3CN/water (pH 1) or 1:1 2,2,2-trifluoroethanol/water (pH 1, acid: trifluoromethane sulfonic acid). The measurements for the Pourbaix diagram were started in a 1:1 co-solvent/water (pH 1, acid: trifluoromethane sulfonic acid, co-solvent: CH_3CN or 2,2,2-trifluoroethanol) at 20 °C with a concentration of $2.5 \cdot 10^{-4}$ mol/L. Subsequently, the pH value was adjusted by the addition of a NaOH solution. For the reference electrode potential of the Ag/AgCl (3M KCl), a value of –0.209 V versus NHE was assumed.[212]

Spectroelectrochemistry:

Spectroelectrochemical experiments in reflexion were performed in an Agilent Cary 5000 Spectrometer in combination with a home-built sample compartment consisting of a cylindrical PTFE cell with a sapphire window and an adjustable three in one electrode (6 mm platinum disc working electrode, 1 mm platinum counter and pseudo reference electrode).

Luminescence spectroscopy:

Standard emission measurements in the UV/Vis: Emission spectra were recorded on PTI QM-4/2003 fluorescence spectrometer and were corrected against the photomultiplier and lamp intensity. The solutions were prepared in 1 cm quartz cuvettes with spectroscopy grade solvents at 20 °C. The maximum absorbance was hereby less than 0.05. The quantum yields were determined using a Hamamatsu Absolute PL Quantum Yield Measurement System. The system is composed of an excitation source that uses a 150 W CW Xenon light source, a monochromator (250-700 nm, FWHM 10 nm), an integrating sphere, and a multi-channel spectrometer capable of simultaneously measuring multiple wavelengths between 300 and 950 nm and counting the number of absorbed and emitted

photons. The reported quantum yields are averaged from values measured at three different excitation wavelengths.

Inert luminescence measurements in the UV/Vis/NIR: Luminescence measurements were carried out in 1 cm quartz cuvettes with dilute solutions with absorbance maxima of less than 0.2. Dichloromethane and acetonitrile (spectroscopy grade) were deoxygenated using the freeze-pump-thaw method. All manipulations of the probes and the cuvettes were performed in a glovebox with an atmosphere of dry nitrogen. Excitation and emission spectra were recorded on a FLSP920 spectrometer, equipped with a 450 W Xenon lamp, double monochromators for the excitation and emission pathways, and photomultiplier (PMT-R928) as detector. The emission was collected at right angles to the excitation source with the emission wavelength selected using a double grated monochromator and detected by a R928-P PMT. The excitation and emission spectra were fully corrected using the standard corrections supplied by the manufacturer for the spectral power of the excitation source and the sensitivity of the detector.

The luminescence lifetimes were measured either *via* time correlated single photon counting (TCSPC) using a 420 nm pulsed ps laser diode (5 mW), or using a μF900 pulsed 60 W xenon microsecond flashlamp, with a repetition rate of 100 Hz, and a multichannel scaling module. For TCSPC mode, the instrument response function (IRF) was measured using a scattering sample and setting the monochromator at the emission wavelength of the excitation light source. The resulting intensity decay is a convolution of the luminescence decay with the IRF and iterative reconvolution of the IRF with a decay function and non-linear least squares analysis was used to analyze the convoluted data.

Determination of the absolute quantum yield was performed as suggested by Friend.[213] First, the diffuse reflection of the sample was determined under excitation. Second, the emission was measured for this excitation wavelength. Integration over the reflected and emitted photons by use of an Ulbricht sphere allows calculating the absolute quantum yield.

Nanosecond transient absorption spectroscopy:

For these experiments, complex **71** was dissolved in dichloromethane and filled in 1 cm sealed quartz cuvettes (Starna, Pfungstadt, Germany). For the inert sample, the solution was purged with argon for 15 min prior to measurement. The pump probe experiments were performed with an Edinburgh LP 920 Laser Flash spectrometer consisting of a Nd:YAG laser (Continuum, Minilite II) operating at 10 Hz, probe light source (xenon arc

lamp), sample chamber and detector (photomultiplier tube). As pump pulse 416 nm light was used and the laser pulse energy was varied between 0.2 mJ and 2.0 mJ with a pulse length of 5 ns. Residuals and autocorrelation function (without any significant structure) served as the main criteria in the evaluation of the fits.

Singlet oxygen sensing:

Indirect method: The CH_3CN solutions contained the dye (either **49a**, **49a′**, **71** or **72** with a OD of 0.1 at λ_{ex}), *p*-nitrosodimethyl aniline (RNO, 24 μM) and imidazole (12 mM), whereas the phosphate buffer solutions (PBS) contained the dye (either **71** or **72** with a OD of 0.1 at λ_{ex}), RNO (20 μM) and histidine (10 mM). The air-saturated solutions were irradiated (λ_{ex} (CH_3CN) = 420 nm, λ_{ex} (PBS) = 440 nm) for different time intervals in a Rayonet RPR-200 chamber reactor (Southern New England Ultraviolet Company). The time-dependent absorbance of the solution was then evaluated. Plots of variations in absorbance at 440 nm in PBS or at 420 nm in acetonitrile (A_0–A, A_0 is the absorbance before irradiation) versus the irradiation times for each sample were prepared and the slope of the linear regression was calculated (S_{sample}). As a reference compound, phenalenone (Φ_{ref} ($^1O_2$) = 95%) was used in both methods, to obtain S_{ref}. Equation (8) was applied to calculate the singlet oxygen quantum yields (Φ_{sample}) for every sample:

$$\Phi_{sample} = \Phi_{ref} \cdot \frac{S_{sample}}{S_{ref}} \cdot \frac{I_{ref}}{I_{sample}} \quad (8)$$

$$I = I_0 \cdot (1 - 10^{A_\lambda}) \quad (9)$$

I (absorbance correction factor) was obtained with Equation (9), where I_0 is the light intensity of the irradiation source in the irradiation interval and A_λ is the absorbance of the sample at wavelength λ.

Direct method: Fluorescence measurements were performed on a Fluorolog-3 spectrofluorometer (JobinYvon Horiba, Model FL3-11) with a 450 W xenon lamp light source and single-grating excitation and emission spectrometers. For high beam intensity, the excitation slits were set to a maximum value of 29.4 nm. A coloured glass filter was placed between the sample and the detector to cut off light below 695 nm. The emission signal was collected at right angle to the excitation path with an IR-sensitive liquid nitrogen cooled germanium diode detector (Edinburgh Instruments, Model EI-L). The detector was biased at 160 V. The signal-to-noise ratio of the signal detected by the Ge-diode was improved with a lock-in amplifier (Stanford Research Systems, model SR510)

referenced to the chopper frequency of 126 Hz. Data acquisition was carried out with DataMax. Samples in aerated acetonitrile were prepared in a luminescence quartz cuvette with an OD = 0.2 at the irradiation wavelength (420 nm). Four different transmittance filters were used to vary the intensity of the irradiation beam. Intensities of irradiation were plotted *vs* the areas of the singlet oxygen peaks at 1270 nm and the slope of the linear regression was calculated (S_{sample}).

Photocatalytic dimerization of 4-nitrobenzyl bromide to 1,2-bis(4-nitrophenyl)ethane:
1 mmol of 4-nitrobenzyl bromide, 2 mol triethylamine and 0.01 mmol photosensitizer were dissolved in dichloromethane in a Schlenk tube. Afterwards, the solution was irradiated with 465 nm LEDs for 12 hours (overnight). Subsequently, the reaction was worked up and the product 1,2-bis(4-nitrophenyl)ethane was isolated by flash chromatography. The variance between different experimental runs is 1%.

Chemically driven water oxidation reactions:
The chemically driven water oxidation reactions were performed under ambient conditions in Schlenk reaction vessels which were connected to pressure sensors from Honeywell (SSCDANN030PAAA5, absolute pressure, 0 to 30 psi). For each measurement 1 g (1.82 mmol) of cerium(IV) ammonium nitrate (CAN) was dissolved in 3 mL of a acetonitrile/water mixture (pH = 1, acid: trifluoromethane sulfonic acid, ratios varying) in a Schlenk flask, and the catalyst solution (400 µL in 1:1 acetonitrile/water (pH 7)) was injected to it through a septum *via* a Hamilton syringe. After the gas evolution had ceased, 500 µL of the gas head space were taken out with a gas tight Hamilton syringe and injected into the gas chromatograph GC-2010 Plus from Shimadzu applied with a thermal conductivity detector (detector current 30 mA, argon as carrier gas) to determine the gas composition at the end of the reaction. The error was estimated by a concentration uncertainty of the used Eppendorf pipettes (5% for 1000 µL-pipette, 15% for 200 µL-pipette and 25% for 20 µL-pipette).

Chemically driven water oxidation reactions for kinetic isotope effect studies:
The kinetic isotope effect experiments were carried out in an Oxygraph Plus System of Hansatech Instruments Ltd. (Clark-type oxygen electrode for electrochemical oxygen detection; more details of the Oxygraph Plus System could be obtained from the Web site of Hansatech Instruments Ltd.). 1.5 mL of a freshly prepared CAN solution (c = 0.7 M, pH 1 solution (H_2O or D_2O) with 59% CH_3CN content) was placed in the Clark electrode

reaction chamber. After the baseline of the measurement was constant, 0.5 mL of the catalyst solution (varying concentrations) were added. During the measurement the reaction temperature was kept constant at 20 °C.

^{18}O-labeling experiment:

MilliQ deionized water was used as $^{16}OH_2$ source ($^{16}OH_2$ with natural abundance of 0.205% ^{18}O).[214] ^{18}O-labeled water was commercially purchased with 97% ^{18}O-labeling and acetonitrile was purchased extra dry. The pH 1 value of the solutions was adjusted by trifluoromethane sulfonic acid. All solutions were degassed by freeze-pump-thaw cycles (4x). Experiment: $[Ru(bda)bpb]_3$ (2.51 mg, 1.45 μmol) and CAN (23.8 mg, 43.4 μmol ≙ 30 equiv.) were dissolved in 0.4 mL of 1:1 $CH_3CN/^{18}OH_2$ (pH 1, 97% ^{18}O) in a Schlenk tube, which was connected to the inlet of a mass spectrometer. The solution of $[Ru^{4+}\text{-}^{18}OH(bda)bpb]_3$ was purged with nitrogen until no $^{32}O_2$ signal could be detected in the mass spectrometer (Typ: 90 of Fa. Finnigan, mode: electron impact). Afterwards the flask is separated from the mass spectrometer by a Schott Produran® tap. Subsequently a freshly prepared 1:1 $CH_3CN/^{16}OH_2$ (pH 1) solution of CAN (c = 14.5 mM, 500 μL ≙ 5 equiv) was injected into the catalyst solution resulting in an ^{18}O labelling degree of the solution of 43%. The addition of 5 eq. CAN ensures that enough oxidation equivalents are present but only one catalytic cycle per $[Ru(bda)bpb]_3$ (1/3 of the Ru centres) is performed (Ru^{4+}-OH|Ru^{4+}-OH|Ru^{4+}-OH + 5 e^- → Ru^{5+}=O|Ru^{4+}-OH|Ru^{4+}-OH + O_2). After the gas evolution has ceased (5 min) the tap was opened and the gas was quantitatively injected into the mass spectrometer and analyzed.

Catalyst stability test after water oxidation:

The following procedure was applied to test the stability of the macrocyclic structure after water oxidation catalysis: 10 mg (5.9 μmol)) of $[Ru(bda)bpb]_3$ were dissolved in 2 mL of 1:1 CH_3CN/water solution (pH 1, acid: trifluoromethane sulfonic acid). After addition of 500 mg (912 μmol) cerium(IV) ammonium nitrate (CAN), vigorous oxygen evolution occurred (~40 catalytic cycles). Subsequent addition of 250 mg of ammonium hexafluoro-phosphate lead to a brown precipitation which was filtered off, washed with water and dried under high vacuum. Afterward, the sample was taken up in 1:1 dichloromethane/methanol, and ascorbic acid was added for reduction. The so prepared sample was then analyzed by MALDI mass spectrometry.

Photocatalytic water oxidation in the three-component system:

The light-driven water oxidation reactions were carried out in an Oxygraph Plus System (Hansatech Instruments Ltd.). Irradiation of the sample was accomplished by a 150 W xenon lamp (Newport) equipped with a 380 nm cutoff filter and a water jacket to remove UV and IR radiation, respectively. The light intensity, with which the sample was irradiated, was 230 mW/cm^2. Before the measurement, all components (catalyst, $[Ru(bpy)_3][Cl]_2$ x 6 H_2O and $Na_2S_2O_8$ were dissolved in 2 mL of 1:1 CH_3CN/phosphate buffer (pH 7.2) solution in the dark ($[Na_2S_2O_8]$ = 37 mM, $[[Ru(bpy)_3][Cl]_2$ x 6 $H_2O]$ = 1.5 mM, [catalyst] = varying). Afterward, the sample was transferred to the reaction chamber and kept in the dark. After the baseline of the measurement was constant, the sample was irradiated. During the measurement the reaction temperature was kept constant at 20 °C.

Computational calculations:

$[Ru(bda)bpb]_3$: The calculated structures have been optimized by using the DFT method and the CAM-B3LYP functional.[215] The optimised structure containing additional water molecules has been obtained in the framework of the RI-DFT method[216] by employing the pbe functional.[217] The def2-SVP basis set[218, 219] and in case of ruthenium, the corresponding effective core potential (ecp) have been used.[220]

Organic ab-perylene compounds: Computational calculations were performed using the Gaussian 09 program package.[221] The DFT calculations were carried out with B3LYP[222, 223, 224] as functional and def2-SVP[225] as basis set. The structures were geometry optimized, followed by frequency calculations on the optimized structures, which confirmed the existence of an energy minimum. Time-dependent (TD)-DFT calculations were carried out on the optimized structure with the lowest energy of the compounds using the same functional (B3LYP) and basis set (def2-SVP) as for the geometry optimization. Long alkyl chains were replaced by ethyl groups to simplify and thus, accelerate the calculations.

Ab-PBI based metal complexes **71** and **72**: Calculations (gas-phase) were performed with the ORCA 3.0.0 program suite.[226] Geometry optimizations of the ground state S_0 for compounds **71** and **72** were carried out with the PBE0[217, 227, 228, 229, 230, 231, 232] functional as implemented in ORCA followed by a single point calculation with the BHandHLYP[233, 234] functional. The choice of PBE0 for the geometry optimization is justified by its widespread use and reliability for the calculation of transition metal complexes, whereas the BHandHLYP functional with high Fock exchange (50%) leads to the elimination of ghost

states when describing charge-transfer, a common problem in TD-DFT.[235, 236, 237, 238] The def2-TZVP[218, 225] basis set was used for all atoms together with the auxiliary basis set def2-TZVP/J in order to accelerate the computations within the framework of RI approximation. For the heavy transition metal atoms, i.e. Ru and Ir, effective core potentials of def2-TZVP quality[220, 225, 239] have been employed and Van der Waals interactions have been considered by an empirical dispersion correction (Grimme-D3).[240, 241] TD-DFT calculations were performed with the BHandHLYP functional. Representations of molecular orbitals and transition densities were produced with orca_plot as provided by ORCA 3.0.0 and with gOpenMol 3.00.[242, 243]

X-ray Crystal Structure Determination:

Single-crystal X-ray diffraction data for *anti*-$(ab)_2$-PBI **63** and $[Cp^*Ir(ab\text{-}PBI)Cl][PF_6]$ **72** were collected at 100 K on a Bruker D8 Quest Kappa Diffractometer using Cu K_α-radiation from an Incoatec IμS microsource with Montel multilayered mirror, a Photon100 CMOS detector and Apex2 software. The structures were solved using direct methods, expanded with Fourier techniques and refined with the Shelx software package.[244] All non-hydrogen atoms were refined anisotropically. Hydrogen atoms were included in the structure factor calculation on geometrically idealized positions.

Anti-$(ab)_2$-PBI **63**: Single crystals of *anti*-$(ab)_2$-PBI **63** suitable for X-ray structural analysis were grown by slow evaporation of a concentrated solution of tetrahydrofuran (THF). The single crystals thus obtained were highly sensitive toward temperature. Therefore, the crystalline material was directly immersed (in solution) into a film of perfluorpolyether, which was precooled to 200 K on a copper substrate. Subsequently, the investigated single crystal was transferred on a Teflon loop to the diffractometer continuously cooled by evaporated liquid nitrogen. The refinement showed at least 2 more disordered THF molecules which could not be modelled satisfactorily. Therefore, the SQUEEZE routine of PLATON was used to remove the electron density. The remaining structure could be refined nicely.[245]

Crystal data for anti-$(ab)_2$-PBI **63** ($C_{60}H_{46}N_6O_4 \bullet 4\ C_4H_8O$): *M*r = 1203.44, 0.34 x 0.23 x 0.19 mm^3, triclinic space group $P\bar{1}$, a = 10.9630(5) Å, α = 97.6970(16)°, b = 18.4513(8) Å, β = 97.8872(16)° c = 33.0607(14) Å, γ = 100.9697(16)°, V = 6414.6(5) $Å^3$, Z = 4, ρ(*calcd)* = 1.246 $g \cdot cm^{-3}$, μ = 0.646 mm^{-1}, $F_{(000)}$ = 2560, $GooF(F^2)$ = 1.065, R_1 = 0.0809, wR^2 = 0.2239 for I>2σ(I), R_1 = 0.0895, wR^2 = 0.2313 for all data, 25241 unique reflections [$\theta \leq$ 72.817°] with a completeness of 99.6% and 1707 parameters, 208 restraints.

Crystallographic data have been deposited with the Cambridge Crystallographic Data Centre as supplementary publication no. CCDC-1489244 These data can be obtained free of charge from The Cambridge Crystallographic Data Centre via www.ccdc.ac.uk/data.request/cif.

[Cp*Ir(ab-PBI)Cl][PF_6] **72**: The crystal was grown by diethyl ether diffusion in an acetonitrile solution of the compound at room temperature.

*Crystal data for [Cp*Ir(ab-PBI)Cl][PF_6]* **72**: ($C_{50}H_{47.50}ClF_6IrN_4O_{4.25}P$); *M*r = 1145.04, 0.089x0.058x0.037 mm^3, triclinic space group P1 *a* = 14.3355(7) Å, α = 80.190(2)°, *b* = 18.1632(8) Å, β = 86.009(2)° *c* = 18.1938(8) Å, γ = 73.842(2)°, *V* = 4482.4(4) $Å^3$, *Z* = 4, ρ(*calcd)* = 1.697 $g \cdot cm^{-3}$, μ = 7.319 mm^{-1}, $F_{(000)}$ = 2290, *T* = 100(2) K, *GooF*(*F2*) = 1.042, R_1 = 0.0460, wR^2 = 0.1132 for I>2σ(I), R_1 = 0.0529, wR^2 = 0.1180 for all data, 15457 unique reflections [$2\theta \leq 66.6°$] with a completeness of 95.3% and 1178 parameters, 21 restraints.

Crystallographic data have been deposited with the Cambridge Crystallographic Data Centre as supplementary publication no. CCDC-1024239. These data can be obtained free of charge from The Cambridge Crystallographic Data Centre via www.ccdc.ac.uk/data.request/cif.

5.2 Synthesis and Characterization

1,4-Bis(pyrid-3-yl) benzene (bpb, 45)

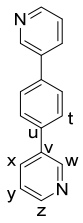

1,4-Dibromo benzene (1 g, 4.24 mmol), pyridine-3-boronic acid (1.56 g, 12.7 mmol), tris(dibenzylideneacetone)dipalladium(0) (100 mg, 0.11 mmol) and triphenyl phosphine (232 mg, 0.89 mmol) were dissolved in 125 mL toluene, 20 mL methanol and 20 mL 2M Na_2CO_3 (all degassed) under inert conditions and heated for 16 h at 70 °C. Afterward, the organic phase was separated and the water phase was extracted three times with 50 mL dichloromethane. The combined organic phases were dried over sodium sulfate, filtered off, and the solvent was then removed under reduced pressure. The crude product was purified by column chromatography (SiO_2, dichloromethane/ethyl acetate 1:1) and recrystallized in cyclohexane to afford slight yellowish crystalline plates. The analytical data are in agreement with those described in literature.[246] Yield: 534 mg (2.42 mmol, 54%). Mp 127 °C. ^{1}H NMR (400 MHz, CD_2Cl_2): δ = 8.80 (dd, ^4J = 2.4, 0.8 Hz, 2H, H^w), 8.49 (dd, ^3J = 4.8 Hz, ^4J = 1.6 Hz, 2H, H^z), 7.84 (ddd, ^{3}J = 7.9 Hz, ^4J = 2.4, 1.6 Hz, 2H, H^x), 7.63 (s, 4H, H^t), 7.29 (ddd, ^3J = 7.9, 4.8 Hz, ^4J = 0.8 Hz, 2H, H^y). ^{13}C NMR (100 MHz, CD_2Cl_2): δ = 148.8, 148.2, 137.6, 135.7, 134.1, 127.7, 123.6. HR-MS (ESI-TOF, positive, acetonitrile/chloroform): *m/z*: $[M + H]^+$ calcd for $[C_{16}H_{13}N_2]^+$ 233,1073; found: 233.1086 (error = –5.5 ppm).

[Ru(bda)bpb]$_3$ (46)

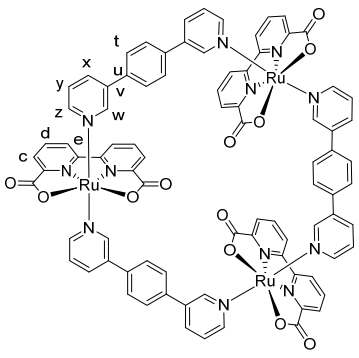

1,4-Bis(pyrid-3-yl) benzene **45** (202 mg, 0.87 mmol) and [Ru(bda)($(CH_3)_2SO)_2$] (455 mg, 0.91 mmol) were dissolved in 250 mL chloroform and 50 mL methanol (all degassed) under inert conditions and heated for 14 h at 60 °C. The red brown solution was cooled down and the solvents were removed under reduced pressure. Column chromatography (Al_2O_3, dichloromethane/methanol 6:1) and crystallisation from the same solution afforded a dark brown solid. Yield: 274 mg (0.16 mmol, 55%). Mp > 300 °C. ^{1}H NMR (400 MHz, CD_2Cl_2/MeOD 5:1 + ascorbic acid): δ = 8.51 (dd, ^3J = 8.1 Hz, ^4J = 1.1 Hz, 2H, H^e), 8.40 (d, ^4J = 2.0 Hz, 2H, H^w), 8.03 (dd, ^3J = 7.8 Hz, ^4J = 1.1 Hz, 2H, H^c), 7.87 (t, ^3J = 7.9, 2H, H^d), 7.74 (ddd, ^3J = 8.0 Hz, ^4J = 2.1 and 1.4 Hz, 2H, H^x), 7.47 (s, 4H, H^t), 7.37 (dd, ^3J = 5.8 Hz, ^4J = 1.4 Hz, 2H, H^z), 7.09 (ddd, ^3J = 8.1 and 5.7 Hz, ^4J = 0.6 Hz, 2H, H^y). ^{13}C NMR (100 MHz, CD_2Cl_2/MeOD 5:1 + ascorbic acid): δ = 173.5,

159.7, 157.0, 151.2, 149.9, 137.2, 136.3, 134.7, 131.9, 127.9, 126.1, 124.9, 124.7. MS (MALDI-TOF, matrix: DCTB, mode: positive): *m/z* calcd for $[C_{84}H54N_{12}O_{12}Ru_3Na]^+$ 1750.11, found 1750.19. HR-MS (ESI-TOF, positive, acetonitrile/chloroform): *m/z* = 1727.1162 calcd for $[C_{84}H_{54}N_{12}O_{12}Ru_3]^+$, found: 1727.1226 (error = –3.7 ppm). CHN of green crystals: calcd for $[Ru^{III}\text{-}OH(bda)bpb]_3 \cdot 3H_2O$ ($C_{84}H_{63}N_{12}O_{18}Ru_3$), C 55.08, H 3.47, N 9.18%; found C 54.84, H 4.24, N 8.71%.

General procedure of the Pictet-Spengler reaction for azabenz-annulation

The mono- or diamino-perylene derivative (1 equiv.), the respective aromatic aldehyde (4-20 equiv.) and activated molecular sieve (3 Å) were placed in a Schlenk flask. Afterward, dry dimethylformamide and trifluoroacetic acid (10 equiv.) were added under inert conditions, and the reaction mixture was stirred at 110 °C for 30 min under nitrogen atmosphere. Subsequently, the inert atmosphere was replaced by pure oxygen, and the reaction mixture was stirred under this oxidative environment at 110 °C until a full conversion of amino-perylene (monitored by TLC). The mixture was quenched by addition of water and neutralized with 15% sodium hydroxide solution. After extraction with dichloromethane, the organic layer was washed twice with brine and twice with water. The crude product was further purified by column chromatography and recrystallization.

In the following, a general structure of azabenz-annulated PBI (ab-PBI) is depicted with indexing of atom and bond positions applied in the nomenclature of the compounds.

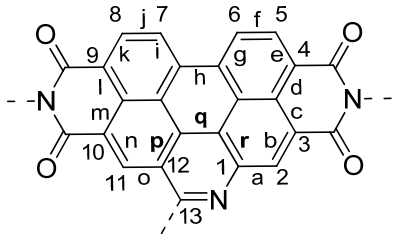

_N,N′_-Bis(2′,6′-diisopropylphenyl)-13-(pyridin-2″-yl)-azabenzo[*pqr*]-perylene-3,4:9,10-tetracarboxylic acid bisimide (ab-PBI, 49a)

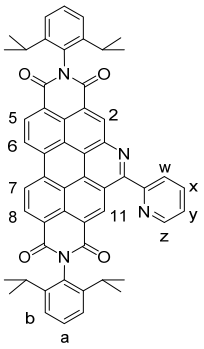

The reaction was performed according to the general Pictet-Spengler reaction procedure using 0.74 g (1.02 mmol) of amino-PBI **47** and 0.72 g (6.72 mmol) of pyridine-2-carboxaldehyde **48a**. The product was obtained as a yellow solid after column chromatography (SiO_2, EtOAc/hexane 1:2) and recrystallization (EtOAc). The analytical data are in agreement with those described in the literature.[173] Yield: 0.43 g (0.53 mmol, 52%). Mp >300 °C. ^{1}H NMR (400 MHz, CD_2Cl_2): δ = 10.52 (s, 1H), 9.63 (s, 1H), 9.45 – 9.40 (m, 2H), 9.22 – 9.18 (m, 2H), 8.96 – 8.94 (m, 1H), 8.62 (ddd, ^3J = 7.9 Hz, ^4J = 1.2 Hz, ^5J = 0.8 Hz, 1H), 8.13 (td, ^3J = 7.8 Hz, ^4J = 1.8 Hz, 1H), 7.62 – 7.55 (m, 3H), 7.44 – 7.41 (m, 4H), 2.90 (sept, ^3J = 6.7 Hz, 4H), 1.24 – 1.19 (m, 24H). ^{13}C NMR (100 MHz, CD_2Cl_2): δ = 164.3, 164.20, 164.20, 164.1, 157.90, 157.87, 149.4, 146.54, 146.52, 144.5, 138.0, 135.7, 135.12, 135.09, 133.9, 131.51, 131.47, 131.45, 130.5, 130.4, 130.1, 130.0, 129.1, 127.7, 126.8, 126.3, 124.73, 124.68, 124.6, 124.5, 124.1, 123.9, 123.6, 123.4, 122.8, 122.7, 120.1, 29.7, 29.6, 24.23, 24.20, 24.16. MS (MALDI-TOF, matrix: DCTB, mode: negative): *m/z* calcd for $[C_{54}H_{44}N_4O_4]^-$ 812.3; found 812.0. HRMS (ESI-TOF, positive, acetonitrile/chloroform): *m/z*: $[M + H]^+$ calcd for $[C_{54}H_{45}N_4O_4]^+$ 813.3441; found: 813.3435 (error = 0.2 ppm). UV/Vis (CH_2Cl_2, nm): λ_{max} (ε_{max} M^{-1} cm^{-1}) = 475 (68,400), 445 (37,200), 431 (26,900), 334 (29,300). CV (CH_2Cl_2, 0.1 M $TBAPF_6$, V *vs* Fc^+/Fc): $E_{1/2}$ = –1.06 ($PBI^{-/0}$), –1.34 ($PBI^{2-/-}$).

_N,N′_-Bis(3′-pentyl)-13-(pyridin-2″-yl)-azabenzo[*pqr*]-perylene-3,4:9,10-tetracarboxylic acid bisimide (ab-PBI, 49a′)

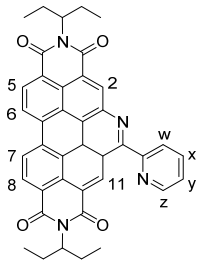

The reaction was performed according to the general Pictet-Spengler reaction procedure using 220 mg (0.40 mmol) of *N,N*′-bis(3′-pentyl)-1-amino-perylene-3,4:9,10-tetracarboxylic acid bisimide and 261 mg (2.44 mmol) of pyridine-2-carboxaldehyde **48a**. The product was obtained as a yellow solid after column chromatography (SiO_2, Toluene/THF 9:1) and recrystallization (THF). Yield: 140 mg (0.22 mmol, 55%). Mp > 300 °C. ^{1}H NMR (400 MHz, THF-d_8, ppm): δ = 10.35 (s, 1H, H^2), 9.19 (s, 1H, H^{11}), 9.15 (d, ^3J = 8.2 Hz, 2H, $H^{6/7}$), 9.08 (d, ^3J = 8.2 Hz, 2H, $H^{6/7}$), 8.85 (d, ^3J = 4.9 Hz, 2H, H^z), 8.83 (d, ^3J = 8.2 Hz, 2H, $H^{5/8}$), 8.76 (d, ^3J = 8.1 Hz, 2H, $H^{5/8}$), 8.57 (d, ^3J = 8.1 Hz, 1H, H^w), 8.07 (d, ^3J = 7.8 Hz,

1H, H^x), 7.53 (dd, ^3J = 7.8 and 5.0 Hz, 1H, H^y), 5.12 – 5.00 (m, 2H, CH), 2.31 – 2.25 (m, 4H, CH_2), 1.16 – 1.87 (m, 4H, CH_2), 0.95 – 0.88 (m, 12H, CH_3). ^{13}C NMR could not be recorded due to the low solubility of the compound. MS (MALDI-TOF, matrix: DCTB, mode: positive): *m/z* calcd for $[C_{40}H_{32}N_4O_4]^+$ 632.2, found 632.2. HR-MS (ESI, positive, acetonitrile/chloroform 1:1): *m/z*: $[M + H]^+$ calcd for $[C_{40}H_{33}N_4O_4]^+$ 633.2496; found: 633.2482 (error = 2.2 ppm). CHN: calcd for $C_{40}H_{32}N_4O_4$, C 75.93, H 5.10, N 8.86%; found (+V_2O_5): C 75.46, H 5.20, N 8.80%. UV/Vis (CH_2Cl_2, nm): λ_{max} (ε_{max} M^{-1} cm^{-1}) = 472 (63,900), 443 (34,400), 334 (25,400), 306 (33,400). CV (CH_2Cl_2, 0.1 M $TBAPF_6$, V *vs* Fc/Fc^+): $E_{1/2}$ = –1.06 ($PBI^{-/0}$), –1.34 ($PBI^{2-/-}$).

N,*N*′-Bis(2′,6′-diisopropylphenyl)-13-(6″-bromopyridin-2″-yl)-azabenzo[*pqr*]-perylene-3,4:9,10-tetracarboxylic acid bisimide (49b)

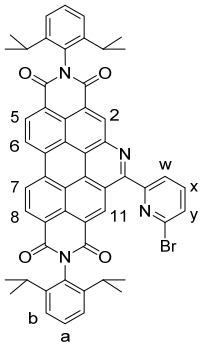

The reaction was performed according to the general Pictet-Spengler reaction procedure using 0.70 g (0.964 mmol) of amino-PBI **47** and 1.0 g (5.36 mmol) of 6-bromo-pyridine-2-carboxaldehyde **48b**. The product was obtained as a yellow solid after column chromatography (SiO_2, EtOAc/hexane 1:2) and recrystallization (MeOH). Yield: 0.49 g (0.55 mmol, 57%). Mp > 300 °C. ^{1}H NMR (400 MHz, CD_2Cl_2): δ = 10.66 (s, 1H), 9.69 (s, 1H), 9.53 – 9.49 (m, 2H), 9.28 (d, ^3J = 8.1 Hz, 1H), 9.24 (d, ^3J = 8.1 Hz, 1H), 8.69 (dd, ^3J = 7.7 Hz, ^4J = 0.8 Hz, 1H), 8.04 (t, ^3J = 7.8 Hz, 1H), 7.83 (dd, ^3J = 7.9 Hz, ^4J = 0.8 Hz, 1H), 7.64 – 7.59 (m, 2H), 7.48 – 7.45 (m, 4H), 2.98 – 2.90 (m, 4H), 1.27 – 1.13 (m, 24H). ^{13}C NMR (100 MHz, CD_2Cl_2): δ = 163.9, 163.8, 163.74, 163.69, 158.0, 155.2, 146.13, 146.11, 144.0, 140.9, 140.0, 135.3, 134.7, 134.0, 133.6, 131.2, 131.1, 131.0, 130.2, 130.1, 129.7, 129.6, 128.8, 128.7, 127.4, 126.0, 125.1, 124.4, 124.20, 124.18, 124.1, 124.0, 123.5, 123.2, 123.1, 122.4, 122.3, 120.0, 29.3, 23.81, 23.78, 23.76. MS (MALDI-TOF, matrix: DCTB, mode: negative): *m/z* calcd for $[C_{54}H_{43}BrN_4O_4]^-$ 890.25; found 890.19. HRMS (ESI-TOF, positive, methanol/chloroform): *m/z*: $[M + H]^+$ calcd for $[C_{54}H_{44}BrN_4O_4]^+$ 891.2540; found: 891.2540 (error = 0.1 ppm). UV/Vis (CH_2Cl_2, nm): λ_{max} (ε_{max} M^{-1} cm^{-1}) = 473 (66,200), 443 (36,300), 432 (27,500), 407 (14,100), 337 (30,400).

_N,N′_-Bis(2′,6′-diisopropylphenyl)-13-(6″-phenyl-pyridin-2″-yl)-azabenzo[*pqr*]-perylene-3,4:9,10-tetracarboxylic acid bisimide (49c)[247]

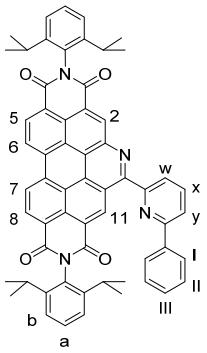

The reaction was performed according to the general Pictet-Spengler reaction procedure using 0.29 g (0.40 mmol) of amino-PBI **47** and 0.48 g (2.62 mmol) of 6-phenyl-pyridine-2-carboxaldehyde **48c**. The product was obtained as a yellow solid after column chromatography (SiO_2, EtOAc/hexane 1:2) and recrystallization (EtOAc). Yield: 134 mg (0.15 mmol, 38%). Mp > 300 °C. ^{1}H NMR (400 MHz, CD_2Cl_2): δ = 10.90 (s, 1H), 9.59 (s, 1H), 9.39 – 9.37 (m, 2H), 9.16 (d, ^3J = 8.3 Hz, 1H), 9.08 (d, ^3J = 8.1 Hz, 1H), 8.59 (dd, ^3J = 7.8 Hz, ^4J = 0.9 Hz, 1H), 8.22 – 8.20 (m, 2H), 8.11 (t, ^3J = 7.9 Hz, 1H), 7.97 (dd, ^3J = 7.9 Hz, ^4J = 0.8 Hz, 1H), 7.49 (t, ^3J = 7.9 Hz, 2H), 7.42 – 7.33 (m, 7H), 2.83 (sep, ^3J = 6.8 Hz, 4H), 1.17 – 1.12 (m, 24H). ^{13}C NMR (100 MHz, CD_2Cl_2): δ = 164.1, 163.93, 163.86, 163.8, 157.2, 157.1, 157.0, 146.2, 146.1, 144.1, 138.9, 138.5, 135.5, 135.2, 134.8, 133.5, 131.2, 131.12, 131.07, 130.3, 130.0, 129.7, 129.6, 129.3, 128.9, 128.8, 127.3, 127.2, 125.9, 124.7, 124.4, 124.2, 123.8, 123.7, 123.5, 123.0, 122.4, 122.3, 121.0, 119.9, 29.29, 29.26, 23.9, 23.82, 23.77, 23.7. MS (MALDI-TOF, matrix: DCTB, mode: positive): *m/z* calcd for $[C_{60}H_{48}N_4O_4]^+$ 888.37; found: 887.96. HRMS (ESI-TOF, positive, acetonitrile/chloroform): *m/z*: $[M + H]^+$ calcd for $[C_{60}H_{49}N_4O_4]^+$ 889.3748; found: 889.3751 (error = 0.3 ppm). UV/Vis (CH_2Cl_2, nm): λ_{max} (ε_{max} M^{-1} cm^{-1}) = 478 (61,700), 448 (34,100), 433 (29,400), 338 (33,900). CV (CH_2Cl_2, 0.1 M $TBAPF_6$, V *vs* Fc^+/Fc): $E_{1/2}$ = –1.08 ($PBI^{-/0}$), -1.36 ($PBI^{2-/-}$).

_N,N′_-Bis(2′,6′-diisopropylphenyl)-13-(2″,2‴-bipyridin-6″-yl)-azabenzo[*pqr*]-perylene-3,4:9,10-tetracarboxylic acid bisimide (49d)

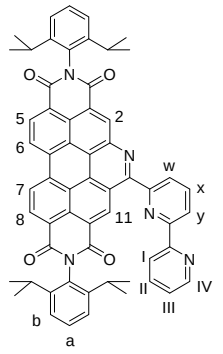

The reaction was performed according to the general Pictet-Spengler reaction procedure using 40 mg (0.07 mmol) of amino-PBI **47** and 92 mg (0.50 mmol) of 6-pyridin-2′-yl- pyridine-2-carboxaldehyde **48d**. The product was obtained as a yellow solid after column chromatography (SiO_2, 99:1 CH_2Cl_2/MeOH) and precipitation (CH_2Cl_2 in *n*-hexane). Yield: 16 mg (18 μmol, 26%). Mp > 300 °C. ^{1}H NMR (400 MHz, CD_2Cl_2): δ = 10.98 (s, 1H), 9.62 (s, 1H), 9.42 – 9.40 (m, 2H), 9.18 (d, ^3J = 8.2 Hz, 1H), 9.11 (d, ^3J = 8.2 Hz, 1H), 8.74 (dd, ^3J = 7.8 Hz, ^4J = 1.0 Hz, 1H), 8.66 – 8.62 (m, 3H), 8.18 (t, ^3J = 7.9 Hz, 1H), 7.68 (td, ^3J = 7.6 Hz, ^4J = 2.0 Hz, 1H),

7.52 – 7.47 (m, 2H), 7.36 – 7.34 (m, 4H), 7.26 (ddd, ^{3}J = 7.5 and 4.7 Hz, ^{4}J = 1.1 Hz, 1H), 2.83 (sep, ^{3}J = 6.9 Hz, 4H), 1.15 – 1.12 (m, 24H). ^{13}C NMR (100 MHz, CD_2Cl_2): δ = 164.3, 164.1, 164.0, 163.9, 156.9, 156.8, 155.9, 155.7, 149.4, 146.3, 146.2, 144.3, 138.8, 137.3, 135.7, 135.4, 135.0, 133.7, 131.3, 131.2, 130.5, 130.2, 129.82, 129.78, 129.0, 127.5, 126.4, 126.0, 124.5, 124.4, 124.2, 124.0, 123.8, 123.7, 123.5, 123.2, 122.6, 122.4, 121.8, 121.4, 120.1, 29.42, 29.40, 24.1, 24.0, 23.9, 23.8. MS (MALDI-TOF, matrix: DCTB, mode: positive): *m/z* calcd for $[C_{59}H_{47}N_5O_4]^+$ 889.36; found: 889.29. HRMS (ESI-TOF, positive, acetonitrile/chloroform): *m/z*: $[M + H]^+$ calcd for $[C_{59}H_{48}N_5O_4]^+$ 890.3701; found: 890.3710 (error = 1.0 ppm). UV/Vis (CH_2Cl_2, nm): λ_{max} (ε_{max} M^{-1} cm^{-1}) = 477 (56,400), 447 (31,200), 432 (26,100), 408 (13,300), 337 (30,500).

N,*N*′-Bis(2′,6′-diisopropylphenyl)-13-phenyl-azabenzo[*pqr*]-perylene-3,4:9,10-tetracarboxylic acid bisimide (49e)

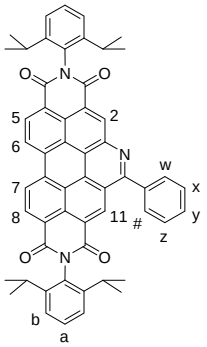

The reaction was performed according to the general Pictet-Spengler reaction procedure using 523 mg (0.69 mmol) of amino-PBI **47** and 1.48 g (13.9 mmol) of benzaldehyde **48e**. The product was obtained as a yellow solid after column chromatography (SiO_2, 99:1 CH_2Cl_2/MeOH) and recrystallization (MeOH). The analytical data are in agreement with those described in literature.[173] Yield: 0.21 g (0.26 mmol, 38%). Mp > 300 °C. ^{1}H NMR (400 MHz, CD_2Cl_2): δ = 9.68 (s, 1H), 9.67 (s, 1H), 9.52 – 9.48 (m, 2H), 9.26 (d, ^{3}J = 8.2 Hz, 1H), 9.23 (d, ^{3}J = 8.2 Hz, 1H), 8.08 – 8.06 (m, 2H), 7.79 – 7.69 (m, 3H), 7.60 – 7.54 (m, 2H), 7.44 – 7.39 (m, 4H), 2.95 – 2.82 (m, 4H), 1.23 – 1.17 (m, 24H). ^{13}C NMR (100 MHz, CD_2Cl_2): δ = 164.4, 164.20, 164.15, 164.0, 162.0, 146.54, 146.46, 145.0, 139.0, 135.9, 135.4, 133.9, 133.5, 131.7, 131.5, 131.4, 131.3, 130.3, 130.22, 130.18, 130.1, 130.0, 129.33, 129.29, 127.6, 126.4, 124.8, 124.6, 124.5, 124.4, 124.2, 124.1, 124.0, 123.6, 122.7, 122.6, 119.7, 29.7, 29.6, 24.19, 24.17, 24.16, 24.1. MS (MALDI-TOF, matrix: DCTB, mode: positive): *m/z* calcd for $[C_{55}H_{45}N_3O_4]^+$ 811.34; found: 810.95. HRMS (ESI-TOF, positive, acetonitrile/chloroform): *m/z*: $[M + H]^+$ calcd for $[C_{55}H_{46}N_3O_4]^+$ 812.3488; found: 812.3483 (error = 0.8 ppm). UV/Vis (CH_2Cl_2, nm): λ_{max} (ε_{max} M^{-1} cm^{-1}) = 477 (59,500), 447 (33,000), 428 (26,100), 405 (13,200), 327 (26,400), 296 (27,600). CV (CH_2Cl_2, 0.1 M $TBAPF_6$, V *vs* Fc^+/Fc): $E_{1/2}$ = –1.04 ($PBI^{-/0}$), –1.35 ($PBI^{2-/-}$).

_N,N′_-Bis(2′,6′-diisopropylphenyl)-13-(3″-(pyridin-2‴-yl)-phenyl)-azabenzo[*pqr*]-perylene-3,4:9,10-tetracarboxylic acid bisimide (49f)

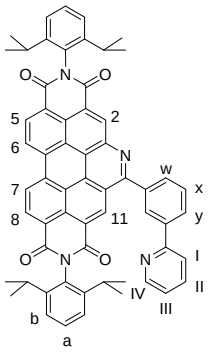

The reaction was performed according to the general Pictet-Spengler reaction procedure using 594 mg (0.82 mmol) of amino-PBI **47** and 630 mg (3.44 mmol) of 3-pyridin-2′-yl-benzaldehyde **48f**. The product was obtained as a yellow solid after column chromatography (SiO_2, 95:5 CH_2Cl_2/EtOAc) and recrystallization (2:2:1 *n*-hexane/ EtOAc/$CHCl_3$). Yield: 155 mg (0.17 mmol, 21%). Mp > 300 °C. ^{1}H NMR (400 MHz, CD_2Cl_2): δ = 9.80 (s, 1H), 9.76 (s, 1H), 9.59 – 9.57 (m, 2H), 9.32 (d, ^3J = 8.3 Hz, 1H), 9.27 (d, ^3J = 8.1 Hz, 1H), 8.77 (m, 1H), 8.72 (ddd, ^3J = 4.8 Hz, ^4J = 1.8 Hz, ^5J = 0.9 Hz, 1H), 8.36 (ddd, ^3J = 7.9 Hz, ^4J = 1.8 and 1.1 Hz, 1H), 8.18 (ddd, ^3J = 7.6 Hz, ^4J = 1.8 and 1.2 Hz, 1H), 7.97 (ddd, ^3J = 8.0 Hz, ^4J = 1.2 Hz, ^5J = 0.8 Hz, 1H), 7.90 (t, ^3J = 7.6 Hz, 1H), 7.84 (td, ^3J = 7.6 Hz, ^4J = 1.8 Hz, 1H), 7.63 – 7.57 (m, 2H), 7.47 – 7.42 (m, 4H), 7.32 (ddd, ^3J = 7.5 and 4.8 Hz, ^4J = 1.1 Hz, 1H), 2.97 – 2.85 (m, 4H), 1.25 – 1.19 (m, 24H). ^{13}C NMR (100 MHz, CD_2Cl_2): δ = 164.0, 163.84, 163.79, 163.7, 161.4, 156.4, 149.8, 146.1, 146.0, 144.7, 140.2, 139.0, 136.9, 135.6, 135.1, 133.6, 133.2, 131.3, 131.2, 131.1, 131.0, 130.0, 129.9, 129.7, 129.6, 129.3, 128.9, 128.1, 127.3, 126.0, 124.5, 124.19, 124.16, 123.83, 123.76, 123.6, 123.1, 122.6, 122.3, 122.2, 120.6, 119.4, 29.24, 29.20, 23.8. MS (MALDI-TOF, matrix: DCTB, mode: negative): *m/z* calcd for $[C_{60}H_{48}N_4O_4]^-$ 888.37; found: 888.31. HRMS (ESI-TOF, positive, acetonitrile/chloroform): *m/z*: $[M + H]^+$ calcd for $[C_{60}H_{49}N_4O_4]^+$ 889.3748; found: 889.3758 (error = 1.1 ppm). UV/Vis (CH_2Cl_2, nm): λ_{max} (ε_{max} M^{-1} cm^{-1}) = 477 (60,400), 447 (33,300), 429 (27,300), 406 (13,300), 328 (29,000), 283 (36,000).

13-(Pyridin-2″-yl)-azabenzo[*pqr*]-perylene-3,4,9,10-tetracarboxylic acid tetra-butyl ester (ab-PTE, 51)

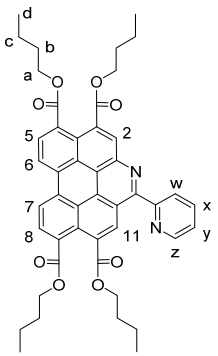

The reaction was performed according to the general Pictet-Spengler reaction procedure using 1.3 g (1.95 mmol) of amino-PTE **50**[37] and 2.5 g (23.4 mmol) of pyridine-2-carboxaldehyde **48a**. The product was obtained as a bright yellow solid after column chromatography (SiO_2, 99:1 → 97:3 CH_2Cl_2/EtOAc) and recrystallization (1:1 *n*-hexane/CH_2Cl_2). Yield: 911 mg (1.21 mmol, 62%). Mp 128–131 °C. ^{1}H NMR (400 MHz, $CDCl_3$): δ = 9.55 (s, 1H), 9.12 (d, ^3J =

8.3 Hz, 2H), 8.99 (s, 1H), 8.88 (ddd, ^3J = 4.9 Hz, ^4J = 1.7 Hz, ^5J = 0.8 Hz, 1H), 8.58 (d, ^3J = 8.2 Hz, 1H), 8.50 (d, ^3J = 8.1 Hz, 1H), 8.33 (ddd, ^3J = 7.8 Hz, ^4J = 1.2 Hz, ^5J = 0.8 Hz, 1H), 8.00 (td, ^3J = 7.7 Hz, ^4J = 1.8 Hz, 1H), 7.49 (ddd, ^3J = 7.6 and 4.8 Hz, ^4J = 1.2 Hz, 1H), 4.41 – 4.30 (m, 8H), 1.83 – 1.68 (m, 8H), 1.54 – 1.39 (m, 8H), 0.98 – 0.90 (m, 12H). ^{13}C NMR (100 MHz, $CDCl_3$): δ = 168.7, 168.5, 168.42, 168.36, 157.7, 156.0, 149.1, 143.2, 137.4, 133.5, 133.1, 133.0, 132.0, 131.3, 130.91, 130.88, 130.1, 129.6, 129.5, 127.7, 126.13, 126.11, 125.6, 125.3, 123.8, 122.6, 122.3, 121.2, 118.8, 65.8, 65.73, 65.69, 65.5, 30.74, 30.66, 30.64, 30.61, 19.33, 19.31, 19.30, 19.28, 13.8. MS (MALDI-TOF, matrix: DCTB, mode: positive): *m/z* calcd for $[C_{46}H_{46}N_2O_8]^+$ 754.33; found 754.34. HRMS (ESI-TOF, positive, acetonitrile/chloroform): *m/z*: $[M + H]^+$ calcd for $[C_{46}H_{47}N_2O_8]^+$ 755.3327; found: 755.3336 (error = 1.2 ppm). UV/Vis (CH_2Cl_2, nm): λ_{max} (ε_{max} M^{-1} cm^{-1}) = 430 (25,700), 407 (24,000), 394 (24,100), 319 (43,400). CV (CH_2Cl_2, 0.1 M $TBAPF_6$, V *vs* Fc^+/Fc): $E_{1/2}$ = –1.60 ($PBI^{-/0}$), –1.88 ($PBI^{2-/-}$).

13-(Pyridin-2″-yl)-azabenzo[*pqr*]-perylene-3,4:9,10-tetracarboxylic acid bisanhydride (ab-PBA, 52)

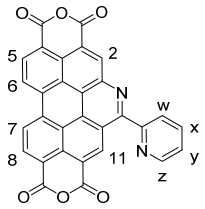

Ab-PTE **51** (679 mg, 0.899 mmol) was dissolved in 79 mL of glacial acid and 1.7 mL of concentrated sulfuric acid. The reaction mixture was heated to 130 °C and after 5 h reaction time a suspension was obtained. Subsequently, 100 mL of water was added to the reaction mixture, and the brown precipitate was separated by filtration and washed successively with acetone, methanol and dichloromethane. High vacuum drying at 60 °C afforded an ocher-colored solid. Yield: 368 mg (0.74 mmol, 83%). Mp > 300 °C. ^{1}H NMR (400 MHz, D_2SO_4): δ = 10.68 – 10.62 (m, 2H), 10.50 (s, 1H), 10.30 (d, ^3J = 8.3 Hz, 1H), 10.25 (d, ^3J = 8.2 Hz, 1H), 10.20 (s, 1H), 10.00 (bd, ^3J = 5.6 Hz, 1H), 9.88 (bt, ^3J = 8.2 Hz, 1H), 9.55 (bd, ^3J = 7.7 Hz, 1H), 9.40 – 9.36 (m, 1H). ^{13}C NMR (100 MHz, D_2SO_4): δ = 163.0, 162.9, 162.3, 162.0, 151.3, 146.5, 144.8, 138.7, 138.6, 138.4, 136.7, 136.3, 135.3, 135.2, 134.3, 133.0, 132.9, 132.3, 131.0, 129.8, 129.5, 128.1, 126.6, 123.9, 123.7, 122.9, 122.5, 120.4, 119.4.

***N,N′*-Bis(2′,5′,8′,11′,15′,18′,21′,24′-octaoxapentacosan-13′-yl)-13-(pyridin-2″-yl)-azabenzo[*pqr*]-perylene-3,4:9,10-tetracarboxylic acid bisimide (ab-PBI^{OEG}, 54)**

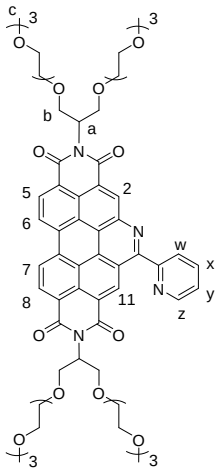

Ab-PBA **52** (50 mg, 0.101 mmol), 2,5,8,11,15,18,21,24-octaoxapentacosan-13-amine **53** (105 mg, 0.275 mmol), imidazole (500 mg) and pyridine (50 µL) were placed in a reaction flask under inert conditions. Afterward, the reaction mixture was heated to 120 °C and the brownish suspension turned slowly into a green solution. After 3 h, the warm reaction mixture (~50 °C) was quenched by the addition of 2 mL 2 N hydrochloric acid and 5 mL of dichloromethane. The organic phase was separated and washed twice with 5 mL of water. The crude product was purified by column chromatography (SiO_2, 99:1 CH_2Cl_2/methanol) to yield an orange solid. Yield: 89 mg (0.073 mmol, 72%). Mp 261–263 °C. ^{1}H NMR (400 MHz, $CDCl_3$): δ = 10.16 (bs, 1H), 9.33 (bs, 1H), 9.11 – 9.08 (m, 2H), 8.99 – 8.91 (m, 3H), 8.45 (ddd, ^3J = 7.8 Hz, ^4J = 1.2 Hz, ^5J = 0.8 Hz, 1H), 8.07 (td, ^3J = 7.7 Hz, ^4J = 1.7 Hz, 1H), 7.54 (ddd, ^3J = 7.8 and 4.8 Hz, ^4J = 1.1 Hz, 1H), 5.80 – 5.72 (m, 2H), 4.24 – 4.19 (m, 4H), 3.99 – 3.97 (m, 4H), 3.76 – 3.50 (m, 25H), 3.48 – 3.45 (m, 15H), 3.40 – 3.37 (m, 8H), 3.23 (s, 6H), 3.22 (s, 6H). ^{13}C NMR (100 MHz, $CDCl_3$): δ = 164.09, 164.05, 164.0, 163.8, 157.12, 157.08, 149.3, 143.7, 137.6, 134.0, 132.7, 129.3, 128.0, 126.6, 126.2, 124.2, 123.9, 123.5, 122.7, 122.4, 122.0, 119.0, 71.8, 70.54, 70.52, 70.49, 70.44, 70.43, 70.40, 69.4, 59.0, 52.5. MS (MALDI-TOF, matrix: DCTB, mode: negative): *m/z* calcd for $[C_{64}H_{80}N_4O_{20}]^-$ 1224.54; found 1224.48. HRMS (ESI-TOF, positive, methanol/chloroform): *m/z*: $[M + H]^+$ calcd for $[C_{64}H_{81}N_4O_{20}]^+$ 1225.5439; found: 1225.5450 (error = 0.9 ppm). UV/Vis (CH_2Cl_2, nm): λ_{max} (ε_{max} M^{-1} cm^{-1}) = 473 (60,300), 444 (32,900), 430 (24,100), 405 (12,200), 333 (26,200), 307 (28,300).

13-(2″,2‴-bipyridin-6″-yl)-azabenzo[*pqr*]-perylene-3,4,9,10-tetracarboxylic acid tetra-butyl ester (ab-PTE, 55)

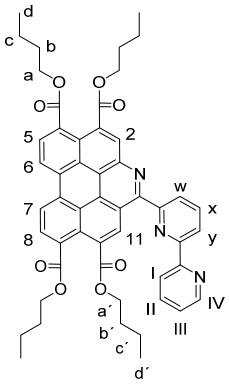

The reaction was performed according to the general Pictet-Spengler reaction procedure using 800 mg (1.2 mmol) of amino-PTE **50**[37] and 1.18 g (6.39 mmol) of 6-pyridin-2′-yl- pyridine-2-carboxaldehyde **48d**. The product was obtained as a bright yellow solid after column chromatography (SiO_2, 97:3 CH_2Cl_2/EtOAc) and recrystallization (1:1 *n*-hexane/CH_2Cl_2). Yield: 656 mg (0.79 mmol, 66%). Mp 172 °C. ^{1}H NMR (400 MHz, $CDCl_3$): δ = 9.84 (s, 1H, H^{11}), 9.09 – 9.06 (m, 2H, H^{6+7}), 8.96 (s, 1H, H^2), 8.73 – 8.71 (m, 1H, H^I), 8.69 (ddd, ^3J = 4.8 Hz, ^4J = 1.8 Hz, ^5J = 0.9 Hz, 1H, H^{IV}), 8.83 (dd, ^3J = 7.9 Hz, ^4J = 0.8 Hz 1H, $H^{y/w}$), 8.56 (d, ^3J = 8.1 Hz, 1H, $H^{5/8}$), 8.53 (dd, ^3J = 7.7 Hz, ^4J = 0.8 Hz, 1H, $H^{y/w}$), 8.47 (d, ^3J = 8.2 Hz, 1H, $H^{5/8}$), 8.14 (t, ^3J = 7.9 Hz, 1H, H^x), 7.82 (td, ^3J = 7.6 Hz, ^4J = 1.7 Hz, 1H, H^{II}), 7.31 (ddd, ^3J = 7.6 and 4.8 Hz, ^4J = 1.0 Hz, 1H, H^{III}), 4.42 – 4.35 (m, 6H, H^a), 4.23 (t, ^3J = 6.9 Hz, 2H, $H^{a'}$), 1.80 – 1.75 (m, 6H, H^b), 1.54 – 1.44 (m, 10H, $H^{b'+c}$), 1.24 – 1.15 (m, 2H, $H^{c'}$), 0.98 – 0.93 (m, 9H, H^d), 0.71 (t, ^3J = 7.4 Hz, 3H, $H^{d'}$). ^{13}C NMR (100 MHz, $CDCl_3$): δ = 168.7, 168.6, 168.6, 168.4, 156.9, 155.9, 155.7, 155.4, 149.2 (C^{IV}), 143.1, 138.5 (C^x), 137.2 (C^{II}), 133.5 (C^2), 133.0, 132.9, 131.9, 131.8 (C^{11}), 130.8, 130.7 ($C^{5/8}$), 130.6, 130.0, 129.7, 129.4 ($C^{5/8}$), 127.7, 126.1, 126.0 ($C^{y/w}$), 125.6, 125.4, 124.0 (C^{III}), 122.6 ($C^{6/7}$), 122.2 ($C^{6/7}$), 121.7 (C^I), 121.2, 121.0 ($C^{y/w}$), 118.7, 65.8 (C^a), 65.8 (C^a), 65.7 (C^a), 65.6 ($C^{a'}$), 30.8 (C^b), 30.7 (C^b), 30.5 ($C^{b'}$), 19.3 (C^c), 19.3 (C^c), 19.1 ($C^{c'}$), 13.9 (C^d), 13.9 (C^d), 13.9 (C^d), 13.7 ($C^{d'}$). MS (MALDI-TOF, matrix: DCTB, mode: positive): *m/z* calcd for $[C_{51}H_{50}N_3O_8]^+$ 831.35; found: 831.38. HR-MS (ESI-TOF, positive, acetonitrile/chloroform): *m/z* $[M + H]^+$ calcd for $[C_{51}H_{50}N_3O_8]^+$ 832.3592; found: 832.3614 (error = 2.6 ppm). UV/Vis (CH_2Cl_2, nm): λ_{max} (ε_{max} M^{-1} cm^{-1}) = 431 (22,600), 407 (21,800), 395 (21,700), 323 (41,600).

13-(2″,2‴-bipyridin-6″-yl)-azabenzo[*pqr*]-perylene-3,4:9,10-tetracarboxylic acid bisanhydride (ab-PBA, 56)

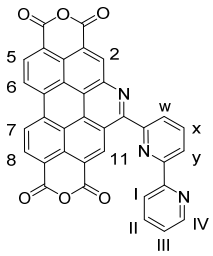

Ab-PTE **55** (754 mg, 0.906 mmol) was dissolved in 80 mL of glacial acid and 1.7 mL of concentrated sulfuric acid. The reaction mixture was heated to 130 °C and after 17 h reaction time a suspension was obtained. Subsequently, 100 mL of water was added to the reaction mixture and the brown precipitate was separated by filtration and washed successively with acetone, methanol and dichloromethane. High vacuum drying at 60 °C afforded an ocher-colored solid. Yield: 439 mg (0.77 mmol, 85%). Mp > 300 °C. ^{1}H NMR (400 MHz, D_2SO_4): δ = 10.84 – 10.80 (m, 2H, $H^{5/6/7/8}$), 10.66 (s, 1H, H^{2}), 10.48 – 10.42 (m, 2H, $H^{5/6/7/8}$), 10.44 (s, 1H, H^{11}), 10.34 (bt, ^{3}J = 8.1 Hz, 1H, H^{x}), 9.97 – 9.93 (m, 3H, H^{w+y+IV}), 9.80 (bt, ^{3}J = 8.4 Hz, 1H, H^{II}), 9.54 (bd, ^{3}J = 7.7 Hz, 1H, H^{I}), 9.31 (bt, ^{3}J = 6.7 Hz, 1H, H^{III}). ^{13}C NMR (100 MHz, D_2SO_4): δ = 163.1, 163.0, 162.4, 162.1, 153.4, 151.2 (C^{II}), 146.0, 145.9 ($C^{w/y/IV}$), 143.3, 141.9, 140.1, 139.0 ($C^{5/6/7/8}$), , 138.6, 137.0 ($C^{5/6/7/8}$), 136.5, 135.6, 135.4 ($C^{w/y/IV}$), 134.3 ($C^{2/11}$), 133.1 ($C^{w/y/IV}$), 132.5 (C^{III}), 131.3 ($C^{5/6/7/8}$), 130.3 (C^{I}), 130.1 ($C^{5/6/7/8}$), 129.7, 128.1, 128.1 ($C^{2/11}$), 127.0, 124.3, 124.2, 124.0, 122.9, 122.6, 120.7, 119.7.

***N*-(12′-Tricosanyl)-1-nitro-perylene-3,4-dicarboxylic acid monoimide-9,10-dicarboxylic acid dioctyl ester (1-nitro-PMIDE, 58)[248]**

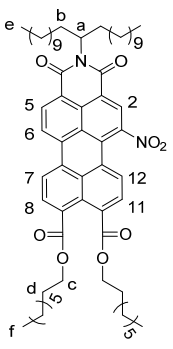

PMIDE **57**[38] (99 mg, 104 µmol) and cerium(IV) ammonium nitrate (88 mg, 160 µmol) were dissolved in 12 mL of dry dichloromethane under inert conditions. Afterward, fuming nitric acid (0.15 mL, 3.60 mmol) was added to the orange solution, and an immediate color change to dark red occurred. The completion of the conversion was monitored by TLC (SiO_2, 1:1 CH_2Cl_2/*n*-hexane). After 15 min, the reaction was quenched by the addition of 2 N NaOH aqueous solution to adjust the pH to ~7. The pH neutral reaction mixture was extracted twice with 100 mL each of dichloromethane. The crude product was purified by column chromatography (SiO_2, CH_2Cl_2/*n*-hexane: 1:1.2 → 1:1) to obtain a dark red solid. Yield: 90 mg (0.09 mmol, 86%). Mp < 30 °C. ^{1}H NMR (400 MHz, CD_2Cl_2): δ = 8.53 (bs, 2H), 8.35 (d, ^{3}J = 8.3 Hz, 1H), 8.30 (d, ^{3}J = 8.1 Hz, 1H), 7.97 (d, ^{3}J = 8.0 Hz, 1H), 7.85 (d, ^{3}J = 8.0 Hz, 1H), 7.80 (d, ^{3}J = 8.0 Hz, 1H), 5.10 – 5.02 (m, 1H), 4.24 – 4.19 (m, 4H), 2.17 – 2.09 (m, 2H), 1.79 – 1.65 (m, 6H), 1.38 – 1.11 (m, 56H),

0.84 – 0.72 (m, 12H). ^{13}C NMR (100 MHz, CD_2Cl_2): δ = 167.9, 167.7, 147.4, 133.7, 132.7, 131.1, 130.5, 130.1, 129.5, 129.3, 128.8, 128.0, 127.6, 127.3, 126.1, 123.9, 66.2, 66.1, 55.0, 32.3, 32.0, 29.8, 29.7, 29.6, 29.5, 29.4, 29.3, 28.7, 27.0, 26.1, 22.8, 14.01, 14.00. MS (MALDI-TOF, matrix: DCTB, mode: negative): *m/z* calcd for $[C_{63}H_{88}N_2O_8]^-$ 1000.65; found 1000.64. HRMS (ESI-TOF, positive, acetonitrile/chloroform): *m/z*: $[M + H]^+$ calcd for $[C_{63}H_{89}N_2O_8]^+$ 1001.6619; found: 1001.6613 (error = 0.6 ppm). UV/VIS (CH_2Cl_2, nm): λ_{max} (ε_{max} M^{-1} cm^{-1}) = 503 (27,200), 361 (6,600), 266 (21,300).

_N_-(12′-Tricosanyl)-1-amino-perylene-3,4-dicarboxylic acid monoimide-9,10-dicarboxylic acid dioctyl ester (1-amino-PMIDE, 59)[248]

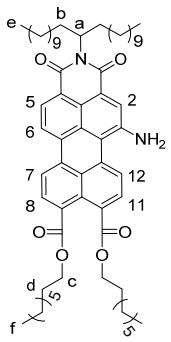

1-Nitro-PMIDE **58** (90 mg, 90 µmol) and tin (II) chloride dihydrate (260 mg, 1.15 mmol) were suspended in 8 mL of tetrahydrofuran. After the reaction mixture was purged with nitrogen for 40 min, the solution was heated to reflux under inert conditions. The completion of the conversion was monitored by TLC (SiO_2, 100:1 CH_2Cl_2/MeOH). After 1 h of reaction time, the solvent was removed under reduced pressure, and the violet solid was dissolved in dichloromethane. The organic solution was washed three times with 100 mL each of water and twice with 50 mL each of sodium hydrogen carbonate solution. The crude product was purified by column chromatography (SiO_2, 100:1 CH_2Cl_2/MeOH) to yield a violet solid. Yield: 31 mg (32 µmol, 36%). Mp < 30 °C. ^{1}H NMR (400 MHz, $CDCl_3$): δ = 8.61 (d, ^3J = 8.1 Hz, 1H), 8.34 – 8.25 (m, 1H), 8.21 (d, ^3J = 8.3 Hz, 1H), 8.14 (d, ^3J = 8.3 Hz, 1H), 8.08 – 8.01 (m, 1H), 7.99 (d, ^3J = 8.3 Hz, 1H), 7.96 (d, ^3J = 7,9 Hz, 1H), 7.19 (s, 2H), 5.09 (bs, 1H), 4.29 – 4.22 (m, 4H), 2.24 – 2.10 (m, 2H), 1.83 – 1.67 (m, 6H), 1.44 – 1.05 (m, 56H), 0.81 (t, ^3J = 6.1 Hz, 6H), 0.77 (t, ^3J = 6.7 Hz, 6H). ^{13}C NMR (100 MHz, $CDCl_3$): δ = 168.6, 168.5, 144.6, 133.7, 133.6, 132.9, 130.39, 130.37, 130.2, 130.0, 129.5, 129.2, 129.0, 128.8, 128.1, 123.7, 122.8, 122.4, 120.8, 65.8, 65.7, 54.6, 32.4, 31.9, 31.8, 29.64, 29.61, 29.59, 29.3, 29.2, 28.6, 27.0, 26.1, 22.7, 14.13, 14.12. MS (MALDI-TOF, matrix: DCTB, mode: negative): *m/z* calcd for $[C_{63}H_{90}N_2O_6]^-$ 970.68; found 970.68. HRMS (ESI-TOF, positive, acetonitrile/chloroform): *m/z*: $[M + H]^+$ calcd for $[C_{63}H_{91}N_2O_6]^+$ 971.6877; found: 971.6872 (error = 0.5 ppm). UV/VIS (CH_2Cl_2, nm): λ_{max} (ε_{max} M^{-1} cm^{-1}) = 535 (8,200), 410 (33,00), 276 (9,300).

_N_-(12′-Tricosanyl)-13-(pyridin-2″-yl)-azabenzo[_pqr_]-perylene-3,4-dicarboxylic acid monoimide-9,10-dicarboxylic acid dioctyl ester (ab-PMIDE, 60)[248]

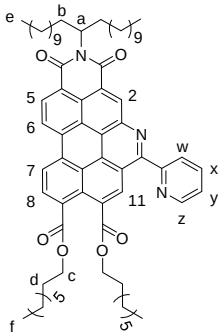

The reaction was performed according to the general Pictet-Spengler reaction procedure using 580 mg (0.60 mmol) of 1-amino-PMIDE **59** and 0.77 g (7.23 mmol) of pyridine-2-carboxaldehyde **48a**. The product was obtained as a yellow-orange solid after column chromatography (SiO_2, gradual CH_2Cl_2 → 9:1 CH_2Cl_2/MeOH). Yield: 388 mg (0.37 mmol, 61%). Mp < 30 °C. ^{1}H NMR (400 MHz, CD_2Cl_2): δ = 9.52 (s, 1H), 8.91 – 8.84 (m, 1H), 8.82 (ddd, ^3J = 4.8 Hz, ^4J = 1.8 Hz, ^5J = 0.9 Hz, 1H), 8.49 (ddd, ^3J = 7.8 Hz, ^4J = 1.2 Hz, ^5J = 0.8 Hz, 1H), 8.47 – 8.39 (m, 1H), 8.39 – 8.29 (m, 2H), 8.21 – 8.13 (m, 1H), 8.06 (td, ^3J = 7.8 Hz, ^4J = 1.8 Hz, 1H), 7.50 (ddd, ^3J = 7.8 Hz, 4.8 Hz, ^4J = 1.2 Hz, 1H), 5.17 (bs, 1H), 4.39 – 4.28 (m, 4H), 2.25 (bs, 2H), 1.93(bs, 2H), 1.88 – 1.76 (m, 4H), 1.53 – 1.42 (m, 4H), 1.42 – 1.02 (m, 52H), 0.86 – 0.77 (m, 6H), 0.76 (t, ^3J = 6.7 Hz, 6H). ^{13}C NMR (100 MHz, CD_2Cl_2): δ = 168.1, 167.9, 164.6, 164.3, 163.6, 163.1, 157.5, 155.2, 148.6, 142.5, 137.2, 134.3, 133.6, 132.1, 131.1, 130.4, 129.1, 128.4, 127.4, 127.1, 126.4, 125.7, 125.2, 124.6, 123.8, 122.3, 122.1, 122.0, 121.5, 121.2, 121.1, 118.3, 66.1, 65.9, 54.7, 32.6, 32.4, 31.9, 29.7, 29.6, 29.5, 29.4, 29.3, 29.2, 28.8, 28.7, 27.2, 26.2, 26.1, 22.7, 22.6, 13.9, 13.8. MS (MALDI-TOF, matrix: DCTB, mode: positive): *m/z* calcd for $[C_{69}H_{91}N_3O_6]^+$ 1057.69; found 1057.67. HRMS (ESI-TOF, positive, acetonitrile/chloroform): *m/z*: $[M + H]^+$ calcd for $[C_{69}H_{92}N_3O_6]^+$ 1058.6981; found: 1058.6979 (error = 0.2 ppm). UV/Vis (CH_2Cl_2, nm): λ_{max} (ε_{max} M^{-1} cm^{-1}) = 454 (36,900), 427 (22,900), 413 (22,600), 392 (11,800), 317 (29,800). CV (CH_2Cl_2, 0.1 M $TBAPF_6$, V *vs* Fc^+/Fc): $E_{1/2}$ = –1.35 ($PBI^{-/0}$), –1.64 ($PBI^{2-/-}$).

_N_-(12′-Tricosanyl)-13-(pyridin-2″-yl)-azabenzo[_pqr_]-perylene-3,4-dicarboxylic acid monoimide-9,10-dicarboxylic acid monoanhydride (ab-PMIMA, 61)[248]

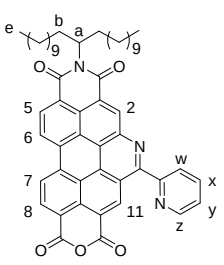

Ab-PMIDE **60** (298 mg, 282 µmol) was dissolved in 25 mL of glacial acid and 0.6 mL of concentrated sulfuric acid and heated to 130 °C. After 5 h of reaction time, an orange suspension was formed, and the completion of the reaction was monitored by TLC (SiO_2, 99:1 CH_2Cl_2/MeOH). Subsequently, 200 mL of water was added to the reaction mixture. The orange precipitate was separated by filtration and washed pH neutral with water. The solid was redissolved in a 9:1 dichloromethane/methanol mixture and

directly used for size exclusion chromatography (Bio-Beads S-X3, 9:1 CH_2Cl_2/MeOH) to isolate the product as an orange solid. Yield: 157 mg (0.19 mmol, 68%). Mp < 30 °C. ^{1}H NMR (400 MHz, CD_2Cl_2): δ = 9.62 (s, 1H), 8.76 – 8.74 (m, 2H), 8.59 (bs, 1H), 8.42 (d, ^3J = 8.3 Hz, 1H), 8.27 – 8.21 (m, 2H), 8.18 (ddd, ^3J = 7.8 Hz, ^4J = 1.2 Hz, ^5J = 0.7 Hz, 1H), 7.96 (td, ^3J = 7.7 Hz, ^4J = 1.8 Hz, 1H), 7.50 (ddd, ^3J = 7.6 and 4.8 Hz, ^4J = 1.1 Hz, 1H), 5.22 – 5.14 (m, 1H), 2.28 – 2.26 (m, 2H), 2.00 – 1.95 (m, 2H), 1.41 – 1.14 (m, 36H), 0.74 (t, ^3J = 6.9 Hz, 6H). ^{13}C NMR (100 MHz, CD_2Cl_2): δ = 163.7, 162.7, 159.0, 158.9, 156.0, 154.9, 148.9, 143.2, 137.6, 135.6, 133.8, 133.6, 133.1, 131.1, 130.2, 129.4, 128.8, 128.2, 127.8, 126.7, 126.0, 125.4, 124.6, 124.0, 123.7, 123.3, 122.6, 121.4, 120.6, 119.9, 118.1, 116.74, 116.70, 55.2, 32.4, 31.9, 29.8, 29.73, 29.70, 29.4, 27.2, 22.7, 13.9. MS (MALDI-TOF, matrix: DCTB, mode: negative): *m/z* calcd for $[C_{53}H_{57}N_3O_5]^+$ 815.43; found 815.38. HRMS (ESI-TOF, positive, acetonitrile/chloroform): *m/z*: $[M + H]^+$ calcd for $[C_{53}H_{58}N_3O_5]^+$ 816.4371; found: 816.4336 (error = 4.2 ppm). UV/Vis (CH_2Cl_2, nm): λ_{max} (ε_{max} M^{-1} cm^{-1}) = 469 (41,700), 472 (24,500), 323(25,800). CV (CH_2Cl_2, 0.1 M $TBAPF_6$, V *vs* Fc^+/Fc): $E_{1/2}$ = –1.05 ($PBI^{-/0}$), –1.31 ($PBI^{2-/-}$).

_N,N′_-Bis(2′,6′-diisopropylphenyl)-*anti*-13,14-di((pyridin-2″-yl)-azabenzo[*pqr*])-perylene-3,4:9,10-tetracarboxylic acid bisimide (*anti*-(ab)$_2$-PBI, 63) and _N,N′_-bis(2′,6′-diisopropylphenyl)-*syn*-13,14-di((pyridin-2″-yl)-azabenzo[*pqr*])-perylene-3,4:9,10-tetracarboxylic acid bisimide (*syn*-(ab)$_2$-PBI, 64)

The reaction was performed according to the general Pictet-Spengler reaction procedure using 1.36 g (1.84 mmol) of a 1,7- and 1,6-diamino-PBI isomer mixture **62** (3:2) and 1.86 g (17.3 mmol) of pyridine-2-carboxaldehyde **48a**. The crude product was first purified by column chromatography (SiO_2, CH_2Cl_2/MeOH, 99:1) to obtain 638 mg (0.697 mmol, 38%) of the isomeric mixture (*anti*-(ab)$_2$-PBI) and *syn*-(ab)$_2$-PBI). After multiple column chromatography (SiO_2, dry packed, 3:1:3 CH_2Cl_2/EtOAc/*n*-hexane), 382 mg (0.417 mmol, 23%) of the orange *anti*-(ab)$_2$-PBI **63** and 236 mg (0.258 mmol, 14%) of the yellow *syn*-(ab)$_2$-PBI **64** were isolated (isomer ratio ~3:2). The analytical data of *syn*-(ab)$_2$-PBI match those reported in the literature.[173] Single crystals suitable for X-ray diffraction were grown by slow evaporation of a saturated solution of *anti*-(ab)$_2$-PBI **63** in THF at room temperature.

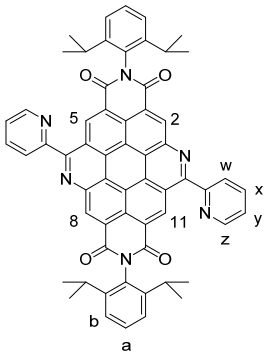

Anti-(ab)$_2$-PBI **63**: Mp > 300 °C. ^{1}H NMR (400 MHz, d$_8$-THF, 233 K): δ = 10.57 (s, 2H), 9.78 (s, 2H), 8.99 (d, ^3J = 7.6 Hz, 2H), 8.43 (d, ^3J = 4.4 Hz, 2H), 8.40 (td, ^3J = 7.4 Hz, ^4J = 1.0 Hz, 2H), 7.77 (ddd, ^3J = 7.5 and 4.8 Hz, ^4J = 0.8 Hz, 2H), 7.72 (dd, ^3J = 8.2 Hz, ^4J = 1.0 Hz, 2H), 7.64 (t, ^3J = 8.2 Hz, 2H), 7.44 (dd, ^3J = 7.9 Hz, ^4J = 1.0 Hz, 2H), 4.20 (sep, ^3J = 6.2 Hz, 2H), 2.66 (sep, ^3J = 6.6 Hz, 2H), 2.00 – 1.94 (m, 12H), 1.04 (d, ^3J = 6.7 Hz, 6H), 0.99 (d, ^3J = 6.7 Hz, 6H). ^{13}C NMR (100 MHz, d$_8$-THF, 233 K): δ = 164.2, 163.9, 158.4, 158.3, 149.3, 147.8, 146.2, 142.0, 138.7, 133.7, 133.2, 132.2, 130.2, 128.2, 126.2, 125.5, 125.2, 125.1, 124.7, 124.6, 123.3, 122.4, 118.2, 117.3, 30.6, 29.9, 26.2, 25.7, 24.5, 24.0. MS (MALDI-TOF, matrix: DCTB, mode: negative): *m/z* calcd for $[C_{60}H_{46}N_6O_4]^-$ 914.36; found 914.31. HRMS (ESI-TOF, positive, acetonitrile/chloroform 1:1): *m/z*: $[M + H]^+$ calcd for $[C_{60}H_{47}N_6O_4]^+$ 915.3653; found: 915.3650 (error = 0.3 ppm). UV/Vis (CH_2Cl_2, nm): λ_{max} (ε_{max} M^{-1} cm^{-1}) = 485 (20,500), 455 (11,000), 414 (46,600), 393 (25,800), 355 (85,400), 338 (64,100). CV (CH_2Cl_2, 0.1 M $TBAPF_6$, V *vs* Fc^+/Fc): $E_{1/2}$ = +1.91 ($PBI^{+/0}$, irrev.), –1.13 ($PBI^{-/0}$), –1.43 ($PBI^{2-/-}$).

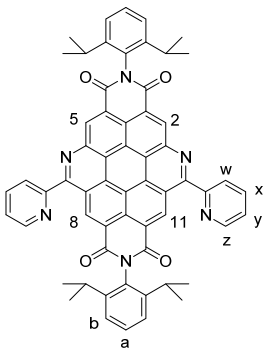

Syn-(ab)$_2$-PBI **64**: Mp > 300 °C. ^{1}H NMR (400 MHz, $CDCl_3$): δ = 11.13 (s, 2H), 10.29 (s, 2H), 9.01 (ddd, ^3J = 4.8 Hz, ^4J = 1.7 Hz, ^5J = 0.9 Hz, 2H), 8.73 (ddd, ^3J = 7.8 Hz, ^4J = 1.2 Hz, ^5J = 0.8 Hz, 2H), 8.15 (td, ^3J = 7.7 Hz, ^4J = 1.8 Hz, 2H), 7.61 (ddd, ^3J = 7.7 and 4.8 Hz, ^4J = 1.1 Hz, 2H), 7.54 – 7.47 (m, 2H), 7.40 – 7.34 (m, 4H), 2.95 (sep, ^3J = 6.7 Hz, 2H), 2.86 (sep, ^3J = 6.9 Hz, 2H), 1.20 (d, ^3J = 6.9 Hz, 12H), 1.16 (d, ^3J = 6.9 Hz, 12H). ^{13}C NMR (100 MHz, $CDCl_3$): δ = 164.2, 164.1, 158.9, 157.5, 149.4, 145.80, 145.76, 143.5, 138.0, 134.8, 132.8, 130.74, 130.68, 130.0, 129.8, 128.8, 127.7, 126.4, 125.4, 124.7, 124.4, 124.2, 123.7, 123.0, 122.5, 120.6, 119.6, 118.6, 29.5, 29.4, 24.2, 24.1. MS (MALDI-TOF, matrix: DCTB, mode: negative): *m/z* calcd for $[C_{60}H_{46}N_6O_4]^-$ 914.36; found 914.32. HRMS (ESI-TOF, positive, acetonitrile/chloroform 1:1): *m/z*: $[M + H]^+$ calcd for $[C_{60}H_{47}N_6O_4]^+$ 915.3653; found: 915.3656 (error = 0.3 ppm). UV/Vis (CH_2Cl_2, nm): λ_{max} (ε_{max} M^{-1} cm^{-1}) = 478 (4,800), 448 (6,800), 429 (42,100), 405 (25,600), 356 (82,900). CV (CH_2Cl_2, 0.1 M $TBAPF_6$, V *vs.* Fc^+/Fc): $E_{1/2}$ = +1.87 ($PBI^{+/0}$, irrev.), –1.16 ($PBI^{-/0}$), –1.44 ($PBI^{2-/-}$).

Syn-13,14-di((pyridin-2″-yl)-azabenzo[_pqr_])-perylene-3,4,9,10-tetracarboxylic acid tetrabutyl ester (_syn_-(ab)$_2$-PTE, 66)

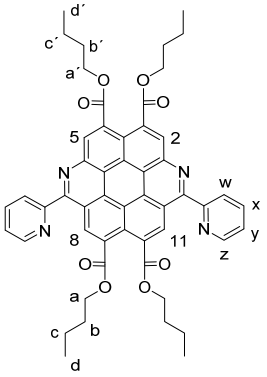

The reaction was performed according to the general Pictet-Spengler reaction procedure using 0.29 g (0.43 mmol) of 1,6-diamino-PTE **65** and 0.91 g (8.5 mmol) of pyridine-2-carboxaldehyde **48a**. The product was obtained as a bright-yellow solid after column chromatography (SiO_2, 99:1 CH_2Cl_2/MeOH) and recrystallization (*n*-hexane/CH_2Cl_2). Yield: 135 mg (0.16 mmol, 37%). Mp 207–208 °C. ^{1}H NMR (400 MHz, $CDCl_3$): δ = 10.37 (s, 2H), 9.62 (s, 2H), 8.98 (ddd, ^3J = 4.8 Hz, ^4J = 1.7 Hz, ^5J = 0.9 Hz, 2H), 8.56 (ddd, ^3J = 7.8 Hz, ^4J = 1.2 Hz, ^5J = 0.8 Hz, 2H), 8.10 (td, ^3J = 7.8 Hz, ^4J = 1.7 Hz, 2H), 7.57 (ddd, ^3J = 7.7 and 4.8 Hz, ^4J = 1.1 Hz, 1H), 4.53 (t, ^3J = 6.8 Hz, 4H), 4.44 (t, ^3J = 6.7 Hz, 4H), 1.92 – 1.85 (m, 4H), 1.81 – 1.74 (m, 4H), 1.61 – 1.53 (m, 4H), 1.50 – 1.43 (m, 4H), 0.99 (t, ^3J = 7.3 Hz, 6H), 0.94 (t, ^3J = 7.4 Hz, 6H). ^{13}C NMR (100 MHz, $CDCl_3$): δ = 168.7, 168.5, 157.9, 157.6, 149.3, 142.4, 137.6, 132.9, 132.4, 131.6, 130.5, 128.1, 127.0, 126.3, 124.1, 122.8, 122.5, 121.8, 121.1, 117.7, 66.1, 65.9, 30.8, 30.6, 19.4, 19.3, 13.9, 13.9. MS (MALDI-TOF, matrix: DCTB, mode: positive): *m/z* calcd for $[C_{52}H_{48}N_4O_8 + H]^+$ 857.35; found 857.25. HRMS (ESI-TOF, positive, methanol/chloroform 1:1): *m/z*: $[M + H]^+$ calcd for $[C_{52}H_{49}N_4O_8]^+$ 857.3545; found: 857.3551 (error = 0.7 ppm). UV/Vis (CH_2Cl_2, nm): λ_{max} (ε_{max} M^{-1} cm^{-1}) = 445 (1,800), 420 (2,400), 384 (18,400), 370 (28,300), 336 (118,800). CV (CH_2Cl_2, 0.1 M $TBAPF_6$, V *vs* Fc^+/Fc): $E_{1/2}$ = –1.68 ($PBI^{-/0}$), –1.98 ($PBI^{2-/-}$).

Syn-13,14-di((pyridin-2″-yl)-azabenzo[_pqr_])-perylene-3,4:9,10-tetracarboxylic acid bisanhydride (_syn_-(ab)$_2$-PBA, 67)

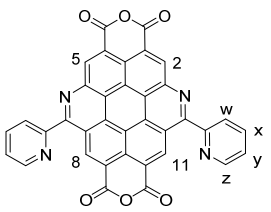

Syn-(ab)$_2$-PTE **66** (95 mg, 0.111 mmol) was dissolved in 10 mL of glacial acid and 0.2 mL of concentrated sulfuric acid. The reaction mixture was heated to 130 °C, and after 17 h of reaction time a suspension was formed. Subsequently, 200 mL of water was added to the cooled reaction mixture and the brown precipitate was separated by filtration and washed successively with water, acetone, methanol and dichloromethane. High vacuum drying at 60 °C afforded the product as an ocher-colored solid. Yield: 64 mg (0.11 mmol, 97%). Mp > 300 °C. ^{1}H NMR (400 MHz, D_2SO_4): δ = 11.51 (s, 2H), 11.41 (s, 2H), 10.28 (bd, ^3J = 5.8 Hz, 2H), 10.14 (bt, ^3J = 8.1 Hz, 2H), 9.91 (bd, ^3J = 7.7 Hz, 2H), 9.40 – 9.36

(m, 2H). ^{13}C NMR (100 MHz, D_2SO_4): δ = 160.3, 160.2, 151.7, 150.8, 147.3, 140.0, 138.0, 136.2, 135.4, 133.9, 133.8, 133.7, 132.1, 129.6, 128.5, 127.1, 124.3, 121.3, 119.1, 119.0.

Ab-PBI dimer 68

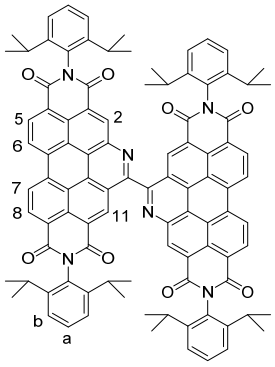

The reaction was performed according to the general Pictet-Spengler reaction procedure using 242 g (0.33 mmol) of amino-PBI **47** and 20 mg of a 40wt% aqueous glyoxal solution (0.12 mmol). Deviating from the standard protocol, *p*-chloranil (245 mg, 1.00 mmol) was added during the inert to oxygen atmosphere change to facilitate the oxidative rearomatization. The product was obtained as an orange solid after two column chromatography's (1st: SiO_2, CH_2Cl_2; 2nd: SiO_2, 9:1 → 6:1 *n*-hexane/EtOAc). Yield: 33 mg (0.022 mmol, 16%). Mp > 300 °C. ^{1}H NMR (400 MHz, $CDCl_3$): δ = 9.72 (s, 2H, H^2), 9.63 (s, 2H, H^{11}), 9.54 – 9.51 (m, 4H, H^{6+7}), 9.31 – 9.26 (m, 4H, H^{5+8}), 7.47 (t, ^3J = 7.8 Hz, 2H, H$^{a'}$), 7.40 (t, ^3J = 7.8 Hz, 2H, H^a), 7.33 (d, ^3J = 7.8 Hz, 4H, H$^{b'}$), 7.24 (d, ^3J = 7.8 Hz, 4H, H^b), 2.82 (sep, ^3J = 6.8 Hz, 4H, CH′), 2.71 (sep, ^3J = 6.8 Hz, 4H, CH), 1.18 – 1.15 (m, 24H, CH_3′), 1.10 (d, ^3J = 6.8 Hz, 12H, CH_3), 1.02 (d, ^3J = 6.8 Hz, 12H, CH_3). ^{13}C NMR (100 MHz, $CDCl_3$, ppm): δ = 163.7, 163.5, 163.4, 157.1, 145.8, 145.6, 144.1, 135.5 (C^2), 135.0, 133.8, 132.7 (C^{11}), 132.1 (C$^{5/8}$), 130.8 (C$^{5/8}$), 130.5, 130.4, 130.3, 129.9 (C^a), 129.8 (C^a), 129.1, 127.7, 126.6, 124.7, 124.5 (C$^{6/7}$), 124.4 (C$^{6/7}$), 124.3 (C^b), 124.2 (C^b), 123.9, 123.6, 123.4, 122.6, 120.2, 29.3 (CH), 29.3 (CH), 24.1 (CH_3), 24.1 (CH_3), 24.1 (CH_3), 24.0 (CH_3). MS (MALDI-TOF, matrix: DCTB, mode: negative): *m/z* calcd for $[C_{98}H_{80}N_6O_8]^-$ 1468.80.63, found: 1468.80. HR-MS (ESI-TOF, positive, acetonitrile/chloroform): *m/z*: $[M + H]^+$ calcd for $[C_{98}H_{81}N_6O_8]^+$ 1469.6110; found: 1469.6132 (error = –1.5 ppm). UV/Vis (CH_2Cl_2, nm): λ_{max} (ε_{max} M^{-1} cm^{-1}) = 470 (90,900), 446 (51,800), 416 (27,300), 342 (38,300), 288 (39,100). CV (CH_2Cl_2, 0.1 M $TBAPF_6$, V *vs.* Fc/Fc^+): $E_{1/2}$ = –1.05 ($PBI^{-/0}$), –1.33 ($PBI^{2-/-}$).

Ab-PBI dimer 69[247]

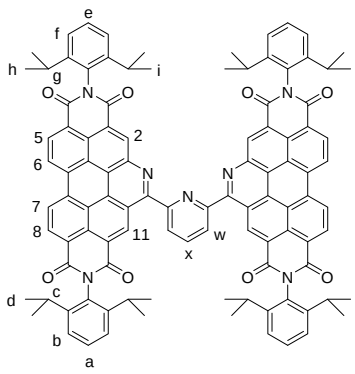

The reaction was performed according to the general Pictet-Spengler reaction procedure using 0.33 g (0.45 mmol) of amino-PBI **47** and 27.5 mg (0.21 mmol) of pyridine-2,6-dicarboxaldehyde. The product was obtained as a yellow solid after column chromatography (SiO_2, 8:1 tetrahydrofuran/ toluene) and recrystallization (EtOAc). Yield: 157 mg (0.101 mmol, 48%). Mp > 300 °C. ^{1}H NMR (400 MHz, CD_2Cl_2): δ = 10.75 (s, 2H, H^{11}), 9.76 (s, 2H, H^2), 9.50 – 9.44 (m, 4H, H^{6+7}), 9.22 (d, ^3J = 8.0 Hz, 2H, H^5), 9.16 (d, ^3J = 8.0 Hz, 2H, H^8), 9.03 (d, ^3J = 8.0 Hz, 2H, H^w), 8.55 (t, ^3J = 8.0 Hz, 1H, H^x), 7.59 (t, ^3J = 7.80 Hz, 2H, H^e), 7.43 (d, ^3J = 7.8 Hz, 4H, H^f), 7.19 (t, ^3J = 7.8 Hz, 2H, H^a), 6.99 (d, ^3J = 8.0 Hz, 2H, H^b), 2.91 (sep, ^3J = 6.7 Hz, 4H, H^g), 2.40 (sep, ^3J = 6.7 Hz, 2H, H^c), 1.22 (d, ^3J = 6.8 Hz, 24H, H^d), 0.93 (d, ^3J = 6.8 Hz, 12H, H^h), 0.26 (d, ^3J = 6.8 Hz, 12H, H^i). ^{13}C NMR (100 MHz, CD_2Cl_2): δ = 164.4, 164.2, 163.9, 163.9, 156.9, 156.6, 146.5, 145.8, 144.9, 139.8 (C^x), 135.9 (C^2), 135.5, 135.4 (C^{11}), 134.0, 131.6 ($C^{5/8}$), 131.4, 131.2, 130.7, 130.4 ($C^{5/8}$), 130.0 (C^e), 129.6 (C^a), 129.0, 127.9, 126.8 (C^w), 126.5, 124.8 ($C^{6/7}$), 124.6 (C^f), 124.3, 124.2 ($C^{6/7}$), 124.2 (C^b), 123.7, 123.5, 123.4, 122.8, 122.4, 120.6, 29. 7 (C^g), 29.3 (C^c), 24.2 (C^d), 24.1 (C^d), 23.7 (C^h), 23.1 (C^i). MS (MALDI-TOF, matrix: DCTB, mode: positive): *m/z* calcd for $[C_{103}H_{83}N_7O_8]^+$ 1545.63, found: 1546.54. HR-MS (ESI-TOF, positive, acetonitrile/chloroform): *m/z*: $[M + Na]^+$ calcd for $[C_{103}H_{83}N_7O_8Na]^+$ 1568.6201; found: 1568.6195 (error = –1.6 ppm). UV/Vis (CH_2Cl_2, nm): λ_{max} (ε_{max} M^{-1} cm^{-1}) = 476 (134,300), 446 (76,400), 433 (61,500), 408 (35,300), 351 (68,400), 338 (69,000). CV (CH_2Cl_2, 0.1 M $TBAPF_6$, V *vs* Fc/Fc^+): $E_{1/2}$ = –1.09 ($PBI^{-/0}$), –1.39 ($PBI^{2-/-}$).

Ab-PBI dimer 70

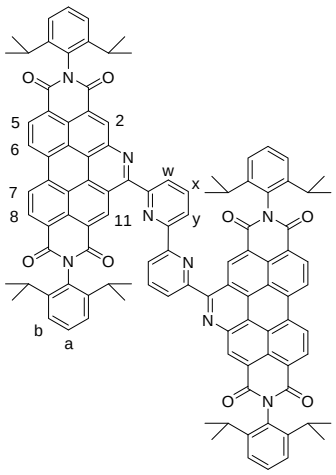

The following reaction was performed under strict exclusion of oxygen and moisture: $NiBr_2(PPh_3)_2$ (164 mg, 0.22 mmol), zinc powder (187 mg, 2.86 mmol) and tetra-*n*-butylammonium iodide (139 mg, 0.35 mmol) were dissolved in 40 mL of dry tetrahydrofuran (color change green to red brown). In a second flask ab-PBI **49b** (312 mg, 0.35 mmol) was dissolved in 10 mL of dry tetrahydrofuran and added to the first solution *via* cannula technique. Afterward, the combined solutions were heated to 50 °C for 16 h. Subsequently, the reaction mixture was poured into 120 mL 2 N aqueous ammonia solution. The basic solution was continuously extracted with chloroform. Then, the combined organic phases were washed five times with 100 mL of water and once with brine. The crude product was further purified by column (SiO_2, 99:1 CH_2Cl_2/MeOH) and size exclusion chromatography (Bio-Beads S-X3, 9:1 CH_2Cl_2/MeOH) to yield a yellow solid. Yield: 265 mg (0.16 mmol, 91%). Mp > 300 °C. ^{1}H NMR (400 MHz, $CDCl_3$): δ = 11.07 (s, 2H, H^{11}), 9.73 (s, 2H, H^2), 9.45 (d, ^3J = 8.3 Hz, 4H, H^{6+7}), 9.26 (d, ^3J = 8.2 Hz, 2H, $H^{5/8}$), 9.20 (d, ^3J = 8.2 Hz, 2H, $H^{5/8}$), 8.94 (dd, ^3J = 8.0 Hz, ^4J = 1.0 Hz, 2H, $H^{w/y}$), 8.76 (dd, ^3J = 7.8 Hz, ^4J = 1.0 Hz, 2H, $H^{w/y}$), 8.10 (t, ^3J = 7.9 Hz, 2H, H^x), 7.50 – 7.47 (m, 4H, H^a), 7.36 (t, ^3J = 7.5 Hz, 8H, H^b), 2.90 – 2.79 (m, 8H, CH), 1.24 - 1.19 (m, 24H, CH_3), 1.16 (d, ^3J = 6.8 Hz, 24H, CH_3). ^{13}C NMR (100 MHz, $CDCl_3$): δ = 164.4, 164.1, 164.1, 164.0, 157.0, 156.8, 155.6, 146.3, 144.4, 139.2, 135.7, 135.4, 135.1, 133.8, 131.4, 131.4, 131.2, 130.6, 130.2, 129.8, 129.0, 128.2, 127.6, 126.7, 126.1, 124.6, 124.4, 124.4, 124.1, 123.9, 123.8, 123.6, 123.2, 122.6, 122.5, 122.4, 120.2, 29.8, 29.5, 29.4, 24.1, 23.9, 23.9, 23.8. MS (MALDI-TOF, matrix: DCTB, mode: negative): *m/z* calcd for $[C_{108}H_{86}N_8O_8]^-$ 1622.66, found: 1622.52. HR-MS (ESI, positive, acetonitrile/chloroform): *m/z*: $[M + H]^+$ calcd for $[C_{108}H_{87}N_8O_8]^+$ 1623.6641; found: 1623.6653 (error = 1.8 ppm). UV/Vis (CH_2Cl_2, nm): λ_{max} (ε_{max} M^{-1} cm^{-1}) = 477 (107,200), 447 (63,000), 432 (53,800), 408 (30,500), 340 (68,600). CV (CH_2Cl_2, 0.1 M $TBAPF_6$, V *vs.* Fc/Fc^+): $E_{1/2}$ = –1.10 ($PBI^{-/0}$), –1.41 ($PBI^{2-/-}$).

Complex $[Ru(bpy)_2(ab\text{-}PBI)][PF_6]_2$ 71

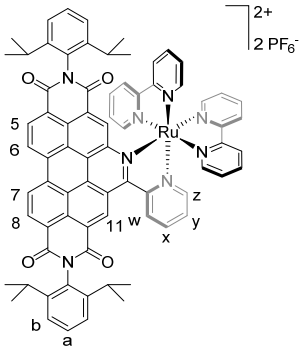

Ab-PBI **49a** (195 mg, 0.240 mmol), $[Ru(bpy)_2Cl_2]$ (140 mg; 0.288 mmol), lithium chloride (61 mg, 1.44 mmol) and silver(I) perchlorate (143 mg, 0.634 mmol) were dissolved in 20 mL of chloroform, 7 mL of ethanol and 1 mL of triethylamine (all degassed) under inert conditions and heated for 18 h at 65 °C. After TLC monitoring (SiO_2, 40:4:1 acetonitrile/water/saturated potassium nitrate solution) indicating an incomplete conversion of **49a**, a second portion of $[Ru(bpy)_2Cl_2]$ (110 mg, 0.227 mmol) and silver(I) perchlorate (140 mg, 0.621 mmol) was added and subsequently heated for 24 h. The brownish reaction mixture was kept in the fridge for two days, and afterwards the precipitate was filtered off through a celite pad. The crude product was further purified by a column chromatography (SiO_2, 40:4:1 acetonitrile/water/saturated potassium nitrate solution). The brown band was collected and a subsequent anion exchange upon the addition of an excess of ammonium hexafluorophosphate was performed. The so formed brown precipitate was filtered off, washed with water and diethyl ether and dried under vacuum. Analytically pure sample could be obtained by additional size exclusion chromatography (CH_2Cl_2/MeOH 9:1, Bio-Beads S-X3). Yield: 250 mg (0.17 mmol, 69%). Mp > 300 °C. ^{1}H NMR (400 MHz, CD_3CN): δ = 10.13 (s, 1H, H^{11}), 9.70 – 9.26 (m, 2H, H^{6+7}), 9.26 (d, ^3J = 8.2, 1H, $H^{5/8}$), 9.13 (d, ^3J = 8.2, 1H, $H^{5/8}$), 8.93 (s, 1H, H^2), 8.88 (d, ^3J = 8.2, 1H, H^w), 8.68 (d, ^3J = 8.1, 1H), 8.63 (d, ^3J = 8.1, 1H), 8.96 - 8.94 (m, 1H, H^z), 8.32 (td, ^3J = 8.0 Hz, ^4J = 1.4 Hz, 1H, H^x), 8.25 – 8.23 (m, 2H), 8.18 – 8.16 (m, 1H), 8.15 – 8.10 (m, 3H), 8.07 (d, ^3J = 5.6, 1H), 7.95 (d, ^3J = 5.7, 1H, H^z), 7.84 (td, ^3J = 8.0 Hz, ^4J = 1.3 Hz, 1H), 7.76 (td, ^3J = 8.0 Hz, ^4J = 1.4 Hz, 1H), 7.63 (d, ^3J = 5.7, 1H), 7.60 – 7.45 (m, 5H, $2H^a$+$2H^b$+H^y), 7.41 – 7.34 (m, 4H, $2H^b$), 7.31 (ddd, ^3J = 8.0 and 5.7 Hz, ^4J = 1.4 Hz, 1H), 7.25 (ddd, ^3J = 8.0 and 5.7 Hz, ^4J = 1.3 Hz, 1H), 3.00 (sept, ^3J = 6.9 Hz, 1H, CH), 2.92 (sept, ^3J = 6.9 Hz, 1H, CH), 2.74 – 2.60 (m, 2H, CH), 1.26 - 1.04 (m, 24H, CH_3). ^{13}C NMR (100 MHz, CD_3CN): δ = 164.3, 164.1, 164.0, 163.4, 161.1, 159.4, 157.9, 157.6, 157.6, 157.1, 154.1, 153.6 (C^z), 152.7, 152.4, 151.9, 148.0, 146.9, 146.8, 146.8, 146.6, 139.2, 139.1, 138.7 (C^x), 138.6, 138.5, 135.4, 134.5, 132.8 (C^w), 132.7 ($C^{5/8}$), 131.6, 131.4 ($C^{5/8}$), 131.4, 131.0 (C^2), 130.5 (C^{11}), 130.4 (C^a), 130.4 (C^a), 130.2, 129.5, 128.8, 128.5, 128.2, 128.1, 128.0 (C^y), 127.8, 127.6, 126.9 ($C^{6/7}$), 126.6 ($C^{6/7}$), 126.4, 125.8, 125.5, 124.9 (C^b), 124.9, 124.8, 124.8, 124.5, 123.8, 123.6, 123.6, 123.5, 123.4, 121.9, 117.9, 29.6, 29.5, 29.4, 29.3, 24.2, 24.0, 23.9, 23.9, 23.8,

23.7. MS (MALDI-TOF, matrix: DCTB, mode: positive): *m/z* calcd for $[C_{74}H_{60}F_6N_8O_4PRu]^+$ 1365.3; found 1365.3. HR-MS (ESI-TOF, positive, acetonitrile/chloroform 1:1): *m/z*: $[M - 2PF_6]^{2+}$ calcd for $[C_{74}H_{60}N_8O_4Ru]^{2+}$ = 610.1901; found: 610.1911 (error = 1.7 ppm). CHN: calcd for $C_{74}H_{60}F_{12}N_8O_4P_2Ru$, C 58.62, H 3.99, N 7.39%; found C 58.50, H 4.33, N 7.18%. UV/Vis (CH_2Cl_2, nm): λ_{max} (ε_{max} M^{-1} cm^{-1}) = 515 (11,900), 470 (45,600), 442 (37,700), 374 (29,100), 289293 (73.300). CV (CH_2Cl_2, 0.1 M $TBAPF_6$, V *vs* Fc/Fc^+): $E_{1/2}$ = +1.02 ($Ru^{3+/2+}$), –0.85 ($PBI^{-/0}$), –1.23 ($PBI^{2-/-}$), –1.86 ($bpy^{-/0}$), –2.15 ($bpy^{-/0}$).

Complex [Cp*Ir(ab-PBI)Cl][PF_6] 72

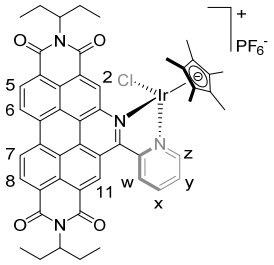

Ab-PBI **49a′** (145 mg, 0.229 mmol), $[Cp^*IrCl_2]_2$ (92 mg; 0.115 mmol) were dissolved in 35 mL of degassed chloroform under inert conditions and heated for 18 h at 40 °C. The reaction mixture was concentrated by evaporation of the organic solvent. Afterward, 20 mL of saturated ammonium hexafluorophosphate ethanol solution was added, and an orange precipitate occurred, and the solid was filtered off and washed with small portions of diethyl ether. The crude product was purified with a column chromatography (Al_2O_3, $CH_2Cl_2 \rightarrow CH_2Cl_2$ + 3% MeOH). Analytical pure dark reddish crystals were obtained after diffusion crystallization of diethyl ether into a high concentrated acetonitrile solution. Yield: 174 mg (0.15 mmol, 67%). Mp > 300 °C. ^{1}H NMR (400 MHz, CD_3CN): δ = 9.99 (s, 1H, H^{11}), 9.81 (s, 1H, H^2), 9.49 – 9.56 (m, 2H, H^{6+7}), 9.20 (d, ^3J = 8.2 Hz, 2H, $H^{5/8}$), 9.15 (d, ^3J = 8.2 Hz, 2H, $H^{5/8}$), 9.13 (dd, ^3J = 5.6 Hz, ^4J = 1.1 Hz, 1H, H^z), 8.81 (d, ^3J = 8.1 Hz, 1H, H^w), 8.42 (td, ^3J = 8.0 Hz, ^4J = 1.2 Hz, 1H, H^y), 8.00 (ddd, ^3J = 8.0 and 5.6 Hz, ^4J = 1.2 Hz, 1H, H^x), 5.21 – 5.11 (m, 2H, CH), 2.41 – 2.29 (m, 4H, CH_2), 2.11 – 2.02 (m, 4H, CH_2), 1.54 (s, 4H, Cp), 1.02 (td, ^3J = 7.5 Hz, ^4J = 1.3 Hz, 12H, CH_3). ^{13}C NMR (100 MHz, CD_3CN): δ =163.7, 156.2, 155.4, 154.1 (C^z), 142.7, 141.0 (C^y), 134.1 (C^2), 133.9, 132.9, 131.8 (C^{5+8}), 130.4 (C^w), 130.3, 129.0 (C^x), 128.8 (C^{11}), 128.1, 127.4, 126.8, 125.8 (C^{6+7}), 125.5, 123.9, 123.0, 122.2, 122.0, 122.0, 121.3, 90.3 (Cp*), 58.0 (CH), 57.9 (CH), 24.7 (CH_2), 24.6 (CH_2), 24.5 (CH_2), 10.5 (CH_3), 7.7 (Cp*-Me). MS (MALDI-TOF, matrix: DCTB, mode: positive): *m/z* calcd for $[C_{50}H_{47}ClIrN_4O_4]^+$ 993.3; found 993.2. HR-MS (ESI-TOF, positive, acetonitrile/ chloroform 1:1): *m/z* : $[M - PF_6]^+$ calcd for $[C_{50}H_{47}ClIrN_4O_4]^+$ 993.2886; found: 993.2880 (error = 0.7 ppm). CHN: calcd for $C_{50}H_{47}ClF_6N_4O_4PIr$, C 52.65, H 4.15, N 4.91%; found:

C 52.97, H 4.25, N 4.77%. UV/Vis (CH_2Cl_2, nm): λ_{max} (ε_{max} M^{-1} cm^{-1}) = 469 (38,800), 440 (33,000), 387 (27,900), 373 (27,900), 293 (29.600). CV (CH_2Cl_2, 0.1 M $TBAPF_6$, V *vs* Fc/Fc^+): $E_{1/2}$ = +1.46 ($Ir^{4+/3+}$, irrev.), –0.82 ($PBI^{-/0}$), –1.11 ($PBI^{2-/-}$), –1.42 ($Ir^{+/3+}$).

Complexes [Ru(bpy)$_2$(*anti*-(ab)$_2$-PBI)][PF$_6$]$_2$ 73 and [Ru(bpy)$_2$(*anti*-(ab)$_2$-PBI)Ru(bpy)$_2$][PF$_6$]$_4$ 74

Anti-ab$_2$-PBI **63** (373 mg, 0.41 mmol)), [Ru(bpy)$_2$Cl$_2$] (99 mg, 0.21 mmol), lithium chloride (47 mg, 1.1 mmol) und silver(I) perchlorate (110 mg, 0.531 mmol) were dissolved in 50 mL of chloroform, 18 mL of ethanol and 2.5 mL of triethylamine (all degassed) under inert conditions and heated for 21 h at 60 °C. Afterward, the dark brown reaction mixture was filtered through a celite pad to remove the AgCl byproduct. In the process of column chromatography purification of the crude product (SiO_2, 40:4:1 acetonitrile/water/saturated potassium nitrate solution) two bands were collected: brown band ([Ru(bpy)$_2$(*anti*-(ab)$_2$-PBI)][PF$_6$]$_2$ **73**) and green band ([Ru(bpy)$_2$(*anti*-(ab)$_2$-PBI)Ru(bpy)$_2$][PF$_6$]$_4$ **74**). Ammonium hexafluorophosphate was added to the respective column fraction solutions to perform an anion exchange. After decreasing the acetonitrile content under reduced pressure, the complexes **73** and **74** as their corresponding hexafluorophosphate salts precipitated out of the solution. The so formed precipitates were filtered off, washed with water and diethyl ether and dried under vacuum. Afterward, size exclusion chromatography (Bio-Beads S-X3, 9:1 CH_2Cl_2/MeOH) was performed to remove excessive salt byproducts and delivered the pure products in their hexafluorophosphate salt form. Yields: 59 mg (0.036 mmol, 17% conversion of Ru) of brown solid [Ru(bpy)$_2$(*anti*-(ab)$_2$-PBI)][PF$_6$]$_2$ **73**: and 58 mg (0.025 mmol, 24% conversion of Ru) of dark green solid [Ru(bpy)$_2$(*anti*-(ab)$_2$-PBI)Ru(bpy)$_2$][PF$_6$]$_4$ **74**.

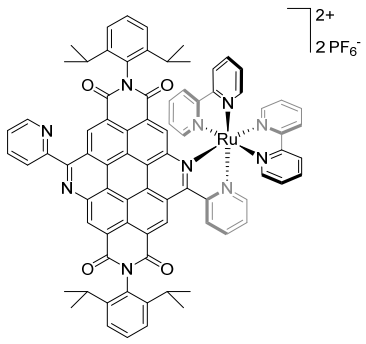

[Ru(bpy)$_2$(*anti*-(ab)$_2$-PBI)][PF$_6$]$_2$ **73**: Mp > 300 °C. ^{1}H NMR (400 MHz, CD_3CN): δ = 11.18 (s, 1H), 10.78 (s, 1H), 10.27 (s, 1H), 9.61 (s, 1H), 9.27 (d, ^3J = 8.2 Hz, 1H), 9.04 (ddd, ^3J = 4.8 Hz, ^4J = 1.7 Hz and 0.9 Hz, 1H), 8.87 (dt, ^3J = 8.0 Hz, ^4J = 1.1 Hz, 1H), 8.76 (bd, ^3J = 8.0 Hz, 1H), 8.72 (bd, ^3J = 7.8 Hz, 1H), 8.45 (td, ^3J = 8.0 Hz, ^4J = 1.4 Hz, 1H), 8.41 (ddd, ^3J = 5.7 Hz, ^4J = 1.4 Hz and 0.6 Hz, 1H), 8.30 – 8.23 (m, 4H), 8.20 (td, ^3J = 8.1 Hz, ^4J = 1.4 Hz, 2H), 8.12 – 8.04 (m, 2H), 7.92 (td, ^3J = 8.0 Hz, ^4J = 1.5 Hz, 1H), 7.78 – 7.39 (m, 12H), 7.32 (ddd, ^3J = 7.5 Hz, ^4J = 5.7 Hz and 1.2 Hz, 1H), 7.24 (ddd, ^3J = 7.5 Hz, ^4J = 5.8 Hz and 1.3 Hz, 1H), 3.20 (sept, ^3J = 6.8 Hz, 1H, CH), 3.06 (sept, ^3J = 6.8 Hz, 1H, CH), 2.88 (sept, ^3J = 6.9 Hz, 1H, CH), 2.80 (sept, ^3J = 6.9 Hz, 1H, CH), 1.32 (d, ^3J = 6.8 Hz, 3H, CH_3), 1.28 (d, ^3J = 6.8 Hz, 3H, CH_3), 1.24 (d, ^3J = 6.8 Hz, 3H, CH_3), 1.23 (d, ^3J = 6.8 Hz, 3H, CH_3), 1.17 – 1.13 (m, 9H, CH_3), 1.11 (d, ^3J = 6.8 Hz, 3H, CH_3). ^{13}C NMR (100 MHz, CD_3CN): δ = 164.64, 164.62 164.5, 163.8, 163.1, 159.7, 159.5, 158.0, 157.9, 157.6, 157.5, 157.2, 154.2, 153.8, 152.7, 152.4, 151.9, 149.7, 147.0, 146.9, 146.8, 146.6, 146.2, 144.1, 139.3, 139.1, 138.9, 138.7, 138.64, 138.56, 135.2, 134.4, 133.5, 133.2, 131.8, 131.6, 130.50, 130.47, 130.2, 129.0, 128.58, 128.56, 128.2, 128.1, 127.5, 127.3, 126.8, 126.8, 126.1, 126.0, 125.8, 125.7, 125.6, 125.5, 124.9, 124.9, 124.8, 124.4, 123.9, 123.6, 123.3, 120.8, 120.5, 120.4, 119.4, 29.6 (CH), 29.5 (CH), 29.4 (CH), 29.33 (CH), 24.27 (CH_3), 24.01 (CH_3), 23.96 (CH_3), 23.94 (CH_3), 23.85 (CH_3), 23.8 (CH_3), 23.7 (CH_3). MS (MALDI-TOF, matrix: DCTB, mode: positive): *m/z* calcd for $[C_{80}H_{62}F_6N_{10}O_4PRu]^+$ 1473.37, found 1473.40. HR-MS (ESI, positive, acetonitrile/chloroform 1:1): *m/z*: $[M - PF_6]^+$ = calcd for $[C_{80}H_{62}N_{10}O_4PF_6Ru]^+$ 1473.3663; found: 1473.3655 (error = 0.5 ppm). CV (CH_2Cl_2, 0.1 M $TBAPF_6$, V *vs* Fc/Fc^+): $E_{1/2}$ = +1.10 ($Ru^{3+/2+}$), –0.87 ($PBI^{-/0}$), –1.24 ($PBI^{2-/-}$), –1.73 ($bpy^{-/0}$), –2.07 ($bpy^{-/0}$).

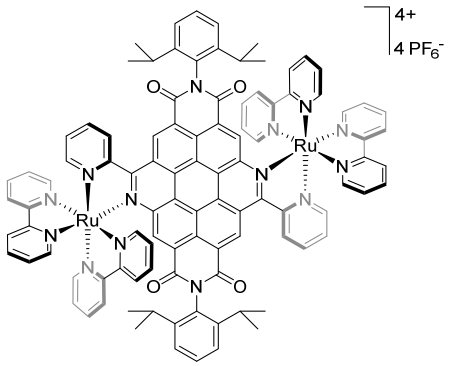

$[Ru(bpy)_2(anti\text{-}(ab)_2\text{-}PBI)Ru(bpy)_2][PF_6]_4$ **74**: Mp > 300 °C. ^{1}H NMR (400 MHz, CD_3CN): δ = 10.72 (s, 1H), 10.71 (s, 1H), 9.60 (s, 1H), 9.58 (s, 1H), 9.19 (t, ^3J = 8.7 Hz, 2H), 8.81 – 8.68 (m, 4H), 8.45 – 8.39 (m, 3H), 8.33 (dd, ^3J = 5.7 Hz, ^4J = 0.7 Hz, 1H), 8.31 – 8.17 (m, 10H), 8.13 (d, ^3J = 8.0 Hz, 1H), 8.10 – 8.06 (m, 3H), 7.96 – 7.89 (m, 2H), 7.74 – 7.60 (m, 8H), 7.54 – 7.41 (m, 8H), 7.36 – 7.29 (m, 2H), 7.24 – 7.15 (m, 2H), 3.03 – 2.73 (m, 4H, CH), 1.25 (d, ^3J = 6.8 Hz, 6H, CH_3), 1.21 – 1.09 (m, 18H, CH_3). ^{13}C NMR (100 MHz, CD_3CN): δ = 163.90, 163.85, 163.8, 163.7, 163.5, 159.3, 157.8, 157.54, 157.48, 157.45, 157.2, 157.1, 154.3, 154.2, 153.80, 153.78, 152.7, 152.6, 152.4, 152.3, 151.9, 151.8, 146.94, 146.93, 146.85, 146.8, 146.7, 146.6, 139.4, 139.2, 138.9, 138.79, 138.76, 138.7, 138.6, 133.8, 131.4, 131.31, 131.26, 130.6, 130.3, 130.2, 129.0, 128.7, 128.6, 128.2, 128.23, 128.20 128.08, 128.06, 127.3, 127.22, 127.21, 127.20, 126.6, 126.4, 125.9, 125.8, 125.6, 125.5, 125.40, 125.38, 125.08, 125.07, 125.0, 124.92, 124.86, 124.6, 124.5, 123.33, 123.28, 120.44, 120.40, 120.3, 120.2, 29.5 (CH), 29.4 (CH), 29.3 (CH), 24.41 (CH_3), 24.37 (CH_3), 23.93 (CH_3), 23.91 (CH_3), 23.84 (CH_3), 23.76 (CH_3), 23.7 (CH_3). MS (MALDI-TOF, matrix: DCTB, mode: positive): *m/z* calcd for $[C_{100}H_{78}F_{18}N_{14}O_4P_3Ru_2]^+$ 2177.33, found 2177.31. HR-MS (ESI, positive, acetonitrile/chloroform 1:1): *m/z*: $[M - PF_6]^+$ calcd for $[C_{100}H_{78}N_{14}O_4P_3F_{18}Ru]^+$ 2177.3385; found: 2177.3363 (error = 1.0 ppm). CV (CH_2Cl_2, 0.1 M $TBAPF_6$, V *vs* Fc/Fc^+): $E_{1/2}$ = +1.13 ($Ru^{3+/2+}$), +1.10 ($Ru^{3+/2+}$), –0.70 ($PBI^{-/0}$), –1.01 ($PBI^{2-/-}$), –1.54 ($bpy^{-/0}$), –1.85 ($bpy^{-/0}$), –2.06 ($bpy^{-/0}$), –2.19 ($bpy^{-/0}$).

Complexes [Ru(bpy)$_2$(*syn*-(ab)$_2$-PBI)][PF$_6$]$_2$ 75 and [Ru(bpy)$_2$(*syn*-(ab)$_2$-PBI)Ru(bpy)$_2$][PF$_6$]$_4$ 76

Syn-ab$_2$-PBI **64** (397 mg, 0.43 mmol), [Ru(bpy)$_2$Cl$_2$] (105 mg, 0.22 mmol), lithium chloride (53 mg, 1.2 mmol) und silver(I) perchlorate (120 mg, 0.579 mmol) were dissolved in 55 mL of chloroform, 19 mL of ethanol and 2.6 mL of triethylamine (all degassed) under inert conditions and heated for 22 h at 60 °C. Afterward, the dark brown reaction mixture was filtered through a celite pad to remove the AgCl byproduct. In the process of column chromatography purification of the crude product (SiO_2, 40:4:1 acetonitrile/water/saturated potassium nitrate solution) two bands were collected: brown band ([Ru(bpy)$_2$(*syn*-(ab)$_2$-PBI)][PF$_6$]$_2$ **75**) and violet band ([Ru(bpy)$_2$(*syn*-(ab)$_2$-PBI)Ru(bpy)$_2$][PF$_6$]$_4$ **76**). Ammonium hexafluorophosphate was added to the respective column fraction solutions to perform an anion exchange. After decreasing the acetonitrile content under reduced pressure, the complexes **75** and **76** as their corresponding hexafluorophosphate salts precipitated out of the solution. The so formed precipitates were filtered off, washed with water and diethyl ether and dried under vacuum. Afterward, size exclusion chromatography (Bio-Beads S-X3, 9:1 CH_2Cl_2/MeOH) was performed to remove excessive salt byproducts and delivered the pure products in their hexafluorophosphate salt form.

Yields: 109 mg (0.066 mmol, 31% conversion of Ru) of brown solid [Ru(bpy)$_2$(*syn*-(ab)$_2$-PBI)][PF$_6$]$_2$ **75** and 89 mg (0.038 mmol, 36% conversion of Ru) of violet solid [Ru(bpy)$_2$(*syn*-(ab)$_2$-PBI)Ru(bpy)$_2$][PF$_6$]$_4$ **76**.

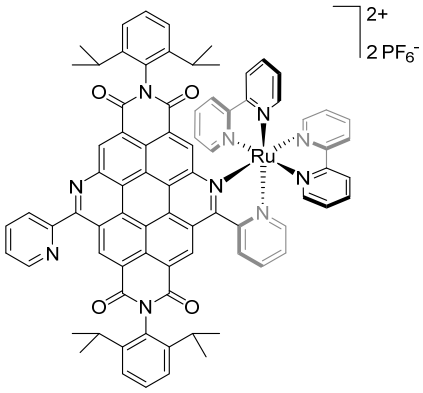

[Ru(bpy)$_2$(*syn*-(ab)$_2$-PBI)][PF$_6$]$_2$ **75**: Mp > 300 °C. ^{1}H NMR (400 MHz, CD$_3$CN): δ = 11.33 (s, 1H), 10.84 (s, 1H), 10.13 (s, 1H), 9.53 (s, 1H), 9.24 (d, ^3J = 8.2 Hz, 1H), 9.08 (ddd, ^3J = 4.8 Hz, ^4J = 1.7 Hz und 0.9 Hz, 1H), 8.89 (dt, ^3J = 8.0 Hz, ^4J = 1.0 Hz, 1H), 8.76 (bd, ^3J = 8.0 Hz, 1H), 8.72 (bd, ^3J = 7.9 Hz, 1H), 8.48 – 8.40 (m, 2H), 8.32 – 8.23 (m, 4H), 8.20 (td, ^3J = 8.2 Hz, ^4J = 1.4 Hz, 2H), 8.13 – 8.04 (m, 2H), 7.92 (td, ^3J = 8.0 Hz, ^4J = 1.3 Hz, 1H), 7.77 (ddd, ^3J = 7.6 Hz, ^4J = 4.9 Hz and 1.2 Hz, 1H), 7.73 – 7.40 (m, 11H), 7.32 (ddd, ^3J = 7.5 Hz, ^{4}J = 5.7 Hz and 1.2 Hz, 1H), 7.23 (ddd, ^3J = 7.5 Hz, ^4J = 5.8 Hz and 1.3 Hz, 1H), 3.17 (sept, ^3J = 6.9 Hz, 1H, CH), 3.06 (sept, ^3J = 6.8 Hz, 1H, CH), 2.90 (sept, ^3J = 6.8 Hz, 1H, CH), 2.82 (sept, ^3J = 6.8 Hz, 1H, CH), 1.32 (d, ^3J = 6.8 Hz, 3H, CH$_3$), 1.27 (d, ^3J = 6.8 Hz, 3H, CH$_3$), 1.24 (d, ^3J = 6.8 Hz, 3H, CH$_3$), 1.22 (d, ^3J = 6.8 Hz, 3H, CH$_3$), 1.18 – 1.16 (m, 9H, CH$_3$), 1.12 (d, ^3J = 6.8 Hz, 3H, CH$_3$). ^{13}C NMR (100 MHz, CD$_3$CN): δ = 164.8, 164.5, 164.4, 163.9, 163.3, 159.7, 159.6, 158.0, 157.9, 157.56, 157.55, 157.2, 154.3, 153.8, 152.7, 152.4, 152.0, 149.8, 146.9, 146.8, 146.6, 144.3, 139.3, 139.1, 138.9, 138.7, 138.6, 136.0, 133.8, 133.7, 131.8, 131.6, 130.8, 130.51, 130.48, 129.0, 128.9, 128.56, 128.54, 128.2, 128.14, 128.06,127.3, 126.7, 126.0 125.8, 125.6, 125.5, 125.1, 125.0, 124.92, 124.90, 124.88, 124.8, 124.7, 124.4, 123.9, 123.5, 123.0, 120.9, 120.1, 120.0, 119.1, 29.6 (CH), 29.5 (CH), 29.43 (CH), 29.37 (CH), 24.3 (CH$_3$), 24.01 (CH$_3$), 23.96 (CH$_3$), 23.94 (CH$_3$), 23.85 (CH$_3$), 23.8 (CH$_3$), 23.7 (CH$_3$). MS (MALDI-TOF, matrix: DCTB, mode: positive): *m/z* calcd for [C$_{80}$H$_{62}$F$_6$N$_{10}$O$_4$PRu]$^+$ 1473.37, found 1473.42. HR-MS (ESI, positive, acetonitrile/chloroform 1:1): *m/z*: [M – PF$_6$]$^+$ calcd for [C$_{80}$H$_{62}$N$_{10}$O$_4$PF$_6$Ru]$^+$ 1473.3663, found: 1473.3666 (error = 0.2 ppm). UV/Vis (CH$_2$Cl$_2$, nm): λ_{max} (ε_{max} M^{-1} cm^{-1}) = 530 (13,300), 430 (39,700), 380 (65,600), 288 (88.900). CV (CH$_2$Cl$_2$, 0.1 M TBAPF$_6$, V *vs* Fc/Fc$^+$): E$_{1/2}$ = +1.11 (Ru$^{3+/2+}$), –0.87 (PBI$^{-/0}$), –1.24 (PBI$^{2-/-}$), –1.73 (bpy$^{-/0}$), –2.08 (bpy$^{-/0}$).

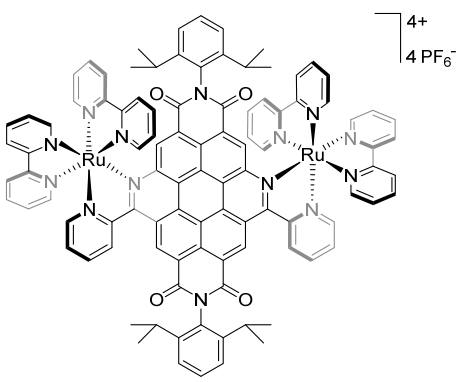

$[Ru(bpy)_2(syn\text{-}(ab)_2\text{-}PBI)Ru(bpy)_2][PF_6]_4$ **76**: Mp > 300°C. ^{1}H NMR (400 MHz, CD_3CN): δ = 10.85 (s, 1H), 10.84 (s, 1H), 9.49 (s, 1H), 9.37 (s, 1H), 9.23 – 9.20 (m, 2H), 8.76 (bd, ^3J = 8.1 Hz, 1H), 8.73 – 8.67 (m, 3H), 8.52 – 8.39 (m, 3H), 8.27 (bd, ^3J = 8.0 Hz, 1H), 8.24 (dd, ^3J = 5.7 Hz, ^4J = 1.1 Hz, 1H), 8.22 – 8.18 (m, 5H), 8.17 – 8.15 (m, 2H), 8.14 – 8.12 (m, 3H), 8.10 (dd, ^3J = 5.6 Hz, ^4J = 0.9 Hz, 1H), 8.07 (dd, ^3J = 5.6 Hz, ^4J = 0.8 Hz, 1H), 8.03 (bd, ^3J = 8.2 Hz, 1H), 7.90 – 7.84(m, 2H), 7.75 (td, ^3J = 7.9 Hz, ^4J = 1.4 Hz, 1H), 7.70 – 7.55 (m, 9H), 7.46 – 7.37 (m, 6H), 7.36 – 7.31 (m, 1H), 7.29 – 7.21 (m, 2H), 7.19 (ddd, ^3J = 7.3 Hz, ^4J = 5.7 Hz and 1.1 Hz, 1H), 3.32 – 2.99 (m, 2H, CH), 2.73 – 2.49 (m, 2H, CH), 1.37 (d, ^3J = 6.8 Hz, 3H), 1.31 (d, ^3J = 6.8 Hz, 3H), 1.29 (d, ^3J = 6.8 Hz, 3H), 1.23 (d, ^3J = 6.8 Hz, 3H), 1.09 (d, ^3J = 6.8 Hz, 3H), 1.06 – 1.04 (m, 9H). ^{13}C NMR (100 MHz, CD_3CN): δ = 164.1, 164.0, 163.8, 163.4, 163.3, 159.34, 159.32, 157.77, 157.75, 157.52, 157.50, 157.44, 157.38, 157.11, 157.05, 154.4, 154.2, 153.8, 152.7, 152.5, 152.32, 152.30, 152.0, 151.7, 147.1, 147.00, 146.98, 146.93, 146.89, 146.85, 146.6, 146.4, 139.4, 139.2, 139.1, 139.0, 138.73, 138.67, 138.6,134.0, 133.9, 131.9, 131.8, 131.5, 131.2, 130.7, 130.60, 130.58, 129.8, 129.7, 129.0, 128.8, 128.74, 128.67, 128.6, 128.2, 128.5, 128.23, 128.21, 128.17, 128.1, 127.7, 127.6, 126.5, 126.4, 125.9, 125.8, 125.6, 125.5, 125.4, 125.3, 125.2, 125.1, 125.0, 124.9, 124.7, 124.5, 123.30, 123.26, 120.0, 119.9, 119.8, 29.6 (CH), 29.7 (CH), 29.6 (CH), 29.5 (CH), 29.3 (CH), 29.2 (CH), 29.1 (CH), 24.2 (CH_3), 24.10 (CH_3), 24.07 (CH_3), 24.0 (CH_3), 23.9 (CH_3), 23.73 (CH_3), 23.70 (CH_3). MS (MALDI-TOF, matrix: DCTB, mode: positive): *m/z* calcd for $[C_{100}H_{78}F_{18}N_{14}O_4P_3Ru_2]^+$ 2177.33, found 2177.41. HR-MS (ESI, positive, acetonitrile/chloroform 1:1): *m/z*: $[M - PF_6]^+$ calcd for $[C_{100}H_{78}N_{14}O_4P_3F_{18}Ru]^+$ 2177.3385, found: 2177.3401 (error = 0.8 ppm). UV/Vis (CH_2Cl_2, nm): λ_{max} (ε_{max} M^{-1} cm^{-1}) = 555 (28,100), 427 (52,100), 376 (78,200), 287 (128,300). CV (CH_2Cl_2, 0.1 M $TBAPF_6$, V *vs* Fc/Fc^+): $E_{1/2}$ = +1.12 ($Ru^{3+/2+}$), +1.10 ($Ru^{3+/2+}$), –0.72 ($PBI^{-/0}$), –1.01 ($PBI^{2-/-}$), –1.53 ($bpy^{-/0}$), –1.84 ($bpy^{-/0}$), –2.04 ($bpy^{-/0}$), –2.18 ($bpy^{-/0}$).

CHAPTER 6 REFERENCES

[1] IEA International Energy Outlook 2016.

[2] N. S. Lewis, D. G. Nocera, *Proc. Natl. Acad. Sci. USA* **2006**, *103*, 15729-15735.

[3] S. Solomon, G.-K. Plattner, R. Knutti, P. Friedlingstein, *Proc. Natl. Acad. Sci. USA* **2009**, *106*, 1704-1709.

[4] G. A. Florides, P. Christodoulides, *Environ. Int.* **2009**, *35*, 390-401.

[5] P. D. Frischmann, K. Mahata, F. Würthner, *Chem. Soc. Rev.* **2013**, *42*, 1847-1870.

[6] K. J. Young, L. A. Martini, R. L. Milot, R. C. Snoeberger Iii, V. S. Batista, C. A. Schmuttenmaer, R. H. Crabtree, G. W. Brudvig, *Coord. Chem. Rev.* **2012**, *256*, 2503-2520.

[7] A. Llobet, *A Key Topic for New Sustainable Energy Conversion Schemes*, John Wiley & Sons, Ltd, **2014**.

[8] J. Barber, *Q. Rev. Biophys.* **2003**, *36*, 71-89.

[9] Y. Tachibana, L. Vayssieres, J. R. Durrant, *Nature Photon.* **2012**, *6*, 511-518.

[10] J. Barber, P. D. Tran, *J. R. Soc. Interface* **2013**, *10*.

[11] S. Berardi, S. Drouet, L. Francas, C. Gimbert-Surinach, M. Guttentag, C. Richmond, T. Stoll, A. Llobet, *Chem. Soc. Rev.* **2014**, *43*, 7501-7519.

[12] D. G. H. Hetterscheid, J. N. H. Reek, *Angew. Chem. Int. Ed.* **2012**, *51*, 9740-9747.

[13] J. D. Blakemore, R. H. Crabtree, G. W. Brudvig, *Chem. Rev.* **2015**, *115*, 12974-13005.

[14] M. D. Kärkäs, O. Verho, E. V. Johnston, B. Åkermark, *Chem. Rev.* **2014**, *114*, 11863-12001.

[15] D. L. Ashford, M. K. Gish, A. K. Vannucci, M. K. Brennaman, J. L. Templeton, J. M. Papanikolas, T. J. Meyer, *Chem. Rev.* **2015**, *115*, 13006-13049.

[16] L. Duan, L. Tong, Y. Xu, L. Sun, *Energ. Environ. Sci.* **2011**, *4*, 3296-3313.

[17] J. Gan, X. Lu, Y. Tong, *Nanoscale* **2014**, *6*, 7142-7164.

[18] S. W. Gersten, G. J. Samuels, T. J. Meyer, *J. Am. Chem. Soc.* **1982**, *104*, 4029-4030.

[19] F. Liu, J. J. Concepcion, J. W. Jurss, T. Cardolaccia, J. L. Templeton, T. J. Meyer, *Inorg. Chem.* **2008**, *47*, 1727-1752.

[20] J. S. Vrettos, J. Limburg, G. W. Brudvig, *Biochim. Biophys. Acta* **2001**, *1503*, 229-245.

[21] G. C. Dismukes, R. Brimblecombe, G. A. N. Felton, R. S. Pryadun, J. E. Sheats, L. Spiccia, G. F. Swiegers, *Acc. Chem. Res.* **2009**, *42*, 1935-1943.

[22] J.-R. Shen, *Annu. Rev. Plant Biol.* **2015**, *66*, 23-48.

[23] G. W. Brudvig, *Philos. Trans. R. Soc. London, Ser. B* **2008**, *363*, 1211-1219.

[24] J. P. McEvoy, G. W. Brudvig, *Chem. Rev.* **2006**, *106*, 4455-4483.

[25] J. P. Collin, J. P. Sauvage, *Inorg. Chem.* **1986**, *25*, 135-141.

[26] K. Nagoshi, S. Yamashita, M. Yagi, M. Kaneko, *J. Mol. Catal. A: Chem.* **1999**, *144*, 71-76.

[27] H. Dau, C. Limberg, T. Reier, M. Risch, S. Roggan, P. Strasser, *ChemCatChem* **2010**, *2*, 724-761.

[28] T. P. Umile, *Catalysis for Sustainability: Goals, Challenges, and Impacts*, CRC Press, **2015**.

[29] A. Melis, *Trends Plant Sci.* **1999**, *4*, 130-135.

[30] S. Mukhopadhyay, S. K. Mandal, S. Bhaduri, W. H. Armstrong, *Chem. Rev.* **2004**, *104*, 3981-4026.

[31] M. M. Najafpour, G. Renger, M. Hołyńska, A. N. Moghaddam, E.-M. Aro, R. Carpentier, H. Nishihara, J. J. Eaton-Rye, J.-R. Shen, S. I. Allakhverdiev, *Chem. Rev.* **2016**, *116*, 2886-2936.

[32] M. Wiechen, H.-M. Berends, P. Kurz, *Dalton Trans.* **2012**, *41*, 21-31.

[33] R. Zong, R. P. Thummel, *J. Am. Chem. Soc.* **2005**, *127*, 12802-12803.

[34] S. Masaoka, K. Sakai, *Chem. Lett.* **2009**, *38*, 182-183.

[35] D. J. Wasylenko, C. Ganesamoorthy, B. D. Koivisto, M. A. Henderson, C. P. Berlinguette, *Inorg. Chem.* **2010**, *49*, 2202-2209.

[36] L. Duan, L. Wang, F. Li, F. Li, L. Sun, *Acc. Chem. Res.* **2015**, *48*, 2084-2096.

[37] L. Duan, F. Bozoglian, S. Mandal, B. Stewart, T. Privalov, A. Llobet, L. Sun, *Nature Chem.* **2012**, *4*, 418-423.

[38] Y. Pushkar, D. Moonshiram, V. Purohit, L. Yan, I. Alperovich, *J. Am. Chem. Soc.* **2014**, *136*, 11938-11945.

[39] X. Sala, S. Maji, R. Bofill, J. García-Antón, L. Escriche, A. Llobet, *Acc. Chem. Res.* **2014**, *47*, 504-516.

[40] W. P. Griffith, in *Ruthenium Oxidation Complexes: Their Uses as Homogenous Organic Catalysts*, Springer Netherlands, Dordrecht, **2011**, pp. 1-134.

[41] D. R. Weinberg, C. J. Gagliardi, J. F. Hull, C. F. Murphy, C. A. Kent, B. C. Westlake, A. Paul, D. H. Ess, D. G. McCafferty, T. J. Meyer, *Chem. Rev.* **2012**, *112*, 4016-4093.

[42] B. A. Moyer, M. S. Thompson, T. J. Meyer, *J. Am. Chem. Soc.* **1980**, *102*, 2310-2312.

[43] K. J. Takeuchi, M. S. Thompson, D. W. Pipes, T. J. Meyer, *Inorg. Chem.* **1984**, *23*, 1845-1851.

[44] A. R. Parent, R. H. Crabtree, G. W. Brudvig, *Chem. Soc. Rev.* **2013**, *42*, 2247-2252.

[45] V. V. Pavlishchuk, A. W. Addison, *Inorg. Chim. Acta* **2000**, *298*, 97-102.

[46] M. Pourbaix, *Atlas of electrochemical equilibria in aqueous solutions*, National Association of Corrosion Engineers, **1974**.

[47] J. J. Concepcion, M.-K. Tsai, J. T. Muckerman, T. J. Meyer, *J. Am. Chem. Soc.* **2010**, *132*, 1545-1557.

[48] E. M. BiochemistryDuffy, B. M. Marsh, J. M. Voss, E. Garand, *Angew. Chem. Int. Ed.* **2016**, *55*, 4079-4082.

[49] L. Duan, A. Fischer, Y. Xu, L. Sun, *J. Am. Chem. Soc.* **2009**, *131*, 10397-10399.

[50] L. Duan, Y. Xu, P. Zhang, M. Wang, L. Sun, *Inorg. Chem.* **2010**, *49*, 209-215.

[51] L. Wang, L. Duan, Y. Wang, M. S. G. Ahlquist, L. Sun, *Chem. Commun.* **2014**, *50*, 12947-12950.

[52] J. Nyhlén, L. Duan, B. Åkermark, L. Sun, T. Privalov, *Angew. Chem. Int. Ed.* **2010**, *49*, 1773-1777.

[53] S. Fukuzumi, J. Jung, Y. Yamada, T. Kojima, W. Nam, *Chem. Asian J.* **2016**, *11*, 1138-1150.

[54] A. Lewandowska-Andralojc, D. E. Polyansky, *J. Phys. Chem. A* **2013**, *117*, 10311-10319.

[55] D. L. Ashford, D. J. Stewart, C. R. Glasson, R. A. Binstead, D. P. Harrison, M. R. Norris, J. J. Concepcion, Z. Fang, J. L. Templeton, T. J. Meyer, *Inorg. Chem.* **2012**, *51*, 6428-6430.

[56] N. Kaveevivitchai, R. Chitta, R. Zong, M. El Ojaimi, R. P. Thummel, *J. Am. Chem. Soc.* **2012**, *134*, 10721-10724.

[57] F. Li, Y. Jiang, B. Zhang, F. Huang, Y. Gao, L. Sun, *Angew. Chem. Int. Ed.* **2012**, *51*, 2417-2420.

[58] L. Wang, M. Mirmohades, A. Brown, L. Duan, F. Li, Q. Daniel, R. Lomoth, L. Sun, L. Hammarström, *Inorg. Chem.* **2015**, *54*, 2742-2751.

[59] A. Hagfeldt, G. Boschloo, L. Sun, L. Kloo, H. Pettersson, *Chem. Rev.* **2010**, *110*, 6595-6663.

[60] C. K. Prier, D. A. Rankic, D. W. C. MacMillan, *Chem. Rev.* **2013**, *113*, 5322-5363.

[61] Q. Zhao, C. Huang, F. Li, *Chem. Soc. Rev.* **2011**, *40*, 2508-2524.

[62] C. Mari, V. Pierroz, S. Ferrari, G. Gasser, *Chem. Sci.* **2015**, *6*, 2660-2686.

[63] A. Juris, V. Balzani, F. Barigelletti, S. Campagna, P. Belser, A. von Zelewsky, *Coord. Chem. Rev.* **1988**, *84*, 85-277.

[64] V. Balzani, A. Juris, *Coord. Chem. Rev.* **2001**, *211*, 97-115.

[65] M. Venturi, A. Credi, V. Balzani, *Coord. Chem. Rev.* **1999**, *185–186*, 233-256.

[66] L. De Cola, P. Belser, *Coord. Chem. Rev.* **1998**, *177*, 301-346.

[67] V. Balzani, G. Bergamini, S. Campagna, F. Puntoriero, in *Photochemistry and Photophysics of Coordination Compounds I* (Eds.: V. Balzani, S. Campagna), Springer Berlin Heidelberg, Berlin, Heidelberg, **2007**, pp. 1-36.

[68] N. D. McClenaghan, Y. Leydet, B. Maubert, M. T. Indelli, S. Campagna, *Coord. Chem. Rev.* **2005**, *249*, 1336-1350.

[69] W. Miao, *Chem. Rev.* **2008**, *108*, 2506-2553.

[70] K. Kalyanasundaram, M. Grätzel, *Coord. Chem. Rev.* **1998**, *177*, 347-414.

[71] R. C. Evans, P. Douglas, C. J. Winscom, *Coord. Chem. Rev.* **2006**, *250*, 2093-2126.

[72] R. Ballardini, V. Balzani, A. Credi, M. T. Gandolfi, M. Venturi, *International Journal of Photoenergy* **2001**, *3*.

[73] V. Balzani, A. Credi, F. M. Raymo, J. F. Stoddart, *Angew. Chem. Int. Ed.* **2000**, *39*, 3348-3391.

[74] V. Balzani, G. Bergamini, P. Ceroni, *Coord. Chem. Rev.* **2008**, *252*, 2456-2469.

[75] V. Balzani, A. Juris, M. Venturi, S. Campagna, S. Serroni, *Chem. Rev.* **1996**, *96*, 759-834.

[76] V. Balzani, S. Campagna, G. Denti, A. Juris, S. Serroni, M. Venturi, *Acc. Chem. Res.* **1998**, *31*, 26-34.

[77] A. Adronov, J. M. J. Frechet, *Chem. Commun.* **2000**, 1701-1710.

[78] P. D. Beer, P. A. Gale, *Angew. Chem. Int. Ed.* **2001**, *40*, 486-516.

[79] S. Campagna, F. Puntoriero, F. Nastasi, G. Bergamini, V. Balzani, in *Photochemistry and Photophysics of Coordination Compounds I* (Eds.: V. Balzani, S. Campagna), Springer Berlin Heidelberg, Berlin, Heidelberg, **2007**, pp. 117-214.

[80] M. D. Ward, *Chem. Soc. Rev.* **1997**, *26*, 365-375.

[81] J. M. R. Narayanam, C. R. J. Stephenson, *Chem. Soc. Rev.* **2011**, *40*, 102-113.

[82] O. Laporte, W. F. Meggers, *J. Opt. Soc. Am.* **1925**, *11*, 459-463.

[83] M. Kasha, *Discuss. Faraday Soc.* **1950**, *9*, 14-19.

[84] J. N. Demas, B. A. DeGraff, in *Topics in Fluorescence Spectroscopy: Probe Design and Chemical Sensing* (Ed.: J. R. Lakowicz), Springer US, Boston, MA, **1994**, pp. 71-107.

[85] M. Sauer, J. Hofkens, J. Enderlein, in *Handbook of Fluorescence Spectroscopy and Imaging*, Wiley-VCH Verlag GmbH & Co. KGaA, **2011**, pp. 1-30.

[86] J. N. Demas, D. G. Taylor, *Inorg. Chem.* **1979**, *18*, 3177-3179.

[87] A. C. Bhasikuttan, M. Suzuki, S. Nakashima, T. Okada, *J. Am. Chem. Soc.* **2002**, *124*, 8398-8405.

[88] K. Nakamaru, *Bull. Chem. Soc. Jpn.* **1982**, *55*, 1639-1640.

[89] J. V. Caspar, T. J. Meyer, *J. Chem. Phys.* **1983**, *87*, 952-957.

[90] C. R. Hecker, A. K. I. Gushurst, D. R. McMillin, *Inorg. Chem.* **1991**, *30*, 538-541.

[91] J.-L. Heully, F. Alary, M. Boggio-Pasqua, *J. Chem. Phys.* **2009**, *131*, 184308.

[92] A. D. McNaught, A. Wilkinson, A. D. Jenkins, P. International Union of, C. Applied, *IUPAC compendium of chemical terminology : the gold book*, International Union of Pure and Applied Chemistry, [Research Triangle Park, N.C.], **2006**.

[93] N. J. Turro, V. Ramamurthy, J. C. Scaiano, *Principles of Molecular Photochemistry: An Introduction*, University Science Books, **2009**.

[94] N. Mataga, T. Okada, H. Masuhara, *Dynamics and Mechanisms of Photoinduced Electron Transfer and Related Phenomena*, Elsevier Science, **2012**.

[95] N. Armaroli, V. Balzani, *Angew. Chem.* **2007**, *119*, 52-67.

[96] N. Armaroli, V. Balzani, *Chem. Eur. J.* **2016**, *22*, 32-57.

[97] V. Balzani, N. Armaroli, *Energy for a Sustainable World: From the Oil Age to a Sun-Powered Future*, Wiley, **2010**.

[98] V. Balzani, A. Credi, M. Venturi, *ChemSusChem* **2008**, *1*, 26-58.

[99] X. Cui, J. Zhao, Z. Mohmood, C. Zhang, *Chem. Rec.* **2016**, *16*, 173-188.

[100] F. Bolletta, A. Juris, M. Maestri, D. Sandrini, *Inorg. Chim. Acta* **1980**, *44*, L175-L176.

[101] G. J. Wilson, A. Launikonis, W. H. F. Sasse, A. W. H. Mau, *J. Phys. Chem. A* **1997**, *101*, 4860-4866.

[102] G. J. Wilson, W. H. F. Sasse, A. W. H. Mau, *Chem. Phys. Lett.* **1996**, *250*, 583-588.

[103] W. Wu, S. Ji, W. Wu, J. Shao, H. Guo, T. D. James, J. Zhao, *Chem. Eur. J.* **2012**, *18*, 4953-4964.

[104] M. B. Majewski, N. R. d. Tacconi, F. M. MacDonnell, M. O. Wolf, *Inorg. Chem.* **2011**, *50*, 9939-9941.

[105] D. S. Tyson, C. R. Luman, X. Zhou, F. N. Castellano, *Inorg. Chem.* **2001**, *40*, 4063-4071.

[106] W. Wu, J. Sun, X. Cui, J. Zhao, *J. Mater. Chem. C* **2013**, *1*, 4577-4589.

[107] O. Johansson, M. Borgström, R. Lomoth, M. Palmblad, J. Bergquist, L. Hammarström, L. Sun, B. Åkermark, *Inorg. Chem.* **2003**, *42*, 2908-2918.

[108] M. Borgström, O. Johansson, R. Lomoth, H. B. Baudin, S. Wallin, L. Sun, B. Åkermark, L. Hammarström, *Inorg. Chem.* **2003**, *42*, 5173-5184.

[109] S. L. Larson, C. M. Elliott, D. F. Kelley, *Inorg. Chem.* **1996**, *35*, 2070-2076.

[110] C. Huang, S. Barlow, S. R. Marder, *J. Org. Chem.* **2011**, *76*, 2386-2407.

[111] F. Würthner, *Chem. Commun.* **2004**, 1564-1579.

[112] F. N. Castellano, *Dalton Trans.* **2012**, *41*, 8493-8501.

[113] F. Würthner, C. R. Saha-Möller, B. Fimmel, S. Ogi, P. Leowanawat, D. Schmidt, *Chem. Rev.* **2016**, *116*, 962-1052.

[114] K. Kodama, A. Kobayashi, T. Hirose, *Tetrahedron Lett.* **2013**, *54*, 5514-5517.

[115] H. Hofmeier, P. R. Andres, U. S. Schubert, in *Metal-Containing and Metallosupramolecular Polymers and Materials, Vol. 928*, American Chemical Society, **2006**, pp. 86-96.

[116] H. El-Batal, K. Guo, X. Li, C. Wesdemiotis, C. N. Moorefield, G. R. Newkome, *Eur. J. Org. Chem.* **2013**, *2013*, 3640-3644.

[117] V. Kunz, V. Stepanenko, F. Würthner, *Chem. Commun.* **2015**, *51*, 290-293.

[118] M. T. Rawls, J. Johnson, B. A. Gregg, *J. Electroanal. Chem.* **2010**, *650*, 10-15.

[119] G. Sathyaraj, M. Kiruthika, T. Weyhermuller, B. U. Nair, *Dalton Trans.* **2012**, *41*, 8460-8471.

[120] O. Novakova, J. Kasparkova, O. Vrana, P. M. van Vliet, J. Reedijk, V. Brabec, *Biochemistry* **1995**, *34*, 12369-12378.

[121] H.-W. Tseng, R. Zong, J. T. Muckerman, R. Thummel, *Inorg. Chem.* **2008**, *47*, 11763-11773.

[122] V. L. Gunderson, E. Krieg, M. T. Vagnini, M. A. Iron, B. Rybtchinski, M. R. Wasielewski, *J. Phys. Chem. B* **2011**, *115*, 7533-7540.

[123] R. K. Dubey, M. Niemi, K. Kaunisto, K. Stranius, A. Efimov, N. V. Tkachenko, H. Lemmetyinen, *Inorg. Chem.* **2013**, *52*, 9761-9773.

[124] A. Chouai, S. E. Wicke, C. Turro, J. Bacsa, K. R. Dunbar, D. Wang, R. P. Thummel, *Inorg. Chem.* **2005**, *44*, 5996-6003.

[125] T. Brietzke, W. Mickler, A. Kelling, H.-J. Holdt, *Dalton Trans.* **2012**, *41*, 2788-2797.

[126] S. D. Bergman, D. Gut, M. Kol, C. Sabatini, A. Barbieri, F. Barigelletti, *Inorg. Chem.* **2005**, *44*, 7943-7950.

[127] S. D. Bergman, I. Goldberg, A. Barbieri, M. Kol, *Inorg. Chem.* **2005**, *44*, 2513-2523.

[128] S. D. Bergman, I. Goldberg, A. Barbieri, F. Barigelletti, M. Kol, *Inorg. Chem.* **2004**, *43*, 2355-2367.

[129] D. J. Gregg, E. Bothe, P. Höfer, P. Passaniti, S. M. Draper, *Inorg. Chem.* **2005**, *44*, 5654-5660.

[130] S. M. Draper, D. J. Gregg, E. R. Schofield, W. R. Browne, M. Duati, J. G. Vos, P. Passaniti, *J. Am. Chem. Soc.* **2004**, *126*, 8694-8701.

[131] J. Bolger, A. Gourdon, E. Ishow, J.-P. Launay, *Inorg. Chem.* **1996**, *35*, 2937-2944.

[132] Y. Sun, S. N. Collins, L. E. Joyce, C. Turro, *Inorg. Chem.* **2010**, *49*, 4257-4262.

[133] G. Pourtois, D. Beljonne, C. Moucheron, S. Schumm, A. Kirsch-De Mesmaeker, R. Lazzaroni, J.-L. Brédas, *J. Am. Chem. Soc.* **2004**, *126*, 683-692.

[134] M. K. Brennaman, J. H. Alstrum-Acevedo, C. N. Fleming, P. Jang, T. J. Meyer, J. M. Papanikolas, *J. Am. Chem. Soc.* **2002**, *124*, 15094-15098.

[135] Y. Liu, R. Hammitt, D. A. Lutterman, L. E. Joyce, R. P. Thummel, C. Turro, *Inorg. Chem.* **2009**, *48*, 375-385.

[136] Y. Sun, M. El Ojaimi, R. Hammitt, R. P. Thummel, C. Turro, *J. Phys. Chem. B* **2010**, *114*, 14664-14670.

[137] Q.-X. Zhou, W.-H. Lei, J.-R. Chen, C. Li, Y.-J. Hou, X.-S. Wang, B.-W. Zhang, *Chem. Eur. J.* **2010**, *16*, 3157-3165.

[138] M. Schulze, V. Kunz, P. D. Frischmann, F. Würthner, *Nature Chem.* **2016**, *8*, 576-583.

[139] L. Tong, L. Duan, Y. Xu, T. Privalov, L. Sun *Angew. Chem. Int. Ed.* **2011**, *50*, 445-449.

[140] R. Staehle, L. Tong, L. Wang, L. Duan, A. Fischer, M. S. G. Ahlquist, L. Sun, S. Rau, *Inorg. Chem.* **2014**, *53*, 1307-1319.

[141] L. Duan, C. M. Araujo, M. S. G. Ahlquist, L. Sun, *Proc. Natl. Acad. Sci. USA* **2012**, *109*, 15584-15588.

[142] A. Sartorel, M. Bonchio, S. Campagna, F. Scandola, *Chem. Soc. Rev.* **2013**, *42*, 2262-2280.

[143] T. R. Cook, P. J. Stang, *Chem. Rev.* **2015**, *115*, 7001-7045.

[144] M. Fujita, M. Tominaga, A. Hori, B. Therrien, *Acc. Chem. Res.* **2005**, *38*, 369-378.

[145] Y. Sato, S.-y. Takizawa, S. Murata, *Eur. J. Inorg. Chem.* **2015**, *2015*, 5495-5502.

[146] N. Song, J. J. Concepcion, R. A. Binstead, J. A. Rudd, A. K. Vannucci, C. J. Dares, M. K. Coggins, T. J. Meyer, *Proc. Natl. Acad. Sci. USA* **2015**, *112*, 4935-4940.

[147] L. Duan, L. Wang, A. K. Inge, A. Fischer, X. Zou, L. Sun, *Inorg. Chem.* **2013**, *52*, 7844-7852.

[148] M. V. Sheridan, B. D. Sherman, Z. Fang, K.-R. Wee, M. K. Coggins, T. J. Meyer, *ACS Catal.* **2015**, *5*, 4404-4409.

[149] J. J. Concepcion, D. K. Zhong, D. J. Szalda, J. T. Muckerman, E. Fujita, *Chem. Commun.* **2015**, *51*, 4105-4108.

[150] F. A. Carey, R. J. Sundberg, *Advanced Organic Chemistry. Part A: Structure and Mechanisms*, Springer, Berlin, **2007**.

[151] L. Vigara, M. Z. Ertem, N. Planas, F. Bozoglian, N. Leidel, H. Dau, M. Haumann, L. Gagliardi, C. J. Cramer, A. Llobet, *Chem. Sci.* **2012**, *3*, 2576-2586.

[152] H. Lv, J. Song, Y. V. Geletii, J. W. Vickers, J. M. Sumliner, D. G. Musaev, P. Kögerler, P. F. Zhuk, J. Bacsa, G. Zhu, C. L. Hill, *J. Am. Chem. Soc.* **2014**, *136*, 9268-9271.

[153] S. Berardi, L. Francàs, S. Neudeck, S. Maji, J. Benet-Buchholz, F. Meyer, A. Llobet, *ChemSusChem* **2015**, *8*, 3688-3696.

[154] L.-X. Xue, T.-T. Meng, W. Yang, K.-Z. Wang, *J. Photochem. Photobiol., B* **2015**, *152, Part A*, 95-105.

[155] M. Schulze, M. Philipp, W. Waigel, D. Schmidt, F. Würthner, *J. Org. Chem.* **2016**, doi:10.1021/acs.joc.1026b01573.

[156] A. Pictet, T. Spengler, *Berichte der deutschen chemischen Gesellschaft* **1911**, *44*, 2030-2036.

[157] H.-Y. Tsai, C.-W. Chang, K.-Y. Chen, *Tetrahedron Lett.* **2014**, *55*, 884-888.

[158] H.-Y. Tsai, K.-Y. Chen, *Dyes and Pigments* **2013**, *96*, 319-327.

[159] H.-Y. Tsai, K.-Y. Chen, *J. Lumin.* **2014**, *149*, 103-111.

[160] R. K. Dubey, N. Westerveld, F. C. Grozema, E. J. R. Sudhölter, W. F. Jager, *Org. Lett.* **2015**, *17*, 1882-1885.

[161] S. Sengupta, R. K. Dubey, R. W. M. Hoek, S. P. P. van Eeden, D. D. Gunbaş, F. C. Grozema, E. J. R. Sudhölter, W. F. Jager, *J. Org. Chem.* **2014**, *79*, 6655-6662.

[162] Y. Zhang, Z. Zhao, X. Huang, Y. Xie, C. Liu, J. Li, X. Guan, K. Zhang, C. Cheng, Y. Xiao, *RSC Adv.* **2012**, *2*, 12644-12647.

[163] J. Kelber, H. Bock, O. Thiebaut, E. Grelet, H. Langhals, *Eur. J. Org. Chem.* **2011**, *2011*, 707-712.

[164] X. Yang, C. Xi, Y. Jiang, *Tetrahedron Lett.* **2005**, *46*, 8781-8783.

[165] D. W. Amos, D. A. Baines, G. W. Flewett, *Tetrahedron Lett.* **1973**, *14*, 3191-3194.

[166] B. Fimmel, M. Son, Y. M. Sung, M. Grüne, B. Engels, D. Kim, F. Würthner, *Chem. Eur. J.* **2015**, *21*, 615-630.

[167] R. J. Lindquist, B. T. Phelan, A. Reynal, E. A. Margulies, L. E. Shoer, J. R. Durrant, M. R. Wasielewski, *J. Mater. Chem. A* **2016**, *4*, 2880-2893.

[168] R. O. Marcon, J. G. dos Santos, K. M. Figueiredo, S. Brochsztain, *Langmuir* **2006**, *22*, 1680-1687.

[169] R. O. Marcon, S. Brochsztain, *Langmuir* **2007**, *23*, 11972-11976.

[170] G. Goretzki, E. S. Davies, S. P. Argent, J. E. Warren, A. J. Blake, N. R. Champness, *Inorg. Chem.* **2009**, *48*, 10264-10274.

[171] B. A. Llewellyn, A. G. Slater, G. Goretzki, T. L. Easun, X.-Z. Sun, E. S. Davies, S. P. Argent, W. Lewis, A. Beeby, M. W. George, N. R. Champness, *Dalton Trans.* **2014**, *43*, 85-94.

[172] M.-J. Lin, M. Schulze, K. Radacki, F. Würthner, *Chem. Commun.* **2013**, *49*, 9107-9109.

[173] L. Hao, W. Jiang, Z. Wang, *Tetrahedron* **2012**, *68*, 9234-9239.

[174] L. L. Merritt, E. Schroeder, *Acta Crys.* **1956**, *9*, 801-804.

[175] N. Nijegorodov, R. Mabbs, W. S. Downey, *Spectrochim. Acta Mol. Biomol. Spectrosc.* **2001**, *57*, 2673-2685.

[176] M. Adachi, Y. Nagao, *Chem. Mater.* **2001**, *13*, 662-669.

[177] Y. Avlasevich, C. Li, K. Mullen, *J. Mater. Chem.* **2010**, *20*, 3814-3826.

[178] N. S. Ham, K. Ruedenberg, *J. Chem. Phys.* **1956**, *25*, 13-26.

[179] C. B. Nielsen, S. Holliday, H.-Y. Chen, S. J. Cryer, I. McCulloch, *Acc. Chem. Res.* **2015**, *48*, 2803-2812.

[180] F. Fernandez-Lazaro, N. Zink-Lorre, A. Sastre-Santos, *J. Mater. Chem. A* **2016**, *4*, 9336-9346.

[181] M. Schulze, A. Steffen, F. Würthner, *Angew. Chem. Int. Ed.* **2015**, *54*, 1570-1573.

[182] W. T. Eckenhoff, R. Eisenberg, *Dalton Trans.* **2012**, *41*, 13004-13021.

[183] M.-T. Youinou, R. Ziessel, *J. Organomet. Chem.* **1989**, *363*, 197-208.

[184] C. Caix, S. Chardon-Noblat, A. Deronzier, R. Ziessel, *J. Electroanal. Chem.* **1996**, *403*, 189-202.

[185] D. Sandrini, M. Maestri, R. Ziessel, *Inorg. Chim. Acta* **1989**, *163*, 177-180.

[186] K. E. Brown, B. S. Veldkamp, D. T. Co, M. R. Wasielewski, *J. Phys. Chem. Lett.* **2012**, *3*, 2362-2366.

[187] W. E. Ford, P. V. Kamat, *J. Chem. Phys.* **1987**, *91*, 6373-6380.

[188] H. Xiang, J. Cheng, X. Ma, X. Zhou, J. J. Chruma, *Chem. Soc. Rev.* **2013**, *42*, 6128-6185.

[189] B. Ventura, H. Langhals, B. Bock, L. Flamigni, *Chem. Commun.* **2012**, *48*, 4226-4228.

[190] S. W. Eaton, L. E. Shoer, S. D. Karlen, S. M. Dyar, E. A. Margulies, B. S. Veldkamp, C. Ramanan, D. A. Hartzler, S. Savikhin, T. J. Marks, M. R. Wasielewski, *J. Am. Chem. Soc.* **2013**, *135*, 14701-14712.

[191] W. E. Ford, H. Hiratsuka, P. V. Kamat, *J. Chem. Phys.* **1989**, *93*, 6692-6696.

[192] D. Schmidt, D. Bialas, F. Würthner, *Angew. Chem. Int. Ed.* **2015**, *54*, 3611-3614.

[193] K. Kalyanasundaram, S. M. Zakeeruddin, M. K. Nazeeruddin, *Coord. Chem. Rev.* **1994**, *132*, 259-264.

[194] M. K. Nazeeruddin, S. M. Zakeeruddin, K. Kalyanasundaram, *J. Chem. Phys.* **1993**, *97*, 9607-9612.

[195] K. Nagarajan, A. R. Mallia, V. S. Reddy, M. Hariharan, *J. Phys. Chem. C* **2016**, *120*, 8443-8450.

[196] J. Baffreau, S. Leroy-Lhez, N. Vân Anh, R. M. Williams, P. Hudhomme, *Chem. Eur. J.* **2008**, *14*, 4974-4992.

[197] Z. Yu, Y. Wu, Q. Peng, C. Sun, J. Chen, J. Yao, H. Fu, *Chem. Eur. J.* **2016**, *22*, 4717-4722.

[198] L. Álvarez-Griera, I. Gallardo, G. Guirado, *Electrochim. Acta* **2009**, *54*, 5098-5108.

[199] I. M. Smallwood, *Handbook of Organic Solvent Properties*, Wiley, **1996**.

[200] E. M. Kober, B. P. Sullivan, T. J. Meyer, *Inorg. Chem.* **1984**, *23*, 2098-2104.

[201] C. Mari, H. Huang, R. Rubbiani, M. Schulze, F. Würthner, H. Chao, G. Gasser, *Eur. J. Inorg. Chem.* **2016**, doi:10.1002/ejic.201600516.

[202] P. R. Ogilby, *Chem. Soc. Rev.* **2010**, *39*, 3181-3209.

[203] R. Schmidt, *Photochem. Photobiol.* **2006**, *82*, 1161-1177.

[204] C. Mari, V. Pierroz, R. Rubbiani, M. Patra, J. Hess, B. Spingler, L. Oehninger, J. Schur, I. Ott, L. Salassa, S. Ferrari, G. Gasser, *Chem. Eur. J.* **2014**, *20*, 14421-14436.

[205] A. Leonidova, V. Pierroz, R. Rubbiani, J. Heier, S. Ferrari, G. Gasser, *Dalton Trans.* **2014**, *43*, 4287-4294.

[206] C. A. Faler, *Tetrahedron Lett.* **2010**, *51*, 5621-5623.

[207] S. Mundinger, U. Jakob, P. Bichovski, W. Bannwarth, *J. Org. Chem.* **2012**, *77*, 8968-8979.

[208] R. Samudrala, X. Zhang, R. M. Wadkins, D. L. Mattern, *Biorg. Med. Chem.* **2007**, *15*, 186-193.

[209] M. R. Hansen, T. Schnitzler, W. Pisula, R. Graf, K. Müllen, H. W. Spiess, *Angew. Chem. Int. Ed.* **2009**, *48*, 4621-4624.

[210] N. A. F. Al-Rawashdeh, S. Chatterjee, J. A. Krause, W. B. Connick, *Inorg. Chem.* **2014**, *53*, 294-307.

[211] R. G. Ball, W. A. G. Graham, D. M. Heinekey, J. K. Hoyano, A. D. McMaster, B. M. Mattson, S. T. Michel, *Inorg. Chem.* **1990**, *29*, 2023-2025.

[212] E. P. Friis, J. E. T. Andersen, L. L. Madsen, N. Bonander, P. Møller, J. Ulstrup, *Electrochim. Acta* **1998**, *43*, 1114-1122.

[213] J. C. de Mello, H. F. Wittmann, R. H. Friend, *Adv. Mater.* **1997**, *9*, 230-232.

[214] R. D. Vocke, *Pure Appl. Chem.* **1999**, *71*, 1593-1607.

[215] T. Yanai, D. P. Tew, N. C. Handy, *Chem. Phys. Lett.* **2004**, *393*, 51-57.

[216] M. Von Arnim, R. Ahlrichs, *J. Comput. Chem.* **1998**, *19*, 1746-1757.

[217] J. P. Perdew, K. Burke, M. Ernzerhof, *Phys. Rev. Lett.* **1996**, *77*, 3865-3868.

[218] A. Schäfer, H. Horn, R. Ahlrichs, *J. Chem. Phys.* **1992**, *97*, 2571-2577.

[219] K. Eichkorn, F. Weigend, O. Treutler, R. Ahlrichs, *Theor. Chem. Acc.* **1997**, *97*, 119-124.

[220] D. Andrae, U. Häußermann, M. Dolg, H. Stoll, H. Preuß, *Theor. Chim. Acta* **1990**, *77*, 123-141.

[221] M. J. Frisch, G. W. Trucks, H. B. Schlegel, G. E. Scuseria, M. A. Robb, J. R. Cheeseman, G. Scalmani, V. Barone, B. Mennucci, G. A. Petersson, H. Nakatsuji, M. Caricato, X. Li, H. P. Hratchian, A. F. Izmaylov, J. Bloino, G. Zheng, J. L. Sonnenberg, M. Hada, M. Ehara, K. Toyota, R. Fukuda, J. Hasegawa, M. Ishida, T. Nakajima, Y. Honda, O. Kitao, H. Nakai, T. Vreven, J. A. Montgomery Jr., J. E. Peralta, F. Ogliaro, M. J. Bearpark, J. Heyd, E. N. Brothers, K. N. Kudin, V. N. Staroverov, R. Kobayashi, J. Normand, K. Raghavachari, A. P. Rendell, J. C. Burant, S. S. Iyengar, J. Tomasi, M. Cossi, N. Rega, N. J. Millam, M. Klene, J. E. Knox, J. B. Cross, V. Bakken, C. Adamo, J. Jaramillo, R. Gomperts, R. E. Stratmann, O. Yazyev, A. J. Austin, R. Cammi, C. Pomelli, J. W. Ochterski, R. L. Martin, K. Morokuma, V. G. Zakrzewski, G. A. Voth, P. Salvador, J. J. Dannenberg, S. Dapprich, A. D. Daniels, Ö. Farkas, J. B. Foresman, J. V. Ortiz, J. Cioslowski, D. J. Fox, Gaussian, Inc., Wallingford, CT, USA, **2009**.

[222] J. P. Perdew, *Phys. Rev. B* **1986**, *33*, 8822-8824.

[223] A. D. Becke, *Phys. Rev. A* **1988**, *38*, 3098-3100.

[224] C. Lee, W. Yang, R. G. Parr, *Phys. Rev. B* **1988**, *37*, 785-789.

[225] F. Weigend, R. Ahlrichs, *PCCP* **2005**, *7*, 3297-3305.

[226] F. Neese, *Wiley Interdiscip. Rev. Comput. Mol. Sci.* **2012**, *2*, 73-78.

[227] C. Adamo, V. Barone, *J. Chem. Phys.* **1999**, *110*, 6158-6170.

[228] J. Tao, J. P. Perdew, V. N. Staroverov, G. E. Scuseria, *Phys. Rev. Lett.* **2003**, *91*, 146401.

[229] J. P. Perdew, J. Tao, V. N. Staroverov, G. E. Scuseria, *J. Chem. Phys.* **2004**, *120*, 6898-6911.

[230] J. P. Perdew, K. Burke, M. Ernzerhof, *Phys. Rev. Lett.* **1997**, *78*, 1396-1396.

[231] J. P. Perdew, M. Ernzerhof, K. Burke, *J. Chem. Phys.* **1996**, *105*, 9982-9985.

[232] M. Ernzerhof, G. E. Scuseria, *J. Chem. Phys.* **1999**, *110*, 5029-5036.

[233] A. D. Becke, *J. Chem. Phys.* **1993**, *98*, 1372-1377.

[234] A. D. Becke, *J. Chem. Phys.* **1993**, *98*, 5648-5652.

[235] L. Goerigk, J. Moellmann, S. Grimme, *PCCP* **2009**, *11*, 4611-4620.

[236] A. Dreuw, M. Head-Gordon, *J. Am. Chem. Soc.* **2004**, *126*, 4007-4016.

[237] F. Neese, *J. Bio.l Inorg. Chem.* **2006**, *11*, 702-711.

[238] L. Goerigk, H. Kruse, S. Grimme, in *Comprehensive Chiroptical Spectroscopy*, John Wiley & Sons, Inc., **2012**, pp. 643-673.

[239] F. Weigend, *PCCP* **2006**, *8*, 1057-1065.

[240] S. Grimme, S. Ehrlich, L. Goerigk, *J. Comput. Chem.* **2011**, *32*, 1456-1465.

[241] S. Grimme, J. Antony, S. Ehrlich, H. Krieg, *J. Chem. Phys.* **2010**, *132*, 154104.

[242] L. Laaksonen, *J. Mol. Graphics* **1992**, *10*, 33-34.

[243] D. L. Bergman, L. Laaksonen, A. Laaksonen, *J. Mol. Graphics Modell.* **1997**, *15*, 301-306.

[244] G. Sheldrick, *Acta Crystallogr. A* **2008**, *64*, 112-122.

[245] A. Spek, *Acta Crystallogr. Sect. A* **1990**, *46*, c34.

[246] D. K. Chand, K. Biradha, M. Kawano, S. Sakamoto, K. Yamaguchi, M. Fujita, *Chem. Asian J.* **2006**, *1*, 82-90.

[247] W. Waigel, Bachelor Thesis, Universität Würzburg **2014**.

[248] M. Philipp, Bachelor Thesis, Universität Würzburg **2015**.

DANKSAGUNG

An dieser Stelle möchte ich mich bei all jenen Menschen bedanken, die mich während der vergangenen Jahre auf die eine oder andere Weise unterstützt haben.

Zuerst möchte ich meinem Doktorvater Prof. Dr. Frank Würthner einen besonderen Dank aussprechen, weil er mir das Vertrauen geschenkt hat an einem neuen und zukunftsorientierten Forschungsgebiet zu arbeiten. Seine Unterstützung bei meinem Stipendienantrag, die vielen fachlichen Diskussionen, die wissenschaftlichen Ratschläge und Hilfestellungen sowie das bereitgestellte erstklassische Arbeitsumfeld haben in großem Maße zum Gelingen dieser Arbeit beigetragen.

Der Stiftung Stipendienfonds des Verbandes der Chemischen Industrie e.V. gebührt mein Dank für die Gewährung eines Kekulé-Stipendiums.
Ferner bedanke ich mich bei den Kooperationspartnern, Dr. Andreas Steffen, Prof. Dr. Gilles Gasser und Prof. Dr. Roland Mitrić, für ihre eingebrachte Expertise und die wissenschaftlichen Diskussionen, die zu einem tieferen Verständnis beigetragen und schlussendlich zu gemeinsamen Veröffentlichungen geführt haben.
Mein spezieller Dank gilt dem Forschungsnetzwerk „Solar Technologies Goes Hybrid“, welches mir einen intensiven Austausch mit anderen Promovierenden, viele interessante Workshops und Exkursionen ermöglicht hat.

Allen Mitarbeitern aus dem Organischen und Anorganischen Institut gilt ein herzlicher Dank für die reibungslose Bereitstellung analytischer Methoden (NMR-Spektroskopie: Dr. Matthias Grüne, Elfriede Ruckdeschel und Patricia Altenberger, Massenspektrometrie: Dr. Michael Büchner, Juliane Adelmann, Herrn Fritz Dadrich und Frau Antje Heckmann, Elementaranalyse: Liselotte Michels und Sabine Timmroth). Außerdem gebührt Dr. Michael Büchner ein besonderer Dank für die vielfältige Unterstützung bei der Durchführung von ^{18}O-isotopenmarkierten MS-Untersuchungen.
Ich bedanke mich bei der kristallographischen Abteilung um Dr. David Schmidt, Dr. Christian Burschka und Ana-Maria Krause für die unzähligen Versuche Molekülstrukturen aufzuklären.
Dr. Vladimir Stepanenko danke ich für die Aufnahme von AFM-Bildern und die anschließende Hilfe bei deren Auswertung.

Mein Dank gilt auch Dr. Andreas Steffen, Merle I. S. Röhr und David Bialas für die Unterstützung und Durchführung theoretischer Berechnungen.
Prof. Dr. Christoph Lambert, Dr. Michael Moos und Dr. Guillaume Grelaud danke ich für die die Möglichkeit der Durchführung der Spektroelektrochemie sowie photokatalytischer Experimente.

Für die zuverlässige Unterstützung bei der Synthese danke ich Petra Seufert-Baumbach. Ferner gilt mein Dank dazu auch allen studentischen Forschungskräften, insbesondere den Bachelor-Studenten Michael Philipp, Sandra Thürauf und Waldemar Waigel sowie den Studenten Melanie Achnich, Sebastian Endres, Kai Oberdorf und Sabine Reising.
Den Mitarbeitern des AK Würthner, Jennifer Begall, Joachim Bialas, Astrid Kudzus, Lisa Otter, Christian Simon, Johannes Thein und Christiana Toussaint, gebührt mein Dank für die stets helfenden Hände bei jeglichen Angelegenheiten, die den Arbeitskreis betrafen.
Ich danke Dr. Chantu-Saha Möller und Dr. David Schmidt für die gründliche Überarbeitung von meinen Manuskripten für wissenschaftliche Publikationen.

Für die große Diskussionsbereitschaft und die tatkräftige Unterstützung spreche ich Dr. David Schmidt, Dr. Matthias Stolte, Dr. Florian Beuerle, Dr. Peter Frischmann und Valentin Kunz einen herzlichen Dank aus.
Des Weiteren bedanke ich mich bei dem gesamten Arbeitskreis Würthner für die schönen Jahre während meiner Doktorarbeit. Die Zeit war stets von einer freundschaftlichen und hilfsbereiten Arbeitsatmosphäre geprägt, welche mir die Eingewöhnung in Würzburg sehr erleichtert hat. In diesem Zusammenhang möchte ich mich besonders bei Alhama, Andi, Annike, Ayan, Christina, David, Eva, Jana, Matze, Pete, Sabine, Stefanie, Valentin und Viktoria für die unterhaltsamen Stammtischabende und andere Unternehmungen bedanken.

Meinen Eltern, Schwiegereltern sowie Freunden bin ich für das fortwährende Verständnis und ihre moralische Unterstützung zu tiefst dankbar.
Ein besonderer Dank gilt meiner Frau Birgit, die mir in der ganzen Zeit ein zuverlässiger Rückhalt war und immer an mich geglaubt hat.

LIST OF PUBLICATIONS

[155] M. Schulze, M. Philipp, W. Waigel, D. Schmidt, F. Würthner, *J. Org. Chem.* **2016**, doi:10.1021/acs.joc.1026b01573.

[201] C. Mari, H. Huang, R. Rubbiani, M. Schulze, F. Würthner, H. Chao, G. Gasser, *Eur. J. Inorg. Chem.* **2016**, doi:10.1002/ejic.201600516

[138] M. Schulze, V. Kunz, P. D. Frischmann, F. Würthner, *Nature Chem.* **2016**, *8*, 576-583.

[181] M. Schulze, A. Steffen, F. Würthner, *Angew. Chem. Int. Ed.* **2015**, *54*, 1570-1573.

[172] M.-J. Lin, M. Schulze, K. Radacki, F. Würthner, *Chem. Commun.* **2013**, *49*, 9107-9109.

OVERVIEW OF SYNTHESIZED COMPOUNDS

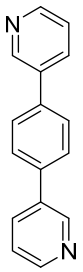

45

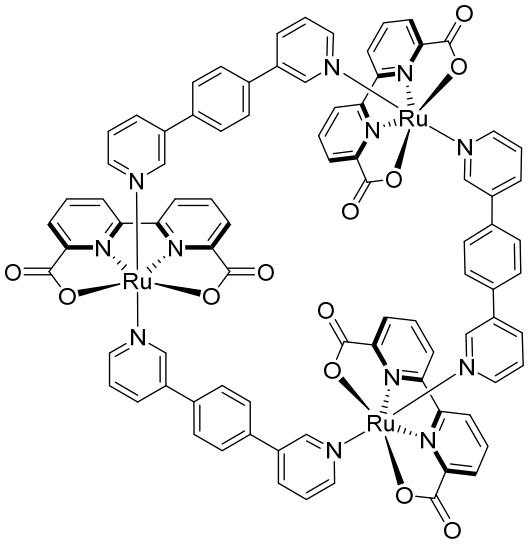

[Ru(bda)bpb]$_3$ **46**

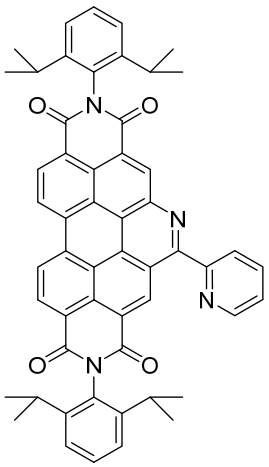

49a

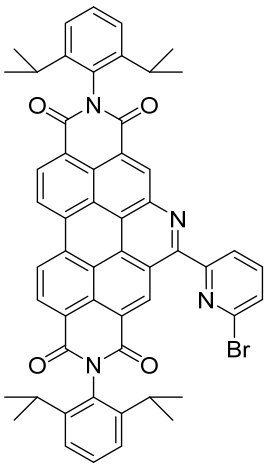

49b

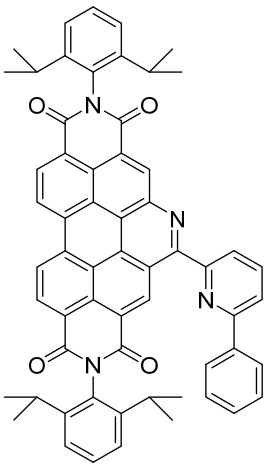

49c

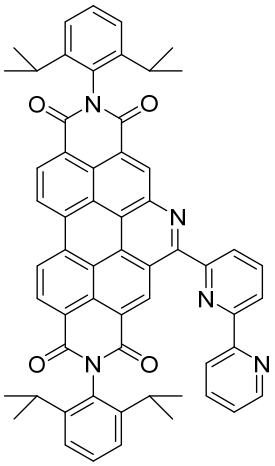

49d

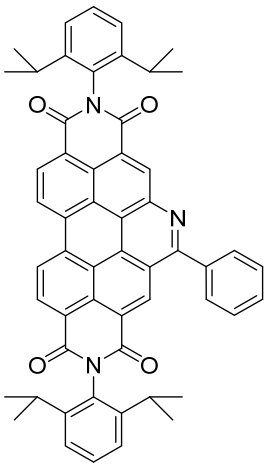

49e

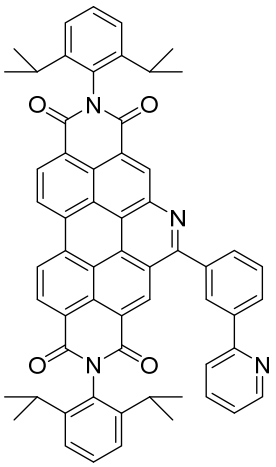

49f

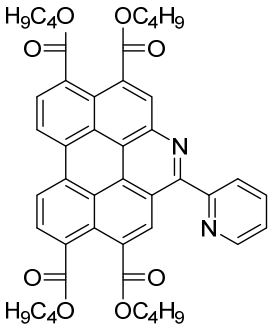

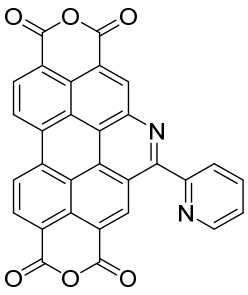

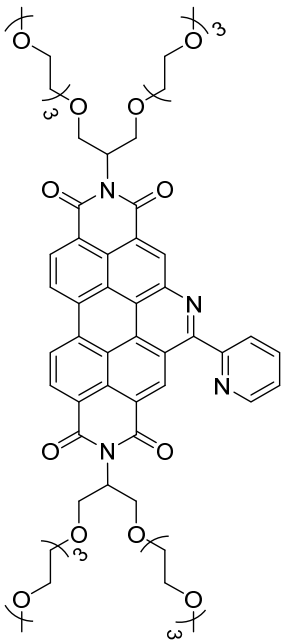

51

52

54

55

56

58

59

60

61

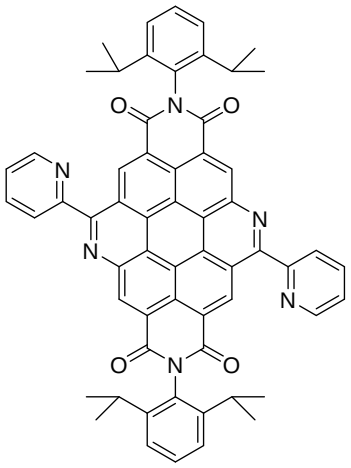

63

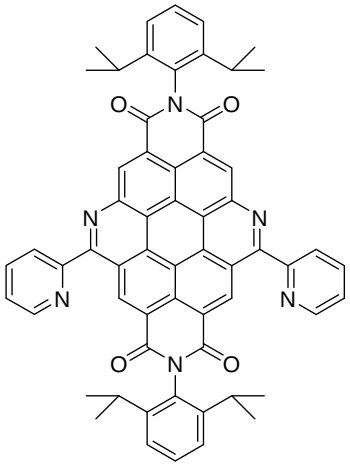

64

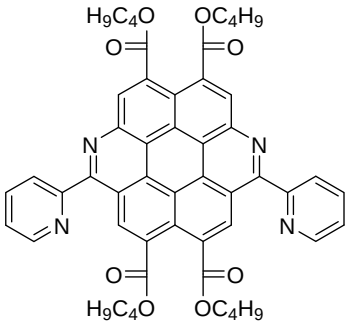

66

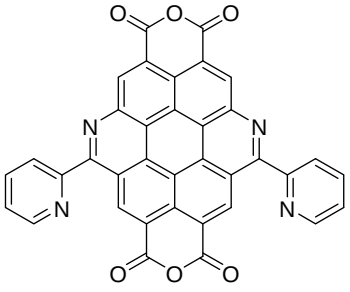

67

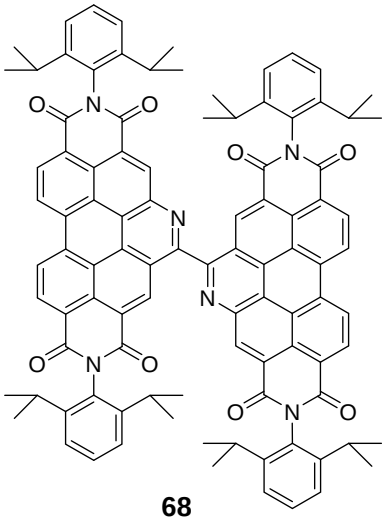

68

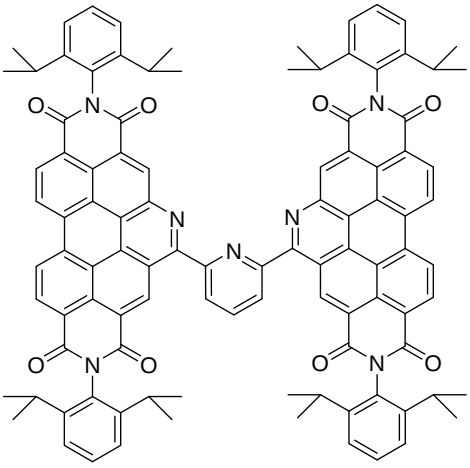

69

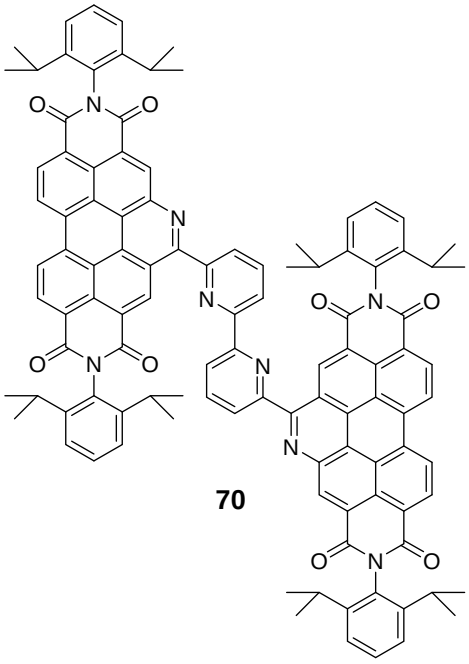

70

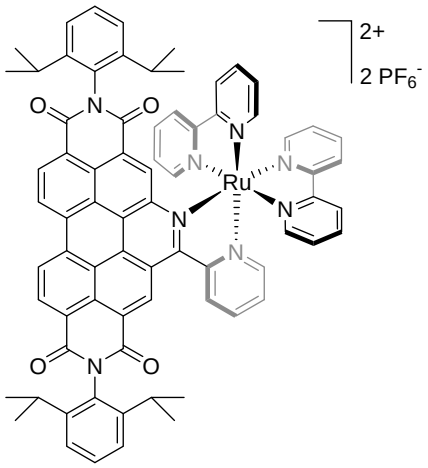

[Ru(bpy)$_2$(ab-PBI][PF$_6$]$_2$ **71**

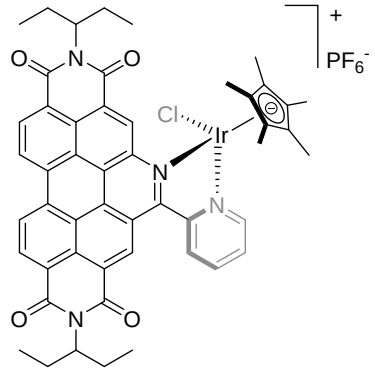

[Cp*Ir(ab-PBI)Cl][PF$_6$] **72**

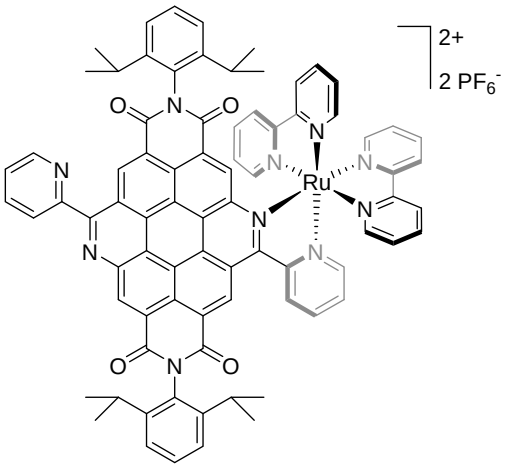

[Ru(bpy)$_2$(*anti*-(ab)$_2$-PBI)][PF$_6$]$_2$ **73**

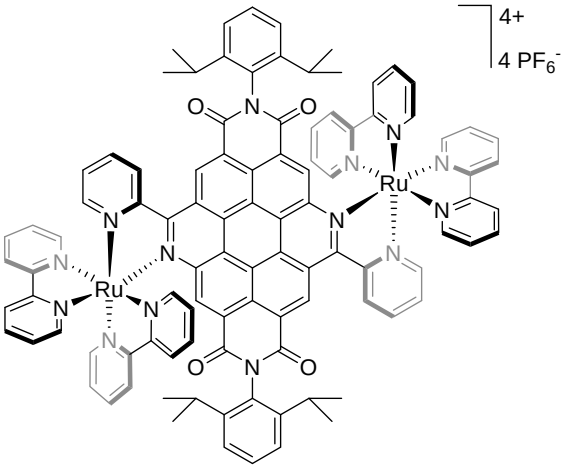

[Ru(bpy)$_2$(*anti*-(ab)$_2$-PBI)Ru(bpy)$_2$][PF$_6$]$_4$ **74**

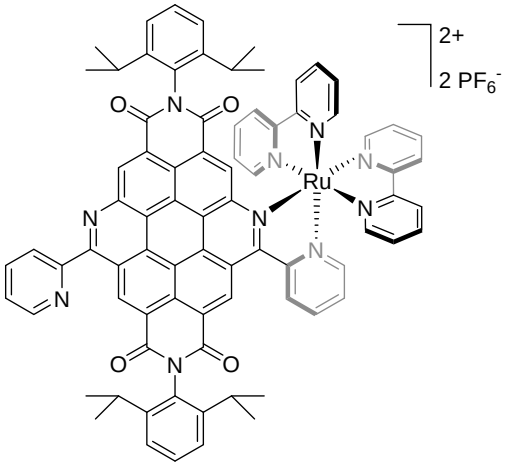

[Ru(bpy)$_2$(*syn*-(ab)$_2$-PBI)][PF$_6$]$_2$ **75**

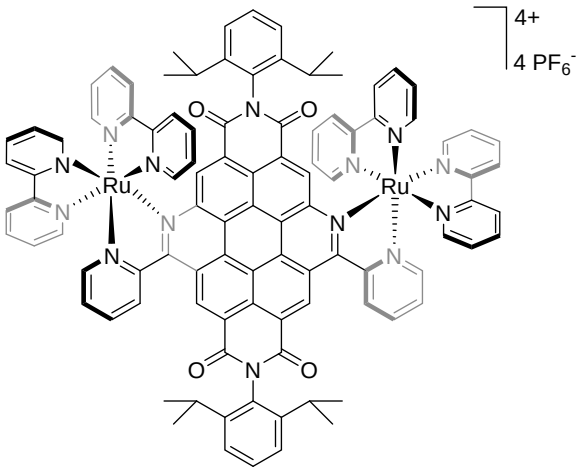

[Ru(bpy)$_2$(*syn*-(ab)$_2$-PBI)Ru(bpy)$_2$][PF$_6$]$_4$ **76**